Quantum Computation in Ultra-thin Topological Insulator Films

Kexin Zhang

Department of Physics, Cavendish Laboratory
University of Cambridge

This dissertation is submitted for the degree of
Doctor of Philosophy

Girton College

September 2019

I would like to dedicate this thesis to my loving mum ...

Declaration

This thesis is the result of my own work and includes nothing which is the outcome of work done in collaboration except as declared in the Preface and specified in the text. It is not substantially the same as any that I have submitted, or, is being concurrently submitted for a degree or diploma or other qualification at the University of Cambridge or any other University or similar institution except as declared in the Preface and specified in the text. I further state that no substantial part of my thesis has already been submitted, or, is being concurrently submitted for any such degree, diploma or other qualification at the University of Cambridge or any other University or similar institution except as declared in the Preface and specified in the text. It does not exceed the prescribed word limit for the relevant Degree Committee.

Kexin Zhang
September 2019

Acknowledgements

I would like to begin by thanking Prof. Crispin Barnes for supervising me throughout the whole course of my PhD. His advice, encouragement, and ideas have all had a significant impact on this work and none of its parts would have been possible without his support. I would also like to express my gratitude to Mr. Hugo Lepage for numerous discussions about physics and the project, and his encouraging words when I face difficulties and challenges in my research. I also want to thank members of the Thin Film Magnetism groups for their friendship and inspiring discussions during our group meetings, in particular to Aleksandar Nikolic, David Arvidsson-Shukur, Mrittunjoy Guha-Majumdar, Jacek Mosakowski, Matthew Applegate, Hugo Lepage, Aleks Lasek, Niall Devlin and Yordan Yordanov. I would like to give special thanks to Hugo Lepage, Aleks Lasek, Niall Devlin for helping me with grammar checking of my thesis. I would also like to thank Jieyi Liu for helpful discussions about experiments, from which I have learnt a lot.

I acknowledge funding from the China Scholarship Council and Cambridge trust.

I am also deeply thankful to the authorities of Girton College for all the academic and financial support I received from them. Girton College has offered me a warm and friendly environment during my stay at Cambridge. I had met many nice people there and had a very good time. I would like to give special thanks to my tutor Dr. Sophia Shellard. Her support has given me enormous courage to face and overcome the difficulties and challenges arisen in my research and life.

I want to give thanks to my friends at Cambridge. In particular to Yujun Qiao, Jinqi Fu, Shanshan Yan, Jiale Feng, Shikang Liang, Huiru Lian, Chen Chen, and all others. Thank you for making my life at Cambridge happy and colourful. Thank you for all of your supports.

Finally, I would like to thank my family, in particular my beloved mother, for her care and love during all these years. You are the one who guided me throughout life and encourage me to pursue my dream. I could not accomplish this work without your encouragement and wise words and all of your support. I am deeply grateful for it.

Abstract

In the past several decades quantum computation has become a rapidly developing research area. The properties particular to quantum systems such as superposition of quantum states, wave function collapse, and quantum entanglement have shone a path to a type of ultra-high-speed and powerful computation that could never be achieved with classical computers, even modern supercomputers. However, there are requirements for building a practical quantum computer and practical schemes of quantum computing usually have to make trade-offs between different requirements. In an ideal case, we would have a quantum computer consisting of many entangled quantum bits (qubits) that have long decoherence times and effective schemes to initialise, control and measure the quantum bits. However, existing implementations of quantum computers have to compromise between different requirements, and we have not yet achieved a quantum computer with full capacity as described in theory. At the same time, the development of solid state physics has brought many new possibilities for quantum computation. The recently discovered topological insulator (TI) has been proposed as a useful material potentially for spintronics and quantum computation owing to its unique topologically-protected surface states. In this thesis, we will investigate theoretically and numerically whether it is possible to construct a suitable two-level quantum system in a TI for quantum computation. We investigate schemes to initialise, control and measure the quantum bits in an ultra-thin TI film.

The thesis is structured as follows: Chapter 1 serves as an introduction to quantum computation, in which we introduced the concept of the Bloch sphere and the requirements for quantum computing and give a brief review of actively researched physical implementations. In Chapter 2, we will focus on the material we use for the physical implementation in this thesis - a 3D TI. We will introduce some concepts essential for the understanding of TIs such as the topological phase and then concentrate on the low energy limit which we used throughout the thesis. In the last part we introduce Floquet-Bloch theory, which is useful for the study of a time-periodic Hamiltonian. In Chapter 3, we introduce the numerical methods used in the study: the finite difference method for spatial discretisation, the staggered leapfrog method and Floquet matrix method for temporal discretisation. In Chapter 4, we present our work for constructing a static charge qubit in the TI system, and effective schemes to initialise,

control and measure a qubit. In Chapter 5, we present our work for constructing a static spin qubit in the TI system and effective schemes to initialise, control and measure a qubit. In Chapter 6 we extend our TI system to include time-periodic fields and present our work for constructing different types of charge qubit and spin qubit in this system, together with an effective scheme to initialise, control and measure a qubit. In Chapter 7, we summarise our work and propose possible work to be done on this topic in the future.

Table of contents

Chapter 1

Introduction

1.1 Introductory remarks

In 1936, Alan Turning proposed a mathematical model of an *automatic machine*. This is a universal machine that can operate under a set of rules and produce a specific output for a given input [110]. Nowadays, the computer has become a common and important tool that pervades society from scientific research to our daily life. Thanks to the development of semiconductor physics, we can make smaller and higher quality electronic chips that are the core of a computer. However, scientists have realised that we are approaching the limit of the power that a classical computer can reach. Is it possible to pursue even greater computational power? The answer might be linked to another important breakthrough in science at the beginning of the 20th century - the discovery of quantum mechanics. After the very first proposals of quantum computing by Benio[11], Manin[79], Feynman[31] and Deutsch [25], research on how to exploit quantum properties of a system for information and computation purposes has never ceased. The quantum properties - superposition of quantum states, wavefunction collapse, and quantum entanglement would potentially make quantum computing far more powerful than the current computers in solving some specific problems requiring a huge amount of bits and time. However, it is not easy to build such a machine. Many physical platforms have been proposed to build a quantum computer such as quantum computers based on photonic qubits [120], trapped ions [33], semiconductor quantum dots [43] and superconducting quits (IBM Q Experience). Each has its own advantages and drawbacks. Any particular platform provides a trade-off between different requirements, such as long decoherence times, qubit controllability and integrability of the system with current techniques (see [86] for a detailed discussion). Those factors together determine the ultimate scalability of an implementation. Until now, there is not yet a qualifying quantum computer that is ready for the demands of today's computing industry.

However, the field of quantum computing is not developed on its own. Development of other fields such as quantum information, quantum communication and semiconductor physics have contributed enormously to the field and have brought with them new energy. In this thesis, we will study such an example. Bi_2Se_3, identified as a 3D time-reversal invariant topological insulator just a decade ago [126], shows intriguing properties of electron conduction on its surfaces when interfaced with a trivial insulator such as air. In particular, the electrons flowing on its surfaces show helical spin texture and are immune to time-reversal invariant local perturbations [3]. TIs have stimulated the field of condensed matter physics and are actively under research [107] [51] [93] [34]. It is proposed to be potentially useful for the applications in spintronics and quantum computation [51]. In this thesis, we will investigate how to use TI (Bi_2Se_3 specifically) as a physical platform for quantum computing and study how to initialise, control and read out a single quantum bit.

In the rest of this chapter, we will introduce some basic concepts for quantum computation and the requirements for a valid quantum computation proposal. Then we will briefly review some physical implementations for quantum computing under active research.

1.2 A general background on quantum computation

The *bit* (binary digits) is the essential concept in classical computation and classical information. It is represented by a binary number, usually denoted as 0 and 1. Every piece of information stored in a classical computer is represented by a bit. In quantum computation and quantum information, an analogy to a bit is called a quantum bit, qubit for short. It is represented by $|0\rangle$ and $|1\rangle$. Unlike the classical bits which only take values of 0 or 1, as the heads and tails of a coin, a qubit can take any intermediate states between $|0\rangle$ and $|1\rangle$ and forms a linear combination (superposition) of the two:

$$|\Phi\rangle = \alpha\,|0\rangle + \beta\,|1\rangle\,, \tag{1.1}$$

with the normalisation condition:

$$|\alpha|^2 + |\beta|^2 = 1. \tag{1.2}$$

$|0\rangle$ and $|1\rangle$ are two orthogonal quantum states and they form a two-dimensional vector space. α and β are sometimes called amplitudes. Every time we measure a qubit, the wavefunction will collapse into $|0\rangle$ or $|1\rangle$, with a probability $|\alpha|^2$ and $|\beta|^2$. If we measure the same qubit state repeatedly, we would be able to extract the information of the linear combination amplitudes of the qubit. This capability of superposition of quantum states, together with

quantum entanglement, extensively enrich the information that can be stored in a quantum system and make them so powerful. To illustrate this, we can compare the information stored in a classical computer of n bits and in a quantum register of n qubits. The information stored in n bits can be described by an array of length n, while for the quantum computer, an n-qubits entangled quantum state can produce 2^n different results, thus the length of array required goes exponentially as 2^n. Therefore, if we have 400 qubits, we have an equivalent classical bits array of length 2^{400}, which has exceeded the number of atoms in the whole universe!

This extraordinary capability of storing a huge amount of information in a quantum system is only the tip of the iceberg. Qubits also provide a possibility to do multiple operations simultaneously and can accomplish some tasks that are impossible on a classical computer. In order to exploit the power of qubits in a quantum calculation, specific algorithms are required. Those quantum algorithms have provided quantum computers with advantages over classical computers in specific tasks. Some famous examples are Shor's factorisation algorithm [103], the Deutsch-Jozsa algorithm [24], or Grover's algorithm for database search [45].

1.2.1 The Bloch sphere

The Bloch sphere is a geometric representation of a qubit state (Fig. 1.1). It provides a useful tool to visualise a single qubit state and it is a fantastic platform to test ideas in quantum computation and quantum information. A point on the Bloch sphere represents a pure quantum state, while a point inside the Bloch sphere represents a mixed quantum state. A pure quantum state is represented by a single state vector, while a mixed quantum state is a statistical ensemble of pure states. A mixed state can be represented by a density matrix and it appears when the complete information of the entire system is inaccessible. For example, when the quantum system under investigation is entangled with its surroundings, the states of the environment are inaccessible. We need to use mixed states to represent the entanglement of the quantum state with its surroundings. The mixed state represents the decoherence of a qubit due to interaction with its environment. In this thesis, our focus is on understanding how to control a single qubit in a pure quantum state. Consideration of decoherence is beyond the scope of the thesis. This is partly because the complexity it would add to the analysis and partly because decoherence mechanisms in TI materials are simply not known at the present time. The Bloch sphere is therefore our main playground to investigate TI single qubits. We should notice that the Bloch sphere is designated for a single qubit, and there are no simple geometric representations for multiple qubits. A qubit state on

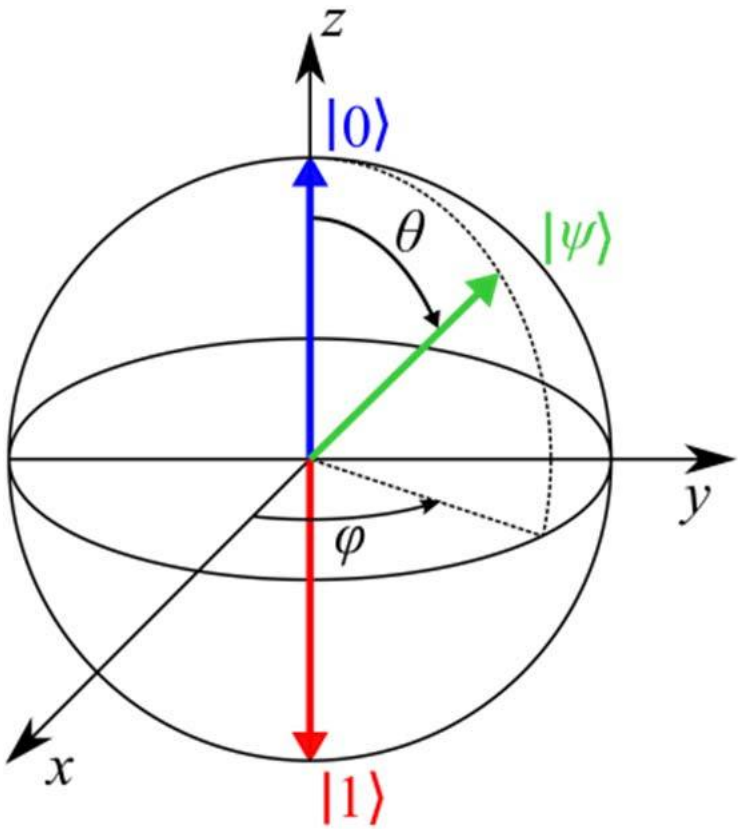

Fig. 1.1 A Bloch sphere, figure taken from [100]

the Bloch sphere is described by:

$$|\Phi\rangle = \cos\left(\frac{\theta}{2}\right)|0\rangle + e^{i\phi}\sin\left(\frac{\theta}{2}\right)|1\rangle . \tag{1.3}$$

The state $|0\rangle$ and state $|1\rangle$ are on the north and south pole respectively. All of the linear combinations of the two states are located on the Bloch sphere between the poles. The Bloch sphere is important in experiments describing single-qubit rotation. To define a qubit rotation, we need to define a rotational axis and the centre of rotation on the Bloch sphere. If we want to rotate a qubit to an arbitrary position on the Bloch sphere, we need to do two rotations with respect to to two orthogonal axes according to Euler's rotation theorem. In this thesis, we decide to study the standard σ_x, σ_y and σ_z rotations which are rotations to the x, y, z axes, separately. The rotational matrices of the three rotations are [85]:

$$\mathscr{R}_x = \begin{pmatrix} \cos\left(\frac{\theta}{2}\right) & -i\sin\left(\frac{\theta}{2}\right) \\ -i\sin\left(\frac{\theta}{2}\right) & \cos\left(\frac{\theta}{2}\right) \end{pmatrix}, \tag{1.4}$$

$$\mathscr{R}_y = \begin{pmatrix} \cos\left(\frac{\theta}{2}\right) & -\sin\left(\frac{\theta}{2}\right) \\ \sin\left(\frac{\theta}{2}\right) & \cos\left(\frac{\theta}{2}\right) \end{pmatrix}, \tag{1.5}$$

$$\mathscr{R}_z = \begin{pmatrix} e^{-i\frac{\theta}{2}} & 0 \\ 0 & e^{i\frac{\theta}{2}} \end{pmatrix}. \tag{1.6}$$

1.2.2 The five requirements for quantum computation

In 2000, DiVincenzo has proposed five requirements for the physical implementation of a quantum computer [27]. They are:

- I. *A scalable system with well-defined qubit states.* A quantum computer must contain multiple qubits and each qubit can be well characterised in a quantum two-level system. As introduced at the beginning of this section, a qubit is written as a linear combination of the basis states $|0\rangle$ and $|1\rangle$ in the two-dimensional complex vector space. A two-qubit state is written as a linear combination of the basis states $|00\rangle$, $|01\rangle$, $|10\rangle$, $|11\rangle$ in the four-dimensional complex vector space. The system should be capable to contain a collection of N qubits that span a 2^N dimensional complex vector space. A single qubit should be *well characterised.* This means several different things. We need to know the internal Hamiltonian of a qubit and the corresponding eigenstates and energies. Also, if there are other energy levels in the system, we need to know the coupling of the qubit states (i.e. $|0\rangle$ and $|1\rangle$) with these states and minimise the probability of the

qubit to go to these states. We need to know the interaction of the qubit with other qubits and with the external field that is used to manipulate the qubit.

- II. *The ability to initialise the qubits to a fiducial state.* Before we start a computational task, we need to set the qubit in a known state. This is a prerequisite for computation since we cannot manipulate an unknown state to output a trustful result. In quantum computation, this is important also for another reason. Quantum error correction requires a continuous fresh supply of qubits in a low-entropy state. Moreover, how fast the qubits can be set to a fiducial state is also of interest. There are in general two ways to bring a qubit to a fiducial state such as $|0\rangle$. If the qubit state is the ground state of the system, we can let the system cool down naturally. Otherwise, we can make a measurement which projects the qubit on to the state of interest or apply some external pulses to rotate a state into the desired one.

- III. *Longer decoherence time than the gate operating time.* Decoherence characterises the interactions of the qubit with its environment. A simplified definition for this time is that it is the characteristic time for a qubit in a pure state $\alpha|0\rangle + \beta|1\rangle$ to be transformed into the mixed state $\rho = |\alpha|^2|0\rangle\langle 0| + |\beta|^2|1\rangle\langle 1|$ entangled with the environment (a more detailed general discussion on this topic can be found in [85]). Apart from the interaction of a single qubit with its surroundings, the possibility of decoherence of the correlated neighbouring qubits should be considered as well. Because decoherence is identified as the principal mechanism for the emergence of classical behaviour in a quantum system, we need to keep the decoherence time long enough to maintain the quantum properties of the system for our intent. The decoherence times link to different degrees of freedom of the qubit and some are irrelevant to the property we are interested in for the state to be a qubit (e.g. the position of a spin qubit), therefore it is the relevant decoherence time that is important. The relevant decoherence time should be much longer than the gate operation time for quantum computation and it is found that a successful quantum computing calculation can be performed if a relevant decoherence time is 10^4-10^5 times the operation time [92].

- IV. *A universal set of quantum logic gates.* The requirement for performing an arbitrary calculation is at the core of quantum computation. We need to be able to perform unitary transformations on the qubits to bring them to desired states. These unitary transformations are implemented physically as quantum logic gates. Fortunately, any arbitrary unitary transformations can be decomposed into a sequence of single-qubit transformations and two-qubit transformations [22]. It is thus possible to define a universal set of quantum gates with a finite number of quantum gates [6] [26]. However,

in reality, the gates are not perfect and both systematic and random errors need to be taken into consideration in the implementation. We need to keep those errors small enough such that the error correction schemes are effective to produce reliable computation outcomes from these unreliable gates. One more complication is that the error correction requires a fully parallel operation. This means that we need to be able to address fractions of qubits in the implementation of gate operations simultaneously. Another factor to consider is that the controlling apparatus are made of quantum mechanical parts as well. Therefore, we need to carefully check that they do not produce any undesired entanglement with our quantum computer.

- V. *A qubit-specific measurement capability.* Finally, we need to be able to read out the computational result, which means that we need to be able to measure the specific qubit. In an ideal case, we desire the measurement of a qubit to be isolated and not dependent on its surroundings nor the nearby qubits. At the same time, measuring a qubit does not cause any changes in other parts of the quantum computer. We say that this ideal measurement has a quantum efficiency of 100%. In reality, the quantum efficiency is always less than this value. However, the quantum efficiency can be less than 100% for quantum computation: there is a trade-off between quantum efficiency and other computational resources. For example, the quantum efficiency of a single-bit output can be improved by repeating the calculation more times or copying the qubit value on a particular basis; however, this increases the computational costs of other aspects. If the measurement can be accomplished in a timescale of 10^{-4} of the decoherence time, its repeated application is beneficial to simplify the process of quantum error correction.

1.2.3 Quantum logic gates

A quantum register is constructed from a quantum circuit consisting of wires and quantum logic gates. Wires can carry around information while quantum logic gates can manipulate a state and change it from one form to another. In classical computation, a small set of logic gates (AND, OR, NOT, etc.) is sufficient to do an arbitrary calculation and we say that the set of logic gates is universal for computation [85]. In a quantum computer, it is also possible to define a universal set of quantum logic gates for quantum computation [6] [26]. It has been proven that a set of quantum logic gates consisting of single-qubit logic gates and entangled two-qubit logic gates is a sufficient set of universal quantum gates to approximate an arbitrary operation to any desired accuracy for a n-qubit system [22]. There are various choices for the universal set of quantum gates. Here we illustrate a universal set of quantum gates consisting

of three gates [85]: the Hadamard gate H, the phase-shift $R(\pi/4)$ gate and the controlled not (cNOT) gate. The first two gates act on a single qubit basis $(|0\rangle, |1\rangle)^T$ and are written as:

$$H = \frac{1}{\sqrt{2}} \begin{pmatrix} 1 & 1 \\ 1 & -1 \end{pmatrix}, \tag{1.7}$$

$$R(\pi/4) = \begin{pmatrix} 1 & 0 \\ 0 & i \end{pmatrix}. \tag{1.8}$$

The controlled not(cNOT) gate acts on the two-qubit basis $(|00\rangle, |01\rangle, |10\rangle, |11\rangle)^T$ and is written as:

$$C_{NOT} = \begin{pmatrix} 1 & 0 & 0 & 0 \\ 0 & 1 & 0 & 0 \\ 0 & 0 & 0 & 1 \\ 0 & 0 & 1 & 0 \end{pmatrix}. \tag{1.9}$$

Quantum Control Theory

The main aim of this thesis is to understand how to control the rotation of a single qubit on the Bloch sphere and move it through a desired angle about a given direction. The general approach to this type of problem is quantum control theory. This theory concerns how a quantum system can be driven to a desired state by control methods [52] [8] [10]. Quantum control theory studies how to establish systematic methods to perform a control task via specifying a path in parameter space [54]. There are various control strategies under the topic of quantum control theory, such as coherent control, variable structure control and incoherent control [54]. The latter two strategies are involved when the quantum system is not controllable using coherent control along [54]. There is also a control strategy based on variational analysis with Floquet theory [116] [10]. This strategy can be very helpful for designing the temporal pulses with simple shapes and a few frequency components [10]. In this thesis we use basic elements of quantum control theory [54] that allow us to consider the effect of a finite rise time in the application of a control pulse. It was not found necessary to go beyond this level of sophistication to achieve $> 99\%$ fidelity for each of the qubits considered.

1.2.4 Physical realisations

In previous subsections, we have discussed a qubit as an abstract mathematical object that is mapped to real physical objects in quantum systems. Here we introduce some physical platforms for quantum computing that are under active research nowadays. For those

interested in this topic, more details on these physical implementations can be found in [33] and [68].

- *Trapped Ions.* Trapped-ion quantum computers are made of ions or charged atomic particles confined and suspended in free space by electromagnetic fields, either by a combination of electric and magnetic fields (Penning trap) [23], or by a time-dependent electric field (Paul trap)[89]. Because the qubits are made of individual ions, they are free of manufacturing defects and form very reliable qubits. The decoherence times are typically in the range of seconds and even longer [68]. They are very promising for building high-quantum-efficiency quantum computers. A significant technical challenge lies in maintaining the radiation control for a satisfying precision for the qubit manipulation [86]. In 2018, scientists can create a controllable 20-qubit entangled system based on trapped ions [33].

- *Photon.* Photons are appealing for quantum information because they interact relatively weakly with their environment; this means potentially long decoherence time for quantum computation. Besides, a photon can travel over long distances without losing coherence. This makes it perfect in long-distance quantum communication [123]. A photonic qubit is in general made of the two polarisation states of a photon. Photons in many ways are good for making qubits; their single-qubit gates can be performed with standard optical devices and they have long decoherence time. However, because they interact weakly, it is difficult to implement two-qubit gates [104]. In linear-optical quantum computing, a strategy to overcome this problem is to use a combination of single-photon operations and measurements which create an effective strong interaction that can be used to perform two-qubit gates (see [61] for a detailed review on linear-optical quantum computing). Significant technical progress with realising photonic quantum computation has been made in the past years such as lower photon loss rates approaching the requirement of quantum error correction and high-efficiency photon detectors [119] [2]. The main problem that is still difficult to solve is to develop a source that produces triplets of entangled photons efficiently [33]. By the time of 2018, an 18-qubit entangled photonic quantum computing system (with six photons and three degrees of freedom) has been proposed [120].

- *Semiconductor Quantum Dots.* Semiconductor qubits can be classified into two kinds depending on whether they are addressed optically or electrically. Optically gated qubits are optical active impurities or quantum dots that can induce strong interactions between photons. They significantly improve the capabilities of photonic qubits [33]. Some examples are the nitrogen-vacancy (NV) centre in diamond [37]

and self-assembled quantum dots [84]. The requirement for controlling each qubit individually with optical access poses constraints on the qubit densities, thus making very difficult to scale up the qubits to a large number [33]. However, this optical gated qubit is useful as an interface between material-based qubits and photonic qubits in quantum communication [123]. Electrically gated qubits on the other hand, have the potential to be scaled up to large amounts because of their small size and similar fabrication techniques to classical electronics. These qubits are defined and operated by applying voltages to lithographically defined metal gates on semiconductor surfaces [74]. However, the current hurdle for the field of electrically gated semiconductor qubits is to develop reliable and high-fidelity two-qubit gates [33]. At the same time, measurement precision needs to be improved and measurement methods need to be compatible with a large qubit array size.

- *Superconductors.* Superconducting quantum computing uses superconducting electronic circuits for quantum computation. A superconducting resonator is coupled to a nonlinear inductor to form an artificial atom at low temperatures: those artificial atoms have quantised energy [33]. The two lowest levels can be accessed in a controllable manner and a superconducting qubit is constructed with these states. The decoherence times of the qubits with the best fabrication techniques are around 100 microseconds today in simple single-mental-layered devices [33]. Several different ways to arrange the inductor, capacitor and Josephson junctions play a trade-off game between simpler control of the system and better isolation of qubits and control of performing quantum gates. However, unlike natural atoms, the superconducting qubits have manufacturing variations. Therefore, the control processor must be able to calibrate the system and the computational resources grow significantly fast when the qubit system is scaled up, which is the major challenge in the field of superconducting quantum computing. By 2018, IBM has announced a 16-qubit processor based on superconducting qubits.

1.3 The TI qubit

The main reason that TIs are considered to be promising materials for quantum computing and spintronics is the robustness of their surface states. These surface states are topologically protected by a combination of the spin-orbit coupling and the time-reversal symmetry in the material (more details about TIs can be found in Ch. 2) [46] [122] [14] [55] [64] [35]. These surface states are protected from backscattering from non-magnetic impurities and they exhibit weak anti-localisation [95] [42]. These properties make TI surface states robust against perturbations from their surroundings, which is highly desired in fault-tolerant

quantum computing. Strictly speaking, TI qubits are similar to semiconductor qubits. It is likely that they can be fabricated using standard techniques such as electron-beam lithography and etching to form a TI quantum dot. Moreover, the TI qubit (a two-level system) is defined naturally when the thickness of a TI is reduced below a critical value [71] or by using a parallel ferromagnetic layer [30]. This reduces the number of Schottky surface gates used and thus reduces the disturbance from surrounding gates. However, the TI qubit is a new idea, with four new types presented in this thesis for the first time, and there are therefore no experimental results to show the performance. The possible decoherence mechanisms in bulk TI materials are still under investigation [70] [53]. In this thesis, we will explore whether a TI qubit is feasible and how to control single-qubit rotations from a theoretical and numerical perspective. Consideration of decoherence and the two-qubit interaction fall outside the scope of this work. With limited computational resources, it made sense to first find all possible types of qubit in TI systems and show how they can be controlled. Decoherence can most simply be modelled by introducing random errors into multiple runs and leads to an exponential decrease in the amplitude of the off-diagonal elements in the qubit density matrix. This will be part of future research once the potential error mechanisms are better known. Modelling the two-qubit interaction for a realistic double-dot system was beyond our group's computational resources at the time of writing.

1.4 Summary and outline

In this chapter we introduced the fundamental concepts of quantum computing and the requirements for physically implementing a quantum computer. Then we reviewed some active implementations for quantum computing.

The rest of this thesis is organised as follows: in Ch. 2, we will provide some knowledge on the essential concepts used to understand the topological aspect of TI and an introduction to Bi_2Se_3 with the focus on a low energy model proposed by Liu *et al.* [72]. We will present a detailed discussion on how this model was derived from the crystal's atomic states. Then we will talk about the Floquet-Bloch theory which is useful for studying a time-periodic system. In Ch. 3, we will present a brief description of the numerical methods we used to approach the problems in the thesis. In Ch. 4 - Ch. 6 we study four different types of TI qubit which are: a static charge qubit (Ch. 4), a static spin qubit (Ch. 5)and two Floquet qubits (Ch. 6). A summary of the present work and a discussion of further work are presented in Ch. 7.

Chapter 2

Theoretical Background

2.1 Introduction

This chapter aims to provide the reader with a general understanding of the theory underlying topological insulators (TIs) and relevant methods used to study it throughout this thesis. This chapter is divided into two main parts: in the first part we discuss essential concepts to understand a topological insulator followed by a detailed discussion of the model TI Hamiltonian used throughout this thesis. We then discuss Floquet-Bloch theory. This is important in the study of TIs under a periodic field.

2.2 Topological insulators

In 1980, von Klitzing *et al.* discovered the quantum hall effect (QHE) in a high-mobility 2D semiconductor under a strong magnetic field [58]. This phenomenon was later recognised by Thouless, Kohmoto, Nightingale, and den Nijs (TKNN) [106] to be topological, in the sense that the Hilbert space of the QHE has an associated non-trivial topology, which distinguishes it from that of an ordinary band insulator. They identified a topological number that is associated with this non-trivial topology - the TKNN number (also now referred to as the first Chern number). This is a single example of many different topological phases that exist [99]. Its discovery was the first in the new field of topological condensed matter. One such exciting discovery is the time-reversal-invariant topological insulators. TI can exist in a 2D material or a 3D material. The bulk-edge correspondence ensures that gapless conducting edge/surface states appear at the boundary of a TI and a trivial insulator. Because the time-reversal (TR) symmetry is preserved in a TI, these edge/surface states are protected and cannot be disturbed by local perturbation in the material. This protection against backscattering means that

TIs have potential applications in low-power electronics and other quantum devices. In this section, I will provide a brief introduction to the concepts of topological band theory for formally determining a topological phase. The focus will be on the 3D topological insulator which is the topic of this thesis. I will then introduce the model Hamiltonian of a 3D topological insulator constructed by Liu *et al* [72], which is the fundamental model we used throughout this thesis. This section provides a short presentation of relevant theories and methods. Interested readers are directed to read these reviews [3] [48][47] for more details.

2.2.1 Essential concepts for topological insulators

In order to understand the topological significance of a TI, we will introduce some important concepts in the topological band theory following the approach of Bernevig and Hughes [13].

Berry Phase

The Berry phase is an important concept in the discussion of topological phases. It represents an accumulated quantum-mechanical phase when the wavefunction is going around the k space in a close loop [15]. It is the foundation of a topological invariant which is used to identify the non-trivial topological phase.

Considering a quantum system $H(\mathbf{R}(t))$ with time-dependent parameters $\mathbf{R}(t)$, when we change the system $H(\mathbf{R}(t))$ adiabatically, we can write out the instantaneous eigenstates $|\phi(\mathbf{R}(t))\rangle$ of the system H as:

$$H(\mathbf{R}(t))\,|\phi(\mathbf{R}(t))\rangle = E(\mathbf{R}(t))\,|\phi(\mathbf{R}(t))\rangle\,. \tag{2.1}$$

The time-dependent Schrodinger equation for the system is:

$$H(\mathbf{R}(t))\,|\Phi(t)\rangle = i\hbar\frac{d}{dt}\,|\Phi(t)\rangle\,. \tag{2.2}$$

When a system is evolving adiabatically, the eigenstates will maintain themselves and does not cross each other, and we have:

$$|\Phi(t)\rangle = e^{-i\theta(t)}\,|\phi(\mathbf{R}(t))\rangle\,. \tag{2.3}$$

Here, the phase term $e^{i\theta(t)}$ is the only degree of freedom of the eigenstate when the system is changing adiabatically.

Substituting 2.3 into 2.2, we arrive at:

$$E(\mathbf{R}(t))\,|\phi(\mathbf{R}(t))\rangle = i\hbar(-i\frac{d}{dt}\theta(t)+\frac{d}{dt})\,|\phi(\mathbf{R}(t))\rangle\,, \tag{2.4}$$

taking scalar product with $\langle\phi(\mathbf{R}(t))|$, we have:

$$E(\mathbf{R}(t)) - i\hbar\,\langle\phi(\mathbf{R}(t)|\frac{d}{dt}|\phi(\mathbf{R}(t)\rangle = \hbar\frac{d}{dt}\theta(t). \tag{2.5}$$

Therefore phase $\theta(t)$ is:

$$\theta(t) = \frac{1}{\hbar}\int_0^t \Big[E(\mathbf{R}(t)) - i\,\langle\phi(\mathbf{R}(t)|\frac{d}{dt}|\phi(\mathbf{R}(t)\rangle\Big]dt. \tag{2.6}$$

The first part on RHS represents a trivial dynamical phase, which only depends on the energy of the eigenstate. The second part represents a non-trivial phase - the Berry phase γ. It contains information about how the wavefunction of the state evolves with $\mathbf{R}$.

$$\begin{aligned} |\Phi(t)\rangle &= e^{i\frac{1}{\hbar}\int_0^t E(\mathbf{R}(t))dt}e^{i\gamma}\,|\phi(\mathbf{R}(t))\rangle\,,\\ \gamma &\equiv i\int_0^t \langle\phi(\mathbf{R}(t)|\frac{d}{dt}|\phi(\mathbf{R}(t)\rangle\,dt. \end{aligned} \tag{2.7}$$

From Eq. 2.7 we can see the Berry phase is not dependent on time explicitly. By a change of variables, we have:

$$\gamma = i\int_0^{\text{end of cycle}} \langle\phi(\mathbf{R})|\frac{d}{d\mathbf{R}}|\phi(\mathbf{R})\rangle\,d\mathbf{R}. \tag{2.8}$$

Therefore, if the system goes back to its original state at time T, the eigenstate $|\phi(\mathbf{R}(t))\rangle$ will be same as the eigenstate $|\phi(\mathbf{R}(t=0))\rangle$, with an extra phase $e^{-i\theta(t)}$ at most.

Time reversal symmetry (TRS)

The effect of time-reversal (TR) operator Θ is to reverse the arrow of time. Therefore it affects all quantities associated with the direction of time flow but it does not affect any spatial quantities, and $[\Theta,\mathbf{X}]=0$. For a half-spin system, the TR operator is written as:

$$\Theta = -is_yK, \tag{2.9}$$

where s_y is the y component of the spin operator and K is the complex conjugate operator. The spin is rotated by π degrees under the effect of TR operator and by applying Θ twice,

the spin goes back to its original state but with a phase of -1. Therefore, we have:

$$\Theta^2 = -1. \tag{2.10}$$

Also, we have:

$$\begin{aligned} \langle \phi | \Theta | \psi \rangle &= - \langle \psi | \Theta | \phi \rangle , \\ \langle \Theta\phi | \Theta\psi \rangle &= \langle \psi | \phi \rangle . \end{aligned} \tag{2.11}$$

These properties of the TR operator stated above enable us to arrive at the Kramer theorem in a TRS preserved Bloch system. In a crystal Hamiltonian H, a general solution is written as:

$$H | \phi_{n\mathbf{k}} \rangle = E_{nk} | \phi_{n\mathbf{k}} \rangle , \tag{2.12}$$

and

$$| \phi_{n\mathbf{k}} \rangle = e^{i\mathbf{k}\cdot\mathbf{x}} | u_{n\mathbf{k}} \rangle . \tag{2.13}$$

$u_{n\mathbf{k}}$ is an eigenstate of the Bloch Hamiltonian. When H preserves TRS, we have :

$$H(-\mathbf{k}) = \Theta H(\mathbf{k}) \Theta^{-1}. \tag{2.14}$$

This identity means that in a TRS preserved system, we have a pair of states with $E(-k) = E(k)$ called a Kramer Pair. Because the Brillouin zone is periodic, at the boundary of Brillouin zone and Γ point (which are called TRIM points), $+k$ and $-k$ are degenerate (see Fig. 2.1). In a topological non-trivial system with TRS, the Kramer pair will 'switch partner' [3]. As a result, the surface states are guaranteed to cross any Fermi energy inside the bulk gap, forming Dirac cone structures (Fig. 2.1).

2.2.2 The Bi_2Se_3 family of topological insulators and their effective low energy models

In 2009, Zhang *et al.* [126] discovered a family of 3D time-reversal-invariant TI materials: Bi_2Se_3, Bi_2Te_3 and Sb_2Te_3. In fact, it is not the first time those materials are discovered. Those materials have been considered as good thermalelectric materials in history [82]. Due to the strong spin-orbit coupling effect present in these materials, the valence band and conducting band are inverted, just like the HgTe/CdTe quantum well heterostructures [65], and gapless helical states are formed on the surface of the materials.

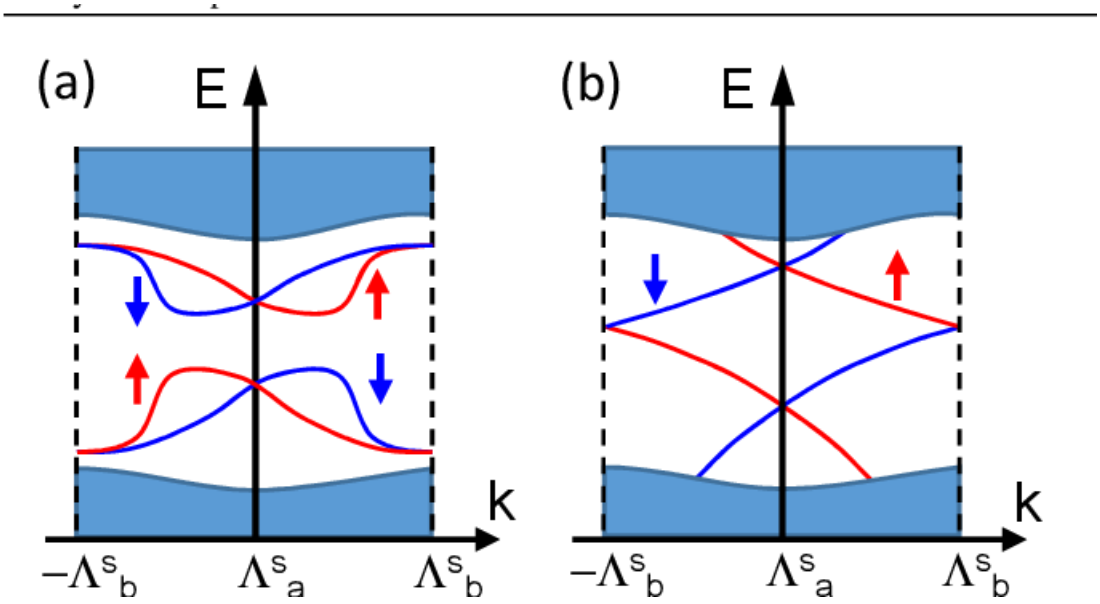

Fig. 2.1 a) A TRS preserved system with a trivial topological number; b) a TRS preserved system with a non-trivial topological number (figure adapted from [3]).

Crystal structure and atomic basis

Bi_2Se_3 family of TIs are layered, stoichiometric crystals. They share the same rhombohedral crystal structure with the space group $D^5_{3d}(R\bar{3}m)$ [126]. Here we take Bi_2Se_3 as an example. Each layer of Bi_2Se_3 is a triangle lattice consisting of a layer of purely Bi atoms or Se atoms. The Bi layer and Se layer grow alternatively on each other and form a five-layer structure (along the z direction in Fig. 2.2). This five-layer structure is tightly bonded together and form a unit cell of the crystal. This five-layer structure is the fundamental unit of the crystal structure of a TI and is called a quintuple layer (QL for short). The QLs are stacked together and form a complete Bi_2Se_3 crystal. The QLs are held together by the van der Waals force, which is much weaker than the bonding force between two atomic layers within a QL. Understanding the electronic states formed in a TI is important to understand its non-trivial electronic structure. From here we would like to guide the reader through a construction of the electronic states formed in TI from the atomic states of Bi and Se atoms. (A figure summarising the steps of constructing the electronic states from atomic orbits is Fig. 2.3.) The atomic configuration of Bi is $6s^26p^3$ and that of Se is $4s^24p^4$. The outermost p orbitals play an important role in the bonding of Bi and Se. Each atomic Bi (or Se) has three p orbitals: p_x, p_y, p_z. The coupling between the neighbouring layers are the strongest. From Fig. 2.2, we see that a Bi and Se atom are always neighbours; therefore, a coupling is induced between their p orbits. This coupling pushes the energy levels of Bi atoms up and the energy levels of Se atoms down. Because the central Se atomic layer is coupled to two Bi atomic

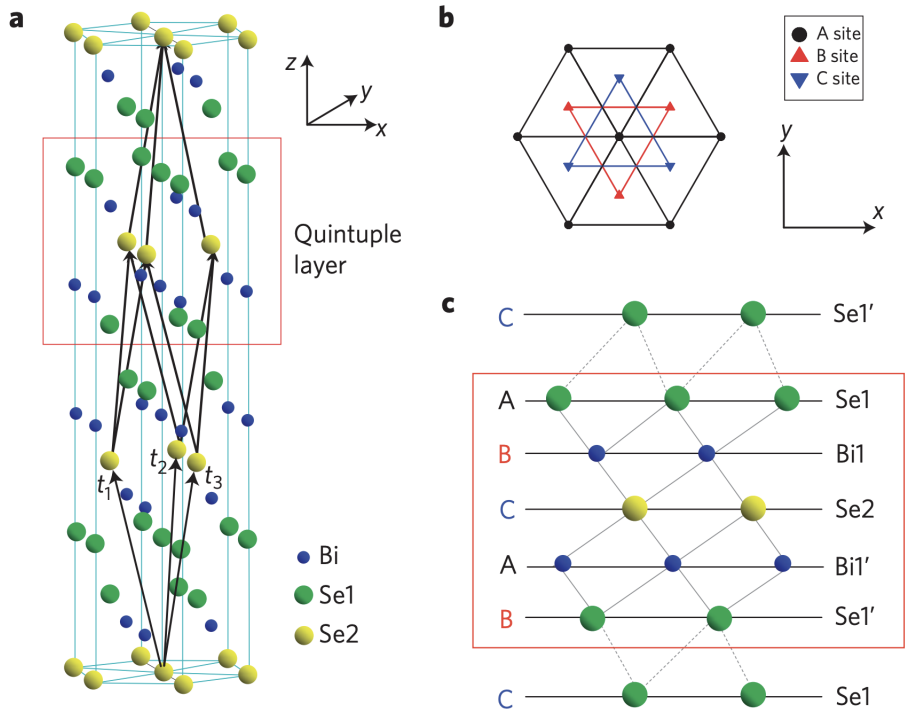

Fig. 2.2 The crystal structure of Bi_2Se_3, adapted from [126].

layers, it is different from the other two Se atomic layers in Fig. 2.2 and found to be lower in energy. Then, owing to the inversion symmetry in Bi_2Se_3, the electronic states in Bi_2Se_3 are also eigenstates of the Parity operator. Therefore, the atomic states between Bi (Se) atoms in the next neighbour layer combine into bonding and anti-bonding states with definite parity as:

$$\left|P1^{\pm}_{x,y,z}\right\rangle = \frac{1}{\sqrt{2}}(\left|B_{x,y,z}\right\rangle \mp \left|B'_{x,y,z}\right\rangle), \tag{2.15}$$

$$\left|P2^{\pm}_{x,y,z}\right\rangle = \frac{1}{\sqrt{2}}(\left|S_{x,y,z}\right\rangle \mp \left|S'_{x,y,z}\right\rangle). \tag{2.16}$$

The upper index indicates the parity of the $|P1(P2)\rangle$ state. Because the crystal has a layered structure, the energy of p_z orbits would be slightly different from p_x and p_y orbits: this effect is called crystal field splitting. It is also found that the $\left|P1^{+}_{z}\right\rangle$ and $\left|P2^{-}_{z}\right\rangle$ orbits are near the Fermi level. In the last step, spin-orbit coupling (SOC) is considered and spin is included. The atomic SOC Hamiltonian is written as: $\hat{H_{so}} = \lambda \mathbf{s} \cdot \mathbf{L}$, where λ depends on the electrostatic potential of the atom. The states of the p_x and p_y orbits are combined into $p_{\pm}$

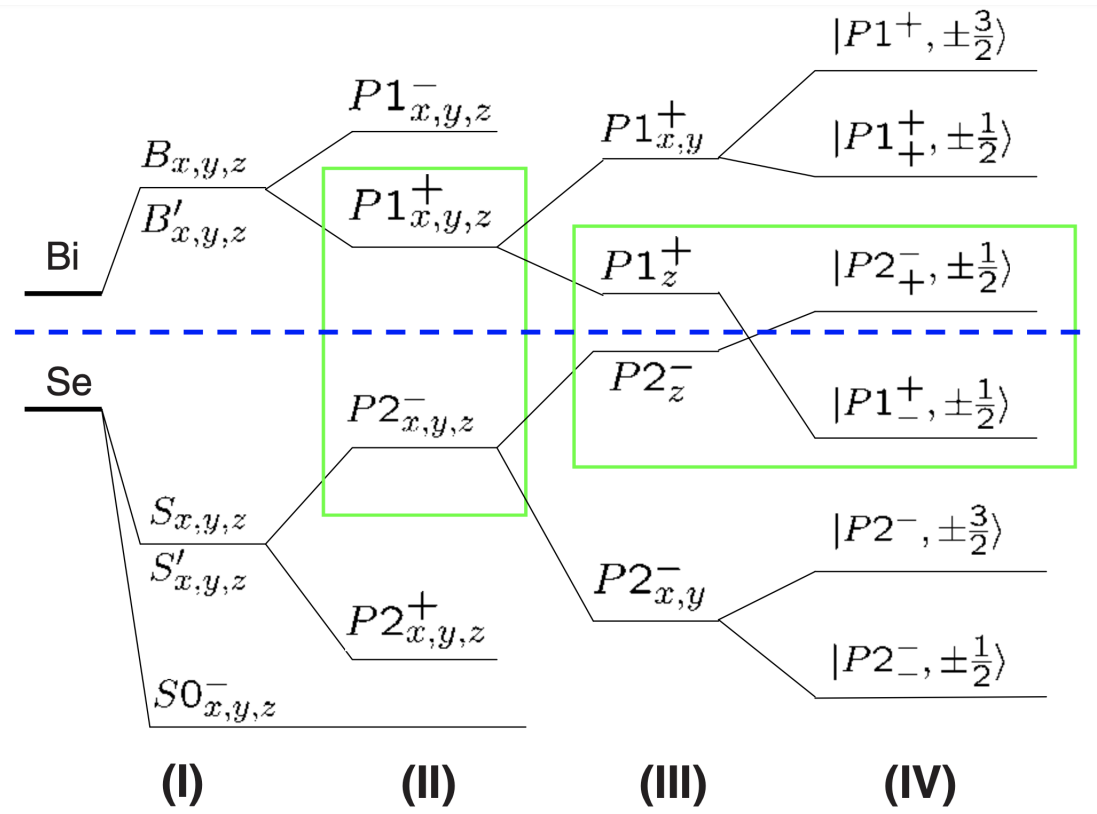

Fig. 2.3 The steps in the construction of the electronic states of a TI from atomic orbits, adapted from [72]. There are four steps needed to understand the band structure of a Bi_2Se_3: **(I)** the hybridization of the atomic orbitals of Bi and Se; **(II)** the formation of bonding and antibonding orbitals due to the inversion symmetry; **(III)** the crystal field splitting; **(IV)** the influence of the SOC.

with definite orbital angular momentum **L** written for convenience as:

$$|P1(2)_+\rangle = -\frac{1}{\sqrt{2}}(|P1(2)_x\rangle + i\left|P1(2)_y\right\rangle), \tag{2.17}$$

$$|P1(2)_-\rangle = \frac{1}{\sqrt{2}}(|P1(2)_x\rangle - i\left|P1(2)_y\right\rangle). \tag{2.18}$$

By introducing SOC to the system, a coupling is introduced between the $P_\pm$ and P_z orbits, and s_z and L_z are no longer good quantum numbers in the system. Since total angular momentum along z (J_z) is still conserved, we can re-express the basis states as eigenstates of J_z (this will be discussed in more detail in 2.2.2). SOC in fact lowers the $\left|P1_z^+\right\rangle$ levels and raises the $\left|P2_z^-\right\rangle$ levels (which are now mixed with $P_\pm$ states) and cause the valence band and conduction band to cross each other. This band inversion is crucial to the appearance of gapless surface states in a TI. The states $\left|P2_+^-, \pm\frac{1}{2}\right\rangle$ and $\left|P1_-^+, \pm\frac{1}{2}\right\rangle$ are found to be the four states near the fermi level. Those states form the basis of the low energy model Hamiltonian used to describe physics near the Fermi level.

Low-energy model Hamiltonian

The model Hamiltonian studied throughout this thesis is based on the low-energy model Hamiltonian of the Bi_2Se_3 family of 3D Topological insulators developed by Liu *et al.* 2010 [72]. In this paper [72], the model Hamiltonian is constructed using $\mathbf{k}\cdot\mathbf{p}$ theory and symmetry principles. The results of these two methods are found to be consistent. We state the model Hamiltonian here. Readers that are interested in a detailed derivation are referred to [72].

Liu's Model Hamiltonian to describe the low-energy physics of Bi2Se3, Bi2Te3 and Sb2Te3 is:

$$H_0 = C(\mathbf{k})I_4 + M(\mathbf{k})\Gamma_5 + B_0\Gamma_4 k_z + A_0(\Gamma_1 k_y - \Gamma_2 k_x), \tag{2.19}$$

where I_4 is 4×4 identity matrix and:

$$\Gamma_5 = \begin{pmatrix} 1 & 0 & 0 & 0 \\ 0 & -1 & 0 & 0 \\ 0 & 0 & 1 & 0 \\ 0 & 0 & 0 & -1 \end{pmatrix}, \Gamma_4 = \begin{pmatrix} 0 & -i & 0 & 0 \\ i & 0 & 0 & 0 \\ 0 & 0 & 0 & -i \\ 0 & 0 & i & 0 \end{pmatrix},$$

$$\Gamma_1 = \begin{pmatrix} 0 & 0 & 0 & -i \\ 0 & 0 & -i & 0 \\ 0 & i & 0 & 0 \\ i & 0 & 0 & 0 \end{pmatrix}, \Gamma_2 = \begin{pmatrix} 0 & 0 & 0 & 1 \\ 0 & 0 & 1 & 0 \\ 0 & 1 & 0 & 0 \\ 1 & 0 & 0 & 0 \end{pmatrix},$$

$$\begin{aligned} C(\mathbf{k}) &= C_0 + C_1 k_z^2 + C_2 |k_{||}|^2, \\ M(\mathbf{k}) &= M_0 + M_1 k_z^2 + M_2 |k_{||}|^2, \\ k_{||} &= k_x - i k_y. \end{aligned}$$

The Γ matrices in the model Hamiltonian are derived from symmetry principles. The constants $C_0, C_1, C_2, M_0, M_1, M_2, A_0$ and B_0 are material-dependent parameters derived from the **k**.**p** theory. These parameters can be obtained either from the scattering experiments (optical matrix elements) or via *ab initio* calculations [72]. The values of those parameters used throughout this thesis are adapted from Liu's paper [72] and are present in Ch. 2. In general, $C(\mathbf{k})$ represents the kinetic energy term of the electrons in the material, and changing C_0 can shift the energy levels of the topological insulator but does not change the relative energy difference of individual bands. $M(\mathbf{k})$ represents the effects of spin-orbit coupling to the electron kinetics in these materials. M_0 and M_1 are important parameters to determine the topological phase of a TI [73]. $M_0 M_1 < 0$ induces a bulk band inversion at the Γ point. In a TI, this comes from spin-orbit coupling, which drags the atomic basis $\left|P1_-^+, \pm\frac{1}{2}\right\rangle$ of Bi down and pushes the atomic basis $\left|P2_+^-, \pm\frac{1}{2}\right\rangle$ of Se up (see Fig. 2.3). $M_0 M_1 > 0$ and $M_0 M_1 < 0$, therefore, distinguish two different topological phases. The first order term A_0 represent a Rashba-type spin-orbit interaction which gives rise to the distinguishable property of the surface states of a TI - the spin-momentum-locking helical spin texture. B_0 induces a coupling between the atomic basis of Bi and Se atoms with the same spin. It is important for the formation of localised states on the surfaces.

Basis of total angular momentum and spin measurement

As mentioned previously in this section, the basis states can be written in terms of eigenstates of total angular momentum along the z direction as SOC is included. Here we will discuss this further, which is important for constructing the spin operator matrices of the system. Followed the discussion in the previous section, we can write p_x and p_y orbits as:

$$|P1(2)_+\rangle = -\frac{1}{\sqrt{2}}(|P1(2)_x\rangle + i\left|P1(2)_y\right\rangle), \tag{2.20}$$

$$|P1(2)_-\rangle = \frac{1}{\sqrt{2}}(|P1(2)_x\rangle - i\left|P1(2)_y\right\rangle). \tag{2.21}$$

Therefore, the matrix form of $H + H_{so}$ (H is the TI Hamiltonian without SOC) can be written as:

$$H + H_{so} = \begin{pmatrix} E_{\Lambda x(y)} + \frac{\lambda}{2} & 0 & 0 & 0 & 0 & 0 \\ 0 & E_{\Lambda x(y)} - \frac{\lambda}{2} & \frac{\lambda}{\sqrt{2}} & 0 & 0 & 0 \\ 0 & \frac{\lambda}{\sqrt{2}} & E_{\Lambda z} & 0 & 0 & 0 \\ 0 & 0 & 0 & E_{\Lambda z} & \frac{\lambda}{\sqrt{2}} & 0 \\ 0 & 0 & 0 & \frac{\lambda}{\sqrt{2}} & E_{\Lambda x(y)} - \frac{\lambda}{2} & 0 \\ 0 & 0 & 0 & 0 & 0 & E_{\Lambda x(y)} + \frac{\lambda}{2} \end{pmatrix}.$$

The basis states are: $(|\Lambda, p_+, \uparrow\rangle, |\Lambda, p_+, \downarrow\rangle, |\Lambda, p_z, \uparrow\rangle, |\Lambda, p_z, \downarrow\rangle, |\Lambda, p_-, \uparrow\rangle, |\Lambda, p_-, \downarrow\rangle)^T$. $\Lambda = P1^+, P2^-$, $E_{\Lambda x(y),z}$ are the energy values of the states $\left|\Lambda, p_(x(y), z)\right\rangle$ and λ is the SOC coupling determined by H_{so}. If we rewrite the Hamiltonian in a diagonal form, the new basis is:

$$\begin{aligned} |1\rangle &= |\Lambda, p_+, \uparrow\rangle, \\ |2\rangle &= u_+^\Lambda |\Lambda, p_z, \uparrow\rangle + v_+^\Lambda |\Lambda, p_+, \downarrow\rangle, \\ |3\rangle &= u_-^\Lambda |\Lambda, p_z, \uparrow\rangle + v_-^\Lambda |\Lambda, p_+, \downarrow\rangle, \\ |4\rangle &= u_+^\Lambda |\Lambda, p_z, \downarrow\rangle + v_+^\Lambda |\Lambda, p_-, \uparrow\rangle, \\ |5\rangle &= u_-^\Lambda |\Lambda, p_z, \downarrow\rangle + v_-^\Lambda |\Lambda, p_-, \uparrow\rangle, \\ |6\rangle &= |\Lambda, p_-, \downarrow\rangle, \end{aligned} \tag{2.22}$$

where the values $u_{\pm}^{\Lambda}$ and $v_{\pm}^{\Lambda}$ can be obtained by diagonalising the 2×2 matrix

$$\begin{pmatrix} E_{\Lambda x(y)} - \frac{\lambda}{2} & \frac{\lambda}{\sqrt{2}} \\ \frac{\lambda}{\sqrt{2}} & E_{\Lambda z} \end{pmatrix}.$$

Because H_{so} commutes with j_z, the basis can be written in terms of j_z. Since $|\Lambda, p_{\pm}\rangle = |\Lambda, l = 1, m_l = \pm 1\rangle$ and $|\Lambda, p_z\rangle = |\Lambda, l = 1, m_l = 0\rangle$, we can identify that $|\Lambda, p_+, \uparrow\rangle$ and $|\Lambda, p_-, \downarrow\rangle$ are the highest and lowest eigenstates of the total angular momentum operator along the z direction, respectively:

$$|\Lambda, p_+, \uparrow\rangle = \left|\Lambda, \frac{3}{2}, \frac{3}{2}\right\rangle, \tag{2.23}$$

$$|\Lambda, p_-, \downarrow\rangle = \left|\Lambda, \frac{3}{2}, -\frac{3}{2}\right\rangle. \tag{2.24}$$

The remaining states $\left|\Lambda, j, m_j\right\rangle$ can be obtained by applying the ladder operator $j_{\mp}$ to the states in Eq. 2.23 and Eq. 2.24. The full set of basis states in terms of eigenstates of J^2 and j_z is:

$$\begin{aligned}
|\Lambda, p_+, \uparrow\rangle &= \left|\Lambda, \frac{3}{2}, \frac{3}{2}\right\rangle, \\
|\Lambda, p_+, \downarrow\rangle &= \frac{1}{\sqrt{3}}\left(\left|\Lambda, \frac{3}{2}, \frac{1}{2}\right\rangle + \sqrt{2}\left|\Lambda, \frac{1}{2}, \frac{1}{2}\right\rangle\right), \\
|\Lambda, p_z, \uparrow\rangle &= \frac{1}{\sqrt{3}}\left(\sqrt{2}\left|\Lambda, \frac{3}{2}, \frac{1}{2}\right\rangle - \left|\Lambda, \frac{1}{2}, \frac{1}{2}\right\rangle\right), \\
|\Lambda, p_z, \downarrow\rangle &= \frac{1}{\sqrt{3}}\left(\left|\Lambda, \frac{1}{2}, -\frac{1}{2}\right\rangle + \sqrt{2}\left|\Lambda, \frac{3}{2}, -\frac{1}{2}\right\rangle\right), \\
|\Lambda, p_-, \uparrow\rangle &= \frac{1}{\sqrt{3}}\left(-\sqrt{2}\left|\Lambda, \frac{1}{2}, -\frac{1}{2}\right\rangle + \left|\Lambda, \frac{3}{2}, -\frac{1}{2}\right\rangle\right), \\
|\Lambda, p_-, \downarrow\rangle &= \left|\Lambda, \frac{3}{2}, -\frac{3}{2}\right\rangle.
\end{aligned} \tag{2.25}$$

By relating the basis in Eq. 2.25 and the basis states in Eq. 2.22, we can express basis of the atomic TI Hamiltonian in terms of basis states of the total angular momentum along the z

direction (j_z):

$$
\begin{aligned}
|1\rangle &= \left|\Lambda, m_j = \frac{3}{2}\right\rangle = |\Lambda, p_+, \uparrow\rangle\,, \\
|2\rangle &= \left|\Lambda_+, m_j = \frac{1}{2}\right\rangle = u_+^\Lambda\,|\Lambda, p_z, \uparrow\rangle + v_+^\Lambda\,|\Lambda, p_+, \downarrow\rangle\,, \\
|3\rangle &= \left|\Lambda_-, m_j = \frac{1}{2}\right\rangle = u_-^\Lambda\,|\Lambda, p_z, \uparrow\rangle + v_-^\Lambda\,|\Lambda, p_+, \downarrow\rangle\,, \\
|4\rangle &= \left|\Lambda_+, m_j = -\frac{1}{2}\right\rangle = u_+^\Lambda\,|\Lambda, p_z, \downarrow\rangle + v_+^\Lambda\,|\Lambda, p_-, \uparrow\rangle\,, \\
|5\rangle &= \left|\Lambda_-, m_j = -\frac{1}{2}\right\rangle = u_-^\Lambda\,|\Lambda, p_z, \downarrow\rangle + v_-^\Lambda\,|\Lambda, p_-, \uparrow\rangle\,, \\
|6\rangle &= \left|\Lambda, m_j = -\frac{3}{2}\right\rangle = |\Lambda, p_-, \downarrow\rangle\,.
\end{aligned}
$$

Therefore, it can be seen immediately that the electronic states are eigenstates of j_z. The double degenerated states $\left|P2_+^-, m_j = \pm\frac{1}{2}\right\rangle$ and $\left|P1_-^+, m_j = \pm\frac{1}{2}\right\rangle$ are the four states that are closest to the Fermi level.

After discussing the atomic origins of the electronic states of TI, we will look at how this is linked to measuring spin of TI surface states. We now know that the J_z operators with respect to the basis of the model Hamiltonian are ($\hbar = 1$):

$$
j_x = \begin{pmatrix} 0 & 0 & \frac{1}{2} & 0 \\ 0 & 0 & 0 & \frac{1}{2} \\ \frac{1}{2} & 0 & 0 & 0 \\ 0 & \frac{1}{2} & 0 & 0 \end{pmatrix},\; j_y = \begin{pmatrix} 0 & 0 & -\frac{i}{2} & 0 \\ 0 & 0 & 0 & -\frac{i}{2} \\ \frac{i}{2} & 0 & 0 & 0 \\ 0 & \frac{i}{2} & 0 & 0 \end{pmatrix},\; j_z = \begin{pmatrix} \frac{1}{2} & 0 & 0 & 0 \\ 0 & \frac{1}{2} & 0 & 0 \\ 0 & 0 & -\frac{1}{2} & 0 \\ 0 & 0 & 0 & -\frac{1}{2} \end{pmatrix}.
$$

The operators $\hat{j_x}$, $\hat{j_y}$ and $\hat{j_z}$ have the same form as the spin operators $\hat{s_x}$, $\hat{s_y}$ and $\hat{s_z}$ for a single electron in a two-site system with spin, $\sigma \otimes \tau$, where σ is the spin matrices and τ is the identity matrix for the two-site system. In fact, in Bi and Se, $u_\pm^\Lambda \gg v_\pm^\Lambda$, with $|u|^2 = 0.75, |v|^2 = 0.25$ for Bi and $|u|^2 = 0.98, |v|^2 = 0.02$ for Se. Therefore, the basis states

to construct the 4×4 model Hamiltonian of TI are approximately:

$$|\psi_1\rangle = \left| P1^+_-, m_j = \frac{1}{2} \right\rangle \approx \left| P1^+_-, p_z, \uparrow \right\rangle, \tag{2.26}$$

$$|\psi_2\rangle = \left| P2^-_+, m_j = \frac{1}{2} \right\rangle \approx \left| P2^-_+, p_z, \uparrow \right\rangle, \tag{2.27}$$

$$|\psi_3\rangle = \left| P1^+_-, m_j = -\frac{1}{2} \right\rangle \approx \left| P1^+_-, p_z, \downarrow \right\rangle, \tag{2.28}$$

$$|\psi_4\rangle = \left| P2^-_+, m_j = -\frac{1}{2} \right\rangle \approx \left| P2^-_+, p_z, \downarrow \right\rangle. \tag{2.29}$$

This basis set is used throughout this thesis, and the corresponding spin operators are the same as j_x, j_y, j_z.

2.3 Fundamentals of Floquet-Bloch theory

In 1965 Shirley [102] proposed a method to solve a time-periodic Hamiltonian in crystals called Floquet-Bloch theory. Floquet-Bloch theory is suitable for the study of strongly driven periodic quantum systems because it respects the periodicity of the perturbation at all levels of approximation, and avoids the occurrence of linear or non-periodic time-varying terms in the time variable [56].

A general periodic Time-Dependent Schrödinger Equation is written as:

$$i\hbar \frac{\partial \Phi(\vec{r},t)}{\partial t} = H\Phi(\vec{r},t), \tag{2.30}$$

where $H(t+T) = H(t)$, and T is the period of the system. According to the Floquet-Bloch theorem, there exists solutions to the equation 2.30 that have the form:

$$\Phi(\vec{r},t) = e^{-i\varepsilon_\alpha t/\hbar} u_\alpha(\vec{r},t), \tag{2.31}$$

where $u_\alpha(\vec{r},t+T) = u_\alpha(\vec{r},t)$.
The solution is similar to a Bloch solution in a spatially periodic system, with a phase term of $-i\varepsilon_\alpha t/\hbar$ and a periodic function $u_\alpha(\vec{r},t)$. Substituting the solution 2.31 into equation 2.30, we arrive at:

$$(H - i\hbar\frac{\partial}{\partial t})u_\alpha(\vec{r},t) = \varepsilon_\alpha u_\alpha(\vec{r},t). \tag{2.32}$$

$H_F = (H - i\hbar\frac{\partial}{\partial t})$ is called the Floquet Hamiltonian, ε_α is a quasi energy called the Floquet energy and $u(\vec{r},t)$ is called a Floquet state. The general solution to Eq. 2.30 is written as:

$$\Phi(\vec{r},t) = \sum_\alpha a_\alpha e^{-i\varepsilon_\alpha t/\hbar} u_\alpha(\vec{r},t). \tag{2.33}$$

Most Floquet Hamiltonians need to be solved numerically; exact solutions exist only for a few of them [56]. The numerical method to solve a Floquet Hamiltonian will be discussed in Ch. 3. In this thesis, we will solve the Floquet Hamiltonian numerically.

2.4 Summary

In this chapter, we provide some background information to understand topological insulators together with an introduction to the model Hamiltonian we used throughout the thesis. Then we introduced the Floquet-Bloch theory to study time-periodic TI systems in this thesis.

Chapter 3

Numerical Methods

In this thesis, the TI Hamiltonian under consideration are four simultaneous ordinary differential equations (ODEs) with the edges along the z direction. There is no simple analytical way to solve these simultaneous equations, not to mention adding time dependence to it. Therefore in this thesis we choose to solve the problems numerically. In this Chapter, I will introduce the main numerical methods used to approach the problems related to the topological insulator systems in this thesis. We will discuss the finite difference method used for spatial discretisation and then two different methods (the Floquet Bloch method and the staggered leapfrog method) for solving the time-dependent Schrödinger equation.

3.1 Spatial discretisation

3.1.1 Finite difference method

The finite difference method is a numerical method used to find approximate solutions to derivatives of a differential equation defined over the region of interest with some boundary conditions. It is a common discretisation method used in numerical studies. The continuous variable of the differential equation is replaced by a finite number of lattice sites with the boundaries properly defined. The derivatives are replaced by the difference operators expressed using the values of $f(x)$ on these lattice sites and these difference operators are derived from the truncated Taylor expansion. If we consider the Taylor expansion of $f(x)$ with x being a continuous variable, we have for $f(x+h)$ and $f(x-h)$:

$$f(x+h) = f(x) + hf'(x) + \frac{h^2}{2}f''(x) + \ldots + \frac{h^n}{n!}f^n(x) + \ldots, \tag{3.1}$$

$$f(x-h) = f(x) - hf'(x) + \frac{h^2}{2}f''(x) + \ldots + (-1)^n\frac{h^n}{n!}f^n(x) + \ldots. \tag{3.2}$$

By subtracting Eq. 3.1 and Eq. 3.2, we obtain the difference operator of first order derivative:

$$f'(x) = \frac{f(x+h) - f(x-h)}{2h} - \frac{1}{2}\sum_{n=1}^{\infty}\frac{h^{2n}}{(2n+1)!}f^{2n+1}(x). \tag{3.3}$$

By adding Eq. 3.1 and Eq. 3.2, we obtain the difference operator of second order derivative:

$$f''(x) = \frac{f(x+h) - 2f(x) + f(x-h)}{h^2} - \sum_{n=1}^{\infty}\frac{h^{2n}}{(2n+2)!}f^{2n+2}(x). \tag{3.4}$$

The first term in Eq. 3.3 and Eq. 3.4 are the approximations for the first and second order derivatives, while the second terms represent the truncation error of this method and are of h^2 for both cases.

By replacing the continuous variable x with the lattice site index n_x and specifying the values of $f(x)$ only with these points and h being the distance between the neighbouring sites, we have expressed the derivatives with the values defined on those discrete lattice sites only.

3.2 Temporal discretisation

3.2.1 The Floquet matrix method

The Floquet mode solutions can be obtained by solving Floquet matrix. Here I will illustrate the method with a two site model as an example:

$$H(t) = \begin{pmatrix} E\cos(\omega t) & -\Delta \\ -\Delta & -E\cos(\omega t) \end{pmatrix}, \tag{3.5}$$

with $\omega = \frac{2\pi}{T}$. This can be written in terms of Pauli matrices:

$$H(t) = E\cos(\omega t)\sigma_z - \Delta\sigma_x = \frac{E}{2}(e^{i\omega t} + e^{-i\omega t})\sigma_z - \Delta\sigma_x. \tag{3.6}$$

Because the Hamiltonian $H(t)$ and the Floquet modes are periodic in time, we can write the Floquet modes in terms of a Fourier series of time t:

$$u(t) = \sum_{n=-\infty}^{\infty} a_n e^{in\omega t}. \tag{3.7}$$

To write out the Floquet matrix, we notice that

$$e^{\pm i\omega t} u(t) = \sum_{n=-\infty}^{\infty} a_{n\mp 1} e^{in\omega t}. \tag{3.8}$$

Substituting 3.7 into 2.32, we obtain a set of simultaneous equations:

$$\sum_{n=-\infty}^{\infty} (\frac{E}{2}\sigma_z(a_{n+1}+a_{n-1}) - \Delta\sigma_x a_n + n\hbar\omega a_n)e^{in\omega t} = \varepsilon_\alpha \hbar \sum_{n=-\infty}^{\infty} a_n e^{i\omega t}. \tag{3.9}$$

And

$$\frac{E}{2}\sigma_z(a_{n+1}+a_{n-1}) - \Delta\sigma_x a_n + n\hbar\omega a_n = \hbar\varepsilon_\alpha a_n. \tag{3.10}$$

Writing this in matrix form we have:

$$H = \begin{bmatrix} \ddots & \ddots & \ddots & \ddots & \ddots & \ddots & \ddots \\ 0 & \frac{E}{2}\sigma_z & (n-1)\hbar\omega - \Delta\sigma_x & \frac{E}{2}\sigma_z & 0 & 0 & 0 \\ 0 & 0 & \frac{E}{2}\sigma_z & n\hbar\omega - \Delta\sigma_x & \frac{E}{2}\sigma_z & 0 & 0 \\ 0 & 0 & 0 & \frac{E}{2}\sigma_z & (n+1)\hbar\omega - \Delta\sigma_x & \frac{E}{2}\sigma_z & 0 \\ \ddots & \ddots & \ddots & \ddots & \ddots & \ddots & \ddots \end{bmatrix}, \tag{3.11}$$

where n is infinite. This Hamiltonian can be solved numerically by defining a finite number of Fourier components n used in the calculation. The $\sum_{n=1}^{n=m} |a_n|^2$ of this finite set of Fourier components should be ≈ 1. A suitable number m can be found in practice by running the simulations with different n and monitoring the norm of the output states.

3.3 The staggered leapfrog method

In the previous section, we have discussed the Floquet-Bloch method to solve a periodically time-varying system. This method is effective to study time-periodic wavefunctions in a quantum system under a periodic field. However, to understand the immediate effect of external fields (pulses) on the time evolution of a specific quantum state, we need another

method describing how the state is influenced by sudden changes at any desired instance. Therefore, we employ the staggered leapfrog method for this task in the thesis.

A general non-relativistic time-dependent Schrödinger's equation (TDSE) is written as:

$$i\hbar\frac{\partial\Phi(\vec{r},t)}{\partial t} = H\Phi(\vec{r},t). \tag{3.12}$$

Time evolution of wavefunction $|\Phi_t\rangle$ can be expressed as:

$$|\Phi(t_1)\rangle = \hat{U}(t_1,t_0)\,|\Phi(t_0)\rangle\,, \tag{3.13}$$

where $\hat{U}(t_1,t_0)$ is the time-evolution operator connecting the quantum state $|\Phi\rangle$ at t_1 and t_0, and is expressed with the time-ordering $\mathscr{T}$ as:

$$\hat{U}(t_1,t_0) = \mathscr{T}\big\{\exp\big[-\frac{i}{\hbar}\int_{t_0}^{t_1}\hat{H}(\tau)d\tau\big]\big\}. \tag{3.14}$$

However, 3.12 and 3.13 are difficult to solve in general and analytical solutions can only be found for simple cases. The continuous variable τ in the integral together with the complex time ordering $\mathscr{T}$ need to be replaced by finite and manageable approximations.

One way to do this is via the Trotter expansion[109]. By using the semi-group property of $\hat{U}(t_1,t_0)$, we have:

$$\hat{U}(t_1,t_0) = \hat{U}(t_1,t_1/2)\hat{U}(t_1/2,t_0). \tag{3.15}$$

The time-evolution operator can be further discretised into N pieces,with smaller and smaller Δt. For an evenly spaced discretization $\Delta t = \frac{t_1-t_0}{N}$, the propagator can be written as a product of time-evolution operators:

$$\hat{U}(t_1,t_0) = \prod_{n=0}^{N-1}\hat{U}_n, \tag{3.16}$$

where $\hat{U}_n = \hat{U}(t_{n+1},t_n)$ and $t_0 = 0$, $t_1 = N\Delta t$. If the time interval Δt is sufficiently small, we can assume that $\hat{H}$ is approximately constant over Δt. Therefore, the propagator is written as:

$$\hat{U}(t+\Delta t,t) = \exp\big(-\frac{i\hat{H}(t)\Delta t}{\hbar}\big). \tag{3.17}$$

However, the resultant propagator is still difficult to solve due to the large number of spatial dimensions of the Hamiltonian used in this thesis. Therefore, we need to further approximate the exponent in Eq. 3.17 via a feasible numerical approach.

Since an exponential function can be written as a Taylor expansion, we have:

$$\hat{U}(t+\Delta t,t) = 1 - \frac{i\hat{H}\Delta t}{\hbar} + \cdots . \tag{3.18}$$

Then, the question is how to estimate of $|\Phi(t+\Delta t)\rangle$ using the Taylor terms in Eq. 3.18. In this thesis, we apply the staggered leapfrog method to solve this problem. The staggered leapfrog method [4][78] is an iteration method that approximates the wavefunction $|\Phi(t+\Delta t)\rangle$ at $t+\Delta t$ with the values of $|\Phi\rangle$ of the two previous time steps t and $t-\Delta t$. Using the first two terms in Taylor expansion in Eq. 3.18, we have :

$$|\Phi(t+\Delta t)\rangle = |\Phi(t-\Delta t)\rangle - 2\frac{i\hat{H}(t)\Delta t}{\hbar}|\Phi(t)\rangle + \mathscr{O}(\Delta t)^3. \tag{3.19}$$

Therefore, we can see that the truncation error of the staggered leapfrog method is of order Δt^3. Because this is an iteration method, the stability must be checked. The von Neumann stability analysis [118] suggests that a computational error is $\varepsilon(t) = |\Phi(t)\rangle - \left|\bar{\Phi}(t)\right\rangle$, where $|\Phi(t)\rangle$ is the wavefunction of the staggered leapfrog method and $\left|\bar{\Phi}(t)\right\rangle$ is the exact solution. Following the analysis, the stability criterion for the staggered leapfrog method is:

$$\Delta t \leq \frac{\hbar}{E_{max}}. \tag{3.20}$$

E_{max} is the highest eigenenergy of the instantaneous Hamiltonian $\hat{H}$. Moreover, we should be aware that the evolution operator used in the staggered leapfrog method is not strictly norm-preserving since there is a truncation error of $\mathscr{O}(\Delta t)^3$. However, as long as the norm is preserved to a good extent, the staggered leapfrog method provide a good approximation of the quantum state at $t+\Delta t$. The norm is monitored in the simulation to guarantee this condition. The accuracy can be further improved by applying the Visschers staggered-time method [117]. The wavefunction is written in terms of its imaginary and real parts $v(t)$ and $u(t)$ respectively, which are calculated at slightly different, staggered times:

$$|\Phi(t)\rangle = u(t) + iv(t+\frac{\Delta t}{2}). \tag{3.21}$$

The corresponding probability density $\rho(t)$ is:

$$\rho(t) = |u(t)|^2 + |v(t+\Delta t)v(t-\Delta t)|^2. \tag{3.22}$$

Eq. 3.21 and Eq. 3.22 provides a cancellation of the errors, therefore the conservation of probability density is improved. This method simplifies to the standard method when $\Delta t \to 0$.

3.4 Summary

In this chapter, we provided an introduction to the numerical methods used throughout the thesis. These are the finite difference method for spatial discretisation, the Floquet matrix method and the staggered leapfrog method for temporal discretization. We will use these numerical methods in the following chapters.

Chapter 4

A Charge Qubit in an Ultra-thin Topological Insulator Film

4.1 Introduction

Although research on topological insulators is still at earlier stages of mainly theoretical studies owing to the challenges in fabrication, it is still of great interest to investigate potential applications of TIs because of their intriguing and beneficial properties. In Ch. 2, we have learnt that because of the preservation of TR symmetry and strong spin-orbit-coupling, the electrons on the Dirac cone are topologically protected. This protection is robust, and the electrons are immune to non-magnetic local perturbation. In quantum computation and quantum information, one of the major challenges to build a practical quantum computer are the inevitable random interactions of the qubit with its surroundings [124] [98]. This happens during operation and measurement. Scientists have endeavoured to solve this problem and quantum error correction (QEC) is the name given to the techniques that address this question [12] [60] [105]. The threshold of a fault-tolerant quantum computing process might be as high as 3% in theory if the computational resources are unconstrained [12] [60] [105] [68]. At the same time, scientists are searching for new physical implementations for quantum computation [108] [81] [94] [83] [80].

In this Chapter, we define and investigate quantum control of a new type of charge qubit in a topological insulator system, with a focus on single-qubit operations. The two-qubit operation is beyond the scope of this thesis but it will be discussed briefly at the end of this chapter in section 4.4. Together with the expected long decoherence time in TI protected by its topology, we hope this qubit would offer a new possibility for a feasible fault-tolerant quantum computer. The rest of this chapter is divided into three sections. In section 4.2, we

discuss how to construct the system numerically from the model Hamiltonian presented in Ch. 2 and how the state in an ultra-thin TI is affected by its thickness, in both cases with and without an electric field. Then in section 4.3 we continue to explore a suitable pair of states of a charge qubit and investigate how to initialise, rotate and read out a single qubit. In the last section 4.5, we address some experimental related questions and challenges and offer some possible solutions.

4.2 System

4.2.1 Model Hamiltonian

In order to simulate a TI thin film with an external electric field, we exploit Liu's model Hamiltonian introduced in Chapter 2 and implement a time-independent electric field term in it along the z direction. The Hamiltonian of a TI with an electric field is:

$$H = C(\mathbf{k})I_4 + M(\mathbf{k})\Gamma_5 + B_0\Gamma_4 k_z + A_0(\Gamma_1 k_y - \Gamma_2 k_x) - E(\mathbf{z})I_4, \tag{4.1}$$

with I_4 is 4×4 identity matrix and:

$$\Gamma_5 = \begin{pmatrix} 1 & 0 & 0 & 0 \\ 0 & -1 & 0 & 0 \\ 0 & 0 & 1 & 0 \\ 0 & 0 & 0 & -1 \end{pmatrix}, \Gamma_4 = \begin{pmatrix} 0 & -i & 0 & 0 \\ i & 0 & 0 & 0 \\ 0 & 0 & 0 & -i \\ 0 & 0 & i & 0 \end{pmatrix},$$
$$\Gamma_1 = \begin{pmatrix} 0 & 0 & 0 & -i \\ 0 & 0 & -i & 0 \\ 0 & i & 0 & 0 \\ i & 0 & 0 & 0 \end{pmatrix}, \Gamma_2 = \begin{pmatrix} 0 & 0 & 0 & 1 \\ 0 & 0 & 1 & 0 \\ 0 & 1 & 0 & 0 \\ 1 & 0 & 0 & 0 \end{pmatrix}.$$

$$\begin{aligned} C(\mathbf{k}) &= C_0 + C_1 k_z^2 + C_2 |k_{||}|^2, \\ M(\mathbf{k}) &= M_0 + M_1 k_z^2 + M_2 |k_{||}|^2, \\ k_{||} &= k_x - i k_y. \end{aligned}$$

The last term stands for the energy difference across the thin film of the external electric field (it is along the z direction) in units of eV. From the Hamiltonian 4.1 we see that it no

longer commutes with **z**. We apply an open boundary condition and replace k_z by:

$$k_z \to -i\partial_z.$$

The resultant simultaneous linear equations are :

$$\begin{aligned}
F\phi_1'' - B_0\phi_2' + A\phi_1 + D\phi_4 &= \varepsilon\phi_1,\\
G\phi_2'' + B_0\phi_1' + B\phi_2 + D\phi_3 &= \varepsilon\phi_2,\\
F\phi_3'' - B_0\phi_4' + D^*\phi_2 + A\phi_3 &= \varepsilon\phi_3,\\
G\phi_4'' + B_0\phi_3' + D^*\phi_1 + B\phi_4 &= \varepsilon\phi_4.
\end{aligned}$$

$$\begin{aligned}
A &= C_0 - eEz + M_0 + C_2|k_{||}|^2 + M_2|k_{||}|^2,\\
B &= C_0 - eEz - M_0 + C_2|k_{||}|^2 - M_2|k_{||}|^2,\\
D &= A_0(ik_x + k_y),\\
F &= C_1 - M_1,\\
G &= C_1 + M_1.
\end{aligned}$$

The Hamiltonian is then solved using the finite difference method described in Ch.3. This can be written as a numerical matrix:

$n_z=1$	$n_z=2$	$n_z=3$	$n_z=4$	$n_z=5$	
H_{-1}	$H_0+2\Sigma$	H_{+1}	0	$\vdots$	$n_z=2$
0	H_{-1}	$H_0+3\Sigma$	H_{+1}	$\vdots$	$n_z=3$
$\vdots$	0	H_{-1}	$H_0+4\Sigma$	H_{+1}	$n_z=4$

where H_0 is the sub-matrix for on-site interaction at n_zth lattice site and $H_0 = \left\langle \vec{\phi}_{n_z} \middle| H \middle| \vec{\phi}_{n_z} \right\rangle$. $H_{\pm1}$ is the sub-matrix for interaction of the lattice site n_z with its nearest neighbour and $H_{\pm1} = \left\langle \vec{\phi}_{n_z\pm1} \middle| H \middle| \vec{\phi}_{n_z} \right\rangle$. $\vec{\phi}_{n_z} = \phi_1, \phi_2, \phi_3, \phi_4$ is the four-basis wave vector at the n_zth site. $\Sigma = (E_{n_{zmax}} - E_{n_{z1}})/n$ is the electric field gradient along the z direction, with $E_{n_{zmax}}$ being the electric energy at the top surface and $E_{n_{z1}}$ being the electric energy at the bottom surface. n is the total number of sites along the z direction.

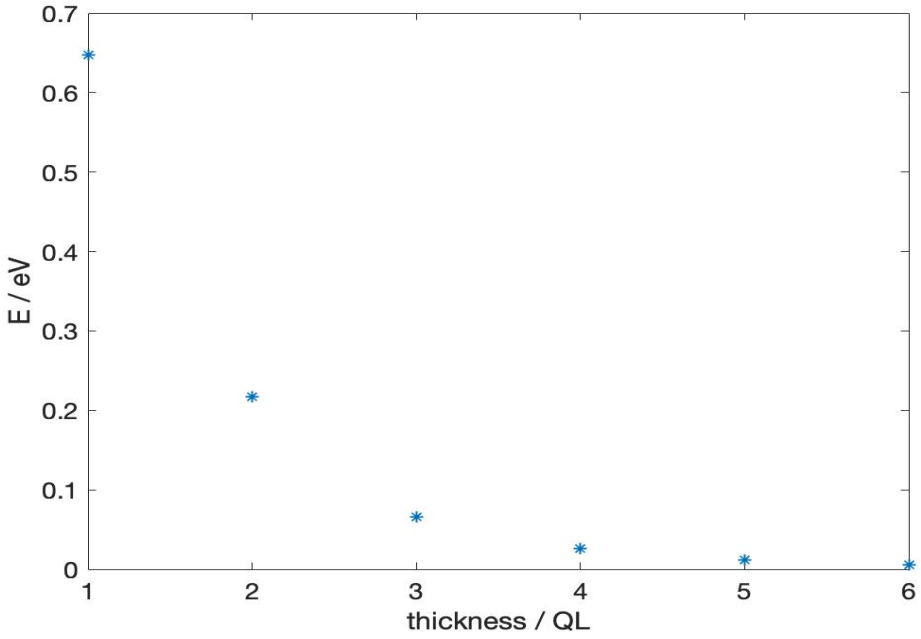

Fig. 4.1 Band gap energy of a gapped Dirac cone vs the thickness of a TI thin film, from 1 QL to 6 QL. The energy E decreases with the thickness of the TI thin film.

4.2.2 Quantum confinement effects in ultra-thin TIs

According to the Pauli exclusion principle, two electrons cannot occupy a state with the same quantum numbers (eg k, s_z). However, this 'happens' in a topological insulator with surface states at the Γ point ($k_x = k_y = 0$) due to the spatial separation of the states and bulk-edge correspondence. As the thickness is reduced, the surface states physically overlap and tunnelling occurs between them. The hybridisation of the surface states opens up a gap in the Dirac cone and the massless fermions become massive. This property of TIs has been well-known in the literature [73] [71] [127]. We will call the resultant hybridised states 'surface states' since they are hybridised surface states. The gap width varies with the thickness of the TI thin film, which in our model it i's found to increase when the thickness of a TI is decreased (see Fig. 4.1).

The appearance of surface states can be understood in terms of the model Hamiltonian of a TI in Eq. 2.19 of Ch. 2. For simplicity, we look at the states at the Γ point. We first turn off the coupling between the atomic Bi and Se basis states with the same spin, i.e. we set $B_0 = 0$. The model produces four bands with a double degeneracy in spin; we call them $\left|P1^+_-, \pm\frac{1}{2}\right\rangle$ (the hole sub-bands) and $\left|P2^-_+, \pm\frac{1}{2}\right\rangle$ (the electron sub-bands). These states are localised bulk states. No surface states appear as the thickness is varied (we call it d in the thesis). When we turn on B_0, the coupling between $\left|P1^+_-, \frac{1}{2}(-\frac{1}{2})\right\rangle$ and $\left|P2^-_+, \frac{1}{2}(-\frac{1}{2}))\right\rangle$ causes a mixing

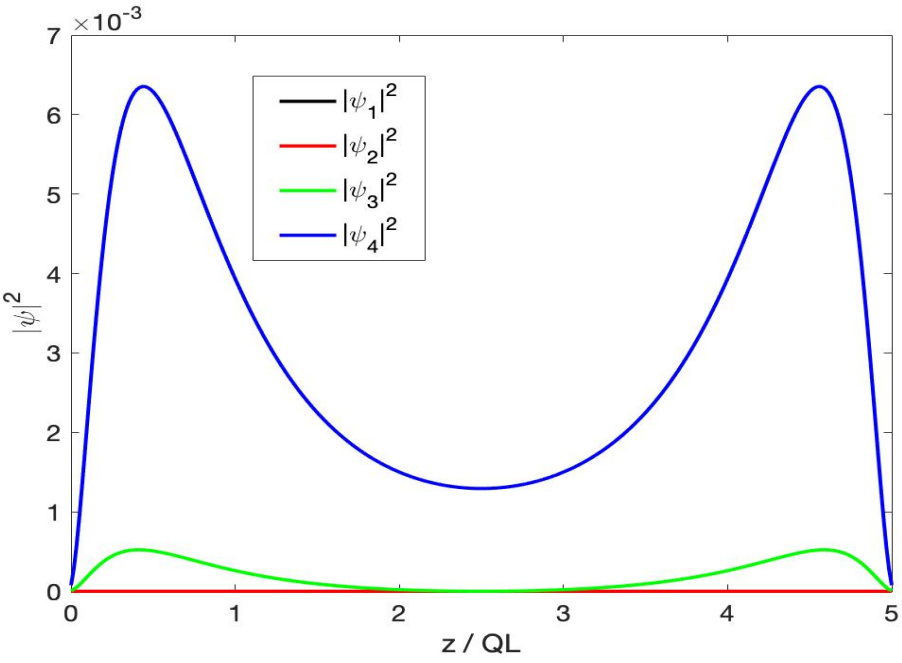

Fig. 4.2 Spatial distributions of the wave function densities of a spin down 'surface state' ($|S1\rangle$) on the hole band at the Γ point in a 5 QL TI thin film. $|\psi_1|^2$ to $|\psi_4|^2$ are the wave function densities of the basis states $|\psi_1\rangle$ to $|\psi_4\rangle$ of the TI Hamiltonian in Eq. 4.1. The detailed electronic states of $|\psi_1\rangle$ to $|\psi_4\rangle$ are shown in Eq. 2.26. The wave function densities of $|\psi_1\rangle$ and $|\psi_2\rangle$ are equal to zero. The wave function density of the 'surface state' spans over the whole thickness of TI, with two peaks near the surfaces.

between the basis states with the same spin, producing a pair of bonding and anti-bonding orbits; this explains the shape of the surface-state wave function in a gaped TI. From the plots (Fig. 4.2 - Fig. 4.5) we can see that each state consists of four wave components; this is because the original tight-binding Hamiltonian is constructed from a Hilbert space of the four atomic basis states described above. Owing to B_0, the resultant states at the Γ point have two non-zero wave components with $s_z = \pm\frac{1}{2}$. Looking at each wave component individually, we see that it is either a bonding or anti-bonding type orbit. The model can be viewed as a double quantum well. When $B_0 = 0$, the tunnelling coefficients between two sub-wells are zero and the sub-wells are uncoupled; when $B_0 \neq 0$, the tunnelling coefficient is non-zero and a mixing between the states in the sub-wells leads to the bonding and anti-bonding orbits. Although the states extend over the whole TI along the z direction, the maximum density is always about 0.5 QL beneath the surfaces. As the thickness increases, the surface states become nearly degenerate with $\Delta E = 10^{-11} eV$ and the tunnelling coefficient becomes very small (see Fig. 4.6).

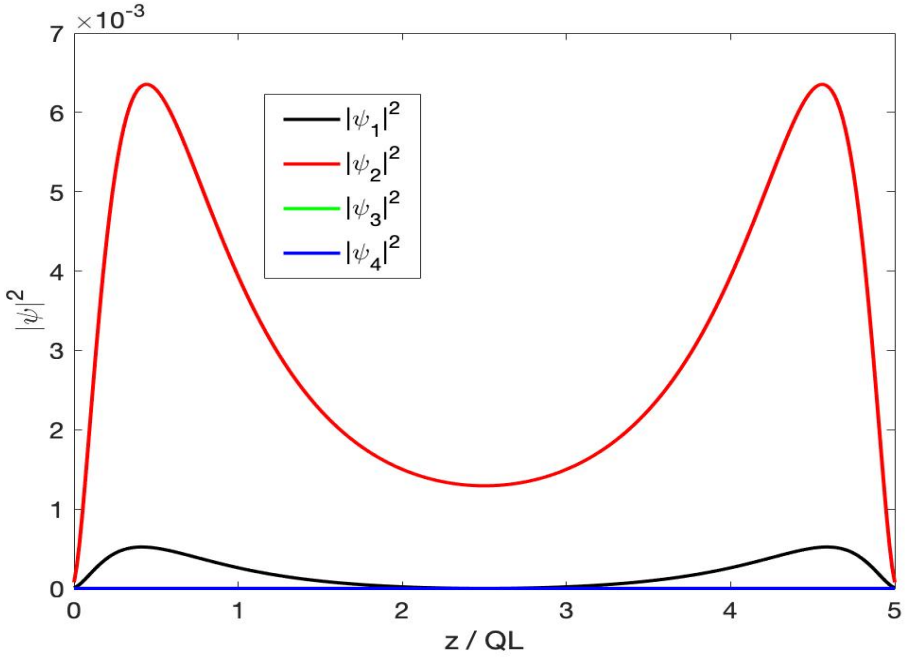

Fig. 4.3 Spatial distributions of the wave function densities of a spin up 'surface state' ($|S2\rangle$) on the hole band at the Γ point in a 5 QL TI thin film. $|\psi_1|^2$ to $|\psi_4|^2$ are the wave function densities of the basis states $|\psi_1\rangle$ to $|\psi_4\rangle$ of the TI Hamiltonian in Eq. 4.1. The detailed electronic states of $|\psi_1\rangle$ to $|\psi_4\rangle$ are shown in Eq. 2.26. The wave function densities of $|\psi_3\rangle$ and $|\psi_4\rangle$ are equal to zero. The wave function density of the 'surface state' spans over the whole thickness of TI, with two peaks near the surfaces.

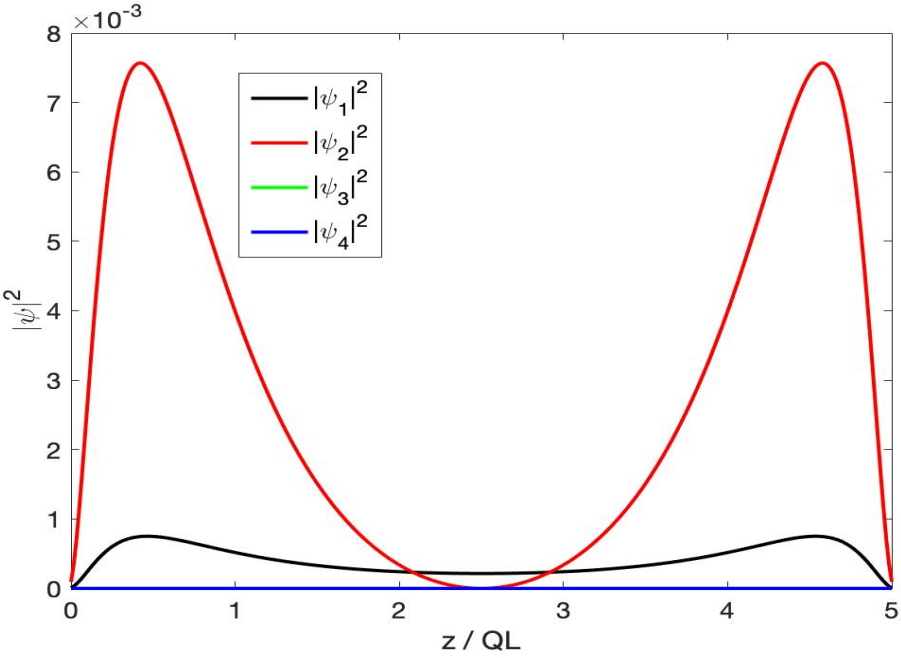

Fig. 4.4 Spatial distributions of the wave function densities of a spin up 'surface state' ($|S3\rangle$) on the electron band at the Γ point in a 5 QL TI thin film. $|\psi_1|^2$ to $|\psi_4|^2$ are the wave function densities of the basis states $|\psi_1\rangle$ to $|\psi_4\rangle$ of the TI Hamiltonian in Eq. 4.1. The detailed electronic states of $|\psi_1\rangle$ to $|\psi_4\rangle$ are shown in Eq. 2.26. The wave function densities of $|\psi_3\rangle$ and $|\psi_4\rangle$ are equal to zero. The wave function density of the 'surface state' spans over the whole thickness of TI, with two peaks near the surfaces.

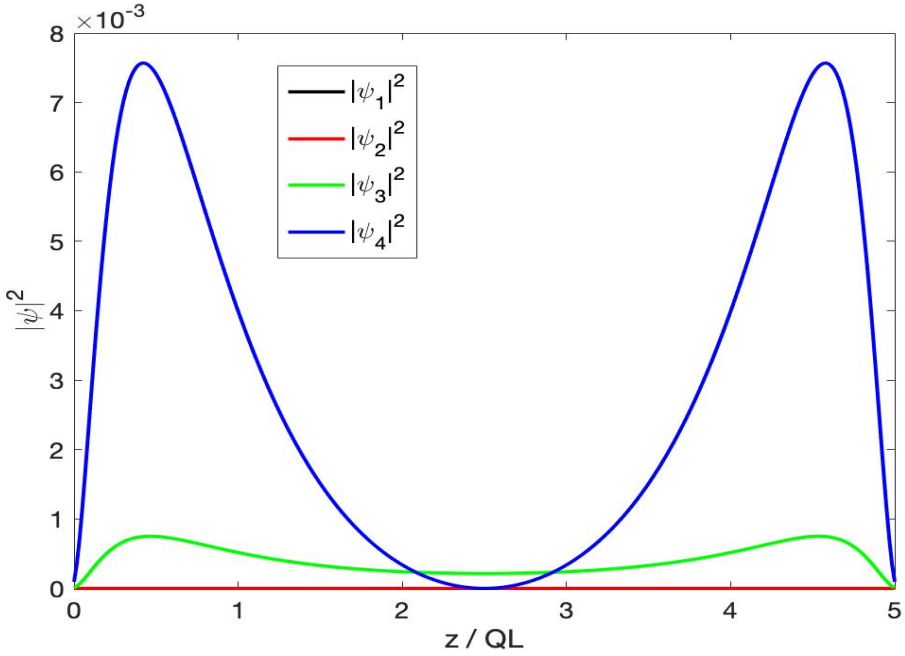

Fig. 4.5 Spatial distributions of the wave function densities of a spin down 'surface state' ($|S4\rangle$) on the electron band at the Γ point in a 5 QL TI thin film. $|\psi_1|^2$ to $|\psi_4|^2$ are the wave function densities of the basis states $|\psi_1\rangle$ to $|\psi_4\rangle$ of the TI Hamiltonian in Eq. 4.1. The detailed electronic states of $|\psi_1\rangle$ to $|\psi_4\rangle$ are shown in Eq. 2.26. The wave function densities of $|\psi_1\rangle$ and $|\psi_2\rangle$ are equal to zero. The wave function density of the 'surface state' spans over the whole thickness of TI, with two peaks near the surfaces.

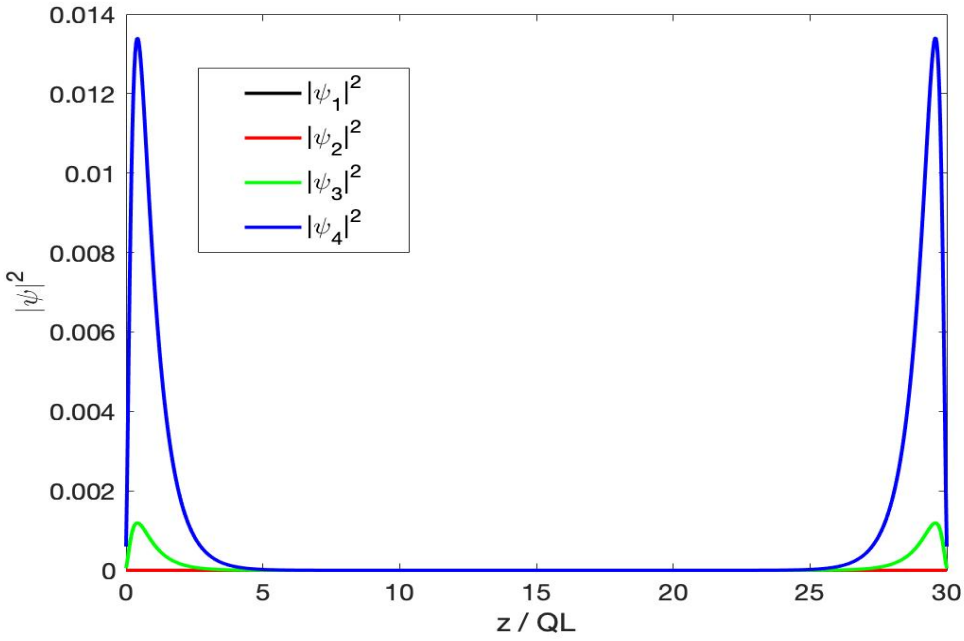

Fig. 4.6 Spatial distributions of the wave function densities of a spin down surface state at the Γ point in a 30 QL TI thin film. $|\psi_1|^2$ to $|\psi_4|^2$ are the wave function densities of the basis states $|\psi_1\rangle$ to $|\psi_4\rangle$ of the TI Hamiltonian in Eq. 4.1. The detailed electronic states of $|\psi_1\rangle$ to $|\psi_4\rangle$ are shown in Eq. 2.26. The wave function densities on $|\psi_1\rangle$ and $|\psi_2\rangle$ are equal to zero. The wave function density of the surface state is localised near the surfaces.

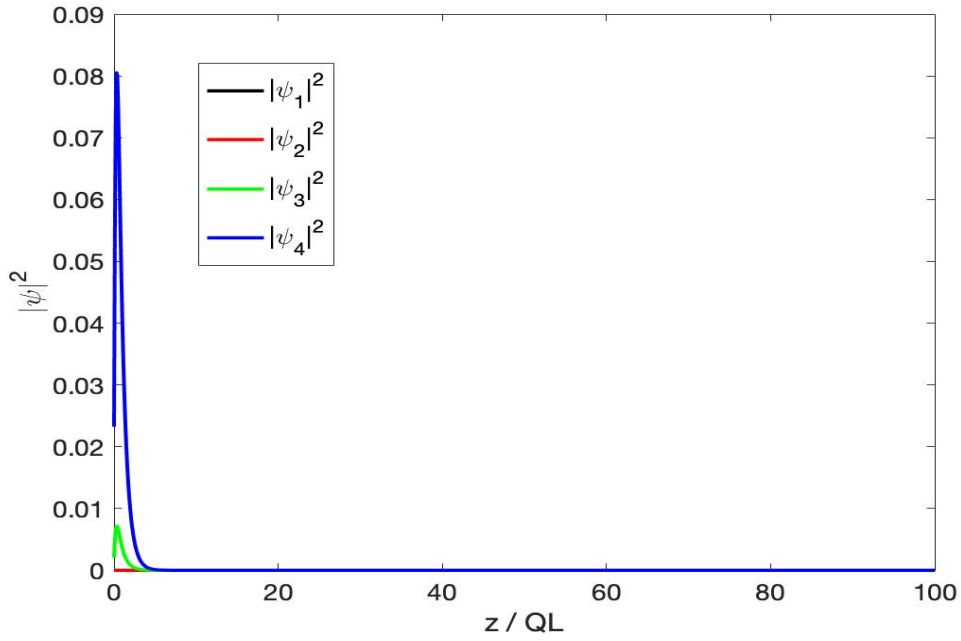

Fig. 4.7 Spatial distributions of the wave function densities of a spin down surface state at the Γ point in a 100 QL TI thin film. $|\psi_1|^2$ to $|\psi_4|^2$ are the wave function densities of the basis states $|\psi_1\rangle$ to $|\psi_4\rangle$ of the TI Hamiltonian in Eq. 4.1. The detailed electronic states of $|\psi_1\rangle$ to $|\psi_4\rangle$ are shown in Eq. 2.26. The wave function densities of $|\psi_1\rangle$ and $|\psi_2\rangle$ are equal to zero. The wave function density of the surface state is localised near the surface.

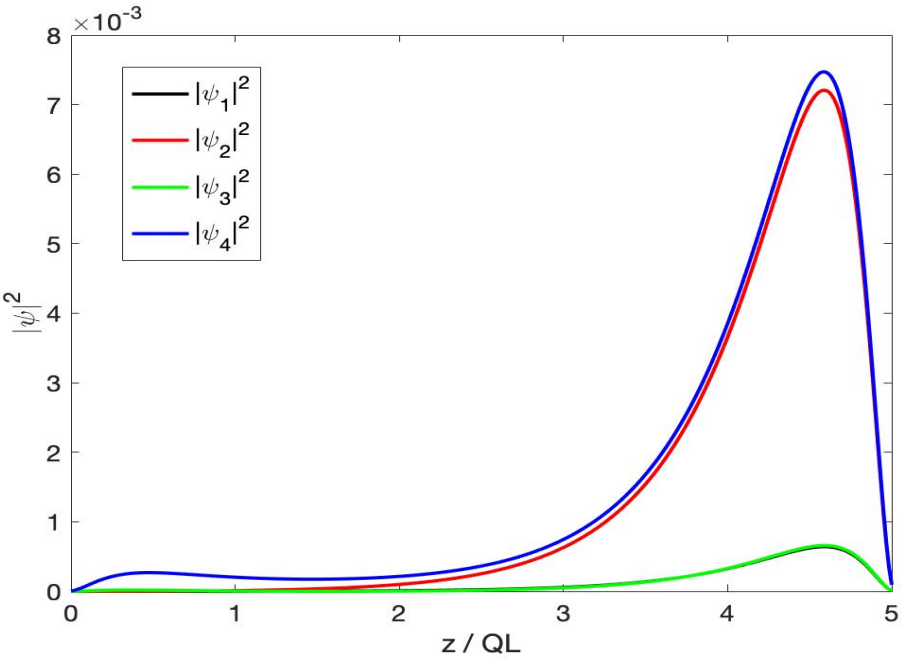

Fig. 4.8 Spatial distributions of the wave function densities of a surface state at $k_x = 0.01$, $k_y = 0$ on the hole band with its spin pointing almost perpendicular ($s_y = -0.49$) to its direction of motion, in a 5 QL TI thin film. $|\psi_1|^2$ to $|\psi_4|^2$ are the wave function densities of the basis states $|\psi_1\rangle$ to $|\psi_4\rangle$ of the TI Hamiltonian in Eq. 4.1. The detailed electronic states of $|\psi_1\rangle$ to $|\psi_4\rangle$ are shown in Eq. 2.26. The wave function density of the surface state spans over the whole thickness of the TI thin film and is mostly concentrated near one surface.

In the large d limit (e.g. 100 QL), the tunnelling coefficients become infinitesimally small and the two 'sub-wells' are almost decoupled. Therefore, the surface state is localised on one surface (Fig. 4.7). Also, we notice that the majoeity of the wave function density is localised around the Se atom (P2), while only a small contribution comes from the Bi atom (P1) for surface states at the Γ point.

For the k values away from the Γ, the situation is complicated due to the addition of the linear spin-orbit coupling term. The resultant states have four non-zero wave components (Fig. 4.8-4.11). The surface states are influenced by both the coupling between the Bi and Se atomic states with same spin, and the Bi and Se atomic states with opposite spin. The former (coefficient B_0) causes the formation of localised states on surfaces, while the latter (coefficient A_0) induces the spin-momentum locking. Because the Hamiltonian maintains a three-fold rotation symmetry in the xy plane, we will pick the surface states at $k_x = 0.01\,\text{Å}^{-1}, k_y = 0$ as our example. (Fig. 4.8-4.11) At a thickness of 5QL, the majority of the wave function density of a surface state is localised around atomic Se states with $s_z = \pm\frac{1}{2}$ with equal weights therefore the combined state almost lies in the $s_x s_y$ plane with $s_y \pm \frac{1}{2}$ for

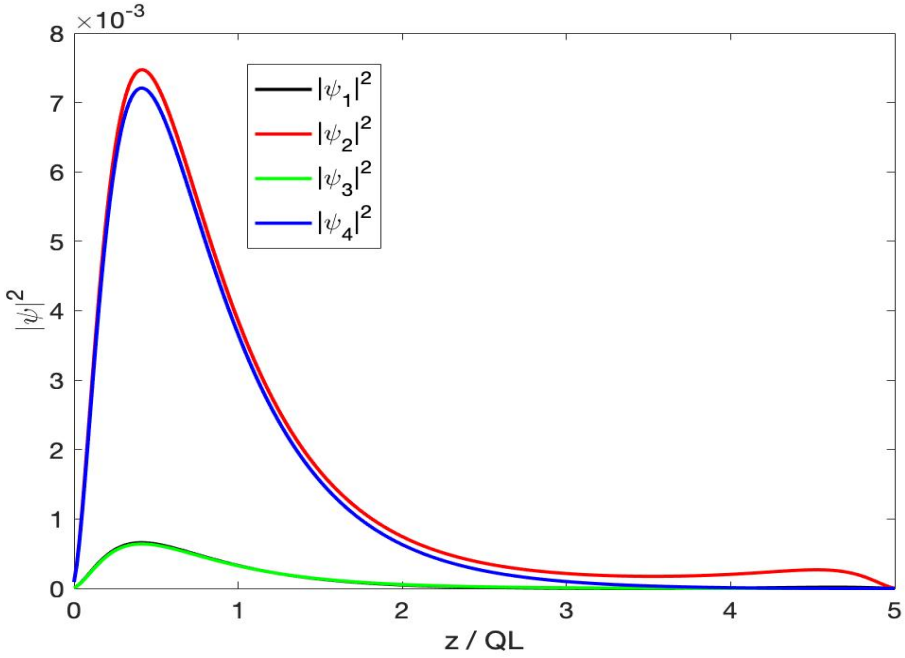

Fig. 4.9 Spatial distributions of the wave function densities of a surface state at $k_x = 0.01$, $k_y = 0$ on the hole band with its spin pointing almost perpendicular ($s_y = 0.49$) to its direction of motion, in a 5 QL TI thin film. $|\psi_1|^2$ to $|\psi_4|^2$ are the wave function densities of the basis states $|\psi_1\rangle$ to $|\psi_4\rangle$ of the TI Hamiltonian in Eq. 4.1. The detailed electronic states of $|\psi_1\rangle$ to $|\psi_4\rangle$ are shown in Eq. 2.26. The wave function density of the surface state spans over the whole thickness of the TI thin film and is mostly concentrated near one surface.

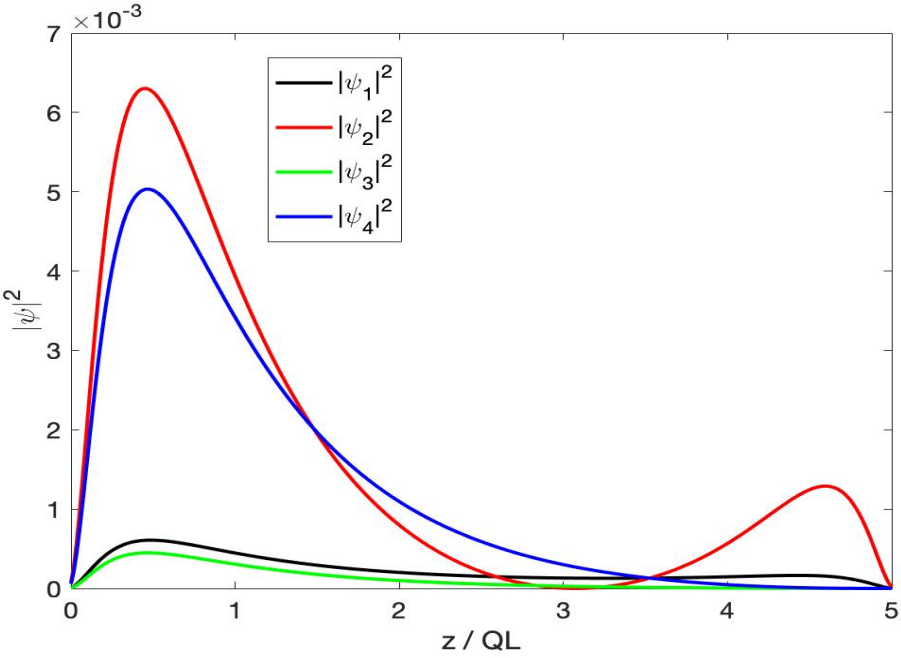

Fig. 4.10 Spatial distributions of the wave function densities of a surface state at $k_x = 0.01$, $k_y = 0$ on the electron band with its spin pointing almost perpendicular ($s_y = -0.44$) to its direction of motion, in a 5 QL TI thin film. $|\psi_1|^2$ to $|\psi_4|^2$ are the wave function densities of the basis states $|\psi_1\rangle$ to $|\psi_4\rangle$ of the TI Hamiltonian in Eq. 4.1. The detailed electronic states of $|\psi_1\rangle$ to $|\psi_4\rangle$ are shown in Eq. 2.26. The wave function density of the surface state spans over the whole thickness of the TI thin film and is mostly concentrated near one surface.

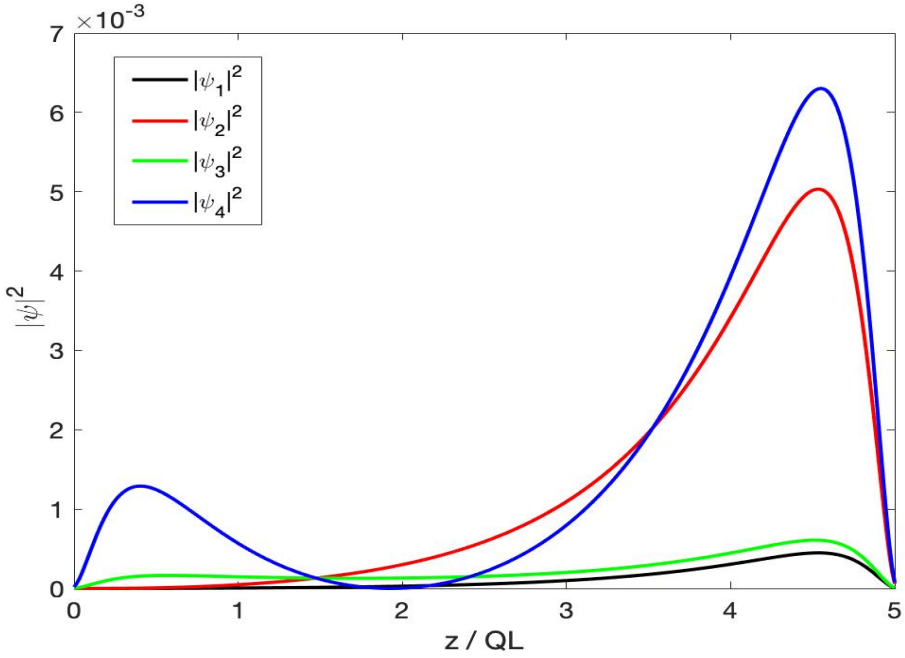

Fig. 4.11 Spatial distributions of the wave function densities of a surface state at $k_x = 0.01$, $k_y = 0$ on the electron band with its spin pointing almost perpendicular ($s_y = 0.44$) to its direction of motion, in a 5 QL TI thin film. $|\psi_1|^2$ to $|\psi_4|^2$ are the wave function densities of the basis states $|\psi_1\rangle$ to $|\psi_4\rangle$ of the TI Hamiltonian in Eq. 4.1. The detailed electronic states of $|\psi_1\rangle$ to $|\psi_4\rangle$ are shown in Eq. 2.26. The wave function density of the surface state spans over the whole thickness of the TI thin film and is mostly concentrated near one surface.

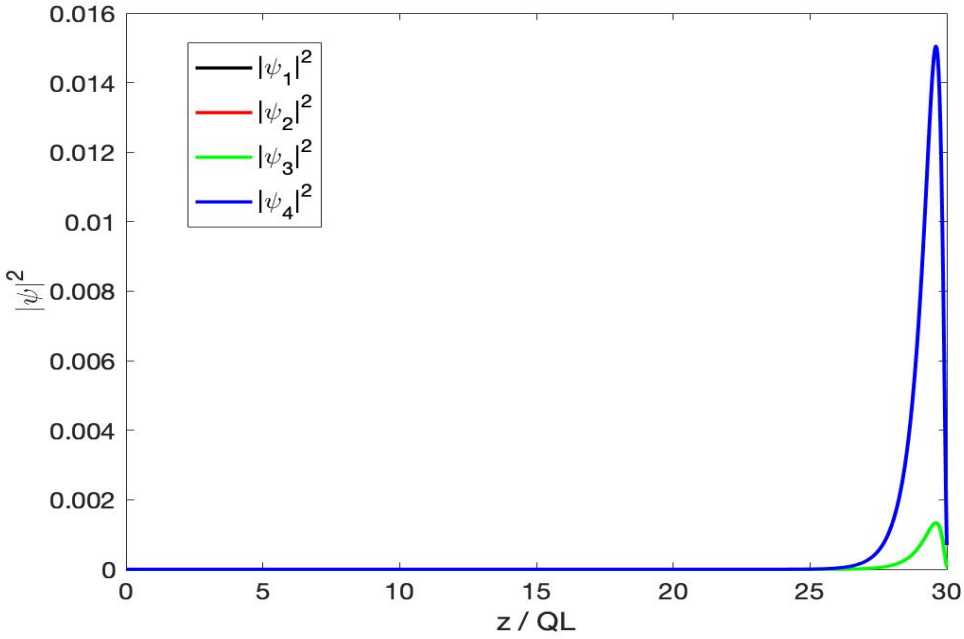

Fig. 4.12 Spatial distributions of the wave function densities of a surface state at $k_x = 0.01$, $k_y = 0$ on the electron band with its spin pointing perpendicular ($s_y = \frac{1}{2}$) to its direction of motion, in a 30 QL TI thin film. $|\psi_1|^2$ to $|\psi_4|^2$ are the wave function densities of the basis states $|\psi_1\rangle$ to $|\psi_4\rangle$ of the TI Hamiltonian in Eq. 4.1. The detailed electronic states of $|\psi_1\rangle$ to $|\psi_4\rangle$ are shown in Eq. 2.26. The wave function density of the surface state is localised near one surface.

the specific states shown in this example. We can see that the wave function densities on the basis states have different shapes. Using Fig. 4.8 as an example, $|\psi_2(z)|^2$ is zero near the surface at $QL = 0$ while $|\psi_4(z)|^2$ has a tail. This is because the surface state at the Γ point has a non-zero wave component on $|\psi_4\rangle$ and a zero wave component on $|\psi_2\rangle$. When moving away from the Γ point along the x direction, $|\psi_2(z)|^2$ and $|\psi_4(z)|^2$ both increase due to A_0. The shape of $|\psi_2(z)|^2$ is a result of a combined effect of spin-orbit coupling and B_0 term, while increase of the wave component on ψ_4 is solely owing to spin-orbit coupling. The spin-momentum locking is perturbed due to the significance of B_0 in an ultra-thin TI film, so the resultant state is not a pure eigenstate of $\hat{s_x}$ operator (we will talk about spin in detail in chapter 5). Therefore, we conclude that the surface states in an ultra-thin TI film are a combined effect of spin-orbit coupling and the quantum confinement effect. When d increases and tunnelling becomes insignificant, the wavefunctions of surface states have exactly the same weight and shape on the atomic basis with opposite spin, recovering the perfect spin-momentum locking (Fig. 4.12).

4.2.3 Effects of a perpendicular electric field

When an electric field along the z direction is applied to the ultra thin TI film, the degenerate spin bands split - this is called Stark effect. The splitting is proportional to the strength of the electric field.

The electric field couples the surface states on the electron band and the hole band with the same spin and k values (Fig. 4.13 and 4.14). This is the fundamental mechanism for the charge-qubit operation used to rotate a TI charge qubit on a Bloch sphere. The single qubit rotation will be discussed in detail in the following section.

When the strength of the electric field becomes too high, the surface state is pushed towards the bulk and coupled with bulk states (Fig. 4.15 and Fig. 4.16). Therefore, we need to keep this in mind and only use an electric field with a moderate strength.

A point to note is that we use E to represent the electric field throughout this chapter, which is the potential energy difference of the electric field across the thickness of the film. The electric field strength is proportional to E since the film is kept at a constant thickness to study a single qubit.

4.3 Single-qubit study

In order to study the quantum control of a charge qubit, we need to define a suitable two-level system. We learnt from the previous section that the there are four surface states at the Γpoint (see Fig.4.2 Fig.4.3 Fig.4.4 Fig.4.5). $|S1\rangle$ is defined as a surface state on the hole band with $s_z = -\frac{1}{2}$. $|S2\rangle$ is defined as a surface state on the hole band with $s_z = \frac{1}{2}$. $|S3\rangle$ is defined as a surface state on the electron band with $s_z = \frac{1}{2}$. $|S4\rangle$ is defined as a surface state on the electron band with $s_z = -\frac{1}{2}$. It is natural to define the qubit state Φ_0 as a state where most charge density is located on the bottom surface (where QL $= 0$) and state Φ_1 as a state where most charge density is on the top surface (where QL $= d$). We have learnt from above that a perpendicular electric field will couple the states on the hole and electron bands with the same quantum number (k, s_z etc.). In this chapter, we decided to use the spin up 'surface state' on the hole band (see Fig. 4.3) and the spin up 'surface state' on the electron band (see Fig. 4.4) in a 5 QL TI. We will call these states $|S_2\rangle$ and $|S_3\rangle$ respectively. By combining the two states in two different ways as :$|S_2\rangle \pm |S_3\rangle$, we obtain a pair of states located on the top/bottom surfaces (Fig. 4.17 and Fig. 4.18). In this chapter, we define our qubit as :

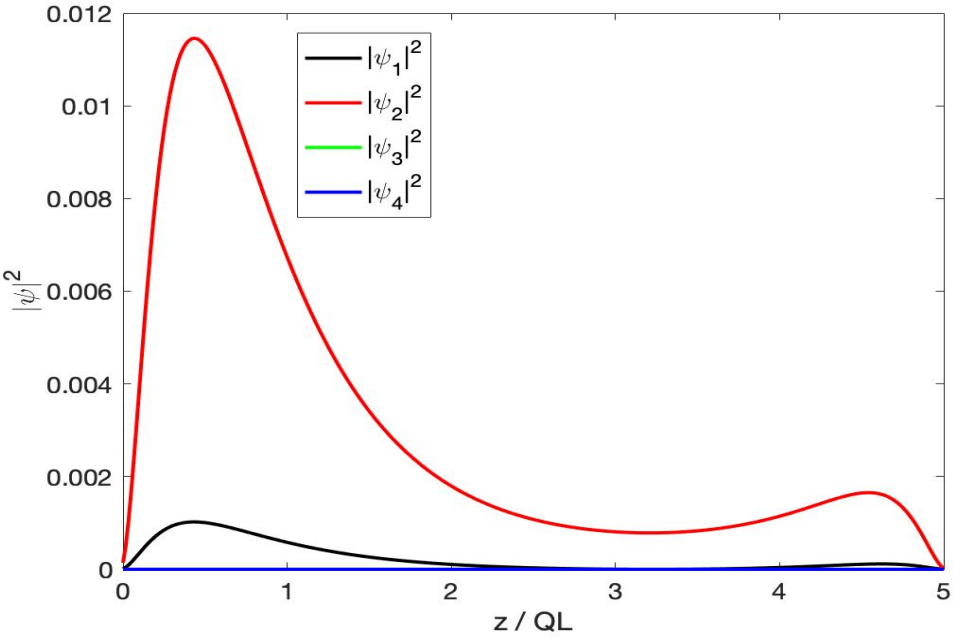

Fig. 4.13 Spatial distributions of the wave function densities of a spin up 'surface state' on the hole band at the Γ point in a 5 QL TI thin film, with an electric field ($E = 0.008\,75\,\text{eV}$, note: E is the potential energy difference of the electric field across the thickness of the film, and we use this to represent the electric field throughout this chapter. The electric field strength is proportional to E.) applied in the z direction. $|\psi_1|^2$ to $|\psi_4|^2$ are the wave function densities of the basis states $|\psi_1\rangle$ to $|\psi_4\rangle$ of the TI Hamiltonian in Eq. 4.1. The detailed electronic states of $|\psi_1\rangle$ to $|\psi_4\rangle$ are shown in Eq. 2.26. The wave function densities of $|\psi_3\rangle$ and $|\psi_4\rangle$ are equal to zero. The wave function density of the 'surface state' spans over the whole thickness of the TI, with most densities being near the surfaces.

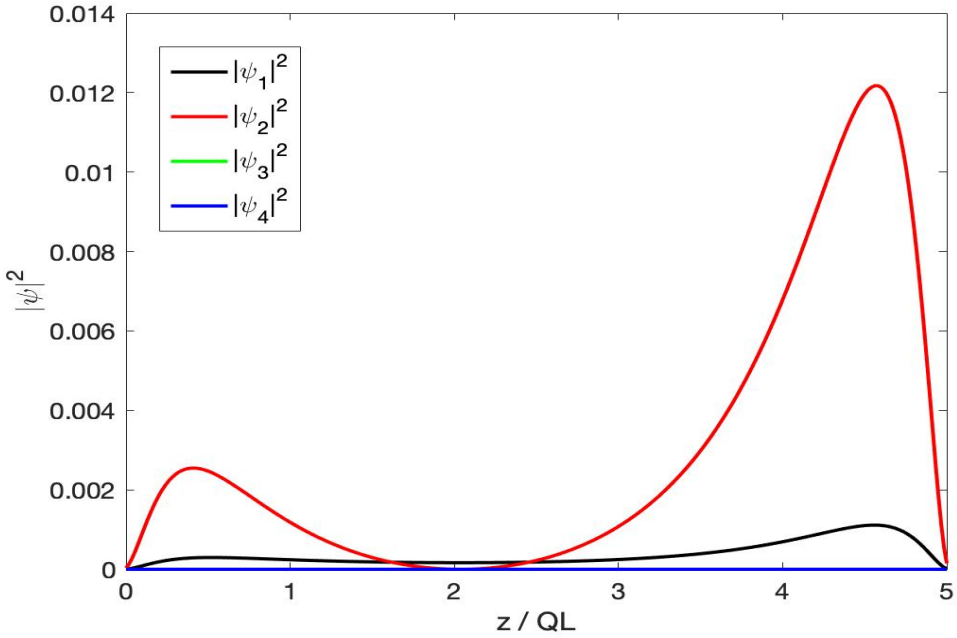

Fig. 4.14 Spatial distributions of the wave function density of a spin up 'surface state' on the electron band at the Γ point in a 5 QL TI thin film, with an electric field ($E = 0.008\,75\,\text{eV}$ note: E is the potential energy difference of the electric field across the thickness of the film, and we use this to represent the electric field throughout this chapter. The electric field strength is proportional to E.) applied in the z direction. $|\psi_1|^2$ to $|\psi_4|^2$ are the wave function densities of the basis states $|\psi_1\rangle$ to $|\psi_4\rangle$ of the TI Hamiltonian in Eq. 4.1. The detailed electronic states of $|\psi_1\rangle$ to $|\psi_4\rangle$ are shown in Eq. 2.26. The wave function densities of $|\psi_3\rangle$ and $|\psi_4\rangle$ are equal to zero. The wave function density of the 'surface state' spans over the whole thickness of the TI, with most densities being near the surfaces.

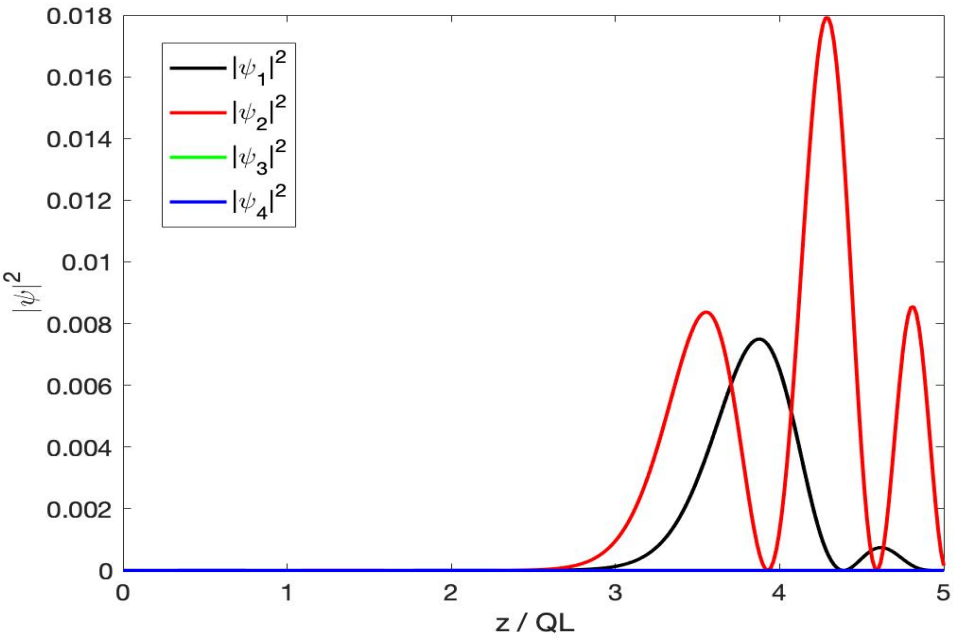

Fig. 4.15 Spatial distributions of the wave function densities of a 'surface state' at $k_x = 0.01$, $k_y = 0$ on the electron band with its spin pointing almost perpendicular ($s_y = -0.44$) to its direction of motion, in a 5 QL TI thin film, with an electric field ($E = 1\,\text{eV}$, note: E is the potential energy difference of the electric field across the thickness of the film, and we use this to represent the electric field throughout this chapter. The electric field strength is proportional to E.) applied in the z direction. $|\psi_1|^2$ to $|\psi_4|^2$ are the wave function densities of the basis states $|\psi_1\rangle$ to $|\psi_4\rangle$ of the TI Hamiltonian in Eq. 4.1. The detailed electronic states of $|\psi_1\rangle$ to $|\psi_4\rangle$ are shown in Eq. 2.26. The wave function densities of $|\psi_3\rangle$ and $|\psi_4\rangle$ are equal to zero. The wave function density is localised near one surface with nodes, indicating that the electron is excited to a higher energy state.

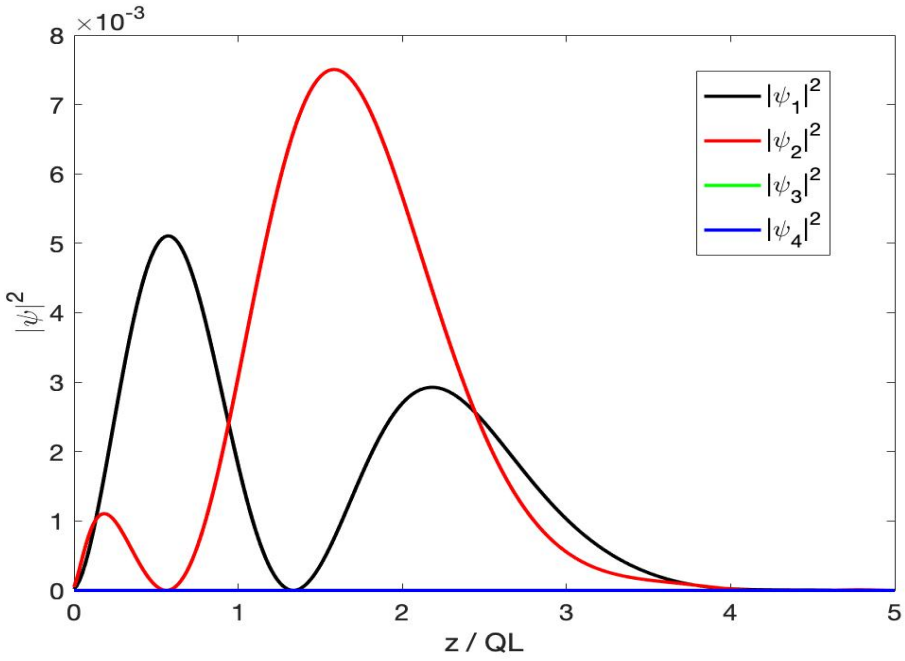

Fig. 4.16 Spatial distributions of the wave function densities of a 'surface state' at $k_x = 0.01$, $k_y = 0$ on the electron band with its spin pointing almost perpendicular ($s_y = 0.44$) to its direction of motion, in a 5 QL TI thin film, with an electric field ($E = 1\,\text{eV}$, note: E is the potential energy difference of the electric field across the thickness of the film, and we use this to represent the electric field throughout this chapter. The electric field strength is proportional to E.) applied in the z direction. $|\psi_1|^2$ to $|\psi_4|^2$ are the wave function densities of the basis states $|\psi_1\rangle$ to $|\psi_4\rangle$ of the TI Hamiltonian in Eq. 4.1. The detailed electronic states of $|\psi_1\rangle$ to $|\psi_4\rangle$ are shown in Eq. 2.26. The wave function densities of $|\psi_3\rangle$ and $|\psi_4\rangle$ are equal to zero. The wave function density is localised near one surface with nodes, indicating that the electron is excited to a higher energy state.

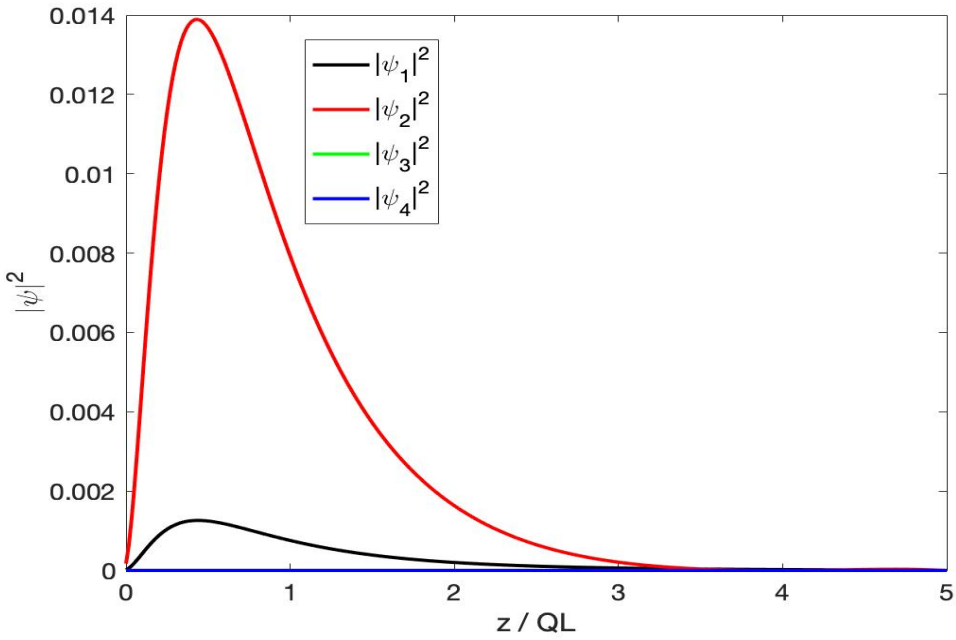

Fig. 4.17 Spatial distributions of the wave function densities of $|\Phi_0\rangle$ at the Γ point in a 5 QL TI thin film. It is a combinational state of the 'surface states' in Fig.4.3 ($|S_2\rangle$) and Fig. 4.4 ($|S_3\rangle$), where $|\Phi_0\rangle = |S_2\rangle - |S_3\rangle$. $|\psi_1|^2$ to $|\psi_4|^2$ are the wave function densities of the basis states $|\psi_1\rangle$ to $|\psi_4\rangle$ of the TI Hamiltonian in Eq. 4.1. The detailed electronic states of $|\psi_1\rangle$ to $|\psi_4\rangle$ are shown in Eq. 2.26. The wave function densities of $|\psi_3\rangle$ and $|\psi_4\rangle$ are equal to zero. The wave function density corresponding to $|\Phi_0\rangle$ is localised on one surface.

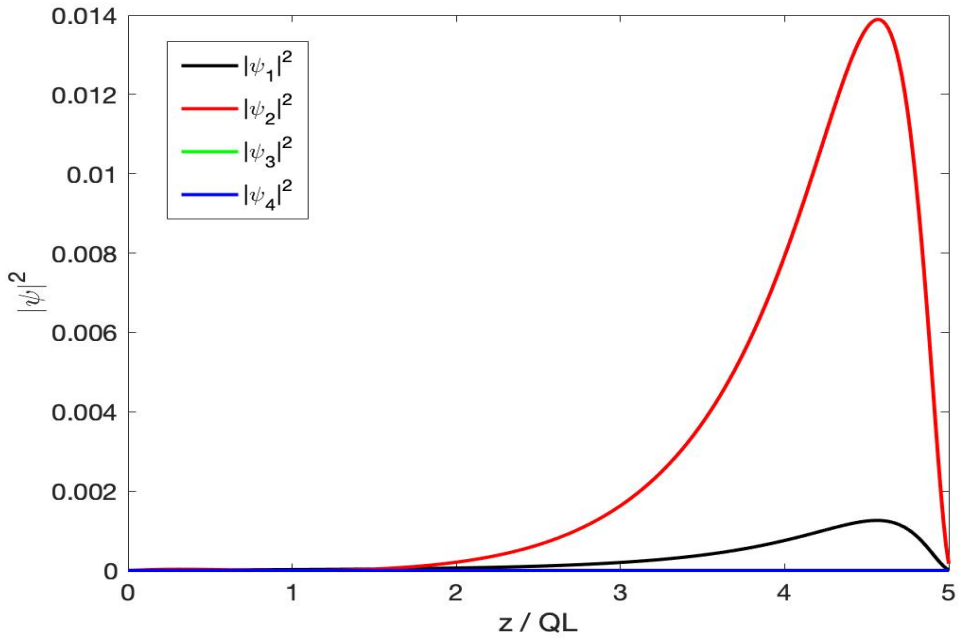

Fig. 4.18 Spatial distributions of the wave function densities of $|\Phi_1\rangle$ at the Γ point in a 5 QL TI thin film. It is a combinational state of the 'surface states' in Fig.4.3 ($|S_2\rangle$) and Fig. 4.4 ($|S_3\rangle$), where $|\Phi_1\rangle = |S_2\rangle + |S_3\rangle$. $|\psi_1|^2$ to $|\psi_4|^2$ are the wave function densities of the basis states $|\psi_1\rangle$ to $|\psi_4\rangle$ of the TI Hamiltonian in Eq. 4.1. The detailed electronic states of $|\psi_1\rangle$ to $|\psi_4\rangle$ are shown in Eq. 2.26. The wave function densities of $|\psi_3\rangle$ and $|\psi_4\rangle$ are equal to zero. The wave function density corresponding to $|\Phi_1\rangle$ is localised on one surface.

$$|\Phi_0\rangle = \frac{1}{\sqrt{2}}(|S_2\rangle - |S_3\rangle), \tag{4.2}$$

$$|\Phi_1\rangle = \frac{1}{\sqrt{2}}(|S_2\rangle + |S_3\rangle). \tag{4.3}$$

A general state on Bloch sphere is:

$$|\Phi\rangle = \cos\left(\frac{\theta}{2}\right)|\Phi_0\rangle + \sin\left(\frac{\theta}{2}\right)|\Phi_1\rangle e^{i\phi}. \tag{4.4}$$

The thickness of a TI thin film is also an important factor when choosing a pair of suitable states. As in the case for charge qubits in a double quantum well, when the sub-wells are too close together, the states are overlapped. The combined states are no longer centred on one side and part of wave function density leaks into other surface, as the case $QL = 1$ shown in Fig. 4.19; this would increase the difficulty to measure the qubit accurately. Alternatively, when the TI becomes too thick, the gap is too small to separate the two levels and thermal excitation will introduce unwanted couplings between the qubit states, which increases the error rate of the qubit system. Therefore, it is a trade-off between the two factors when choosing a suitable thickness to establish our charge qubit system in TI. In this chapter, we choose a 5 QL TI as our system to study a charge qubit.

Another factor to consider is the valid range of k values to use for the qubit system. This is related to setting up a suitable Fermi level in an experiment. As we see from Fig. 4.4 and Fig. 4.10, the state is symmetric around the centre at the Γ point. Away from the Γ point, the state is no longer symmetric, with a growing tail of the atomic state with opposite spin owing to spin-orbit effect. The resultant state is insensitive to the electric field due to the spin-orbit effect and is difficult to do qubit operations with it. Therefore, we need to select states in a range of k close to the Γ point. We find that within our model, a state with $|k|$ value up to $0.0002\,\text{Å}^{-1}$ (with spin $< s_z >= 0.498$) is still a good state for qubit operation. A way to determine whether a state can be a good qubit state is by measuring its spin. If the spin is mostly along s_z, then the effect of quantum confinement is dominant and the state is suitable. Otherwise, spin-orbit coupling is significant and the state is not suitable for charge qubit operations.

When the electron is in a combined state of a two-level system, the phase of the state will vary periodically in time. An electron in a combined state can be written as:

$$|\Phi\rangle = e^{-i\varepsilon_{S_2}t/\hbar}(\alpha|S_2\rangle + \beta e^{i(\varepsilon_{S_2}-\varepsilon_{S_3})t/\hbar}|S_3\rangle). \tag{4.5}$$

From equation 4.5, we see that $|\Phi\rangle$ will experience a periodic phase variation inversely proportional to the energy difference of the two levels $|\varepsilon_{S_2} - \varepsilon_{S_3}|$. This sets up a time scale

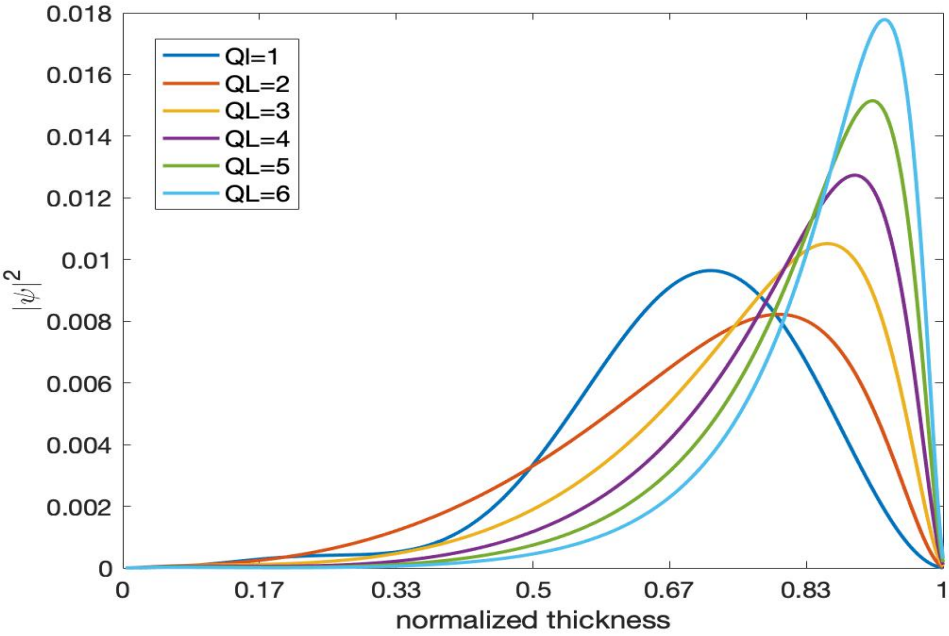

Fig. 4.19 Spatial distributions of the total wave function density ($|\psi_1|^2+|\psi_2|^2+|\psi_3|^2+|\psi_4|^2$) of a 'surface state' at the Γ point in TI thin films of various thickness (1 QL - 5 QL). $|\psi_1|^2$ to $|\psi_4|^2$ are the wave function densities on the basis states $|\psi_1\rangle$ to $|\psi_4\rangle$ of the TI Hamiltonian in Eq. 4.1. The detailed electronic states of $|\psi_1\rangle$ to $|\psi_4\rangle$ are shown in Eq. 2.26. The figure indicates that the thinner the TI thin film is, the more the wave function density of the electron spread out across the TI thin film.

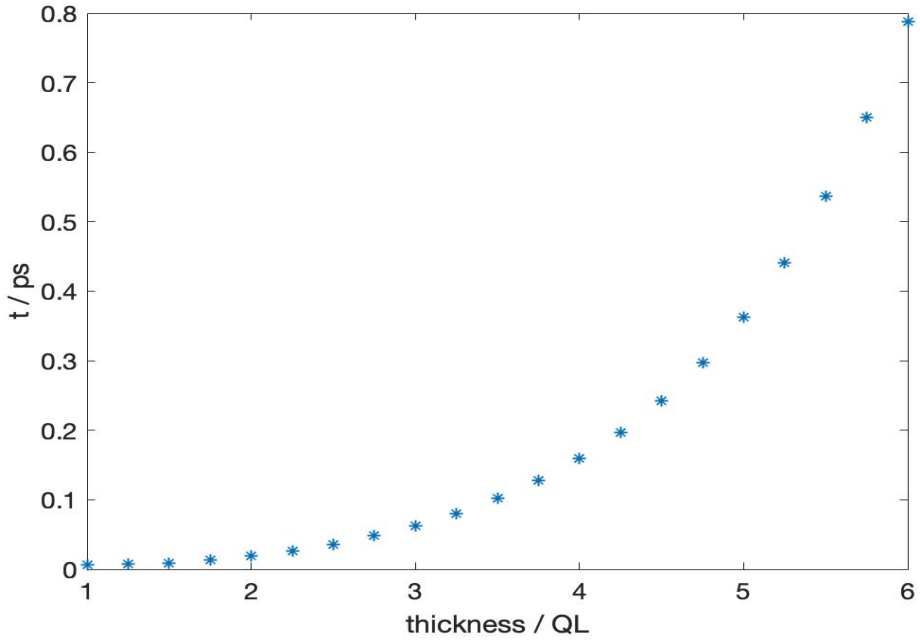

Fig. 4.20 Oscillation period of a TI thin film initially in the $|\Phi_0\rangle$ state vs various thickness (1 QL - 5 QL). The period increases with the thickness of TI thin film, since the band gap energy decreases with the thickness of TI thin film.

for the operation time of a qubit rotation on the Bloch sphere. In Fig. 4.20, we can see that the operation time is on a scale of (10^{-3}-10^{-1} ps); more specifically, it is 0.3626 ps for 5 QL TI.

4.3.1 Initialisation

In a quantum computation experiment, we always need to initialise our qubit into a known state so we can decide what operation will be applied to it later in the experiment. In the rest of this chapter, we choose to study a localised qubit in a TI quantum dot (i.e. the quantum states at $k = 0$). Here we choose the initial state to be $|\Phi_0\rangle$ (Fig. 4.17). This can be done by setting the Fermi level in or below the gap of the Dirac cone; then the hole bands of the Dirac cone are filled while the electron bands are empty. When we apply a static electric field to the TI system, the electron will be excited to a combined state of Φ_0 and Φ_1. By applying a pulse with suitable strength for an appropriate time duration, the electron will go to state Φ_0. In our simulation, it is found to be a pulse of $E = 0.008\,75$ eV (note: here, E is the potential energy difference of the electric field across the thickness of the film, and we use this to represent the electric field throughout this chapter. The electric field strength is proportional to E.) , and duration $t = 0.13$ ps.The spin is preserved during this electric dipole transition. Alternatively,

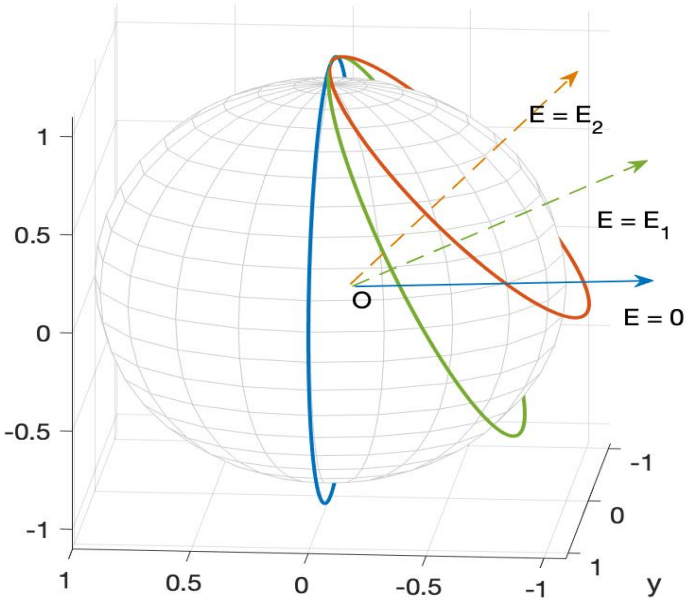

Fig. 4.21 Traces of a single qubit rotation on a Bloch sphere when a static electric field is applied perpendicular to the TI thin film, with E being the energy difference across the film between 0 eV and 0.008 75 eV and $E_1 < E_2$. The traces indicate that the rotation is governed by a single rotational matrix with an axis lying in the xz plane. When there is no electric field applied, the trace is a rotation with respect to the x axis (blue trace). When the electric field switches on, the rotational axis tilts from the x axis and becomes a combination of rotations with respect to the x and z axes (the cases $E = E_1$ and $E = E_2$ correspond to the green and orange traces, respectively.). As the electric field increases, the rotational axis tilts toward the z axis. Note that the Bloch sphere is drawn at 90% size to clarify the diagram.

an electron can be injected into the electron band of the system. In order to find the suitable strength and time duration of the pulse, we need to understand how the qubit is rotated under a static perpendicular electric field on the Bloch sphere. We apply a static electric field perpendicular to the TI quantum dot with the various energy differences between the top and bottom surfaces ($(0 - 0.07\,\text{eV})$) and find that the qubit rotates in a close circle on the Bloch sphere (Fig. 4.21). The axis of the circle always goes through the centre of the Bloch sphere and lies on the xz plane. This rotation is independent of the initial position of the qubit on the Bloch sphere. Because the axis always lies in the xz plane irrespective of the strength, a qubit starting from a surface state (e.g. $|S2\rangle$) will rotate into states $|\Phi_0\rangle$ or $|\Phi_1\rangle$ at half of the rotational period. Therefore, if we find a pulse such that the rotational axis is at 45° with respect to the z axis, after half of the rotational period the qubit will be exactly at $|\Phi_0\rangle$ (or $|\Phi_1\rangle$, depending on the direction of the electric field). The angle of the axis with respect to z

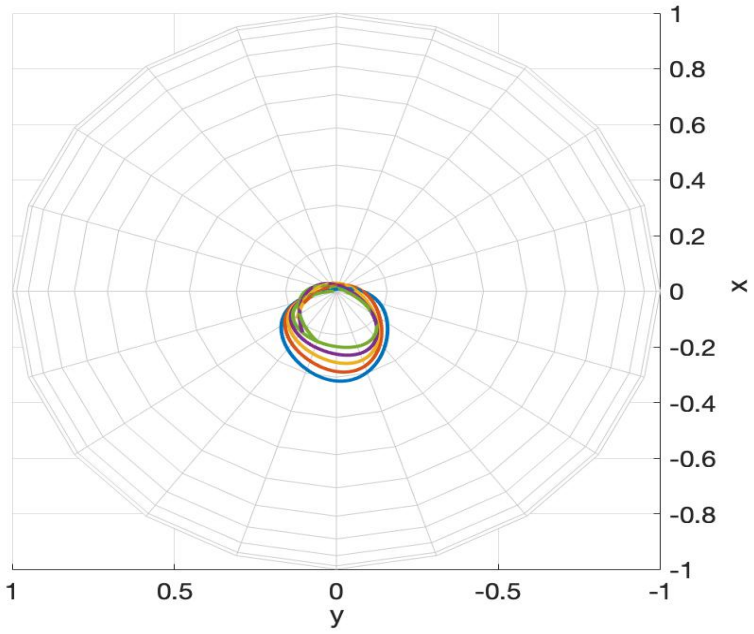

Fig. 4.22 Traces of a single qubit rotation on a Bloch sphere when a static electric field is applied perpendicular to the TI thin film, with E being the energy differences across the film larger than 0.0525 eV (blue trace: 0.0525 eV, orange trace: 0.0530 eV, yellow trace: 0.0535 eV, purple trace: 0.0540 eV and green trace: 0.0545 eV). The traces are no longer circular since the electronic fields are too large which significantly modifies the states during the operation. Note that the Bloch sphere is drawn at 90% size to clarify the diagram.

axis is found to be inversely proportional to the strength applied (Fig. 4.23). When there is no field applied to the system, the qubit rotates spontaneously following a closed circle with the rotational axis at 90°(see Fig. 4.21). This rotation is described by equation 4.5. We can see that as the field becomes larger, the angle is closer to zero. However, from Fig. 4.22 and section 4.2.3, we see that the qubit does not follow a circular trace any longer when the field becomes too high and the bulk states may interact with the qubit. Therefore, we need to keep the electric field at a moderate strength to reduce the error rate during operation.

4.3.2 Qubit operation

In order to rotate the qubit to an arbitrary location on a Bloch sphere, we need to manipulate the qubit with respect to two orthogonal axes. From the last subsection 4.3.1, we see that when there is no field present, the qubit rotates with respect to the x axis, achieving the σ_x rotation. The rotational period is proportional to the band gap width and was shown in Fig. 4.20 for TIs of various thickness. The equation of this rotation for a state on the same path

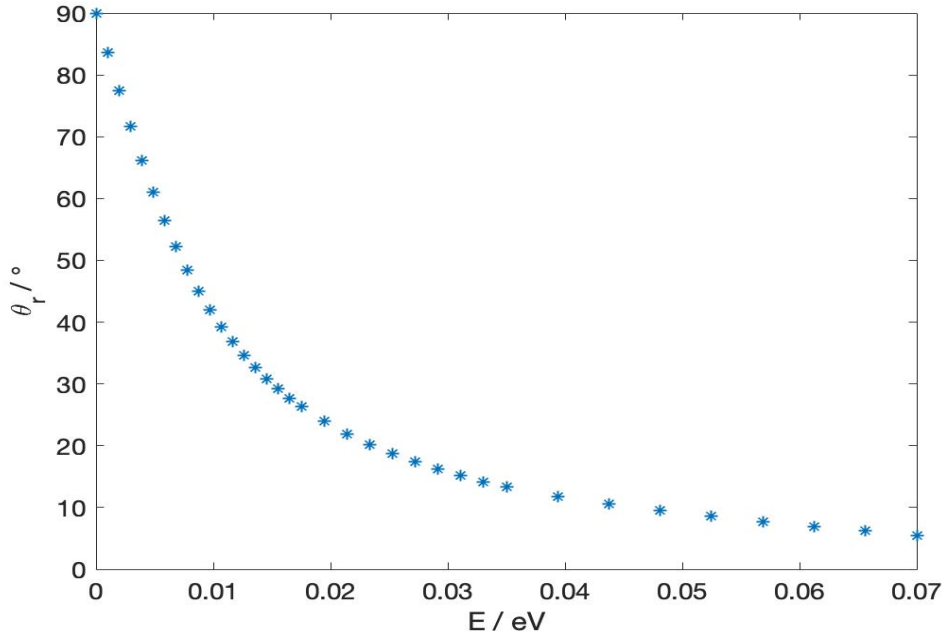

Fig. 4.23 Angle of the rotational axis with respect to the z axis when a static electric field is applied perpendicular to the TI thin film; θ_r is the conventional polar angle used in spherical coordinate systems. θ_r decreases with E, the energy difference across the film.

with Φ_0 and Φ_1 is:

$$|\Phi_{t'}\rangle = \hat{\mathscr{R}}_x(\theta,\phi)\,|\Phi_{t_0}\rangle\,, \tag{4.6}$$

$$= \cos\left(\frac{\theta_{t'}}{2}\right)|\Phi_0\rangle + \sin\left(\frac{\theta_{t'}}{2}\right)e^{i\phi_{t_0}}\,|\Phi_1\rangle\,. \tag{4.7}$$

The rotation operator $\hat{\mathscr{R}}_x(\theta,\phi)$ only changes the θ angle: $\Delta\theta = \omega_x(t'-t_0)$, where ω_x is the angular frequency of the qubit rotation without the field. Because ω_x is proportional to the band gap width, it is easy to obtain in an experiment via the relation $\omega_x = \frac{(E_{electron}-E_{hole})}{\hbar}$. In subsection 4.3.1 we saw that when a static electric field is applied, the qubit undergoes a rotation in a closed circle on the Bloch sphere (Fig. 4.21). We note here that the Bloch spheres in the thesis are plotted at 90% size to clarify the single-qubit rotation diagrams. However, the rotational axis is not orthogonal to the x axis and it has a finite component along the x axis in general (Fig. 4.23). Theoretically, we should be able to rotate the qubit with respect to the z axis when the electric field is sufficiently large. But according to our numerical simulation, the result in Fig. 4.22 shows that when the electric field is too large the circular trace is significantly distorted, so we need to find an alternative effective σ_z or σ_y rotation. By applying the electric field in the opposite direction, we find that the rotational

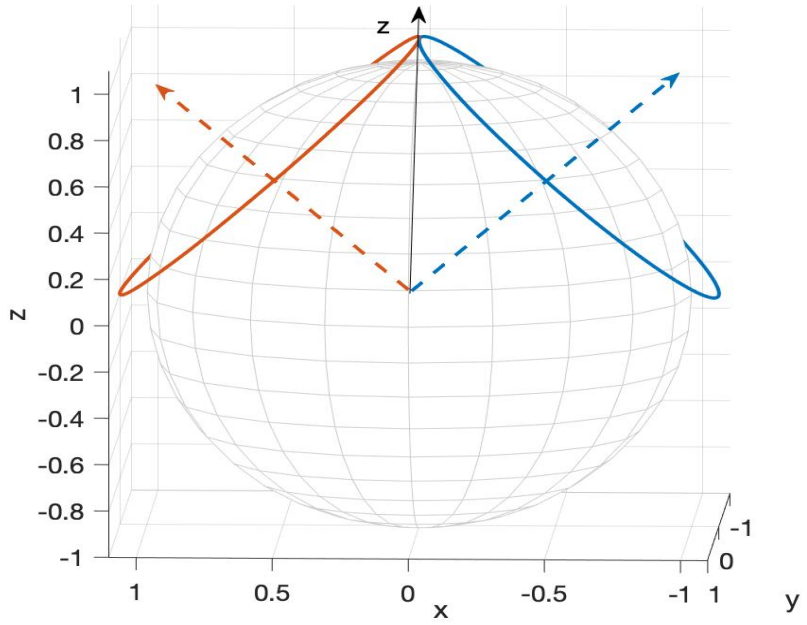

Fig. 4.24 Traces of single qubit rotations with a static electric field applied perpendicular to the TI thin film (blue trace, blue dotted line with arrow being the rotational axis) and the same field applied in a reverse direction (orange trace, orange dotted line with arrow being the rotational axis). The rotational axis is reflected with respect to the z axis. Note that the Bloch sphere is drawn at 90% size to clarify the diagram.

axis is reflected symmetrically to the z axis (Fig. 4.24). Therefore, if we apply a pulse with linear $+E$ and $-E$, we may be able to cancel out the rotation with respect to the x axis. However, this is not trivial, and we were not able to find a two-part pulse that outputs an effective σ_z rotation. Inspired by a previous study in double quantum well in our group, we decided to study whether a three-part pulse can accomplish an effective σ_z rotation. A σ_z rotation on a Bloch sphere is:

$$|\Phi_{t'}\rangle = \hat{\mathscr{R}}_z(\theta,\phi)\,|\Phi_{t_0}\rangle\,, \tag{4.8}$$

$$= \cos\left(\frac{\theta_{t_0}}{2}\right)|\Phi_0\rangle + \sin\left(\frac{\theta_{t_0}}{2}\right)e^{i(\phi_{t'})}\,|\Phi_1\rangle\,, \tag{4.9}$$

which only changes the phase angle ϕ.

We find that a three-part pulse is able to accomplish a position-independent effective σ_z rotation (Fig. 4.26). The pulse consists of three linear pulses at the same strength (Fig. 4.25). We apply a linear pulse E for a duration t_1, then reverse the direction of the field (-E) for a duration t_2, and then switching back to E for a duration t_1; in this way, we are able to perform

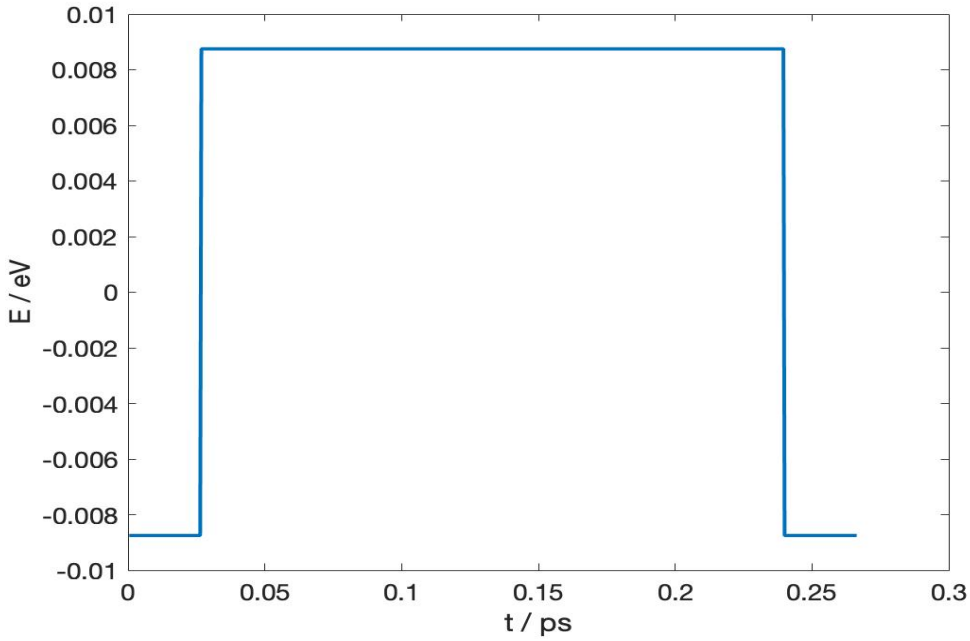

Fig. 4.25 Three-part electric pulse used to achieve an effective σ_z rotation. A static electric field of $E = 0.008\,75\,\text{eV}$ is applied perpendicular to the TI thin film in the first part of the pulse, followed by the same field applied in the opposite direction. The third part of the pulse is identical to the first part of the pulse, with the same time duration. The second part of the pulse is significantly longer than the first (and third) part of the pulse in this specific case.

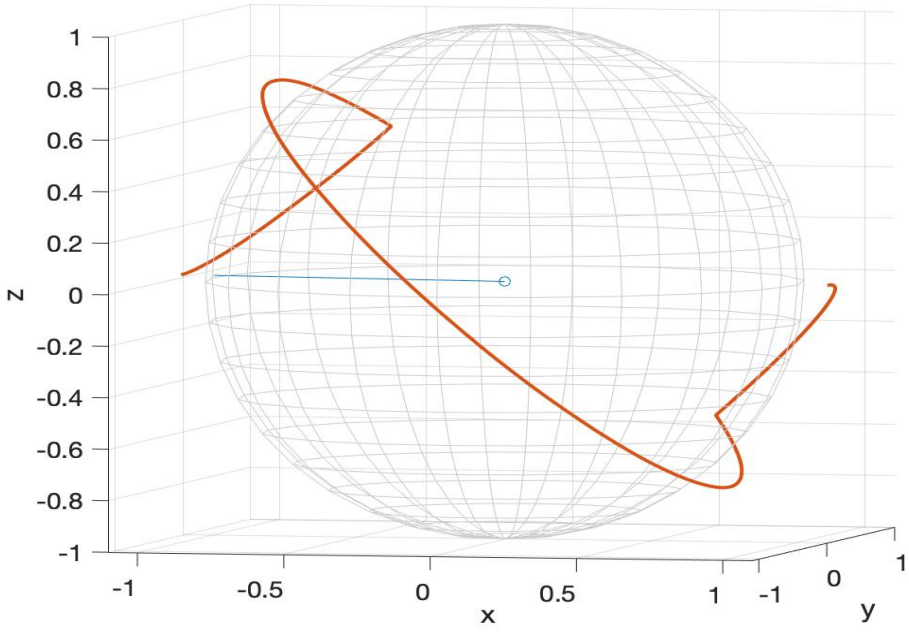

Fig. 4.26 Trace (orange colour) of an effective $180^\circ\sigma_z$ rotation on the Bloch sphere, for a qubit initially at $\theta = 90^\circ, \phi = 0^\circ$. The blue pointer indicates the ending position of the rotation. θ and ϕ are the conventional polar and azimuthal angles used in spherical coordinate systems. Note that the Bloch sphere is drawn at 90% size to clarify the diagram.

an effective σ_z rotation. Like for the initialisation pulse, the strength of the electric field and the duration t_1 and t_2 need to be chosen carefully.

We will now show how the pulse works to give an effective σ_z rotation. From Fig. 4.27 we see that the qubit first rotates along the path t_1 for a time $t = t_1$, then rotates along the path t_2 for $t = t_2$, and eventually rotates along the path t_3 for $t = t_3$ ($t_3 = t_1$). By observing the effective trace, we can see that all of the three parts of the pulse contribute to the σ_z rotation, while the second and third part are chosen carefully to cancel out the extra rotation along the x axis: t_1 and t_2 need to be matched to completely cancel out the σ_x rotation. We keep the strength fixed, set the duration t_1 and find a matching duration of t_2. We choose to study a qubit at Φ_0 at $t = 0$ since, according to Eq. 4.8, $|\Phi_{t'}\rangle = |\Phi_0\rangle$, it is easy to measure experimentally. Because reversing the direction of the field of a moderate strength always yields a rotation with respect to a reflected axis, we decide to use the pulse with the same initialisation strength of $E = 0.008\,75\,\text{eV}$, which gives an axis of 45° with respect to the z axis. Pulses with other strengths are able to accomplish an effective σ_z rotation as well as a matching t_1 and t_2 (see Fig. 4.28). A correct duration t_2 is found by applying a two-part pulse being the first part equal to t_1 with $+E$, the second part equal to T_E with $-E$, where T_E

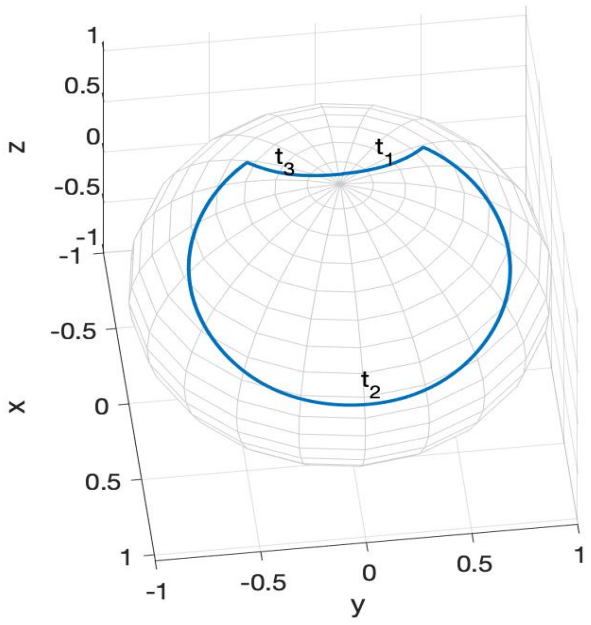

Fig. 4.27 Trace of an effective σ_z rotation for a qubit initially at $\theta = 0^\circ$, $\phi = 0^\circ$ [following the direction of the path $t_1 \rightarrow t_2 \rightarrow t_3(t_3 = t_1)$]. θ and ϕ are the conventional polar and azimuthal angles used in spherical coordinate systems. The qubit returns to its original state as expected. The rotation is achieved by applying a three-part pulse shown in Fig. 4.25. The static field is applied perpendicular to the TI thin film for t_1. Then the field's direction is reversed for t_2 and is switched back for t_1. Note that the Bloch sphere is drawn at 90% size to clarify the diagram.

Table 4.1 t_1,t_2 and $\Delta\phi$ in an effective σ_z rotation. t_1 and t_2 are the time durations of the three-part pulse shown in Fig. 4.25 and ϕ is the conventional azimuthal angles used in spherical coordinate systems.

$t_1(ps)$	0.007	0.013	0.020	0.026	0.033	0.040	0.046	0.053	0.060
$t_2(ps)$	0.251	0.245	0.242	0.240	0.239	0.240	0.244	0.248	0.253
$\phi(^\circ)$	26	51	73	93	112	128	142	157	170

is the total time to complete a full rotation under a static field $-E$, so the qubit will return to the same position at the end of duration t_1. By searching for $\Phi_{t_1+t_2}$ along the path satisfying the condition: $\theta_{t_1+t_2} = \theta_{t_1}$, we find the corresponding time t_2. From Fig. 4.29 we see that this is, in fact, the time duration to go to the other crossing point B for two individual rotations with axis 1 and axis 1' and the same initial position at ($A = \Phi_{t_1}$); t_2 is the time duration to go to B along path 2 from A. Here we show some matching t_1 and t_2 values (table 4.1) and the corresponding phase angle rotated in Fig. 4.30.

The operation time and $\Delta\phi$ of an effective σ_z rotation both increase with t_1 in general. (Fig. 4.31). A total time of 0.31 ps accomplishes a rotation close to 180°. In fact, we do not need to further increase t_1 to achieve a rotation of more than $\Delta\phi = 180^\circ$ but we can simply reverse the direction of the field while keeping t_1 and t_2 the same. The resultant rotation at $t = t_1 + t_2$ will have $\Delta\phi' = -\Delta\phi$.

Fidelity is an important concept in the study of qubit control and is defined for the TI qubit as:

$$\mathscr{F}_{t_0,t_1} = |\left\langle \Phi_{\theta,\phi} \middle| \Phi_{t_1} \right\rangle|^2. \tag{4.10}$$

$\Phi_{\theta,\phi}$ is the corresponding state on the Bloch sphere after a designed rotation. The fidelity of an effective σ_z rotation with rotational angle at $\Delta\phi = 93^\circ$ is shown in Fig. 4.32. The fidelity of this rotation is as high as 99.9% (Fig. 4.32). The small errors could come from the numerical calculations since the staggered leapfrog method is an approximation method. This confirms that the effective σ_z rotation for the TI charge qubit is indeed position-independent and this three-part pulse is able to accomplish an effective σ_z rotation with very high fidelity.

4.3.3 Read-out

In order to measure the qubit, the coefficients on a Bloch sphere in Eq. 4.4 need to be related to measurable properties. For a charge qubit in a TI quantum dot, the TI quantum dot is sandwiched between a source electrode and a drain electrode [50] (More information about the experimental set-up of the TI quantum dot will be discussed in the following section.). When an electron tunnels to the source/drain electrode, it causes a change in the source-drain

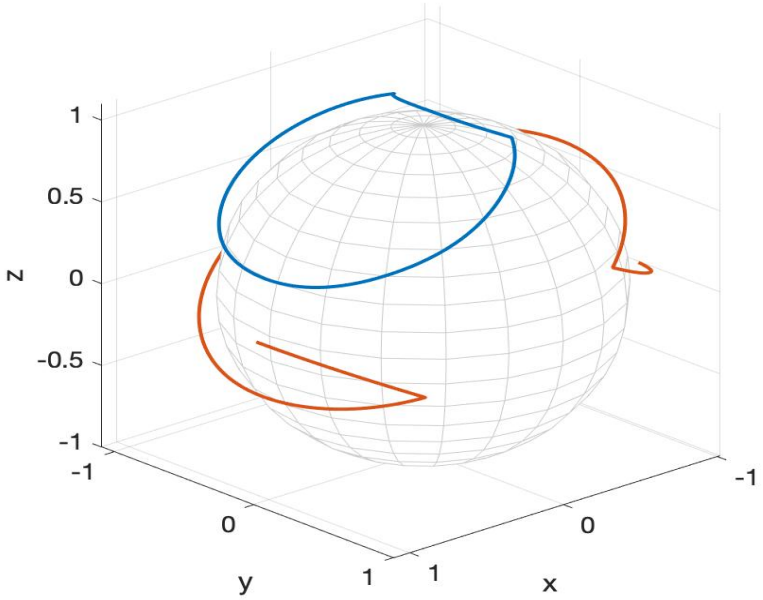

Fig. 4.28 Two traces of the effective 158° σ_z rotations for the qubit initially at Φ_0 (blue trace; note that σ_z rotation adds an overall phase to the qubit at Φ_0, which can be ignored) and at $\theta = 90°$, $\phi = 0°$ (orange trace). θ and ϕ are conventional polar and azimuthal angles used in spherical coordinate systems. The pulse applied is the three-part pulse shown in Fig. 4.25 with the magnitude $|E| = 0.01653\,\text{eV}$. Note that the Bloch sphere is drawn at 90% size to clarify the diagram.

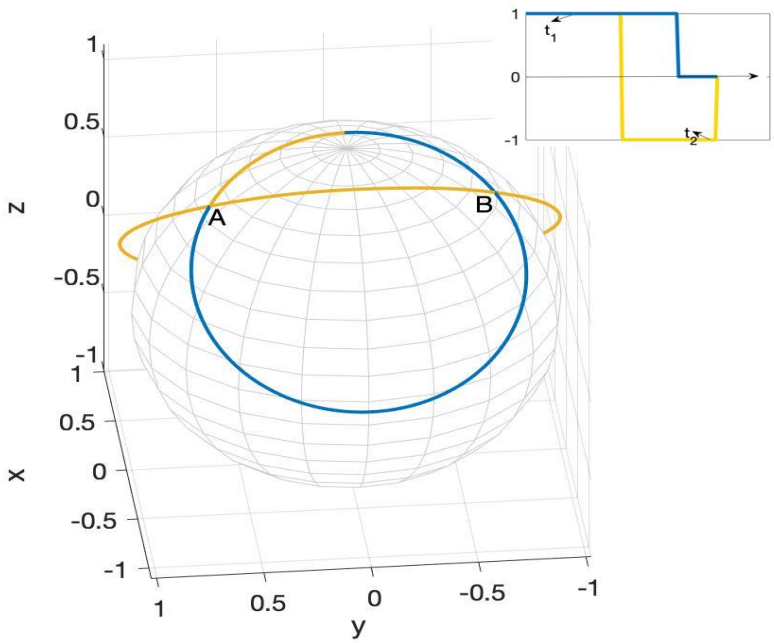

Fig. 4.29 Two traces of a single qubit rotation with different types of electric field pulses for the qubit at Φ_0. Blue trace: a full circular single qubit rotation with a static electric field applied perpendicular to the TI thin film. Yellow trace: a single qubit rotation under a two-part pulse, which consist of two static but opposite electric fields(at the same energy difference across the film, E, as path 1). The first part of the pulse is applied for t_1 and the second part of the pulse is applied during a whole period for a full circular rotation. This figure is useful to find the corresponding t_2 in the three-part pulse(Fig. 4.25) for σ_z rotation. The time taken for the qubit on path 2 to point A on the Bloch sphere is recorded as t_1 and the time duration taken from A to B on path 2 is the corresponding time t_2 (the longer orange route goes over the sphere in the figure). Note that the Bloch sphere is drawn at 90% size to clarify the diagram. The inset shows the pulse profiles to achieve the two traces.

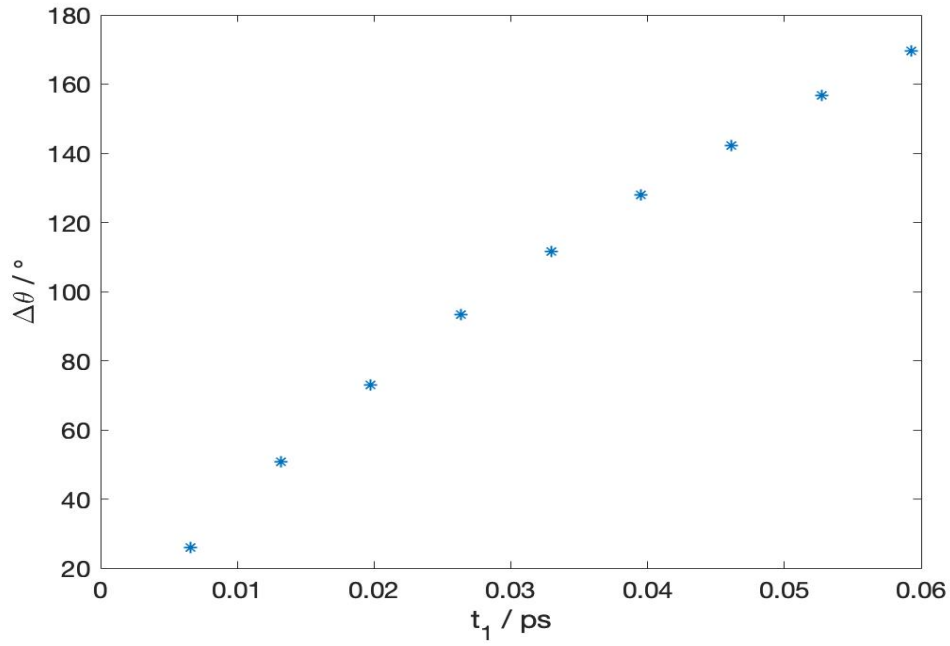

Fig. 4.30 $\Delta\theta$ in an effective σ_z rotation vs t_1. θ is the conventional polar angle used in spherical coordinate systems and t_1 is the time duration of the first part of three-part pulse shown in Fig. 4.25.

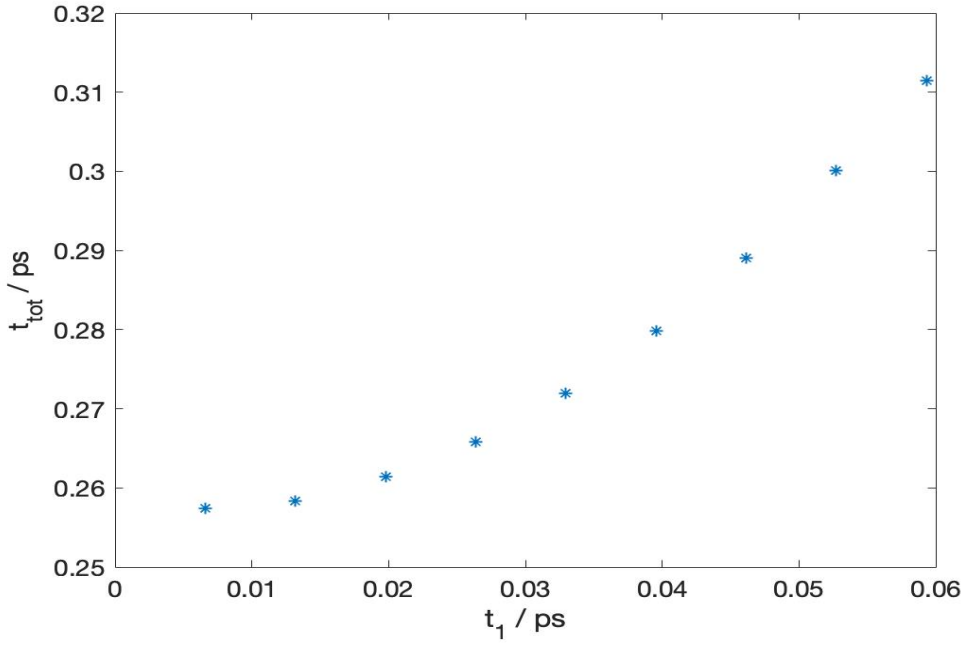

Fig. 4.31 Total operation time of an effective σ_z rotation vs t_1. t_1 is the time duration of the first part of three-part pulse shown in Fig. 4.25.

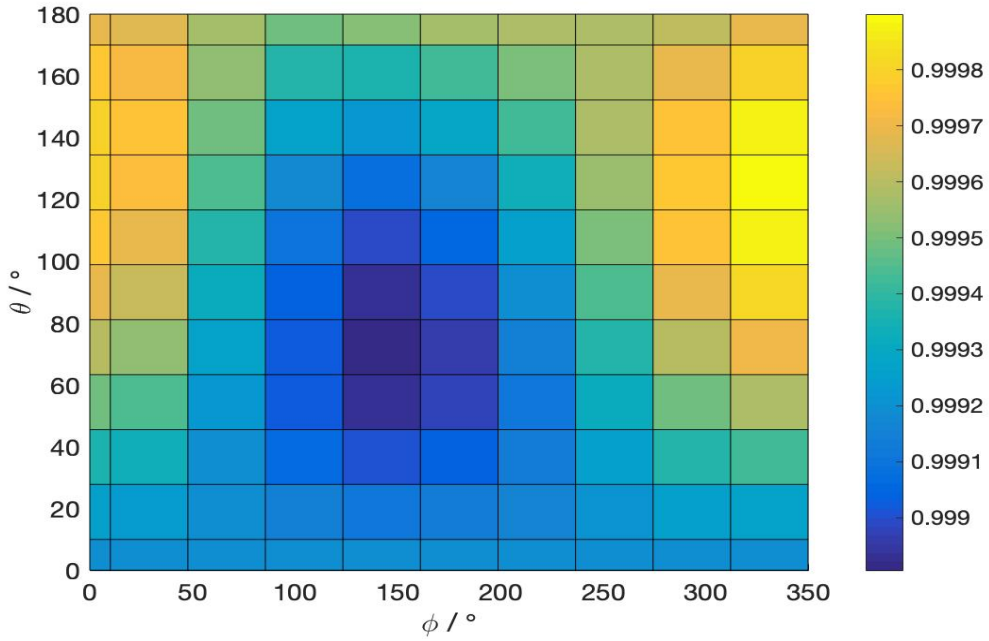

Fig. 4.32 Fidelity of an effective σ_z rotation for $\Delta\phi = 93^\circ$ vs various qubit states (in the range of $\theta \in [0^\circ, 180^\circ]$, $\phi \in [0^\circ, 350^\circ]$) on the Bloch sphere. θ and ϕ are conventional polar and azimuthal angles used in spherical coordinate systems. This figure shows that the effective σ_z is indeed universal and position-independent. The fidelity is extremely high, which is over 99.9%.

current. $I_e = I_m - I_B$, where I_e, I_m and I_B being, respectively, the current caused by a single electron, the current measured and the source-drain current where there is no electron. In this section, we assume $I_B = 0$ for simplicity. The measurement is done by measuring the current I_e. We define the current I_0 as the current flowing into the electrode attached to the top surface of TI and I_1 as the current flowing into the electrode attached to the bottom surface. Because the qubit states we use are located on top/bottom surfaces, the wave function can be written as:

$$\Phi_0(z) = \Phi_{T0}(z) + \Phi_{B0}(z), \tag{4.11}$$

$$\Phi_1(z) = \Phi_{T1}(z) + \Phi_{B1}(z), \tag{4.12}$$

where $\Phi_{T0(1)}$ and $\Phi_{B0(1)}$ are wave function with all of the electron density located on the top/bottom surfaces.

Since $\Phi_0(z)$ and $\Phi_1(z)$ are orthogonal, we have:

$$\int_{-z}^{z} \Phi_0(z)^* \Phi_1(z) dz = \int_{-z}^{z} \Phi_{T0}(z)^* \Phi_{T1}(z) dz + \int_{-z}^{z} \Phi_{T0}(z)^* \Phi_{B1}(z) dz + \tag{4.13}$$

$$\int_{-z}^{z} \Phi_{B0}(z)^* \Phi_{T1}(z) dz + \int_{-z}^{z} \Phi_{B0}(z)^* \Phi_{B1}(z) dz \tag{4.14}$$

$$= 0, \tag{4.15}$$

and

$$\int_{-z}^{z} \Phi_{T0}(z)^* \Phi_{B1}(z) dz = \int_{-z}^{z} \Phi_{B0}(z)^* \Phi_{T1}(z) dz = 0. \tag{4.16}$$

Since there is no overlap between wave functions located on the top and bottom surfaces.

$$\int_{-z}^{z} \Phi_{T0}(z)^* \Phi_{T1}(z) dz = -\int_{-z}^{z} \Phi_{B0}(z)^* \Phi_{B1}(z) dz. \tag{4.17}$$

For a general qubit state on the Bloch sphere, we can write:

$$\Phi(z) = \alpha \Phi_0(z) + \beta \Phi_1(z), \tag{4.18}$$

$$= \alpha(\Phi_{T0}(z) + \Phi_{B0}(z)) + \beta(\Phi_{T1}(z) + \Phi_{B1}(z)). \tag{4.19}$$

where $\alpha = \cos\left(\frac{\theta}{2}\right)$ and $\beta = \sin\left(\frac{\theta}{2}\right) e^{i\phi}$.

To measure the probability of Φ on the top surface, we have:

$$P_T = \int_0^z \Phi(z)^* \Phi(z) dz = \int_0^z (\alpha^* \Phi_{T0}^*(z) + \beta^* \Phi_{T1}^*(z))(\alpha \Phi_{T0}(z) + \beta \Phi_{T1}(z)) dz, \tag{4.20}$$

which can be written as:

$$P_T = |\alpha|^2 P_0 + |\beta|^2 P_1 + \alpha^* \beta \int_0^z \Phi_{T0}^*(z)\Phi_{T1}(z)dz + \alpha\beta^* \int_0^z \Phi_{T1}^*(z)\Phi_{T0}(z)dz. \tag{4.21}$$

The integrals P_0 and P_1 can be obtained by measuring the current through the top surface when the qubit is in the state Φ_0 or Φ_1. The latter two terms are the overlap of Φ_0 and Φ_1 on the top surface. Recalling Eq. 4.2 and making use of the values of $\int_0^z S2^*S3dz$ and $\int_0^z S2^*S2dz$:

$$\int_0^z S2^*S3dz = \frac{1}{4}(P_1 - P_0 + \int_0^z \Phi_{T0}^*(z)\Phi_{T1}(z)dz - \int_0^z \Phi_{T1}^*(z)\Phi_{T0}(z)dz), \tag{4.22}$$

$$\int_0^z S2^*S2dz = \frac{1}{4}(P_1 + P_0 + \int_0^z \Phi_{T0}^*(z)\Phi_{T1}(z)dz + \int_0^z \Phi_{T1}^*(z)\Phi_{T0}(z)dz). \tag{4.23}$$

We have the overlapping integrals:

$$P_{01} = \int_0^z \Phi_{T0}^*(z)\Phi_{T1}(z)dz = 2\int_0^z S2^*S3dz + 2\int_0^z S2^*S2dz - P_1, \tag{4.24}$$

$$P_{10} = \int_0^z \Phi_{T1}^*(z)\Phi_{T0}(z)dz = -2\int_0^z S2^*S3dz + 2\int_0^z S2^*S2dz - P_0. \tag{4.25}$$

Recall $|\alpha|^2 + |\beta|^2 = 1$. α and β then can be calculated from Eq. 4.21.

At the Γ point, since the wave functions of the qubit state Φ_0 and Φ_1 are mirror image of each other, we have:

$$P_{01} = P_{10} = 0. \tag{4.26}$$

Eq. 4.21 then reduces to:

$$P_T = |\alpha|^2 P_0 + |\beta|^2 P_1. \tag{4.27}$$

P_T can be simply related to $|\alpha|$ and $|\beta|$ as:

$$|\alpha|^2 = \frac{P_1 - P_T}{P_1 - P_0}, \tag{4.28}$$

$$|\beta|^2 = \frac{P_T - P_0}{P_1 - P_0}. \tag{4.29}$$

$$\tag{4.30}$$

The current I_0 through the top surface is proportional to P_T as $I_0 = nP_T$, where n is the current density. Therefore, the probability of finding an electron on the top surface is directly linked to the superposition coefficients of the qubit state. Hence, we are able to read the output of

the wave function of a charge qubit in TI and, therefore, fulfils the DiVincenzo criterion V (see Ch.1).

4.4 The two-qubit gate

The two-qubit operation for TI quantum dots is analogous to that implemented in semiconductor double quantum dots. It can be realised by electrostatically coupling two adjacent TI quantum dots, as proposed for semiconductor quantum dots in [101] and [36], or driven by microwaves [90] or acoustic waves [7]. For example, the two-qubit interaction Hamiltonian for two TI quantum dots positioned in parallel in the two-qubit logic state basis $|00\rangle$, $|01\rangle$, $|10\rangle$, $|11\rangle$ can be described by:

$$H = \frac{J}{4}\sigma_z^1 \otimes \sigma_z^2, \tag{4.31}$$

where $J = U_{TT} + U_{BB} - U_{TB} - U_{TB}$ is the electrostatic coupling between the two quantum dots. U_{TT}, U_{BB} and U_{TB} are the electrostatic coupling energies of the two quantum dots with electrons staying on the top, bottom, or top and bottom surfaces of TI quantum dot 1 and TI quantum dot 2. They can be related to the capacitance of the relevant part of the quantum dot by a capacitance model [111]. $U_{TT(BB)} = e^2 C_{TT(BB)}/C_\Sigma^2$ and $U_{TB} = e^2 C_{TB}/C_\Sigma^2$, where $C_{TT(BB)}$ is the capacitance between top (bottom) surfaces of the TI quantum dots, C_Σ is the total capacitance of a single TI quantum dot and C_{TB} is the capacitance between the top and bottom surface of TI quantum dot 1 and TI quantum dot 2. Detailed computation using an electrostatic interaction between TI qubits was beyond the resources of the group. It would have required tens of millions of position basis states. This work is now being considered for our GPU servers.

4.5 Discussion and summary

In this chapter we have proposed a static charge qubit in an ultra-thin TI fulfilling the DiVincenzo's criteria I, II, IV, V. (Ch. 1) This is a charge qubit of high fidelity (99.9%) which can be read out easily using conventional techniques, such as with a quantum point contact or a single-electron transistor [44]. A possible experimental setup for this TI quantum dot is described in Hayashi's paper [49] for their semiconductor double quantum dot, with a source and a drain electrode. In the case of a TI quantum dot, there is no need to implement gates to define the quantum dot. This simplifies the procedure of manufacturing a quantum dot in TI. The source-drain voltage is used for the initialisation, single-qubit operation and measurement process. Like other semiconductor quantum dots, decoherence is expected to occur in a

TI quantum dot. TI quantum dots are a new research field so there is no experimental measurement of decoherence times of a TI qubit and the underlying decoherence mechanisms are under active research [53] [70]. However, given the similarity to a semiconductor quantum dot, a rough estimate of the decoherence time would be longer than 100 ns [49], which is the decoherence time of a GaAs quantum dot. The difference in decoherence time is attributed to the weak coupling of the isolated qubit to the noise from quantum fluctuations of charge in the surrounding gates and a reduction in the obtention of high-frequency noise to travel down to the qubit [49]. Because we do not need many gates to define a TI quantum dot, the decoherence time could be longer than the GaAs case where the background charge fluctuation and noise in the gate voltages are a significant cause of decoherence. Also, because of the topological protection of a TI, we would expect this qubit to have longer decoherence time. In this section we will discuss some questions related to realising such a qubit in an experiment. From section 4.3 we see that the operation time is of order of 0.1 ps, which would require a fast pulse. Although it is desirable to have fast qubits, which allow for high speed calculation and fits error correction schemes, the operation time of a few 0.1 ps is beyond the capability of controlling apparatus. Typical electric field pulsing times are in a range of a few tens to thousands of picoseconds [50]. Although the operation time can be increased by using a smaller electric field, it is still much lower than the range of the operation times we desire. One way to solve this problem is to run the operation for multiple periods additional to the operation time, i.e. $t_1' = t_1 + nT_E$ where T_E is the period of the qubit rotation under a static electric field of the same strength. In this way, we can control the operation time to be in the range that controlling apparatus can manage and yet still be very fast. The same is true for the electric field strength: since the qubit can rotate in any direction on a Bloch sphere under a moderate electric field with a carefully designed pulse operation times t_1 and t_2, we are able to design a pulse within the equipment capacity in terms of strength and pulse operation time. The next question we will consider is the energy of qubit. If we inject an electron with an energy of the quantum state of the electron band at the Γ point, we will have a qubit of a single electron. From subsection 4.3.3, we know the qubit state Φ_0 and Φ_1 at the Γ point are mirror images of each other and have zero wave function density on the opposite surface. This offers a convenient way to measure the qubit in an experiment. If we inject a wave packet of electrons with the same energy (the momentum k can be different) to one of the surfaces, we have prepared the electrons in one of the qubit states. In fact those electrons can be viewed as a single qubit since they have same behaviour under an electric pulse on their Bloch sphere. Indeed, at small k values, the qubits are almost identical (Fig. 4.33 and Fig. 4.34). In this way, we can obtain a stronger tunnelling current since the density of state in the momentum space is proportional to k^2.

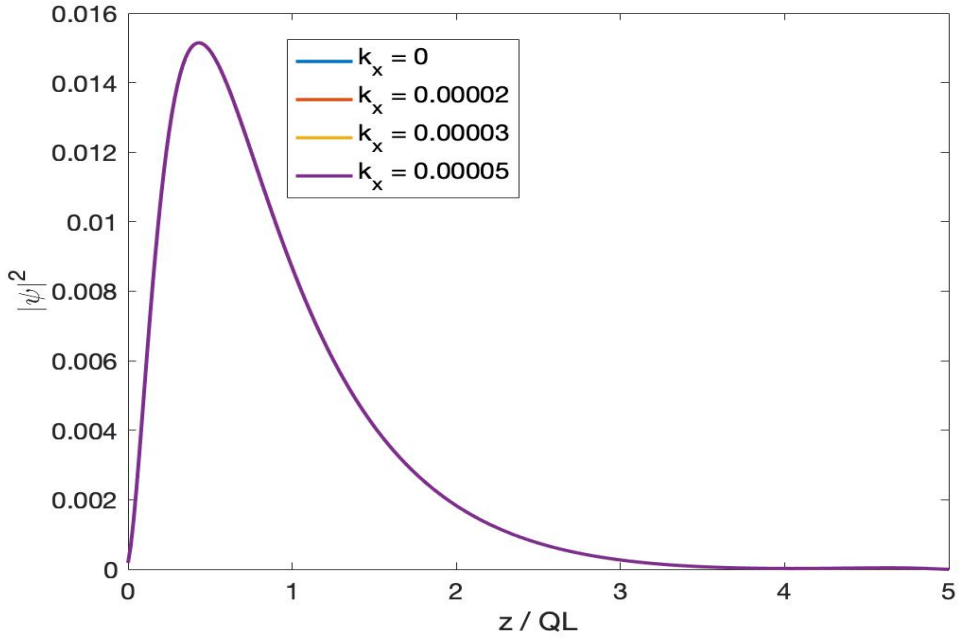

Fig. 4.33 Spatial distributions of the total wave function density ($|\psi_1|^2+|\psi_2|^2+|\psi_3|^2+|\psi_4|^2$) of combined states Φ_0 (as in Eq. 4.2) at various k_x positions with a fixed $|k| = 0.00005\,\text{Å}^{-1}$ in a 5 QL TI thin film. $|\psi_1|^2$ to $|\psi_4|^2$ are the wave function densities on the basis states $|\psi_1\rangle$ to $|\psi_4\rangle$ of the TI Hamiltonian in Eq. 4.1. The detailed electronic states of $|\psi_1\rangle$ to $|\psi_4\rangle$ are shown in Eq. 2.26. The spatial distributions of those qubits are almost overlapped.

However, as mentioned in subsection 4.3.3 and Fig.4.15 and Fig. 4.16, a small tail increment owing to the spin-orbit effect. In the valid qubit range, we have calculated the overlap of $|\langle S2|S3\rangle|^2$ and $|\langle S3|S3\rangle|^2$ at $|k| = 0.00005\,\text{Å}^{-1}$ on the top surfaces, and find it to be 0.11 and 0.13, respectively. Therefore, the overlap is small enough and could possibly be omitted in a measurement.

In this Chapter, we have proposed an implementation scheme of a charge qubit in an ultra-thin TI. A single qubit rotation can be controlled by electric pulses. We have shown that the charge qubit can be initialised, rotated arbitrarily on a Bloch sphere, and read out. This qubit is similar to a charge qubit in a double quantum well and can be manufactured as a quantum dot.

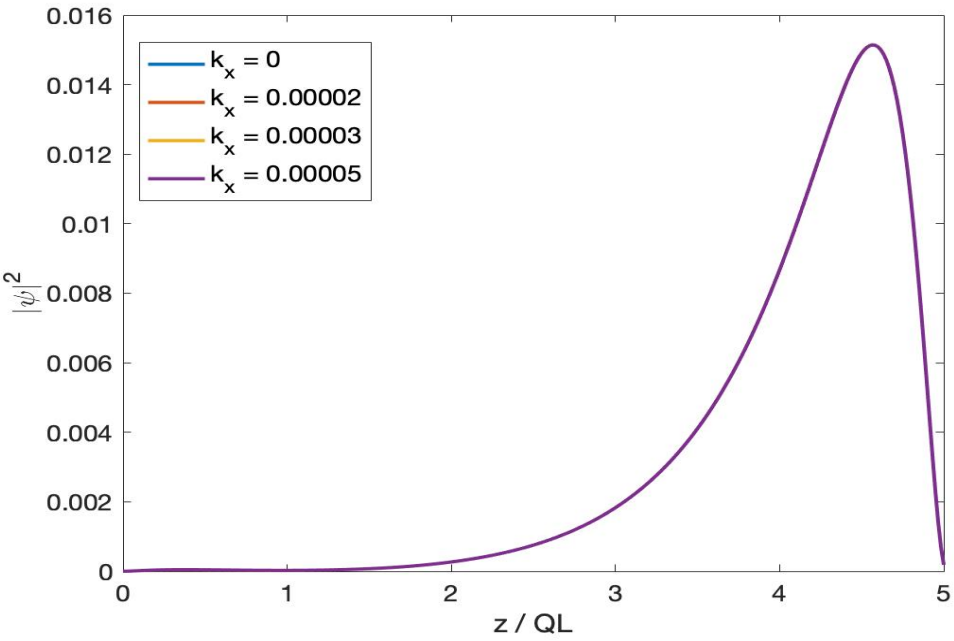

Fig. 4.34 Spatial distributions of the total wave function density ($|\psi_1|^2+|\psi_2|^2+|\psi_3|^2+|\psi_4|^2$) of combined states Φ_1 (as in Eq. 4.2) at various k_x positions with a fixed $|k| = 0.00005\,\text{Å}^{-1}$ in a 5 QL TI thin film. $|\psi_1|^2$ to $|\psi_4|^2$ are the wave function densities on the basis states $|\psi_1\rangle$ to $|\psi_4\rangle$ of the TI Hamiltonian in Eq. 4.1. The detailed electronic states of $|\psi_1\rangle$ to $|\psi_4\rangle$ are shown in Eq. 2.26. The spatial distributions of those qubits are almost overlapped.

Chapter 5

A Spin Qubit in An Ultra-thin TI Film

5.1 Introduction

Since the discovery of a spin in the Stern-Gerlach experiment in 1921, the study of spin physics has never ceased. As an internal degree of freedom of a particle, it has led to many interesting fundamental phenomena and new discoveries in physics. One famous example is the quantum spin hall effect [63]. Thanks to the development of techniques related to spin physics, we can measure and control this internal degree of freedom of a particle and create a different type of qubit other than a charge qubit. Since the first proposals of using a nuclear spin [39] or an electron spin in a quantum dot [74] for quantum computing in 1997, the study of a spin qubit has been a very active research field [29] [19] [59]. Spin states of particles are promising for quantum computation and quantum-information processing, and have been studied in various physical systems [1] [28] [113]. There are two main types of spin qubits: the first one makes use of a nuclear spin [39], while the second one exploits electron spins in confined quantum dots [74]. In an ultra-thin TI quantum dot, we can define a spin type of qubit with electrons on surface states with opposite spins that are separated by a hybridisation gap. The prominent decay channels for spin qubits is the spin-orbit interaction and hyperfine interaction [59] [57] [32]. Decay through the spin-orbit interaction is a phonon-mediated process that will relax the qubit to the lower energy state in the two-level system and it is considered to be the major source of decoherence for electron spin qubits [59]. It has been calculated in [57] that the relaxation time is, $T_1 \propto \frac{\hbar(\Delta\varepsilon)^4}{(g\mu_B B)^5}$, where $\Delta\varepsilon$ is the band gap difference of the two-level system and $g\mu_B B$ is the Zeeman splitting induced by the magnetic field. For an ultra-thin TI, $T_1 \approx 0.01\,\mathrm{s}$ under a magnetic field as large as 1 T. It should be noticed that when the magnetic field becomes very large, the relaxation time is increased rather than decreased [40], because the phonon size becomes much smaller than the quantum dot, and the phonon-induced effects average out when integrating over the whole electron

wavefunction [59] [40]. Moreover, as the charge qubit (Ch. 4), we found the spin qubit in an ultra-thin TI are very fast in terms of single qubit rotations and operation time $t_p \ll T_1$.

In this chapter, we will investigate how to use the electrons on the gapped Dirac cone for a single-spin-qubit study and how external pulses move the qubit on its Bloch Sphere. Advanced quantum control of the corresponding two-qubit operation is beyond the scope of this thesis but will be discussed briefly at the end of this chapter in Sec. 5.5. We will start the chapter by introducing the modified TI Hamiltonian with an in-plane magnetic field and discuss the effect of the magnetic field on the states in Sec. 5.2. Then we will define a suitable two-level system for studying a spin qubit in Sec. 5.3, followed by the study of initialisation, quabit rotation and qubit measurement in Sec. 5.3.1 - Sec. 5.3.3. In the last Sec. 5.5, we discuss some experimental related questions and possible solutions.

5.2 System

5.2.1 Model Hamiltonian

When a magnetic field is applied to a topological insulator, there are two type of effects to be considered. The first one is the orbit effect and the second one is the Zeeman effect. In this chapter, we apply an in-plane static magnetic field to an ultra-thin TI film and study how the surface states change with this field. The model Hamiltonian of a TI with an in-plane magnetic field is:

$$H = H_0(\mathbf{k}' + \frac{e\mathbf{A}}{\hbar}) + H_{Ze}, \tag{5.1}$$

here H_0 is the original TI Hamiltonian described in chapter 2 with $\mathbf{k}$ substituted of by $\mathbf{k}' + \frac{e\mathbf{A}}{\hbar}$, where $\mathbf{A}$ represents the vector field. $\mathbf{k}' + \frac{e\mathbf{A}}{\hbar}$ is the Peierls substitution [77] representing the orbit effect of a magnetic field. The Zeeman splitting is represented by an extra Hamiltonian H_{Ze}.

Because H_0 preserves the in-plane rotational symmetry along the z direction, the choice of the direction of a magnetic field on the xy plane makes no difference physically. The effect of the field along different directions can be related by rotating the reference frame on the xy plane. In this chapter, we decide to consider a magnetic field along the y direction. We have chosen a gauge in which the vector field $\mathbf{A} = (Bz, 0, 0)$ and $k_x = k'_x + \frac{eBz}{\hbar}$. The resultant Hamiltonian still commutes with k_x and k_y, but no longer commutes with k_z. The modified

terms in the Hamiltonian H_0 are:

$$\begin{aligned}
C(\mathbf{k}) &= C_0 + C_1 k_z^2 + C_2 k_y^2 + C_2 (k_x' + \frac{eBz}{\hbar})^2, \\
M(\mathbf{k}) &= M_0 + M_1 k_z^2 + M_2 k_y^2 + M_2 (k_x' + \frac{eBz}{\hbar})^2, \\
A_0 &= A_0, \\
B_0 &= B_0.
\end{aligned}$$

Then we add an atomic Zeeman term to our model Hamiltonian $H_0(k_x')$. The atomic Zeeman Hamiltonian is:

$$H_{Ze} = -\mu \cdot \mathbf{B} = -\frac{\mu_B (g_{ef} \mathbf{J})}{\hbar} \cdot \mathbf{B}, \tag{5.2}$$

where μ is the magnetic moment, μ_B is the Bohr magneton, $\mathbf{J}$ is the total angular momentum operator, g_{ef} is the effective gyromagnetic ratio of Bi_2Se_3 and $\mathbf{B}$ is the magnetic field. In fact, the effective gyromagnetic ratio of Bi_2Se_3 is different for different atomic orbits, as we will see soon. H_{Ze} commutes with the total angular momentum $\mathbf{J}^2$ and j_z. Following the discussion on basis states in Ch. 2, we know that the basis of H_0 are eigenstates of the total angular momentum j_z. Therefore, the Zeeman term for our TI model can be written as:

$$H_{Ze} = \frac{\mu_B}{\hbar} (B_x \cdot j_x + B_y \cdot j_y + B_z \cdot j_z). \tag{5.3}$$

Here, $J_i (i = x, y, z)$ are the matrices of the total angular momenta along the x, y and z directions (discussed in Ch. 2) multiplied by the effective g-factor for Bi_2Se_3. The values are adapted

from [72] (See table. 5.2.1). In matrix form, $J_i(i = x, y, z)$ are:

$$J_x = \begin{pmatrix} 0 & 0 & \frac{\hbar}{2}g_{1p} & 0 \\ 0 & 0 & 0 & \frac{\hbar}{2}g_{2p} \\ \frac{\hbar}{2}g_{1p} & 0 & 0 & 0 \\ 0 & \frac{\hbar}{2}g_{2p} & 0 & 0 \end{pmatrix},$$

$$J_y = \begin{pmatrix} 0 & 0 & \frac{-i\hbar}{2}g_{1p} & 0 \\ 0 & 0 & 0 & \frac{-i\hbar}{2}g_{2p} \\ \frac{i\hbar}{2}g_{1p} & 0 & 0 & 0 \\ 0 & \frac{i\hbar}{2}g_{2p} & 0 & 0 \end{pmatrix},$$

$$J_z = \begin{pmatrix} \frac{\hbar}{2}g_{1z} & 0 & 0 & 0 \\ 0 & \frac{\hbar}{2}g_{2z} & 0 & 0 \\ 0 & 0 & \frac{-\hbar}{2}g_{1z} & 0 \\ 0 & 0 & 0 & \frac{-\hbar}{2}g_{2z} \end{pmatrix}.$$

The adapted effective g-factor values are:

g_{1p}	g_{2p}	g_{1z}	g_{2z}
-4.12	4.80	-25.4	4.10

We can see that absolute values of the entries in J_x and J_y are the same in Bi_2Se_3 and this confirms that the direction of the in-plane magnetic field makes no physical difference to the system. Then we apply the finite difference method described in Chap. 3 to H in Eq. 5.1 and obtain the numerical Hamiltonian for a TI thin film under a magnetic field:

Table 5.1 Numerical Hamiltonian of a TI under a magnetic field

$n_z = 1$	$n_z = 2$	$n_z = 3$	$n_z = 4$	$n_z = 5$	
$H'_{0,z=1} + H_{Ze}$	H_{+1}	0	$\vdots$	$\vdots$	$n_z = 1$
H_{-1}	$H'_{0,z=2} + H_{Ze}$	H_{+1}	0	$\vdots$	$n_z = 2$
0	H_{-1}	$H'_{0,z=3} + H_{Ze}$	H_{+1}	$\vdots$	$n_z = 3$
$\vdots$	0	H_{-1}	$H'_{0,z=4} + H_{Ze}$	H_{+1}	$n_z = 4$

5.2.2 Effects of an in-plane magnetic field

When a static in-plane magnetic field is applied to a TI with well separated surfaces, the Dirac cone splits along the direction that is perpendicular to the field (Fig. 5.1). This can

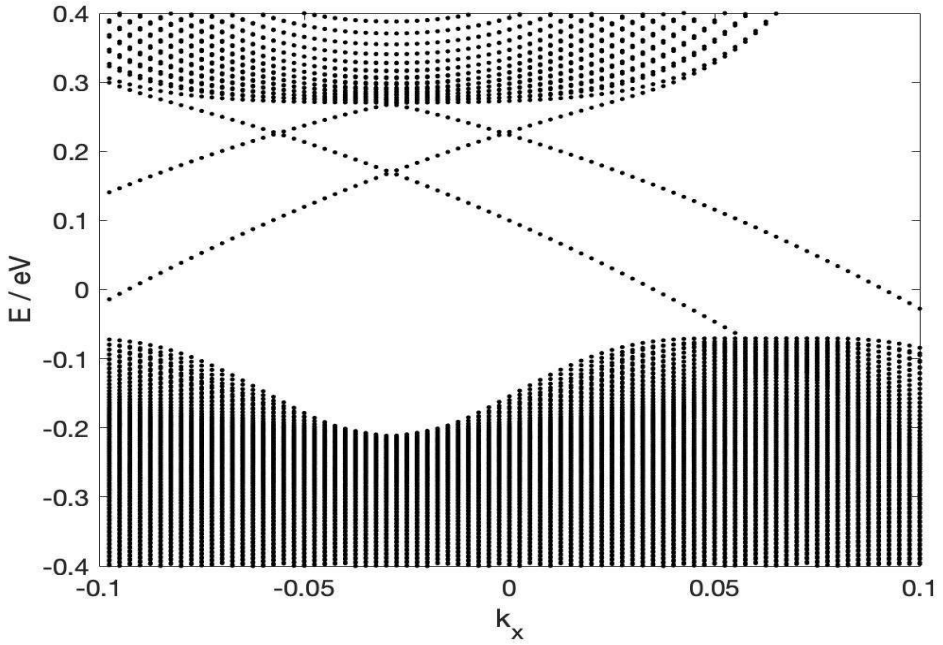

Fig. 5.1 Band structure of a 40 QL TI thin film with an in-plane static magnetic field ($B_y = 10\,\mathrm{T}$) along the k_x axis and $k_y = 0$. The Dirac cones located on the opposite surfaces split along the perpendicular direction of electron motion owing to the effect of the magnetic field.

be understood by thinking about the magnetic force experienced by electrons moving under a perpendicular magnetic field. The vector potential $A_x = Bz$ creates a gradient along the z direction for the electrons moving in the x direction. Therefore, the Dirac cones located on the top and bottom surfaces are shifted in the momentum space along the k_x direction by different amounts. The Zeeman effect creates a splitting between the spin degenerate bands, which lifts the spin-down electronic bands and lowers the spin-up electronic bands. However, the Zeeman effect is less significant than the orbit effect for a moderate magnetic field in a TI thin film.

In an ultra-thin TI where the Dirac cones are gapped, the orbital effect causes the Dirac cones to be shifted in the k_x direction. Because the hybridised surface states are expanded over both surfaces, the two cones are shifted by almost the same amount. The slight difference is owing to the different distribution over the z axis. The Zeeman effect causes a splitting in spin-up and spin-down bands (Fig. 5.2).

From Chapter 4 we know that the states on the gaped Dirac cone are governed by two different effects - hybridisation and spin-orbit coupling. For states near the Γ point, the hybridisation effect dominates and the states show features of bonding and anti-bonding orbits. On the other hand, for states far away from the Γ point, the spin-orbit coupling

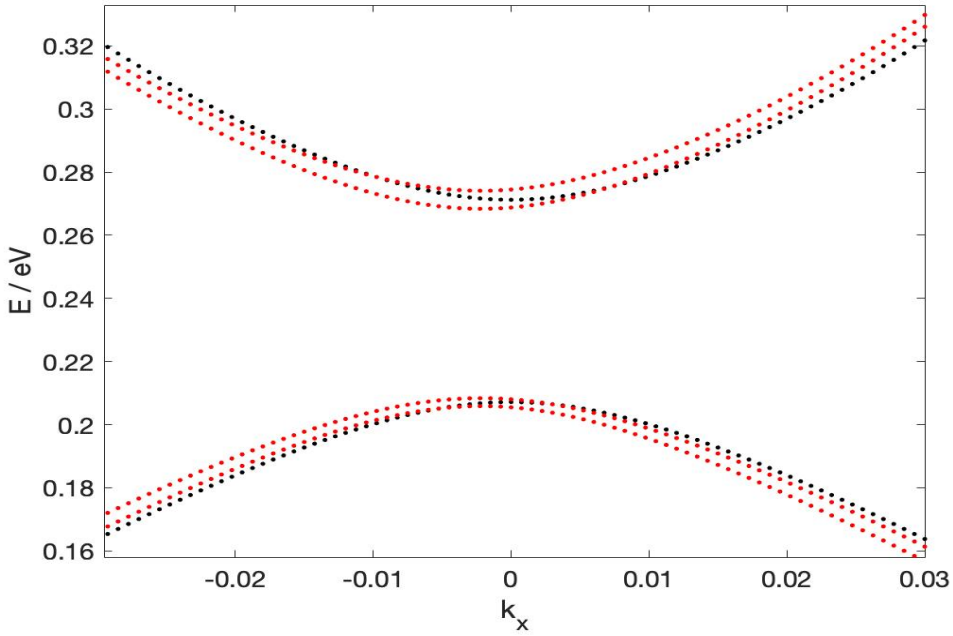

Fig. 5.2 Band structure of a 3 QL TI thin film with an in-plane static magnetic field ($B_y = 10\,\mathrm{T}$, red dots) and without the field (black dots) along the k_x axis and $k_y = 0$. The Dirac cones are hybridised and gapped in the 3 QL TI thin film, and the degenerate spin levels split owing to the effect of the magnetic field.

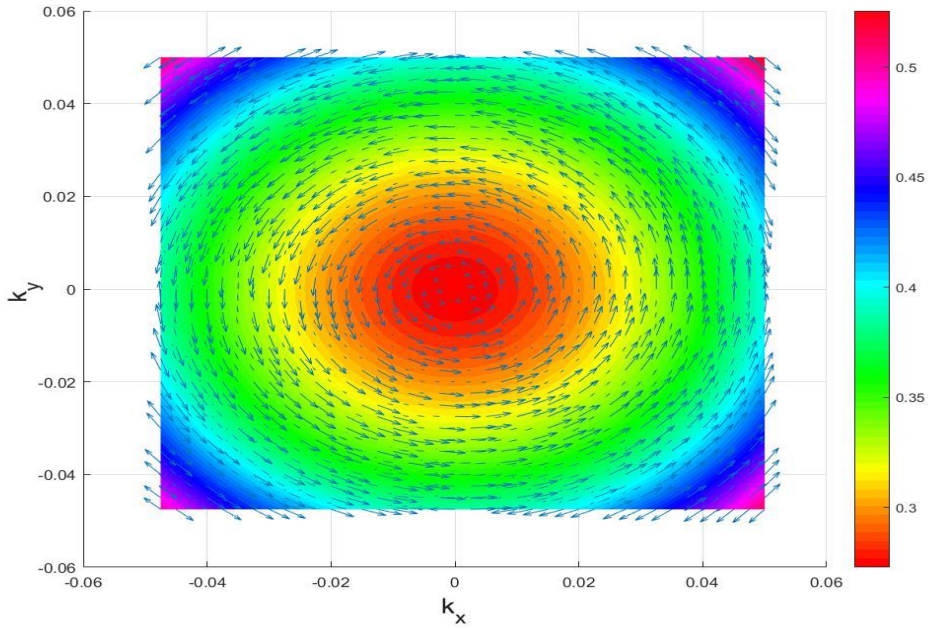

Fig. 5.3 False colour plot of an electron band of a 3 QL TI thin film with the colours indicating the energy levels (in units of eV) in the $k_x - k_y$ plane. The electron band is one of the degenerate spin bands of the gapped Dirac cone. The arrow indicates spin orientation of the energy state at that point in the momentum space. The figure shows that the electron band posing a circular symmetry in $k_x - k_y$ plane. The spin is perpendicular to the direction of motion of the electron and most of the spins rotate clockwise. There are a few spins rotating anticlockwise since the spin bands are degenerate.

dominates and states are more localised on one side. The spin of the states in those regions show different features as well (Fig. 5.3). In regions near the Γ point (the centre in Fig. 5.3), the states are hybridised. Therefore, the s_x and s_y components of such states are very small and the spin aligns almost the s_z direction: this can be seen more clearly from Fig. 5.6. In the region away from the Γ point, the spin-orbit coupling dominates and the states maintain the spin-momentum locking property. It is also worth mentioning that although the spin-orbit coupling dominates in the region that is away from the Γ point, those states are still influenced by the hybridisation. Therefore, they have larger $< s_z >$ values compared to those on an intersecting Dirac cone.

When an in-plane magnetic field is applied to the system, the spins of states are affected by the field and show interesting features. The degenerate gaped Dirac cone (electron bands and hole bands) splits into two. Fig. 5.4 and Fig. 5.5 show the lower electron band and the lower hole band. From Fig. 5.4 and Fig. 5.5, we see that the spins of the states form a pattern that is symmetric around the $k_x = 0$ axis. On the electron band (Fig. 5.4), the spins

form a pattern that is like the field lines repelling each other around the $k_x = 0$ axis. On the hole band (Fig. 5.5), the spins form a pattern that is like the field lines attracting each other around the $k_x = 0$ axis. Along the $k_x = 0$ axis, the spins align with the magnetic field in the s_y direction. This feature is due to the splitting of the degenerate bands according to their s_y components. The states with $+ < s_y >$ values go to the lower band while the states with $- < s_y >$ values go to the upper band. From the comparison of the s_y component of a hole band with/without a field (see Fig. 5.11 and Fig. 5.12) we can see that the s_y component is positive everywhere on the hole band under a magnetic field B_y, but it has positive values and negative values when there is no field. The spin-momentum locking property of the bands is still preserved to some extent but the degenerate bands split according to their s_y components. Therefore, the helical spin texture is symmetric around the $k_x = 0$ axis. With the magnetic field, states near theΓ point where hybridisation dominates, tend to have their spin aligned with the direction of the field (the s_y direction) (Fig. 5.10) and the resultant s_z component becomes zero (Fig. 5.8). Moving away from the Γ point, where the spin-orbit coupling dominates, spin-momentum locking is preserved to some extent (apart from the $k_x = 0$ axis). Therefore, an in-plane magnetic field will cause the s_y components of the states to increase and it splits the degenerate bands with respect to their s_y components.

5.3 Single-qubit study

In order to do a spin-qubit study, we need to choose a suitable pair of states. The states should have opposite spins and be separated by an energy gap. From the last section, we learnt that, under an in-plane magnetic field, the states near the Γ points would lie in the direction that is parallel or anti-parallel to the field, while the states away from the Γ point still have some features of spin-momentum locking. We need to be able to operate the qubits using the magnetic field. It is desired to have a pair of states that will respond to the field effectively; therefore, we are interested in the region dominated by the hybridisation effect. We chose the states near the Γ point as our qubit state since the spin is maximally along the z direction and it responds to the field effectively (see Fig. 5.6 and fig. 5.7). The states in the region $|k| <= 0.000\,25\,\text{Å}^{-1}$ are suitable for the spin qubit study (Fig. 5.14 and Fig. 5.13). The states at the Γ point have the maximum s_z components at $s_z = \pm\frac{1}{2}$. In this chapter we define our qubit using the states at the Γ point in a 3 QL TI, which are:

$$|\Phi_0\rangle = |S2\rangle\,, \tag{5.4}$$

$$|\Phi_1\rangle = |S4\rangle\,. \tag{5.5}$$

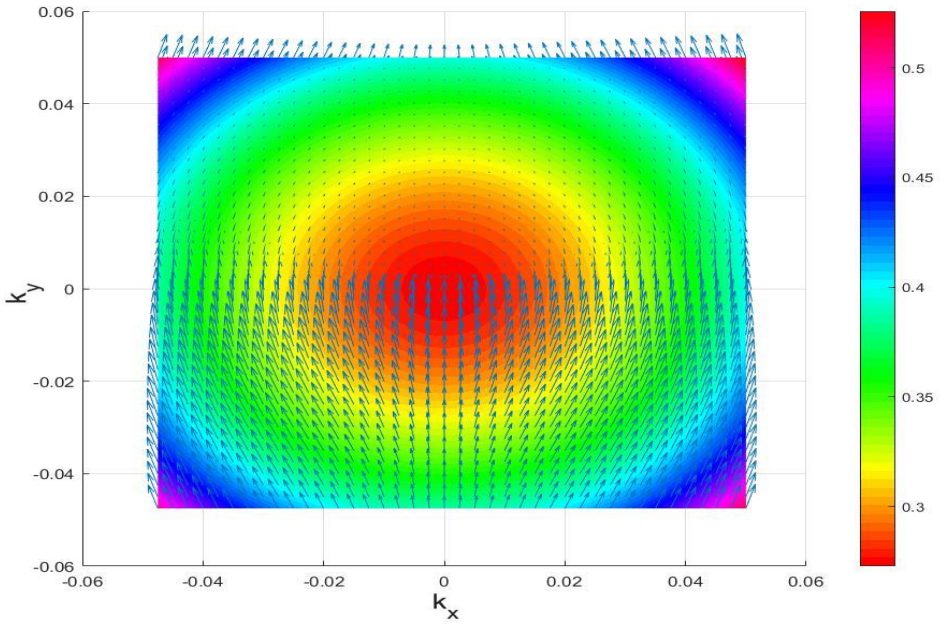

Fig. 5.4 False colour plot of an electron band of a 3 QL TI thin film with an in-plane static magnetic field $B_y = 0.2\,\mathrm{T}$ on the $k_x - k_y$ plane. The colours indicate the energy levels (in units of eV). The arrow indicates the spin orientation of the energy state at that point in the momentum space. The degenerate electron bands split with respect to their spin component s_y, with all $s_y > 0$ energy states on the same band. The figure is viewed perpendicularly to the $k_x - k_y$ plane from above. The spins of states located at $k_y > 0$ possesses negative s_z components and, thus, go into the plane. The figure shows that the electron band possesses a circular symmetry on the $k_x - k_y$ plane.

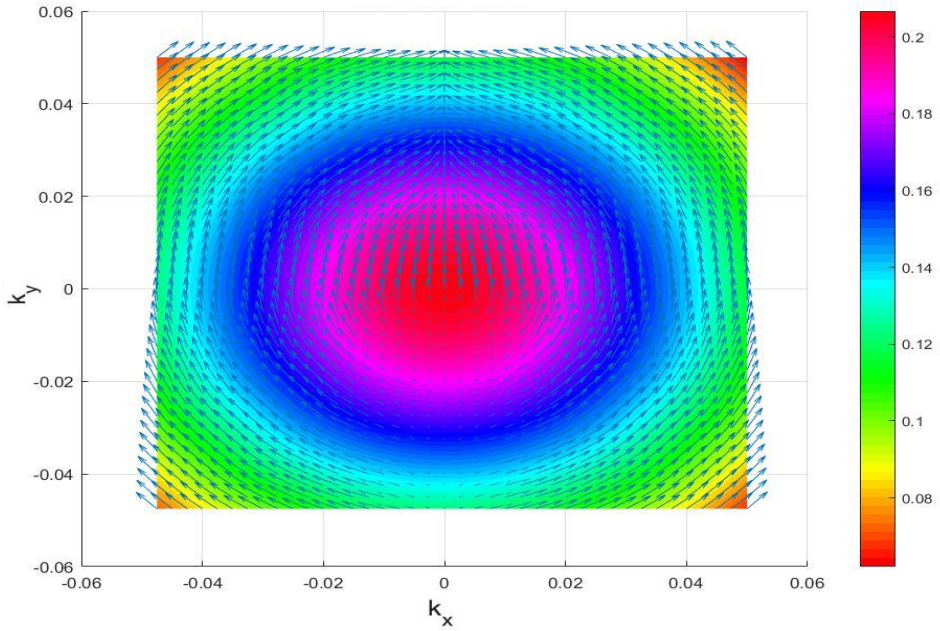

Fig. 5.5 False colour plot of a hole band of a 3 QL TI thin film with an in-plane static magnetic field $B_y = 0.2\,\mathrm{T}$ on the $k_x - k_y$ plane. The colours indicate the energy levels (in units of eV). The arrow indicates the spin orientation of the energy state at that point in the momentum space. The degenerate electron bands split with respect to their spin component s_y, with all $s_y > 0$ energy states on the same band. The figure is viewed perpendicularly to the $k_x - k_y$ plane from above. The spins of states located at $-0.02 < k_y < 0$, $-0.018 < k_x < 0.018$ possesses negative s_z components and, thus, go into the plane. The figure shows that the hole band possesses a circular symmetry near the Γ point and an octagonal symmetry when moves away from the Γ point on the $k_x - k_y$ plane.

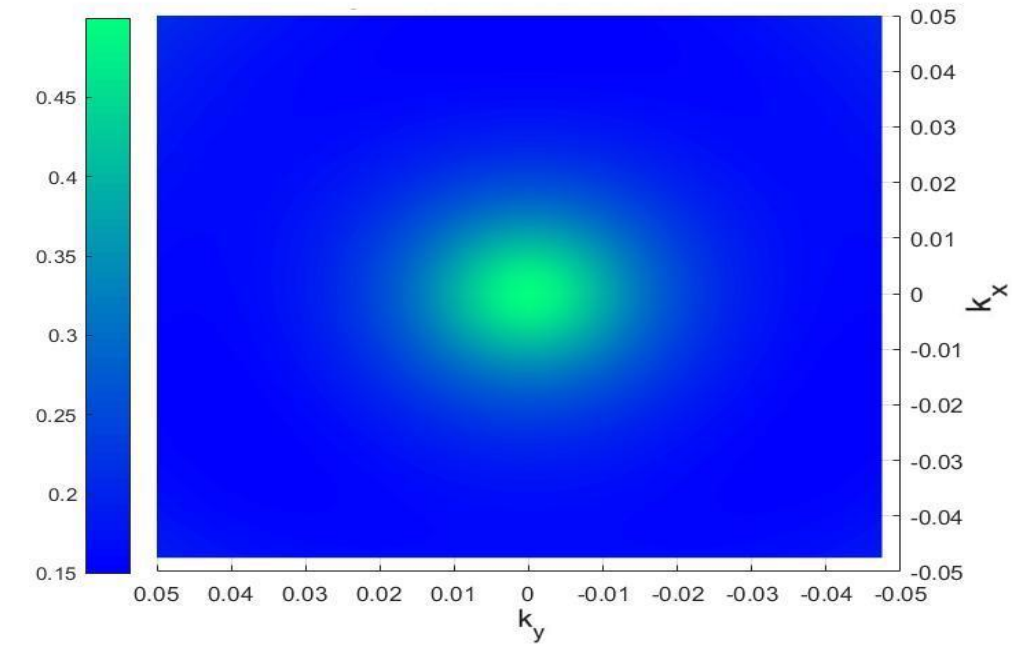

Fig. 5.6 False colour plot of the $< s_z >$ values of the states on an electron band of a 3 QL TI thin film on the $k_x - k_y$ plane. The colours indicate the values of $< s_z >$ ($\hbar = 1$). The $< s_z >$ values are larger for the states near the Γ point.

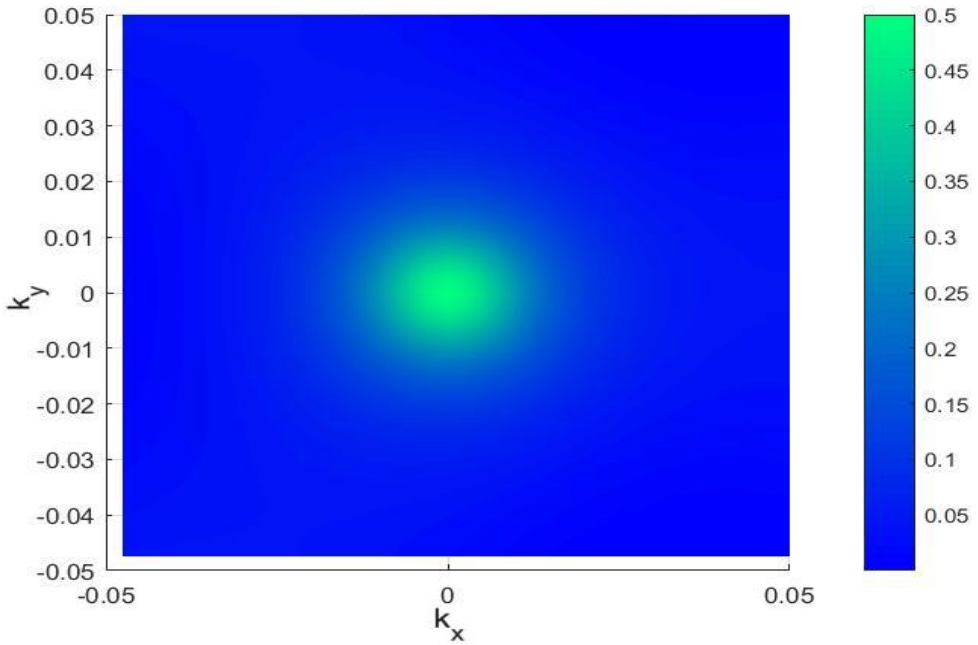

Fig. 5.7 False colour plot of the $< s_z >$ values of the states on a hole band of a 3 QL TI thin film on the $k_x - k_y$ plane. The colours indicate the values of $< s_z >$ ($\hbar = 1$). The $< s_z >$ values are larger for the states near the Γ point.

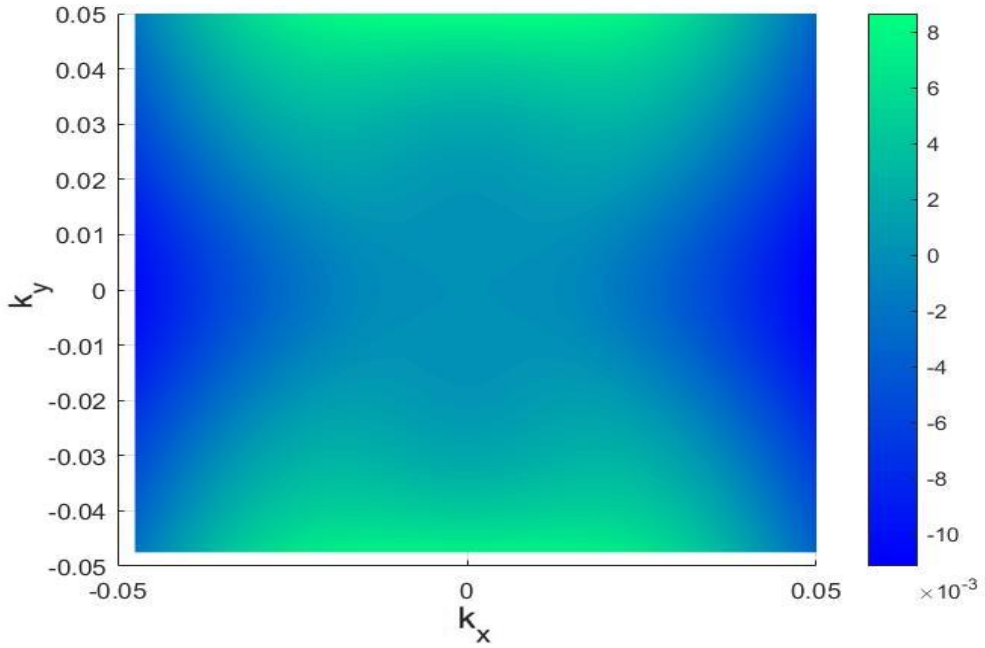

Fig. 5.8 False colour plot of the $< s_z >$ values of the states on an electron band of a 3 QL TI thin film with an in-plane static magnetic field $B_y = 0.2\,\mathrm{T}$ on the $k_x - k_y$ plane. The colours indicate the values of $< s_z >$ ($\hbar = 1$). The $< s_z >$ values are significantly reduced when a magnetic field is applied.

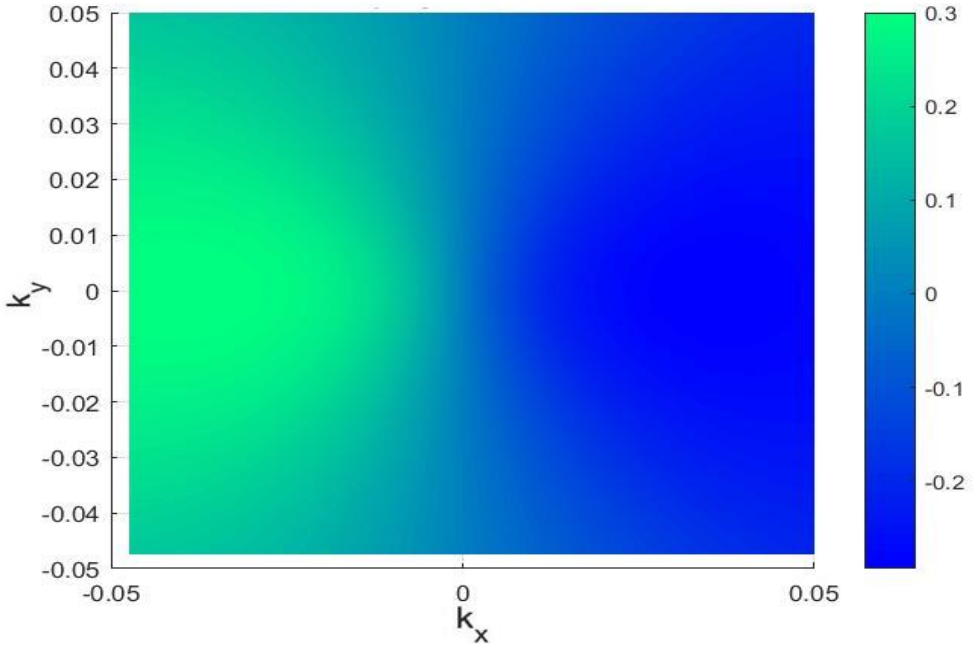

Fig. 5.9 False colour plot of the $< s_y >$ values of the states on an electron band of a 3 QL TI thin film on the $k_x - k_y$ plane. The colours indicate the values of $< s_y >$ ($\hbar = 1$). The $< s_y >$ values are positive for states at $k_x < 0$ and negative for states at $k_x > 0$.

Here, $|S2\rangle$ and $|S4\rangle$ are the eigenstates of the gapped Dirac cone of an ultra-thin TI of 3 QL (see Fig. 5.15 and Fig. 5.16) defined in Sec. 4.3. A general state on the Bloch sphere is written as:

$$|\Phi\rangle = \cos\left(\frac{\theta}{2}\right)|\Phi_0\rangle + e^{i\phi}\sin\left(\frac{\theta}{2}\right)|\Phi_1\rangle\,. \tag{5.6}$$

5.3.1 Initialisation

In this chapter, we decide to study a localised spin qubit in a TI quantum dot (i.e the quantum states at $k = 0$). Because the spin qubits $|\Phi_0\rangle$ and $|\Phi_1\rangle$ are eigenstates of an ultra-thin TI, it is easier to initialise than a charge qubit. We can control the Fermi level to be in the middle of or below the gap. Then the spin qubit is initialised in the hole band at thermal equilibration at a sufficiently low temperature. Alternatively, the qubit can be initialised by optical pumping [5].

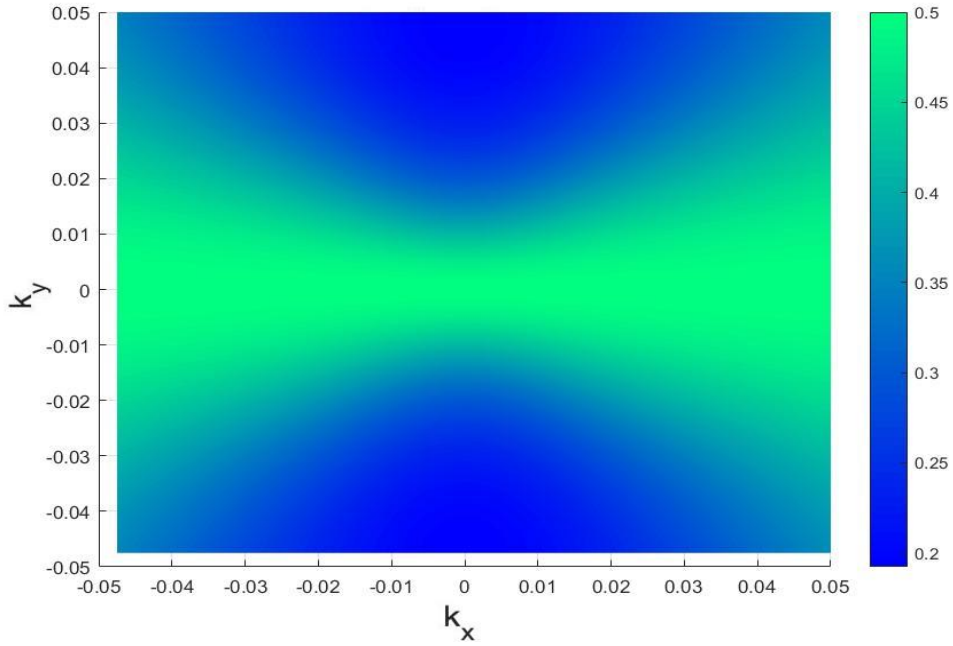

Fig. 5.10 False colour plot of the $< s_y >$ values of the states on an electron band of a 3 QL TI thin film with an in-plane static magnetic field $B_y = 0.2\,\mathrm{T}$ on the $k_x - k_y$ plane. The colours indicate the values of $< s_y >$ ($\hbar = 1$). The $< s_y >$ values are positive for all states on this band and larger at those points near the $k_y = 0$ axis.

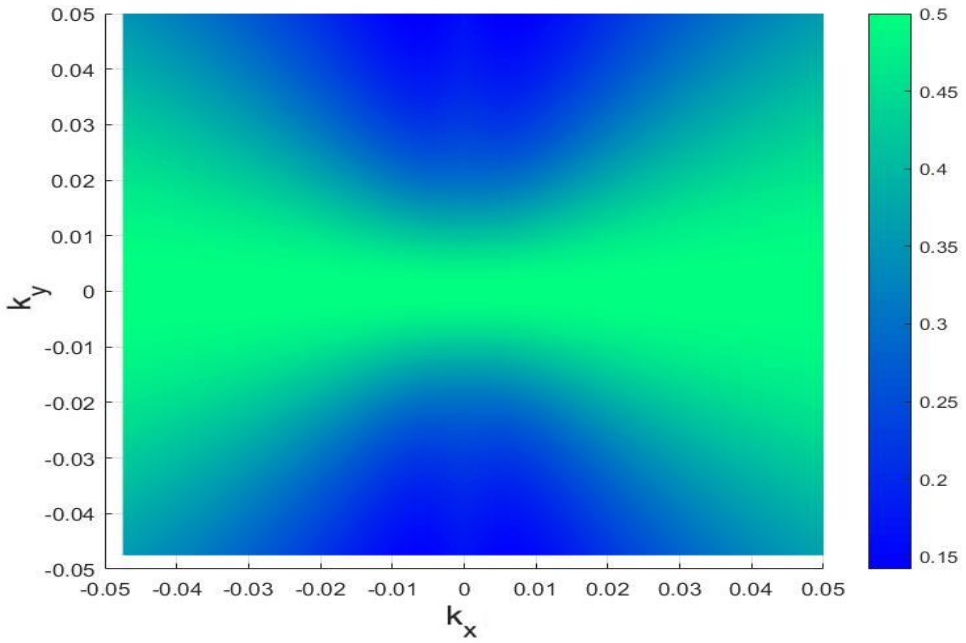

Fig. 5.11 False colour plot of the $< s_y >$ values of the states on a hole band of a 3 QL TI thin film with an in-plane static magnetic field $B_y = 0.2\,\mathrm{T}$ on the $k_x - k_y$ plane. The colours indicate the values of $< s_y >$ ($\hbar = 1$). The $< s_y >$ values are positive for all states on this band and larger at those points near the $k_y = 0$ axis.

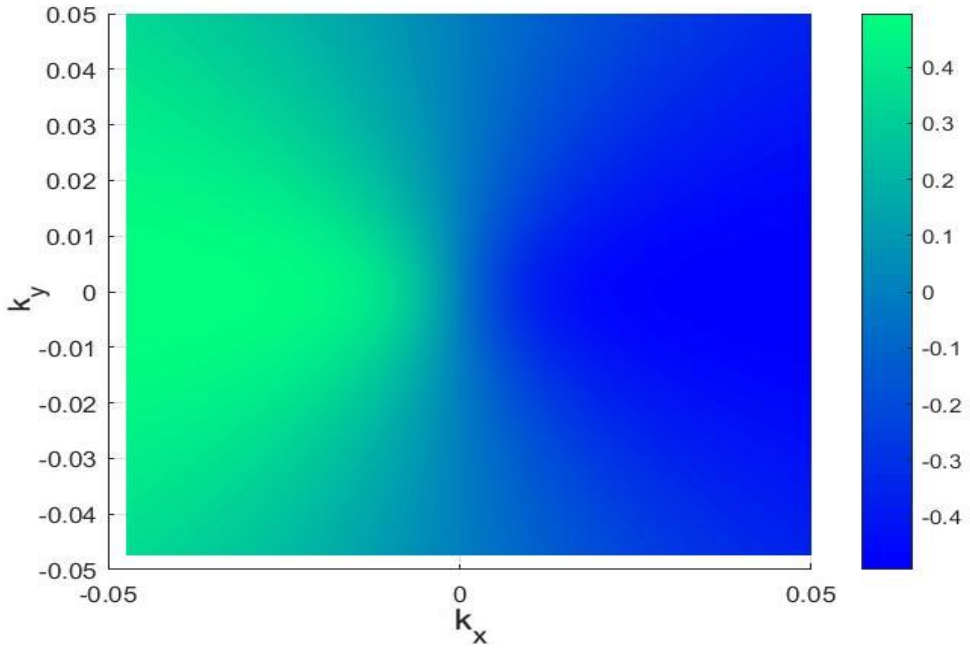

Fig. 5.12 False colour plot of the $< s_y >$ values of the states on a hole band of a 3 QL TI thin film on the $k_x - k_y$ plane. The colours indicate the values of $< s_y >$ ($\hbar = 1$). The $< s_y >$ values are positive for states at $k_x < 0$ and negative for states at $k_x > 0$.

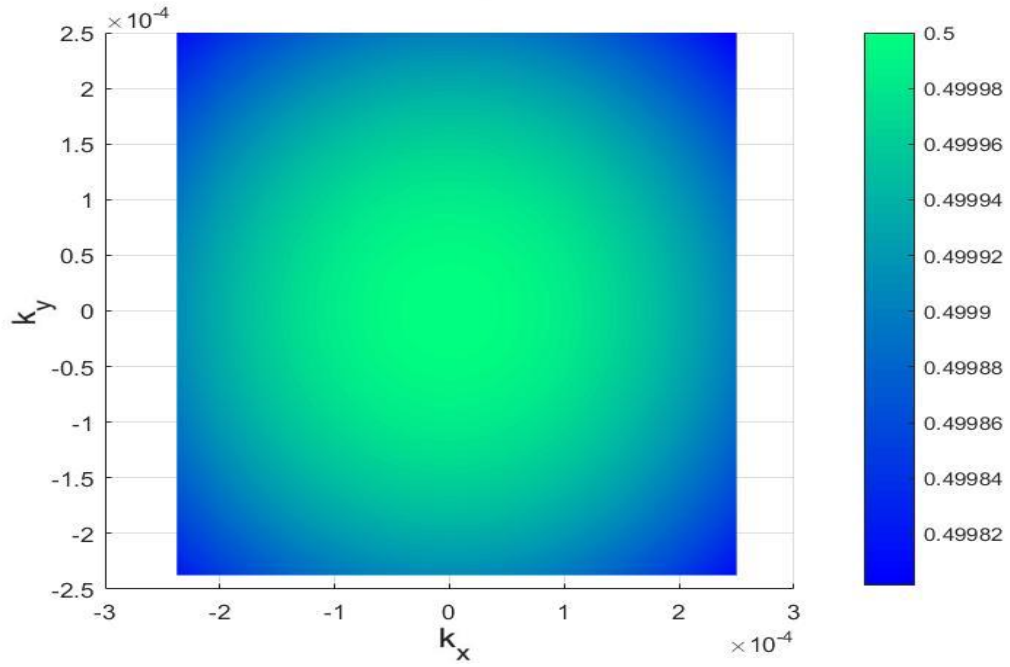

Fig. 5.13 False colour plot of the $< s_z >$ values of the states on an electron band of a 3 QL TI thin film on the $k_x - k_y$ plane. The colours indicate the values of $< s_z >$ ($\hbar = 1$). The $< s_z >$ values are larger for states near the Γ point and $s_z = \frac{1}{2}$ at the Γ point.

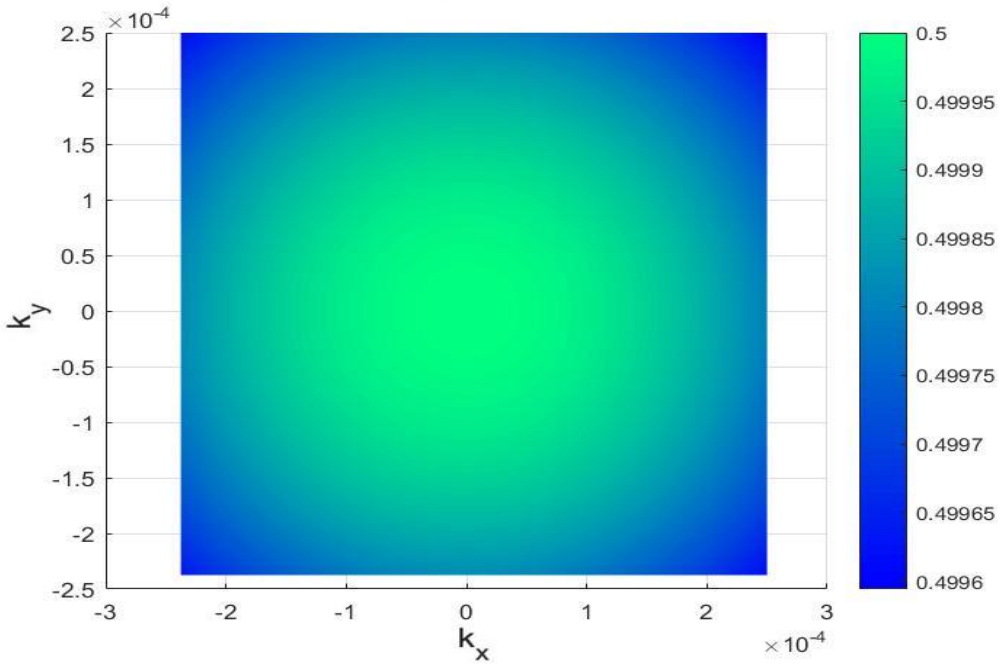

Fig. 5.14 False colour plot of the $< s_z >$ values of the states on a hole band of a 3 QL TI thin film on the $k_x - k_y$ plane. The colours indicate the values of $< s_z >$ ($\hbar = 1$). The $< s_z >$ values are larger for states near the Γ point and $s_z = -\frac{1}{2}$ at the Γ point.

5.3.2 Qubit manipulation

In this section we study how to manipulate the spin qubit on the Bloch sphere. Like with the charge qubit, the combined states $\alpha |\Phi_0\rangle + \beta |\Phi_1\rangle, \alpha \neq 0, \beta \neq 0$ will evolve in time as the phase varies periodically. From the blue trace in Fig. 5.17 and Fig. 5.18, we see this is equivalent to a σ_z rotation on the Bloch sphere. We note here that the Bloch spheres in the thesis are plotted at 90% size to clarify the single-qubit rotation diagrams. The period of this σ_z rotation is short in terms of a qubit operation (0.1 ps in a 3 QL TI) and it depends on the energy difference of the states we use. The period T_{res} of the σ_z rotation of a spin qubit has the same dependence vs thickness as the σ_x rotation of a charge qubit (Fig. 4.20).

When a magnetic field is applied to the system, the qubit will rotate on the Bloch sphere. When we apply a static field to the qubit, the resultant trace is different from the trace of a charge qubit under a static electric field. From Fig. 5.17 we see that the trace is a spiral rather than a closed circle. The higher the magnitude of the magnetic field, the more it deviates from a closed circular path. From Fig. 5.19 we see that $\Delta\phi$ vs different field strength is very small and periodic with a period close to T_{res}. If we consider the change of ϕ in the rotating frame of a Bloch sphere spinning around z axis at ω_{res} (Fig. 5.20), we see that the rotation under a static field can be resolved into a σ_z rotation at $\approx \omega_{res}$ plus a rotation with an axis on

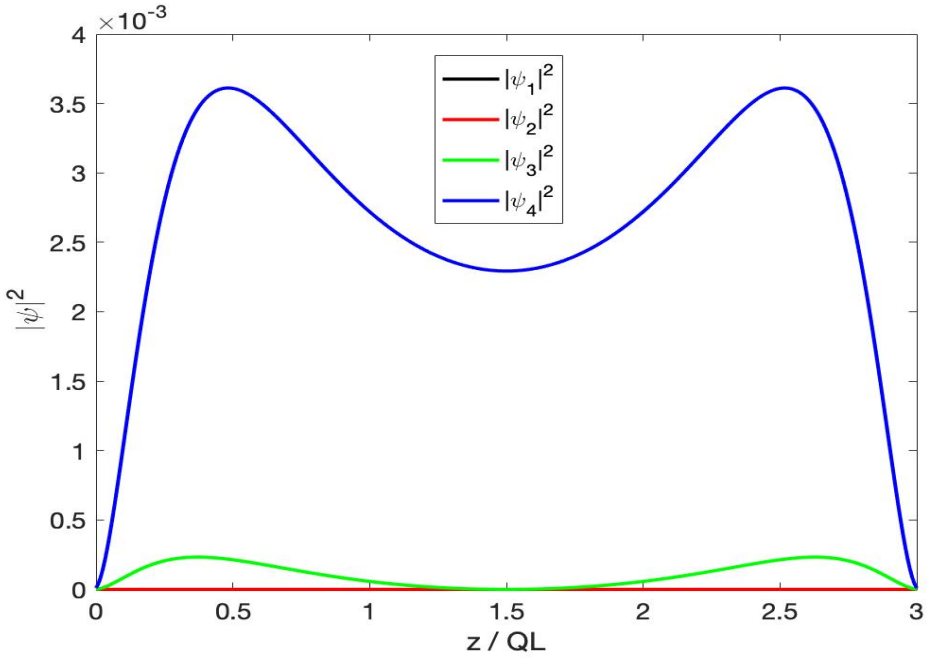

Fig. 5.15 Spatial distributions of wave function densities of a spin down 'surface state' on the hole band at the Γ point in a 3 QL TI thin film with energy equal to 0.2067 eV. $|\psi_1|^2$ to $|\psi_4|^2$ are the wave function densities of the basis states $|\psi_1\rangle$ to $|\psi_4\rangle$ of the TI Hamiltonian in Eq. 4.1. The detailed electronic states of $|\psi_1\rangle$ to $|\psi_4\rangle$ are shown in Eq. 2.26. The wave function densities on $|\psi_1\rangle$ and $|\psi_2\rangle$ are equal to zero. The wave function density of the 'surface state' spans over the whole thickness of TI, with two peaks near the surfaces. This is the logic state Φ_0 defined for the qubit study in this chapter.

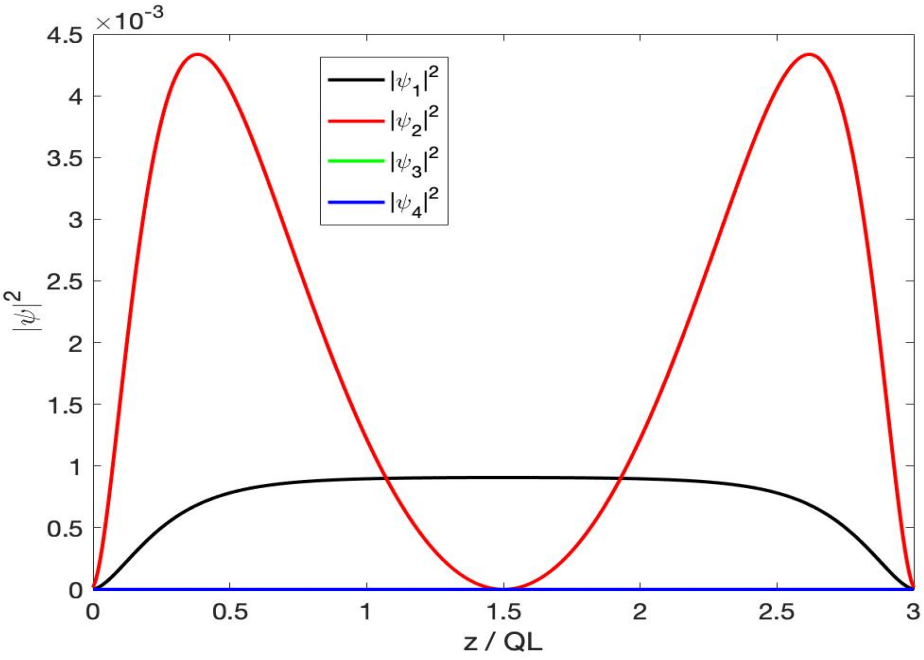

Fig. 5.16 Spatial distributions of wave function densities of a spin up 'surface state' on the electron band at the Γ point in a 3 QL TI thin film,with energy equals to 0.2731 eV. $|\psi_1|^2$ to $|\psi_4|^2$ are the wave function densities of the basis states $|\psi_1\rangle$ to $|\psi_4\rangle$ of the TI Hamiltonian in Eq. 4.1. The detailed electronic states of $|\psi_1\rangle$ to $|\psi_4\rangle$ are shown in Eq. 2.26. The wave function densities of $|\psi_3\rangle$ and $|\psi_4\rangle$ are equal to zero. The wave function density of the 'surface state' spans over the whole thickness of TI, with two peaks near the surfaces. This is the logic state Φ_1 defined for the qubit study in this chapter.

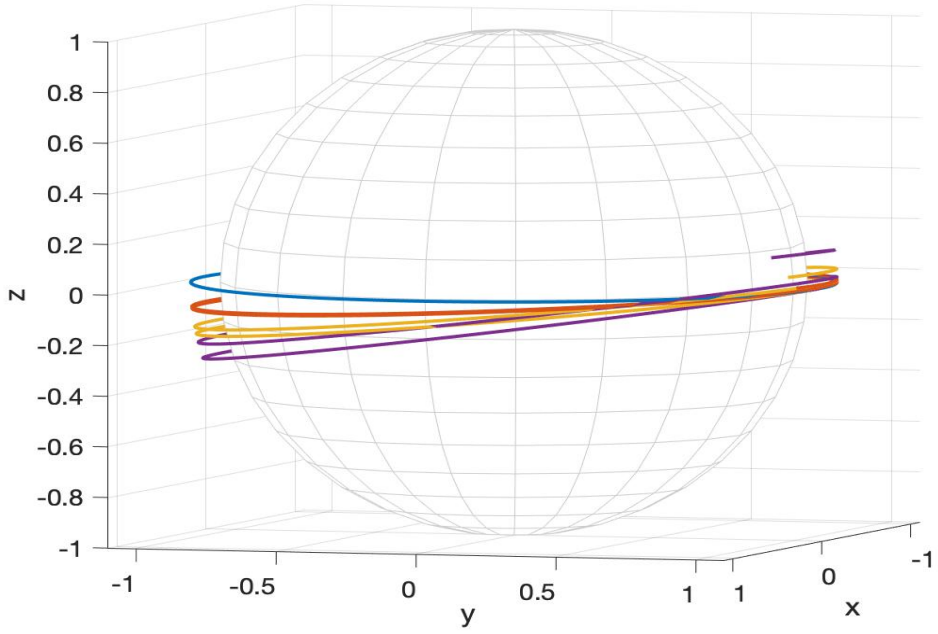

Fig. 5.17 Traces of single qubit rotations with an in-plane static magnetic field applied to the TI thin film at various strengths: $B = 0$ (blue), $B = 3.3\,\mathrm{T}$ (orange), $B = 6.7\,\mathrm{T}$ (yellow) and $B = 10\,\mathrm{T}$ (purple). Note that the Bloch sphere is drawn at 90% size to clarify the diagram.

the xy plane. The resultant rotation of a linear pulse is position-dependent. Therefore, we continue to study whether a pulse sequence can promote a (effective) σ_y rotation. We study some linear pulse sequences which consist of two/three linear pulses of the same strength as the charge qubit case (Ch. 4). We find that a two-part pulse can produce effective σ_y rotations on some positions but not on the whole Bloch sphere.

Now we study whether a cosine pulse can produce an effective σ_x or σ_y rotation. The trace of the qubit under such pulse is also a spiral but the increment in θ is even compared with the linear pulse (Fig. 5.21). We find that a cosine pulse at ω_{res} can produce an effective σ_y rotation at nT_{res} (see Fig. 5.22 and Fig. 5.23), where $n \in Z$. This is an effective rotation with high fidelity which is position independent (Fig. 5.28). By changing the amplitude of the field, we can promote rotations of different angles (Fig.5.27). From Fig. 5.27 and Fig. 5.26, we can see that the angle rotated in this σ_y rotation is proportional to the magnitude $|B|$; however, the higher the magnitude, the higher ϕ is. This means that the state deviates more from a σ_y rotation; nevertheless, the fidelity is still high and acceptable even for a field as high as 23T (Fig. 5.28). To understand what the cosine pulse does to the qubit, we can view the rotation in the rotating frame at ω_{res}. We see that the path overlapping with the path of a σ_y rotation at nT_{res} (Fig. 5.25). This explains why the effective σ_y rotation occurs at nT_{res}; at

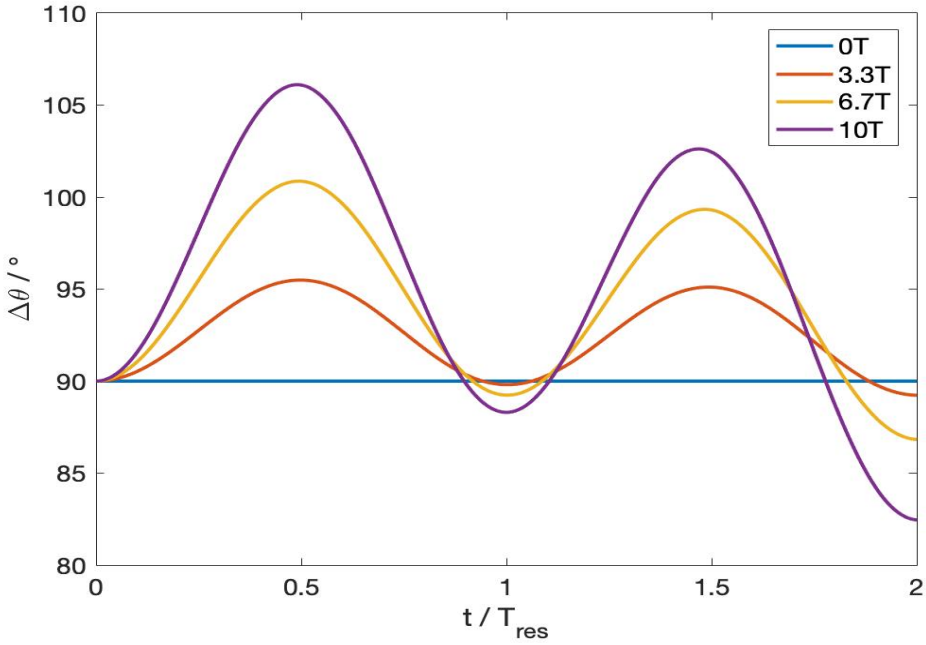

Fig. 5.18 $\Delta\theta$ in a single qubit rotation with an in-plane static magnetic field at various strengths during a time $2T_{res}$. θ is the conventional polar angle used in a spherical coordinate system. T_{res} is the natural period of a combined state $\alpha\left|\Phi_0\right\rangle + \beta\left|\Phi_1\right\rangle, \alpha \neq 0, \beta \neq 0$ that goes back to its original position on the Bloch sphere when there is no field applied. The figure shows that the θ angle changes periodically on the Bloch sphere with a changing amplitude. θ does not change when there is no field applied.

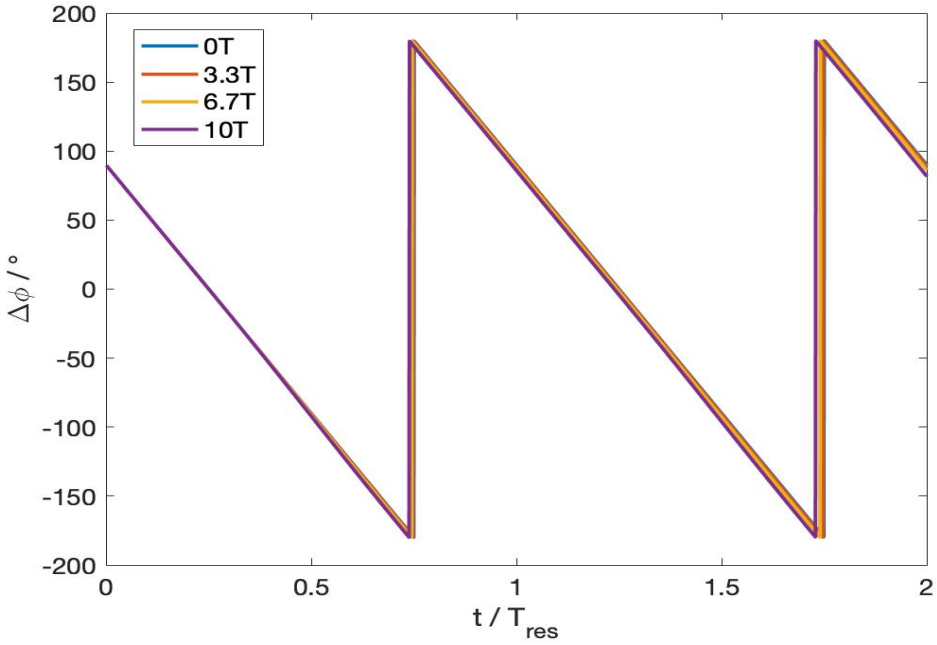

Fig. 5.19 $\Delta\phi$ in a single qubit rotation with an in-plane static magnetic field at various strengths during a time $2T_{res}$. ϕ is the conventional azimuthal angle used in a spherical coordinate system. T_{res} is the natural period of a combined state $\alpha|\Phi_0\rangle + \beta|\Phi_1\rangle, \alpha \neq 0, \beta \neq 0$ that goes back to its original position on the Bloch sphere when there is no field applied. The figure shows that the ϕ angle changes periodically on the Bloch sphere with a slight difference in periodicity with the field strength.

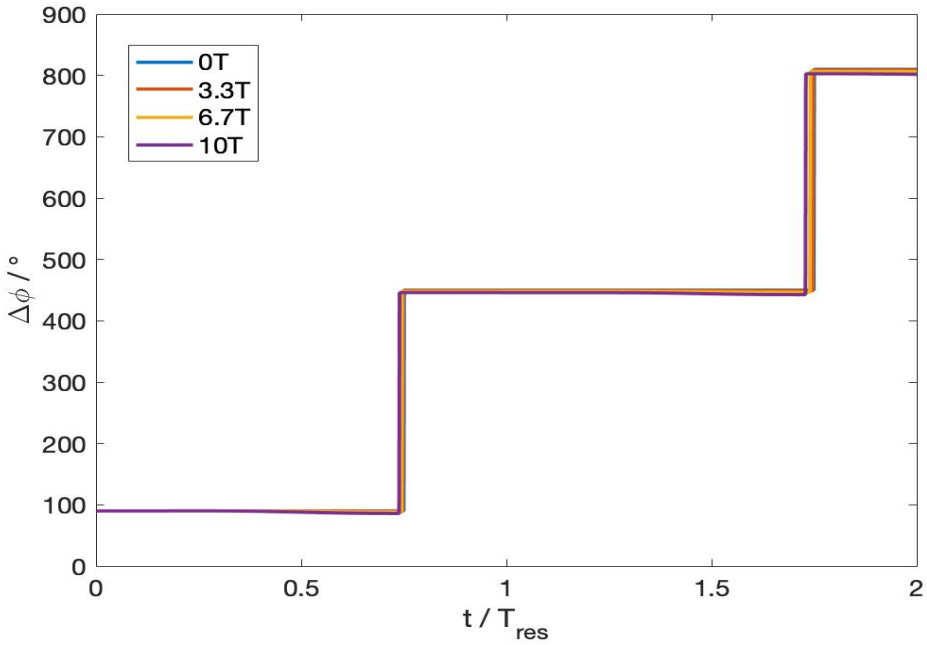

Fig. 5.20 $\Delta\phi$ in a single qubit rotation in a rotating frame at ω_{res} to the z axis, with an in-plane static magnetic field at various strengths during a time $2T_{res}$. ϕ is the conventional azimuthal angle used in a spherical coordinate system. T_{res} and ω_{res} are the natural period and frequency of a combined state $\alpha|\Phi_0\rangle + \beta|\Phi_1\rangle, \alpha \neq 0, \beta \neq 0$ that goes back to its original position on the Bloch sphere when there is no field applied. The figure shows that the ϕ angle is almost constant on the rotating Bloch sphere. The large jump to the next step ($\Delta\phi = 360^\circ$) occurs when the Bloch sphere completes a whole period of rotation.

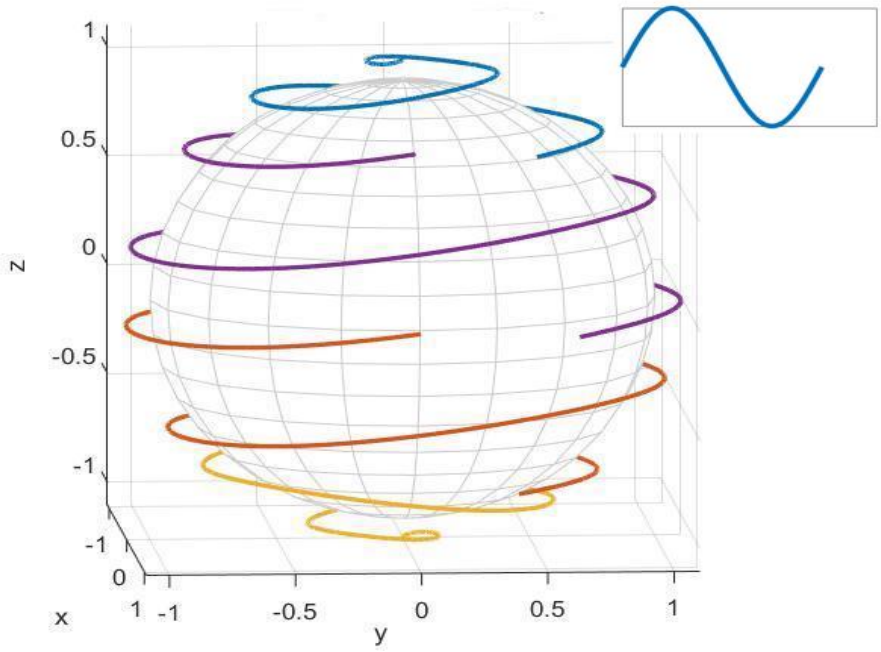

Fig. 5.21 Traces of single qubit rotations with an in-plane oscillating magnetic field applied to the TI thin film at various initial positions on the Bloch sphere. The traces (blue: $\theta = 0^\circ$,$\phi = 0^\circ$, purple: $\theta = 45^\circ$,$\phi = 0^\circ$, orange: $\theta = 90^\circ$,$\phi = 0^\circ$ and yellow: $\theta = 180^\circ$,$\phi = 0^\circ$) show that the change in latitude of single qubit rotations with the oscillating magnetic field is evener than with a static field. θ and ϕ are the conventional polar and azimuthal angles used in a spherical coordinate system. The inset shows the shape of the pulse. Note that the Bloch sphere is drawn at 90% size to clarify the diagram.

$t = nT_{res}$, the rotating Bloch sphere overlaps with the Bloch sphere of our static spin qubits. From the pulses studied above, we can understand the effect of a magnetic field as: when we apply an in-plane magnetic field to the qubit, the natural rotation does not stop. This is unlike the case of the TI charge qubit. The qubit will continue rotating spontaneously with an extra effect owning to the magnetic field. Larger angles can be achieved by waiting for longer times.

What if we change the frequency of the field? If the frequency of the pulse is higher than ω_{res}, we can see from the Fig. 5.29 that the qubit tends to rotate around a smaller and smaller region as the frequency increases when we view it in the rotating frame. There is no effective σ_y or σ_x rotation found when a pulse of high frequency is applied. On the other hand, if the frequency is less than ω_{res}, the qubit rotates along a different axis (Fig. 5.30). However, because of the mismatch of the frequency with the rotational frame, the angle rotated is position-dependent.

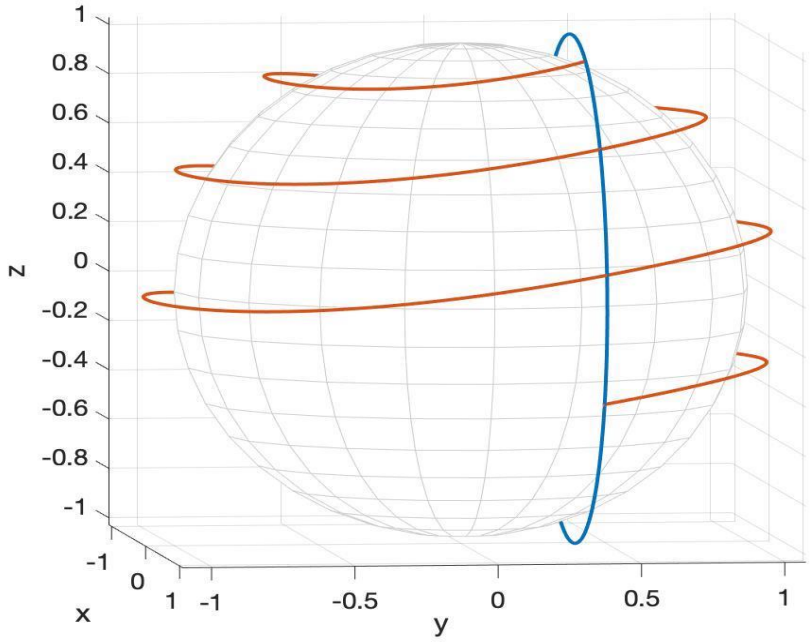

Fig. 5.22 The trace of an effective σ_y rotation (orange) at the initial position $\theta = 30^\circ$ and $\phi = 45^\circ$ on the Bloch sphere with an in-plane oscillating magnetic field applied to the TI thin film for $3T_{res}$. θ and ϕ are the conventional polar and azimuthal angles used in a spherical coordinate system. T_{res} is the natural period of a combined state $\alpha|\Phi_0\rangle + \beta|\Phi_1\rangle, \alpha \neq 0, \beta \neq 0$ that goes back to its original position on Bloch sphere when there is no field applied. The blue trace indicates a σ_y rotation. The initial and final positions of the orange trace are on the trace of a σ_y rotation. Note that the Bloch sphere is drawn at 90% size to clarify the diagram.

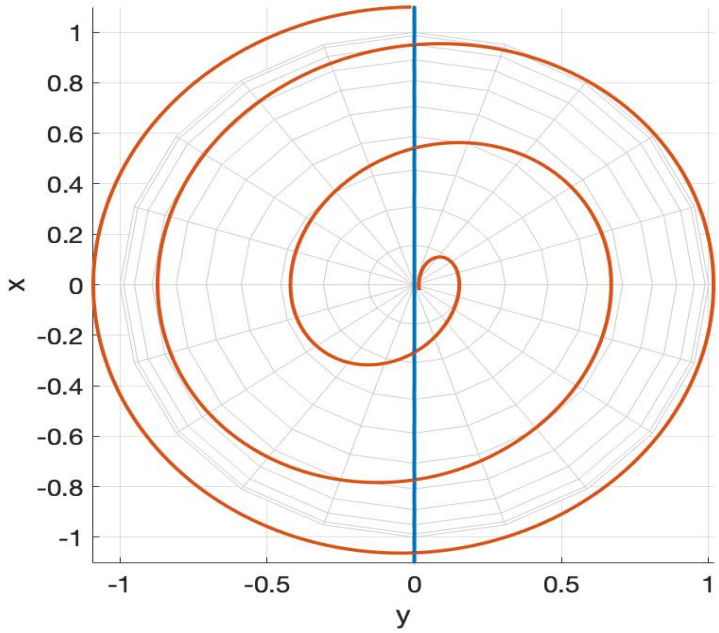

Fig. 5.23 The trace of an effective σ_y rotation (orange) with the initial position $\theta = 90^\circ$ and $\phi = 0^\circ$ on the Bloch sphere with an in-plane oscillating magnetic field applied to the TI thin film for $3T_{res}$. θ and ϕ are the conventional polar and azimuthal angles used in a spherical coordinate system. T_{res} is the natural period of a combined state $\alpha|\Phi_0\rangle + \beta|\Phi_1\rangle, \alpha \neq 0, \beta \neq 0$ that goes back to its original position on Bloch sphere when there is no field applied. The blue trace indicates a σ_y rotation. The initial and final positions of the orange trace are on the trace of a σ_y rotation. Note that the Bloch sphere is drawn at 90% size to clarify the diagram.

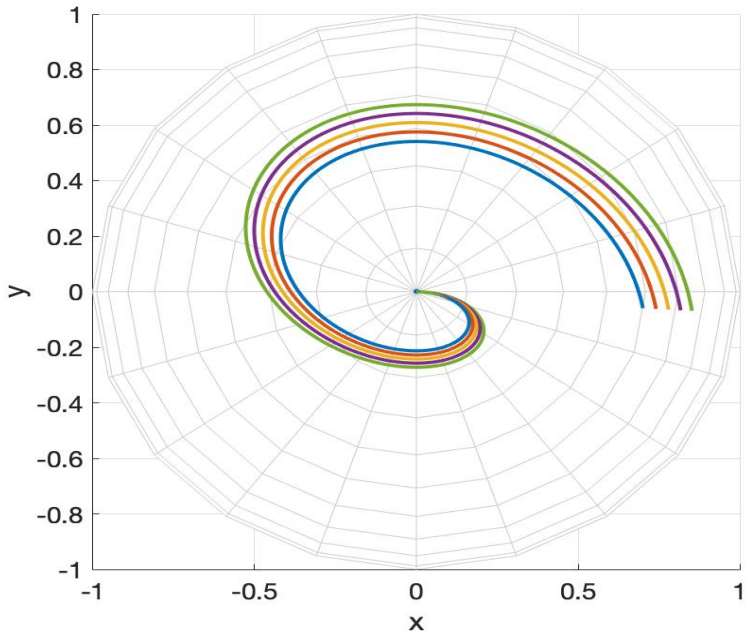

Fig. 5.24 Traces of effective σ_y rotations from Φ_0 on the Bloch sphere, with an in-plane oscillating magnetic field of various strengths applied to the TI thin film for T_{res}. T_{res} is the natural period of a combined state $\alpha|\Phi_0\rangle + \beta|\Phi_1\rangle, \alpha \neq 0, \beta \neq 0$ that goes back to its original position on the Bloch sphere when there is no field applied. The traces (blue: $B = 15\,\mathrm{T}$, orange: $B = 16\,\mathrm{T}$, yellow: $B = 17\,\mathrm{T}$, purple: $B = 18\,\mathrm{T}$ and green: $B = 19\,\mathrm{T}$) show that the stronger the field is, the larger the change in latitude of the qubit is. Note that the Bloch sphere is drawn at 90% size to clarify the diagram.

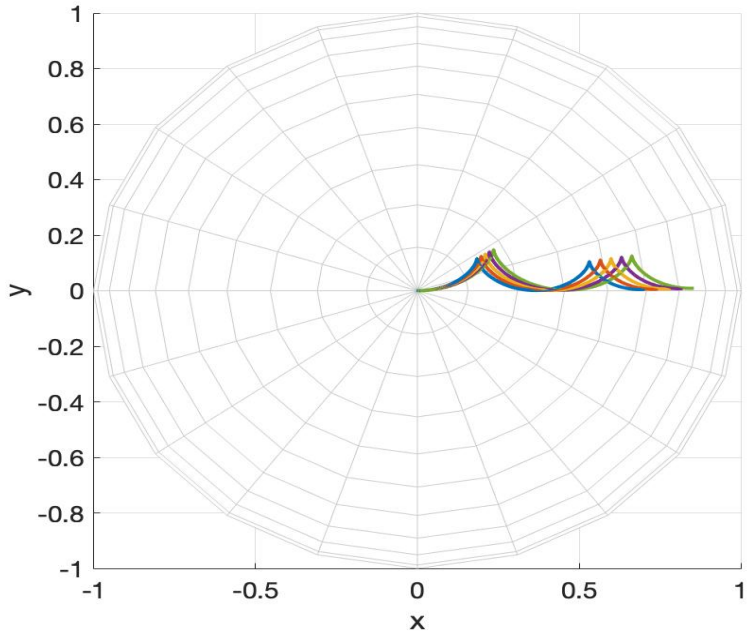

Fig. 5.25 Traces of effective σ_y rotations from Φ_0 on the Bloch sphere (same conditions as Fig. 5.24) viewed in a rotating frame at ω_{res} to the z axis with an in-plane oscillating magnetic field of various strengths applied to the TI thin film for T_{res}. T_{res} and ω_{res} are the natural period and frequency of a combined state $\alpha|\Phi_0\rangle + \beta|\Phi_1\rangle, \alpha \neq 0, \beta \neq 0$ that goes back to its original position on the Bloch sphere when there is no field applied. The traces (blue: $B = 15\,\mathrm{T}$, orange: $B = 16\,\mathrm{T}$, yellow: $B = 17\,\mathrm{T}$, purple: $B = 18\,\mathrm{T}$ and green: $B = 19\,\mathrm{T}$) show that the stronger the field is, the larger the change in latitude of the qubit is. Note that the Bloch sphere is drawn at 90% size to clarify the diagram.

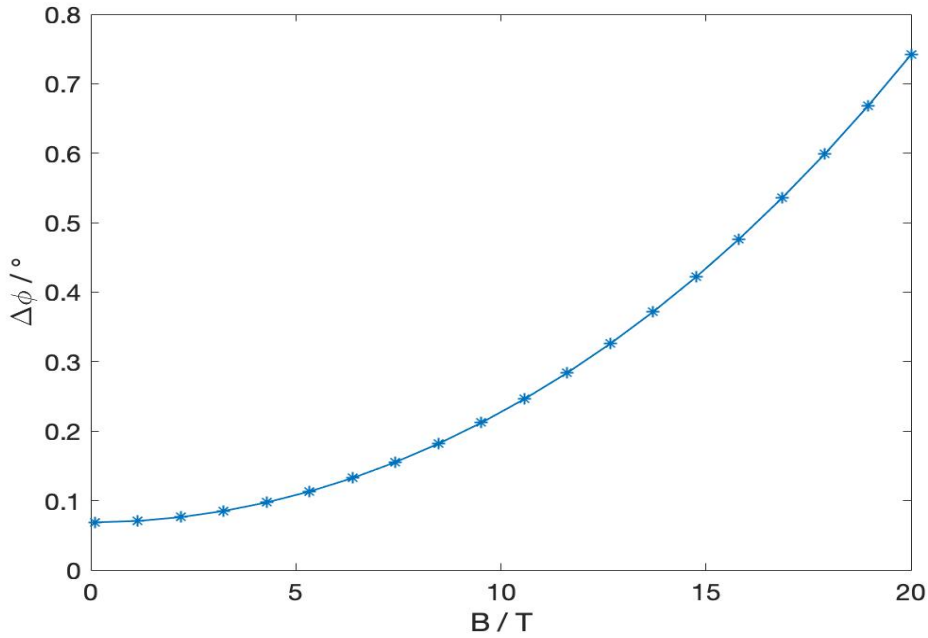

Fig. 5.26 $\Delta\phi$ in an effective σ_y rotation during a time $t = T_{res}$ vs the in-plane oscillating magnetic field strengths. ϕ is the conventional azimuthal angle used in a spherical coordinate system. T_{res} is the natural period of a combined state $\alpha |\Phi_0\rangle + \beta |\Phi_1\rangle, \alpha \neq 0, \beta \neq 0$ that goes back to its original position on Bloch sphere when there is no field applied. The figure shows that $\Delta\phi$ increases with the field strength.

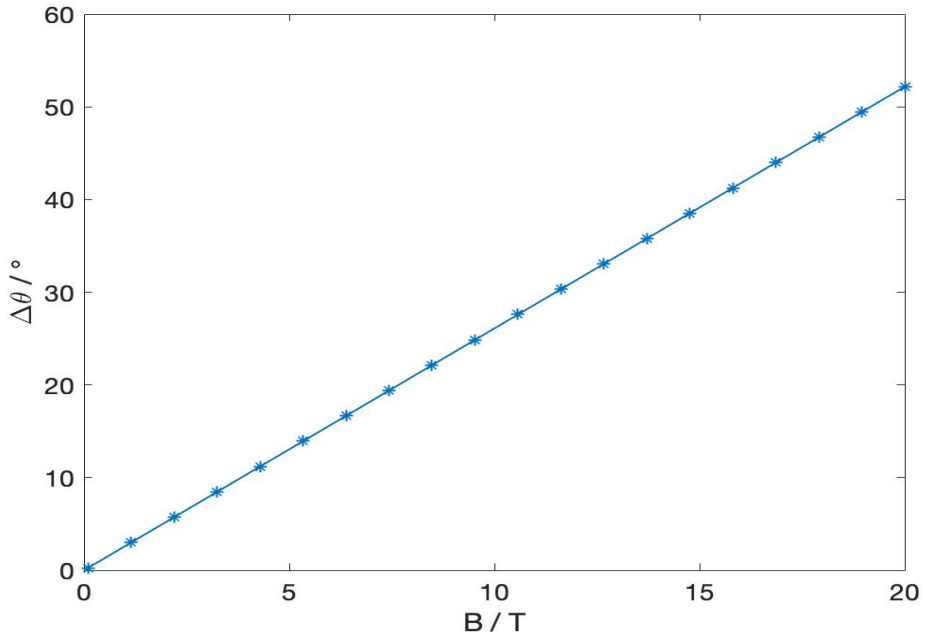

Fig. 5.27 $\Delta\theta$ in an effective σ_y rotation for a $t = T_{res}$ duration vs the in-plane oscillating magnetic field strengths. θ is conventional polar angle used in spherical coordinate system. T_{res} is the natural period of a combined state $\alpha |\Phi_0\rangle + \beta |\Phi_1\rangle, \alpha \neq 0, \beta \neq 0$ to goes back to its original position on Bloch sphere when there is no field applied. The figure shows that $\Delta\theta$ increases linearly with the field strength.

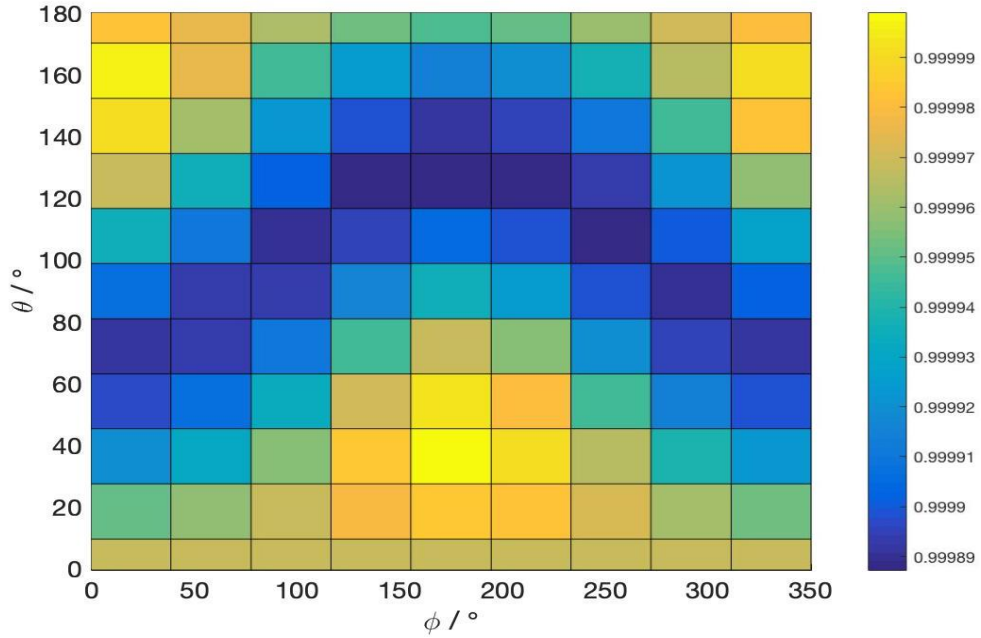

Fig. 5.28 Fidelity of effective σ_y rotations at $B = 23\,\mathrm{T}$ for a $t = T_{res}$ duration. Fidelity of an effective σ_y rotation with an in-plane oscillating magnetic field of 23 T vs various qubit states (in the range $\theta \in [0, 180^\circ]$, $\phi \in [0, 350^\circ]$) on the Bloch sphere for T_{res}. θ and ϕ are the conventional polar and azimuthal angles used in a spherical coordinate system. T_{res} is the natural period of a combined state $\alpha |\Phi_0\rangle + \beta |\Phi_1\rangle, \alpha \neq 0, \beta \neq 0$ that goes back to its original position on Bloch sphere when there is no field applied. The figure shows that $\Delta\theta$ increases linearly with the field strength. This figure shows that the effective σ_y is indeed universal and position-independent. The fidelity is extremely high, which is over 99.99%.

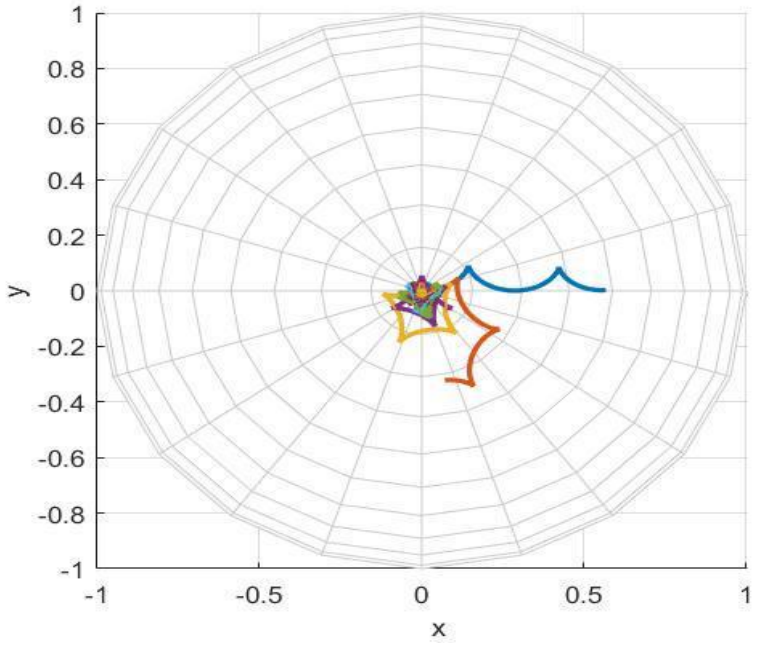

Fig. 5.29 Traces of single qubit rotations from Φ_0 on the Bloch sphere viewed in a rotating frame at ω_{res} to the z axis with an in-plane oscillating magnetic field of various frequency applied (blue: $\omega = \omega_{res}$, orange: $\omega = 2\omega_{res}$, yellow: $\omega = 3\omega_{res}$, purple: $\omega = 4\omega_{res}$ and light blue: $\omega = 5\omega_{res}$) to the TI thin film for T_{res}. T_{res} and ω_{res} are, respectively, the natural period and frequency of a combined state $\alpha |\Phi_0\rangle + \beta |\Phi_1\rangle, \alpha \neq 0, \beta \neq 0$ that goes back to its original position on Bloch sphere when there is no field applied. The traces show that the higher the frequency of field is, the smaller the change in latitude of the qubit is. Note that the Bloch sphere is drawn at 90% size to clarify the diagram.

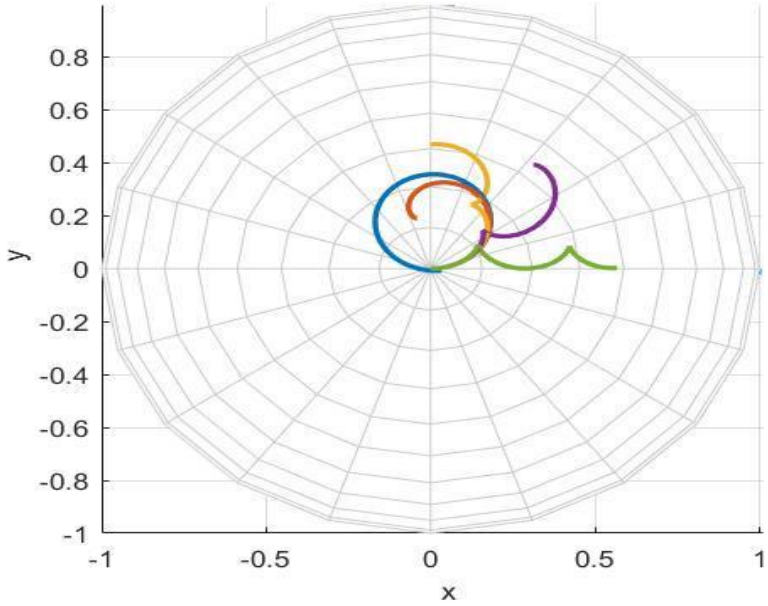

Fig. 5.30 Traces of single qubit rotations from Φ_0 on the Bloch sphere viewed in a rotating frame at ω_{res} to the z axis with an in-plane oscillating magnetic field of various frequency applied (blue: $\omega = 0$, orange: $\omega = \frac{1}{4}\omega_{res}$, yellow: $\omega = \frac{1}{2}\omega_{res}$ purple: $\omega = \frac{3}{4}\omega_{res}$ and green: ω_{res}) to the TI thin film for T_{res}. T_{res} and ω_{res} are, respectively, the natural period and frequency of a combined state $\alpha|\Phi_0\rangle + \beta|\Phi_1\rangle, \alpha \neq 0, \beta \neq 0$ that goes back to its original position on Bloch sphere when there is no field applied. The traces indicate that when the frequency is smaller than the natural frequency ω_{res}, the qubit follows an effective rotation on a different axis. However, this rotation is position-dependent. Note that the Bloch sphere is drawn at 90% size to clarify the diagram.

5.3.3 Read-out

In this section we discuss how to link the coefficients α and β in Eq. 5.6 on the Bloch sphere to some quantities that can be measured physically. There are various ways to measure the spin of an electron (both directly and indirectly) in the literature [38] [96] [9]. For example, read-out of a single spin qubit in a quantum dot can be achieved by combing spin-to-charge conversion with real-time single-charge detection [97] [114] [76]. We know that Φ_0 is a spin up state with $s_z = \frac{1}{2}$ and Φ_1 is a spin down state with $s_z = -\frac{1}{2}$. We can measure the spin current flowing through the leads attached to the top/bottom surfaces to find the proportion of Φ_0 and Φ_1 of the resultant state.

From Fig. 5.15 and Fig. 5.16, we see that Φ_0 and Φ_1 are symmetric around the centre in the z direction. Therefore, we can measure the spin current through one surface. We can write the states as:

$$\Phi_0(z) = \Phi_{T0}(z) + \Phi_{B0}(z), \tag{5.7}$$

$$\Phi_1(z) = \Phi_{T1}(z) + \Phi_{B1}(z). \tag{5.8}$$

The current through top surface related to the states are:

$$I_{T0} = I_{T0\downarrow} + I_{T0\uparrow}, \tag{5.9}$$

$$I_{T1} = I_{T1\downarrow} + I_{T1\uparrow}. \tag{5.10}$$

Where $I_{TX\downarrow}$ and $I_{TX\uparrow}$ (for $X = 0, 1$) are the spin currents with $s_z = \downarrow$ and $s_z = \uparrow$ corresponding to the states Φ_0 and Φ_1 on the top surface. The spin current $(I_{T0\downarrow}, I_{T0\uparrow}, I_{T1\downarrow}, I_{T1\uparrow})$ related to those states can be measured at the initialisation since we can prepare the qubit in those states. Since the current I is proportional to the electron density of a state, the spin current through the top surface for a general state is :

$$I_T = \frac{1}{2}(|\alpha|^2 I_{T0} + |\beta|^2 I_{T1}), \tag{5.11}$$

$$= \frac{1}{2}(|\alpha|^2 (I_{T0\downarrow} + I_{T0\uparrow}) + |\beta|^2 (I_{T1\downarrow} + I_{T1\uparrow})). \tag{5.12}$$

Because we also have the relation

$$|\alpha|^2 + |\beta|^2 = 1, \tag{5.13}$$

we can obtain the coefficients ($|\alpha|^2$ and $|\beta|^2$) by solving Eq. 5.11 and Eq.5.13 simultaneously. We obtain:

$$|\alpha|^2 = \frac{2I_T - I_{T1\downarrow} - I_{T1\uparrow}}{I_{T0\downarrow} + I_{T0\uparrow} - I_{T1\downarrow} - I_{T1\uparrow}}, \tag{5.14}$$

$$|\beta|^2 = \frac{2I_T - I_{T0\downarrow} - I_{T0\uparrow}}{I_{T1\downarrow} + I_{T1\uparrow} - I_{T0\downarrow} - I_{T0\uparrow}}. \tag{5.15}$$

If we use the state at the Γ point for spin qubit, the Eq. 5.9 and Eq. 5.10 are:

$$I_{T0} = I_{T0\downarrow}, \tag{5.16}$$

$$I_{T1} = I_{T1\uparrow}. \tag{5.17}$$

And we have:

$$|\alpha|^2 = \frac{2I_T - I_{T1\uparrow}}{I_{T0\downarrow} - I_{T1\uparrow}}, \tag{5.18}$$

$$|\beta|^2 = \frac{2I_T - I_{T0\downarrow}}{I_{T1\uparrow} - I_{T0\downarrow}}. \tag{5.19}$$

5.4 The two-qubit gate

The two-qubit gate could be realised in the same way as for semiconductor quantum dots [74]. The electrons with opposite spins in neighbouring TI quantum dots (one electron in each dot) can interact by exchange interaction [74]. The interaction can be described by the Heisenberg Model as:

$$H = JS_1 \otimes S_2. \tag{5.20}$$

J is the exchange energy and $S_{1(2)}$ is the spin of the electron in quantum dot 1(2). In experiments, this two-qubit gate can be implemented by gating a tunnelling barrier between two neighbouring TI quantum dots and operated electrically as proposed in paper [74]. There are also other methods to operate a two-qubit gate, such as using microwaves [115] or acoustic waves [7] [69], or optical control [21]. The computational overhead in modelling this type of qubit is even greater than for the charge qubit.

5.5 Discussion and summary

In this chapter we have discussed a spin qubit in an ultra-thin TI film that fulfils the requirements of DiVincenzo criteria (I, II, IV, V). A possible experimental setup would be similar to

the setup of a single spin qubit in a double quantum dot in paper [66], where the quantum dot defined by gates is replaced by a sufficiently thin topological insulator quantum dot. The oscillating magnetic field that drives the qubit rotation can be generated by applying a radio-frequency (RF) signal to an on-chip coplanar stripline (CPS) positioned near the TI dot [66]. Then, we will talk about some possible issues linked to experimental situations. We know that the frequency of the oscillating magnetic field is linked to the natural frequency of the two-level system and it is a few GHz. This frequency is very high for the current experimental condition. Because the frequency is inverse proportional to the thickness of TI, one way to reduce the frequency is to use a thicker TI film. The amplitude of a time-varying magnetic field is also a limiting factor in experiments. However, from Fig. 5.27 we learnt that the angle rotated at each period is proportional to the amplitude $|B|$. Because this is an ultra-fast operation of a few 0.1 ps, a small magnetic field would be desirable to rotate the qubit for significant angles. This allows the apparatus to produce controllable pulses. Moreover, the smaller the amplitude of a field, the higher the fidelity would be. Therefore, we would desire an oscillating magnetic field with high frequency and a small amplitude. Decoherence is an important issue to consider for a quantum computer. For a spin qubit in a quantum dot, there are various sources of decoherence. The fluctuations in the gate voltages and magnetic fields can be regarded as extrinsic sources of decoherence and those can be reduced with improved electronics [19]. However, there are also intrinsic sources of decoherence. The electronic spin can couple to phonons in the surrounding lattice or fluctuate by spin-orbit interactions [59]. In addition to this, the electronic spin can interact with the surrounding nuclear spins via contact hyperfine interaction [59]. Given the similarity of a spin qubit in a TI quantum dot to a spin qubit in a semiconductor quantum dot, the decoherence time at low magnetic fields ($\leq 100\,\mathrm{mT}$) is estimated to be about $1\mu s$ [91] [67] and it is possible to increase the decoherence time by multiple-pulse Carr–Purcell–Meiboom–Gill echo sequence [17]. The next question to think about is the accompanying current produced in the experiment when a time-varying magnetic field is applied to the system. We know that a magnetic field in the y direction will produce a EMF along the edges in the xz plane. This is equivalent to a voltage along the edges. This voltage causes the states to move along the edges but does not affect their spin. In this case, we need to measure both the top and bottom surfaces to obtain the coefficients:

$$|\alpha|^2 = \frac{I_T + I_B - I_{T1\downarrow} - I_{T1\uparrow} - I_{B1\downarrow} - I_{B1\uparrow}}{I_{T0\downarrow} + I_{T0\uparrow} + I_{B0\downarrow} + I_{B0\uparrow} - I_{T1\downarrow} - I_{T1\uparrow} - I_{B1\downarrow} - I_{B1\uparrow}}, \tag{5.21}$$

$$|\beta|^2 = \frac{I_T + I_B - I_{T0\downarrow} - I_{T0\uparrow} - I_{B0\downarrow} - I_{B0\uparrow}}{I_{T1\downarrow} + I_{T1\uparrow} + I_{B1\downarrow} + I_{B1\uparrow} - I_{T0\downarrow} - I_{T0\uparrow} - I_{B0\downarrow} - I_{B0\uparrow}}. \tag{5.22}$$

In this chapter, we studied a static spin qubit constructed using the surface states with opposite spin in an ultra-thin TI film. We found that the qubit can be initialized and rotate to an arbitrary position on a Bloch Sphere if we choose the pulse strength and frequency carefully. Also, the spin qubit can be measured by measuring the spin current flowing on the top/bottom surface.

Chapter 6

Field Dressing TIs And Floquet TI Qubits

6.1 Introduction

In recent years, the fast development of laser and ultra-fast spectroscopy techniques have enabled scientists to gain more control of a quantum system that is out of equilibrium. Floquet engineering - a concept that can date back to the times of the inverse Faraday effect [112], is beneficial from this technical development and interests in this field is growing fast in recent years [88] [62] [87] [16]. Floquet engineering is the subject of controlling a quantum system with time-periodic driving fields and it has provided a useful tool to study non-equilibrium systems. Floquet-Bloch theory[102] is the core of this subject. In single-body problems, Floquet-Bloch theory maps a time-dependent Hamiltonian to a stationary Hamiltonian with one extra dimension of discrete Fourier modes (we call it $n\hbar\omega$ here, $n \in Z$). This dimension comes from the time periodicity of the system, which is analogous to the crystal momentum space in a spatially periodic system. This $n\hbar\omega$ can be considered as a fictitious electric field along the extra dimension and it is important in the classification of topological phases in non-equilibrium quantum system [41] [88]. If the fictitious field ($\hbar\omega$) is small, the system can be thought of as a lattice problem in higher dimensions in a weak electric field [88] [41]. The Floquet-Bloch states produced are not just mathematical structures indicating how the field interacts with the system. They can be observed in experiments. The Floquet-Bloch states on the surface of a topological insulator has been observed in 2013 [121]. In this chapter, we apply the Floquet-Bloch theory to ultra-thin TI films under two different periodic fields separately and study the quasi states in the region where ω is small. We found that a carefully tuned small periodic field at a frequency matching the energy difference of the

two states (if we set $\hbar = 1$) can couple the desired surface states in a static TI and produce two types of quasi electronic states suitable for quantum computation. This completes our study of various types of qubit systems in a topological insulator. These Floquet TI qubits are simple to control since a single qubit rotation is fully controlled by adjusting the amplitude of the field, which can be achieved using standard Amplitude Modulation techniques [20]. Moreover, a recent paper has pointed out that the Floquet-engineered quantum states are more robust to external noise acting on the qubit, and can be prepared with a high fidelity [18]. These advantages make the Floquet TI qubit an interesting topic to study. The rest of this chapter is divided into two parts according to the types of time-periodic field applied to the ultra-thin TI film. We study a Floquet charge qubit in an ultra-thin TI film in a time-periodic electric field in section 6.2 and a Floquet spin qubit in an ultra-thin TI film in a time-periodic magnetic field in section 6.3.

6.2 Floquet charge qubits

6.2.1 Model Hamiltonian

The model Hamiltonian of a topological insulator thin film with a periodically time-varying electric field is constructed using the Floquet method described in Ch. 2. The time-dependent Schrödinger equation of the system is:

$$i\hbar\frac{d}{dt}\left|\Phi\right\rangle = H'\left|\Phi\right\rangle, \tag{6.1}$$

$$H' = H_0 - E_0(\mathbf{z})\cos(\omega t). \tag{6.2}$$

Here $E_0(\mathbf{z})\cos(\omega t)$ is the time-periodic electric field in the z direction. E_0 is the electric energy difference per unit length in the z direction. H_0 is the model Hamiltonian of topological insulator (Eq. 2.19) in Ch. 2. Like the case studied in Ch. 4, the Hamiltonian no longer commutes with k_z. Therefore we replace k_z with $-\frac{\partial}{\partial z}$. Since the Hamiltonian satisfying: $H'(t,\mathbf{r}) = H'(t+T,\mathbf{r}+\mathbf{R})$, we can apply the Floquet-Bloch ansatz in Ch. 2: $\left|\Phi_{\alpha,\mathbf{k}}(\mathbf{r},z,t)\right\rangle = e^{i\mathbf{k}\mathbf{r}-i\varepsilon_{\alpha,\mathbf{k}}t/\hbar}\left|u_{\alpha,\mathbf{k}}(\mathbf{r},t)\right\rangle\phi(z)$. α is the band index. $\mathbf{k}$ is the wave vector, and $\mathbf{r} = (x,y)$. Substituting the ansatz into Eq. 6.1, we map the time-dependent Schrödinger equation to an eigenvalue equation in which t and k are both parameters:

$$H_F\left|u_{\alpha,\mathbf{k}}\right\rangle = \varepsilon_{\alpha,\mathbf{k}}\left|u_{\alpha,\mathbf{k}}\right\rangle, \tag{6.3}$$

$$H_F = H' - i\hbar\frac{\partial}{\partial t}. \tag{6.4}$$

Here u is periodic in r and t, and is called a Flqouet-Bloch state. $\varepsilon_{\alpha,k}$ is called the quasienergy and determines how the wave function $\Phi_{\alpha,k}(\mathbf{r},z,t)$ evolves in time. The time dependent part $u(t)$ can be written in terms of its Fourier components:

$$u(t) = \sum_{n=-\infty}^{\infty} a_n e^{in\omega t}, \tag{6.5}$$

while the time varying term in 6.2 is written as:

$$\cos(\omega t)u(t) = \frac{1}{2}(e^{i\omega t} + e^{-i\omega t})u(t), \tag{6.6}$$

$$= \frac{1}{2}\sum_{n=-\infty}^{\infty}(a_{n-1}e^{in\omega t} + a_{n+1}e^{in\omega t}). \tag{6.7}$$

The Hamiltonian H_F then can be viewed as the outer product of the composed Hilbert space: $H_{temp} \otimes H_0(z)$. H_{temp} is the Fourier space of $u(t)$ and $H_0(z)$ includes all the spatial information. The Hamiltonian H_F is then solved numerically using the Floquet matrix method described in Ch. 3. The numerical matrix is written as:

$n=-2$	$n=-1$	$n=0$	$n=+1$	$n=2$	
$\mathbf{H_0}-2\hbar\omega$	$\mathbf{H_{+1}}$	0	$\vdots$	$\vdots$	$n=-2$
$\mathbf{H_{-1}}$	$\mathbf{H_0}-\hbar\omega$	$\mathbf{H_{+1}}$	0	$\vdots$	$n=-1$
0	$\mathbf{H_{-1}}$	$\mathbf{H_0}$	$\mathbf{H_{+1}}$	$\vdots$	$n=0$
$\vdots$	0	$\mathbf{H_{-1}}$	$\mathbf{H_0}+\hbar\omega$	$\mathbf{H_{+1}}$	$n=+1$

Here $\mathbf{H_0}$ and $\mathbf{H_{\pm 1}}$ are sub-matrices representing interactions with the Fourier components in temporal space H_{temp}, with $\mathbf{H_0} = \left\langle \vec{\phi}_{n_{z2},n} \middle| H \middle| \vec{\phi}_{n_{z1},n} \right\rangle$ and $\mathbf{H_{\pm 1}} = -\frac{1}{2}E_0(n_{z2}\Delta z)\left\langle \vec{\phi}_{n_{z1},n\pm 1} \middle| \vec{\phi}_{n_{z1},n} \right\rangle$, being H the original TI Hamiltonian 2.19. The term $\mathbf{H_{\pm 1}}$ represents the time-varying field in Eq 6.2. Here we can see that the time dependent interaction with the field is included in the off-diagonal blocks and the time evolution of the Fourier states are included as $n\hbar\omega$ in the central diagonal blocks of the numerical matrix 6.2.1. The index acts like a fictitious electric field along the Fourier dimension n. The resultant numerical solutions are of the form:

$$\vec{\phi}_{n_z,n} = \{\phi_{1,-i}, \phi_{2,-i}, ...\phi_{z,-i}, \phi_{2,-i+1}, ...\phi_{z,i}\}. \tag{6.8}$$

where i and z are indices of the Fourier components and lattice sites respectively. The corresponding Floquet-Bloch state with quasi-energy $\varepsilon_{\alpha,n}$ is

$$u_{\alpha,\mathbf{k},n}(z,t) = \sum_{m=-i}^{m=i} a_m e^{im\omega t}\left|\phi_{n_z,n}\right\rangle, \tag{6.9}$$

and the time dependent Floquet solution to Eq. 6.1 is

$$|\Phi_{\mathbf{k}}(z,t)\rangle = e^{-i\varepsilon_{\alpha,n,t}/\hbar} u_{\alpha,\mathbf{k},n}(z,t). \tag{6.10}$$

A general solution is :

$$|\Phi_{\mathbf{k}}(z,t)\rangle = \sum_{\alpha} b_{\alpha} e^{-i\varepsilon_{\alpha,nt}/\hbar} u_{\alpha,\mathbf{k},n}(z). \tag{6.11}$$

6.2.2 Ultra-thin TI under a periodic electric field

By applying the Floquet method we have converted a time dependent Schrödinger equation to an eigenvalue problem. By solving the numerical matrix in Table 6.2.1, we obtain the Floquet states $u_{\alpha,n}$ and their quasi energies $\varepsilon_{\alpha,n}$. From Fig. 6.1 and Fig. 6.2 we can see that the quasi energy forms a band plot that is similar to the band structure plot of a semiconductor. The is due to the fact that now we have many copies of a stationary band. This is because that when we solve the Floquet matrix in Table 6.2.1, we obtain a group of Floquet solutions $u_{\alpha,n}$ which have quasi energy

$$\varepsilon_{\alpha,n} = \varepsilon_{\alpha,0} + n\hbar\omega. \tag{6.12}$$

Therefore, we have n replicas of the quasi energy state $u_{\alpha,\mathbf{k},0}$ with energy differences of $n\hbar\omega$. Those states represent the same time dependent physical solution as in Eq. 6.10. From Fig 6.1 and 6.2 we also notice that these quasi-bands show a familiar gapped Dirac cone structure with multiple replicas. This is because the quasienergy ε_{α} is a function of the parameters $|E|$ and ω. $|E|$ is the amplitude of the potential energy difference of the electric field across the thickness of the film and ω is the field frequency. We use $|E|$ (and E for a static field) to represent the electric field throughout this chapter. The electric field strength is proportional to $|E|$ since the film is kept at a constant thickness to study a single qubit. When the interaction $|E|$ is small (in a perturbation region), $\varepsilon_{\alpha,0} \approx \varepsilon_{\alpha}$, where ε_{α} is the eigenenergy of the original Hamiltonian H_0. $\varepsilon_{n,\alpha} \to \varepsilon_{\alpha} + n\hbar\omega$ as $|E| \to 0$. If the interaction $|E|$ is very high, the states are distorted. Interesting features appear when we apply a field at the frequency that equals the energy difference between two levels $\omega = \frac{\varepsilon_{\alpha}-\varepsilon_{\beta}}{\hbar}$ (where $\varepsilon_{\alpha} > \varepsilon_{\beta}$). If $|E| = 0$, the states can intersect each other when $\varepsilon_{\alpha} + (n-1)\hbar\omega = \varepsilon_{\beta} + (n\hbar\omega)$. When $|E| \neq 0$, the interaction operator will couple the states if they belong to the same symmetry group and develop into avoided crossings. This happens when we apply a resonant driving field with frequency $\omega_{res} = \frac{\Delta\varepsilon}{\hbar}$ to the ultra-thin TI, where $\Delta\varepsilon$ is the energy difference of two surface states on the gapped Dirac cone. The energy levels $\varepsilon_{S1(S2)}$ and $\varepsilon_{S4(S3)}$ belong to the same symmetry group ($|S1\rangle$ to $|S4\rangle$ are defined in Sec. 4.3). At, $\omega = \frac{\varepsilon_{S1(S2)}-\varepsilon_{S4(S3)}}{\hbar}$, the

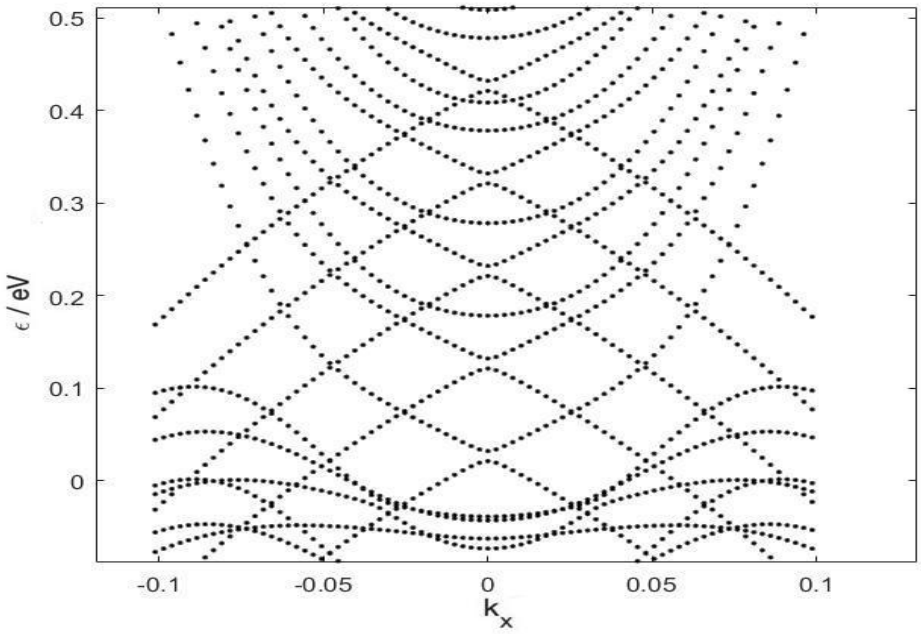

Fig. 6.1 Floquet band structure of a 5 QL TI thin film with a perpendicular oscillating electric field at $\omega = 10\omega_{res}$ along the k_x axis. The Floquet bands are replicas of the bare TI bands without a field. ω_{res} is the natural frequency of a combined state $\alpha |\Phi_0\rangle + \beta |\Phi_1\rangle, \alpha \neq 0, \beta \neq 0$ that goes back to its original position on the Bloch sphere when there is no field applied.

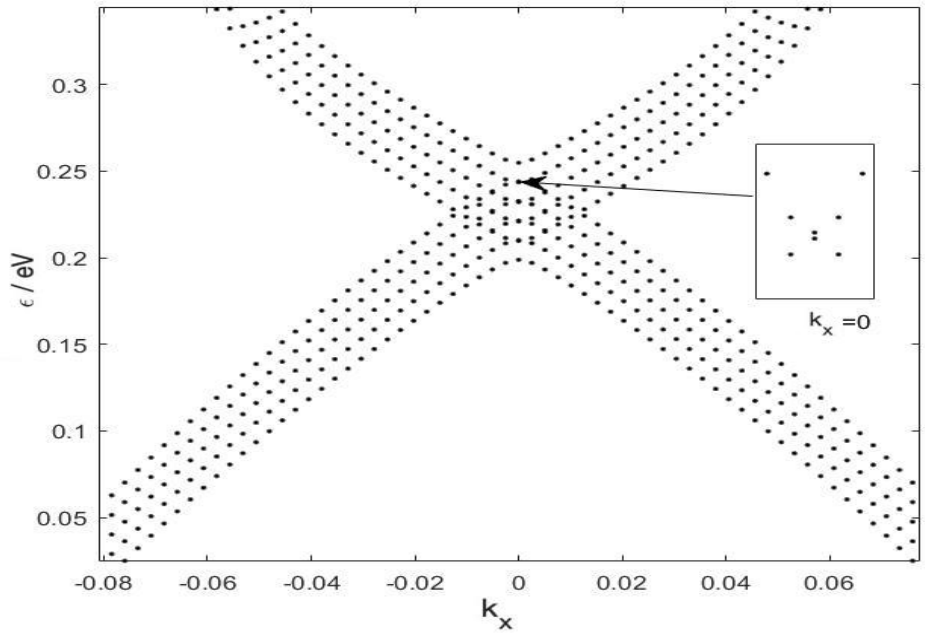

Fig. 6.2 Floquet band structure of the Gapped Dirac cone in a 5 QL TI thin film with a perpendicular oscillating electric field at ω_{res} along the k_x axis. The Floquet bands are replicas of the bare TI bands without a field. ω_{res} is the natural frequency of a combined state $\alpha|\Phi_0\rangle + \beta|\Phi_1\rangle, \alpha \neq 0, \beta \neq 0$ that goes back to its original position on the Bloch sphere when there is no field applied. The figure shows that when $\omega = \omega_{res}$, the Floquet states are very close to each other with a small gap.

quasienergies are related as:

$$\varepsilon_{S1(S2),0} + n\hbar\omega_{res} = \varepsilon_{S4(S3),0} + (n-1)\hbar\omega_{res}. \tag{6.13}$$

When $|E| \neq 0$, the quasi-states will interact and develop into avoided crossings.

Now we are at the point to study how the wavefunction $\Phi_{n,SX}$ responds to the periodic electric field. Like the quasi energies, $\Phi_{n,SX}$ depends on the parameters of $|E|$ and ω as well. We will take the Floquet states $\Phi_{1,S1}$ and $\Phi_{0,S4}$ as our example, where the original states Φ_{S1} and Φ_{S4} are defined in Ch. 4. Starting from a stationary state Φ_{SX_0} and adiabatically switching on the interacting field, we will transfer the system into a quasienergy state $\Phi_{n,SX}$ (Fig. 6.3). The interaction can be divided into three different regimes according to ω. $|E|$ in all cases (if not mentioned specifically) is kept in the perturbation region to avoid wavefunction mixing with bulk bands (distortion).

At the region where $\omega \ll \omega_{res}$, $\varepsilon_{1,S1} < \varepsilon_{0,S4}$ for $|E| \neq 0$. The quasi-states are similar to these static states under a static field and there is no interaction between the two states since they are far apart in terms of quasienergy. As $|E| \to 0$, the quasi-states will recover the shape of the time-independent states of H_0.

At the region where $\omega \approx \omega_{res}$, switching on/off the interacting field amplitude $|E|$ generates two different regimes of interaction. If the amplitude $|E| \to 0$, $\varepsilon_{1,S1} = \varepsilon_{0,S4}$ and the two levels intersect each other so the quasi-states are $\Phi_{1,S1} = e^{i(\varepsilon_{S1}+\omega t)/\hbar}\Phi_{S1_0}$ and $\Phi_{0,S4} = e^{i\varepsilon_{S4}/\hbar}\Phi_{S4_0}$. If the amplitude $|E| \neq 0$, $\varepsilon_{1,S1} \neq \varepsilon_{0,S4}$. Since Φ_{S1} and ϕ_{S4} belong to the same symmetry group, the two levels will repel each other and form an avoided crossing when the quasienergies are close to each other. This is why we see an anti-crossing when $|E| \neq 0$ in Fig 6.2. The resultant states are combined states of Φ_{S1} and ϕ_{S4}. From Fig 6.3 we can see that $\varepsilon_{1,S1} < (>)\varepsilon_{0,S4}$ at $\omega < (>)\omega_{res}$; therefore, the Floquet states $\Phi_{1,S1}$ and $\phi_{0,S4}$ exhibit jump discontinuities at the resonant frequency. The Floquet states near the resonant frequency are partially combined and have a maximal superposition at ω_{res}(Fig. 6.4 and Fig. 6.5).

At the region where $\omega \gg \omega_{res}$, the frequency is too high for the system to react in time. The Landau-Zener transition [125] occurs and the Floquet states are decoupled (the off-diagonal blocks become insignificant). Regardless of the amplitude $|E|$ (in the perturbation regime), the Floquet states are frozen and look like the time-independent states of a bare system H_0. When $|E|$ becomes very high, the states are distorted and mix with the bulk bands.

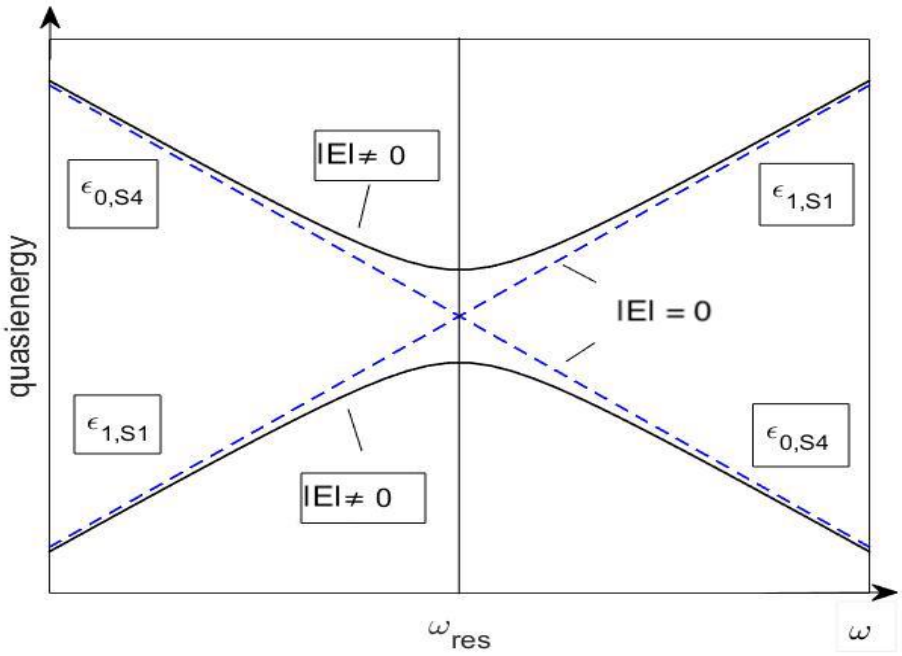

Fig. 6.3 A diagram illustrates the trend of quasienergies $\varepsilon_{0,S4}$ and $\varepsilon_{1,S1}$ of Floquet states $\Phi_{0,S4}$ and $\Phi_{1,S1}$, respectively, vs the frequency ω for interaction amplitudes $|E| = 0$ and $|E| \neq 0$, note: $|E|$ is the amplitude of the potential energy difference of the electric field across the thickness of the film, and we use this to represent the electric field throughout this chapter. The electric field strength is proportional to $|E|$. When the frequency $\omega \to 0$ and $\omega \gg \omega_{res}$, the Floquet energies $\varepsilon_{0,S4}$ and $\varepsilon_{1,S1}$ are closer to the case of energy states without an applied field. When the frequency $\omega \to \omega_{res}$, the Floquet energies of the two states get closer to each other but behave differently in the cases of interaction amplitudes $|E| = 0$ and $|E| \neq 0$. In the case $|E| = 0$, they will intersect with each other; however, if $|E| \neq 0$, an anti-crossing occurs and the two states swap.

6.2.3 Floquet charge qubit definition

From the discussion above, we learnt that with a field at driving frequency $\hbar\omega \approx \Delta\varepsilon$ and of a proper chosen magnitude, the field-dressing system produces a pair of Floquet states located on the top/bottom surfaces. The pair of Floquet states are the combined surface states of the bare system and they evolve in time following Eq. 6.10. However, just like the Rabi oscillation of a two-level system, the degree of coupling of the bare states depends on the amplitude and frequency of the electric field. When the frequency of the field is close to the Rabi frequency ($\omega = \frac{\Delta\varepsilon}{\hbar}$), the coupling increases dramatically and the resultant Floquet states become more localised on the opposite surfaces. Amplitude is also an important factor to the degree of coupling; however, it is less effective compared to the frequency. In an experiment we should first tune the frequency of the field to a value near $\omega = \frac{\Delta\varepsilon}{\hbar}$, and then tune the amplitude of the field to refine the qubit. The amplitude should be small so that the interaction of the state with the electric field is insignificant and the interaction of the two states is primary. In this case, we can obtain a pair of combined states like those found in the static TI system without any field in Ch. 4. In order to exploit these Floquet states as a qubit state, we aim to create a pair of states that are maximally localised on the top/bottom surfaces like the combined states in a bare TI in Ch. 4. With a field of a matching frequency ($\omega = 0.011n.u$) and amplitude ($|E| = 0.00064eV$, where $|E|$ is amplitude of the potential energy difference of the electric field across the thickness of the film. We use it to represent the electric field throughout the chapter. The electric field strength is proportional to $|E|$.), we are able to obtain a pair of qubit states (u_0 and u_1) which have identical spatial profiles to the static qubit states (ϕ_0 and ϕ_1) in Ch. 4 at $t = 0$, with an overlap $\langle u_0|\phi_0\rangle = 1$ and $\langle u_1|\phi_1\rangle = 1$ (Fig. 6.4 and Fig. 6.5). It is worth mentioning that the frequency is slightly less than the energy difference $\Delta\varepsilon$ of the bare system given that the interaction of a single state with the field makes the quasienergy slightly different from the corresponding energies in a static system.

The Floquet states evolve in time (See Fig. 6.6 and Fig. 6.7). At any instance, the Floquet-state pair forms a mirror image of each other and the overlap between them is always zero (that is, they are orthogonal to each other at any time). This property enables us to define a new type of charge qubit states in a field-dressing TI: we call them the Floquet charge qubit. Unlike the static charge qubit studied in Ch. 4, they are dynamic and evolve in time. Therefore, the Bloch sphere defined with this Floquet-charge-qubit pair is also rotating in time. The qubit states are defined as

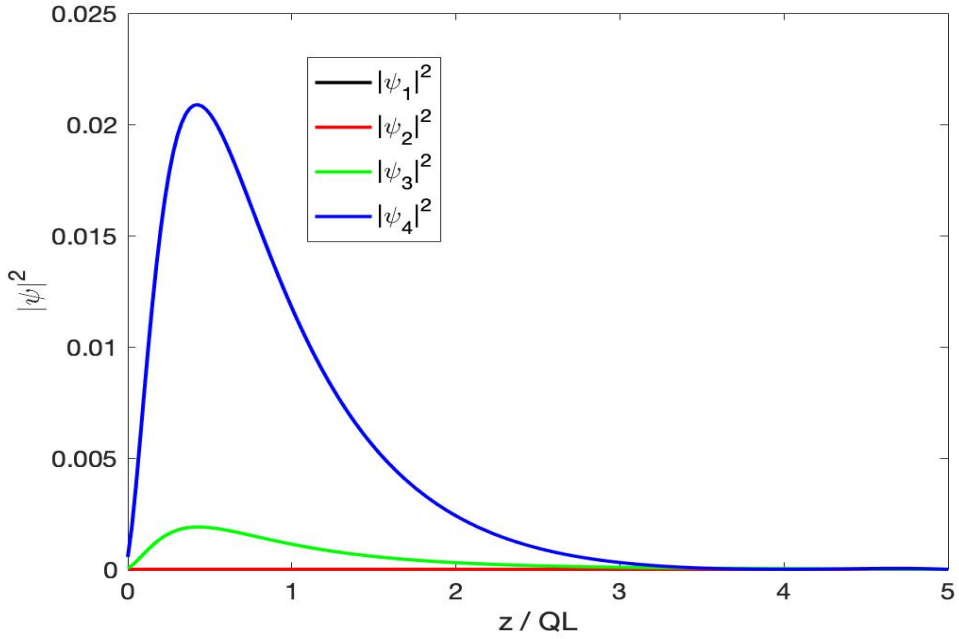

Fig. 6.4 Spatial distributions of wave function densities of $u_0(t=0)$ at the Γ point in a 5 QL TI thin film.This state is obtained by applying a perpendicular oscillating electric field with $\omega = \omega_{res}$ and a small amplitude $|E| = 0.00064\,\text{eV}$ (the amplitude of the potential energy difference across the film), similar to the combinational state of the 'surface states' in Fig.4.17. However, unlike the charge qubit studied in Ch. 3, $u_0(t)$ is time dependent. $|\psi_1|^2$ to $|\psi_4|^2$ are the wave function densities of the basis states $|\psi_1\rangle$ to $|\psi_4\rangle$ of the TI Hamiltonian in Eq. 4.1. The detailed electronic states of $|\psi_1\rangle$ to $|\psi_4\rangle$ are shown in Eq. 2.26. The wave function densities of $|\psi_1\rangle$ and $|\psi_2\rangle$ are equal to zero. The wave function density of $u_0(t=0)$ is localised on one surface.

$$|\Phi_0(t)\rangle = e^{-i\varepsilon_{u_0}t/\hbar}\,|u_0(t=0)\rangle\,, \tag{6.14}$$

$$|\Phi_1(t)\rangle = e^{-i\varepsilon_{u_1}t/\hbar}\,|u_1(t=0)\rangle\,. \tag{6.15}$$

A general state on the dynamical Bloch sphere is:

$$\Phi(t) = \alpha\Phi_0(t) + \beta\Phi_1(t). \tag{6.16}$$

In this chapter, we decide to study the qubit states at the Γ point in a 5 QL TI. It should be noticed that just like the static qubit, the Floquet qubit are spin degenerate; therefore we have two-qubit states available at the same energy at the Γ point. In this chapter, we study a charge qubit with $s_z = -\frac{1}{2}$.

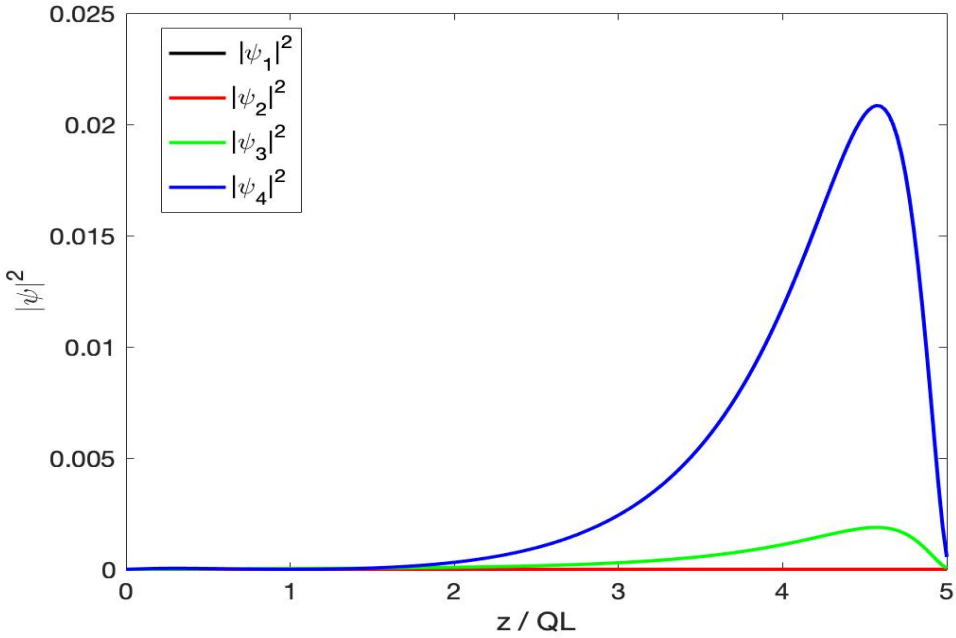

Fig. 6.5 Spatial distributions of wave function densities of $u_1(t=0)$ at the Γ point in a 5 QL TI thin film.This state is obtained by applying a perpendicular oscillating electric field with $\omega = \omega_{res}$ and a small amplitude $|E| = 0.000\,64\,\text{eV}$ (the amplitude of the potential energy difference across the film). It is similar to the combinational state of the 'surface states' in Fig.4.18. However, unlike the charge qubit studied in Ch. 3, $u_1(t)$ is time dependent. $|\psi_1|^2$ to $|\psi_4|^2$ are the wave function densities of the basis states $|\psi_1\rangle$ to $|\psi_4\rangle$ of the TI Hamiltonian in Eq. 4.1. The detailed electronic states of $|\psi_1\rangle$ to $|\psi_4\rangle$ are shown in Eq. 2.26. The wave function densities of $|\psi_1\rangle$ and $|\psi_2\rangle$ are equal to zero. The wave function density of $u_1(t=0)$ is localised on one surface.

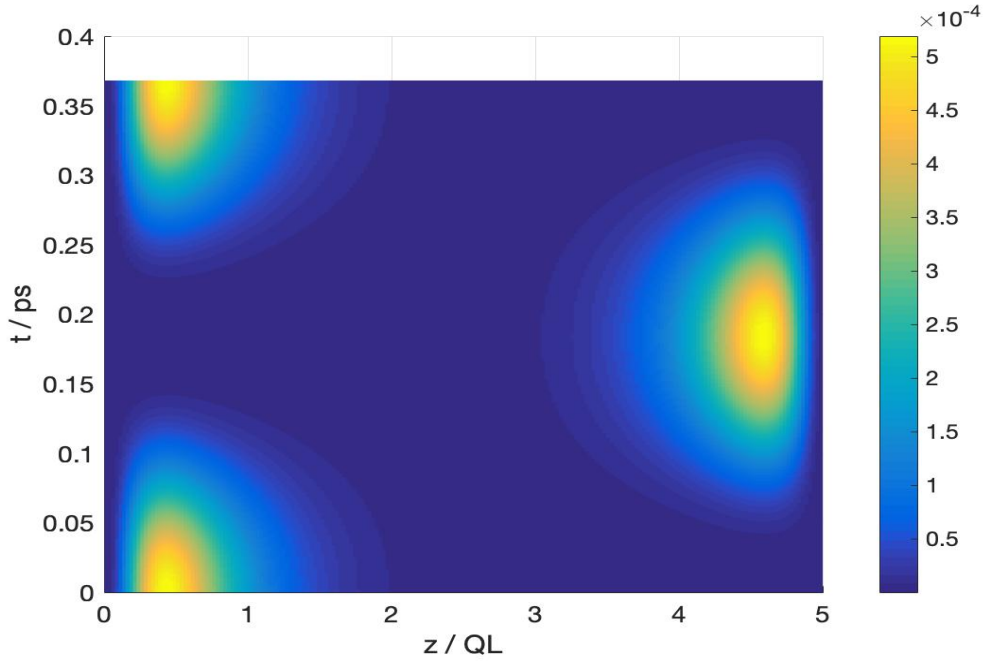

Fig. 6.6 Time evolution of $u_0(t)$ in the TI thin film for T_{res}. T_{res} is the natural period of a combined state $\alpha|\Phi_0\rangle + \beta|\Phi_1\rangle, \alpha \neq 0, \beta \neq 0$ that goes back to its original position on the Bloch sphere when there is no field applied. The vertical axis is time (in picoseconds) and the horizontal one is depth in the TI thin film. The colour indicates the electron density. The yellow colour indicates that the electron is located on the top surface of the thin film at $t = 0$.

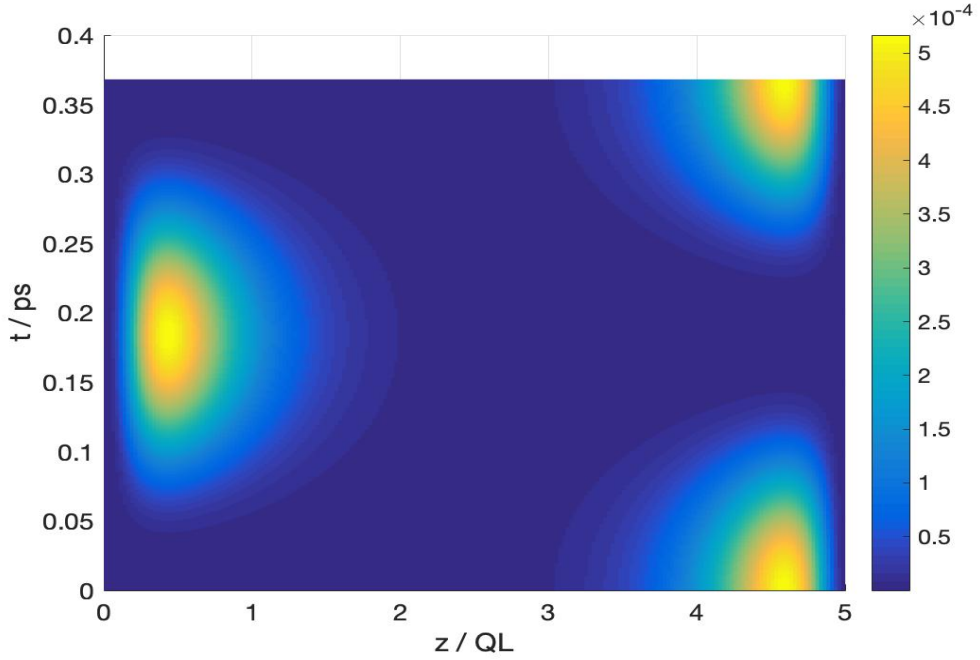

Fig. 6.7 Time evolution of $u_1(t)$ in the TI thin film for T_{res}. T_{res} is the natural period of a combined state $\alpha|\Phi_0\rangle + \beta|\Phi_1\rangle, \alpha \neq 0, \beta \neq 0$ that goes back to its original position on the Bloch sphere when there is no field applied. The vertical axis is time (in picoseconds) and the horizontal one is depth in the TI thin film. The colour indicates the electron density. The yellow colour indicates that the electron is located on the bottom surface of the thin film at $t = 0$.

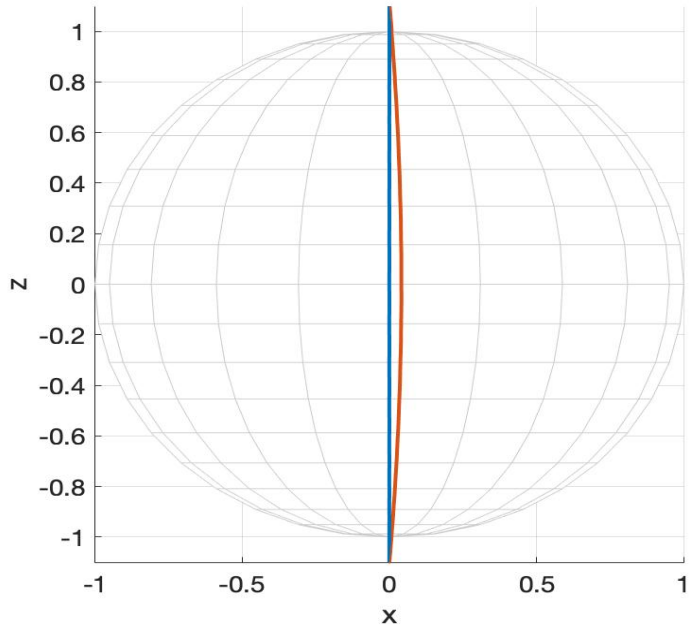

Fig. 6.8 Two traces of a single qubit rotation with/without an oscillating electric field applied perpendicular to the TI thin film. Blue trace: a full circular single qubit rotation when there is no electric field applied to the TI thin film. Orange trace: a single qubit rotation when an oscillating electric field with ω_{res} is applied perpendicularly to the TI thin film. ω_{res} is the natural frequency of a combined state $\alpha|\Phi_0\rangle + \beta|\Phi_1\rangle, \alpha \neq 0, \beta \neq 0$ that goes back to its original position on the Bloch sphere when there is no field applied. The traces are viewed in a static frame, with $u_0(t=0)$ ($u_1(t=0)$) being the north (south) pole of the Bloch sphere. This figure indicates that the paths overlap near the poles and that path 2 deviated from path 1 near the equator. Note that the Bloch sphere is drawn at 90% size to clarify the diagram.

6.2.4 Single-qubit study

The initialisation process is similar to initialise a static charge qubit. We keep the Fermi level below or in the middle of the surface band gap and then apply an oscillating electric field to the system. When the field frequency ω approaches $\omega \approx \frac{\Delta\varepsilon}{\hbar}$, we will see a tunnelling current periodically appearing on the top (or bottom) surface. This current reaches a maximum when the Floquet states are equally combined surface states (see Eq. 6.14 and Eq. 6.15). If the surface states are not equally combined, we can see that the current density does not vanish periodically. When we see a periodically disappearing current flowing on one surface, we have prepared an Floquet qubit at $|0\rangle$ or $|1\rangle$.

We know that the Bloch sphere of a Floquet qubit is rotating. Therefore, any operation applied to the qubit is with respect to the time-varying Bloch sphere. When there is no field applied, the qubit will rotate spontaneously like the static charge qubit in Chap. 4;

however, the trace is slightly different from the trace with a driving field (Fig. 6.8). We note that the Bloch spheres in the thesis are plotted at 90% size to clarify the single-qubit rotation diagrams. We compare the two paths and find they are slightly different when the qubit is close to the equator on the Bloch sphere; this is because the driving field has a finite amplitude which perturbs the state. The field is maximum when the qubit is at the equator on the Bloch sphere, so the states are perturbed because of this electric bias. In order to be able to rotate the qubit to an arbitrary position on the Bloch Sphere, we study whether we can realise two rotations with respect to two orthogonal axes.

The first rotation we discuss here is the σ_x rotation. Since the Bloch sphere is rotating, we cannot obtain this rotation by turning off the field as in the case of a static TI charge qubit. However, since we know that the qubit rotates on the Bloch sphere following a closed circle with axis in the x direction, we can relabel the state at time t' as $t = 0$ which is equivalent to a σ_x rotation. We first define u_0 and u_1 as the static wave functions shown in Fig. 6.4 and Fig. 6.5. We can either turn off the field or wait for a time duration $t = t_1$ and then relabel the time $t = t_1 \rightarrow t = 0$. After a time t_1, the qubit has rotated over an angle of $\omega_x t_1$ along the x axis, with $\omega_x = \omega_{res}$ the natural frequency of the qubit system.

σ_z and σ_y rotations are more difficult to achieve. If we apply a static field with amplitude $|E|$ to the system, the path of the qubit rotation is more complicated than the one in the static case since the Bloch sphere is rotating continuously (Fig. 6.9 and Fig. 6.10). The trace is in fact a periodic rotation with respect to the axis r on the xz plane, with $\omega_r \propto |E|$, plus a continuous σ_x rotation with $\omega_x = \frac{\Delta\varepsilon}{\hbar}$. The path depends on the relative frequencies ω_x and ω_r. Therefore, it is difficult to define a standard way to perform σ_z and σ_y rotations with a static field. We now turn to look at a square pulse and explore how the qubit rotates with respect to it.

From Fig 6.9 and Fig. 6.10 we see that a smaller electric field produces a smaller change in θ during the same time period. This is closer to a desired σ_z rotation but $\Delta\theta$ is position dependent (See Fig. 6.10). Therefore, we decide to apply a square pulse with a small amplitude (we used $|E| = 0.002\,\mathrm{eV}$) to the qubit. We found that when a square pulse with the positive part and negative part set to be the same duration ($\frac{T}{4}$) is applied, $\Delta\theta$ is more or less cancelled out and we have a nearly effective σ_z rotation (Fig 6.11). From Fig. 6.12 and Fig. 6.13 we see that at $\frac{T}{2}$ and T ($T = \frac{2\pi}{\omega_x}$), the values of $\Delta\theta$ are closer to zero and the ones for $\Delta\phi$ are almost the same. Although there is still a position-dependent finite $\Delta\theta$ left (with a maximum difference of 2.58° in Fig. 6.12), we see that an alternative linear pulse can produce a nearly effective σ_z rotation at times $\frac{T}{2}$ and T. Inspired by this pulse, we decide to continue to study whether a cosine pulse would be better to induce a high-fidelity effective σ_z rotation. We keep the electric field amplitude the same for comparison and vary

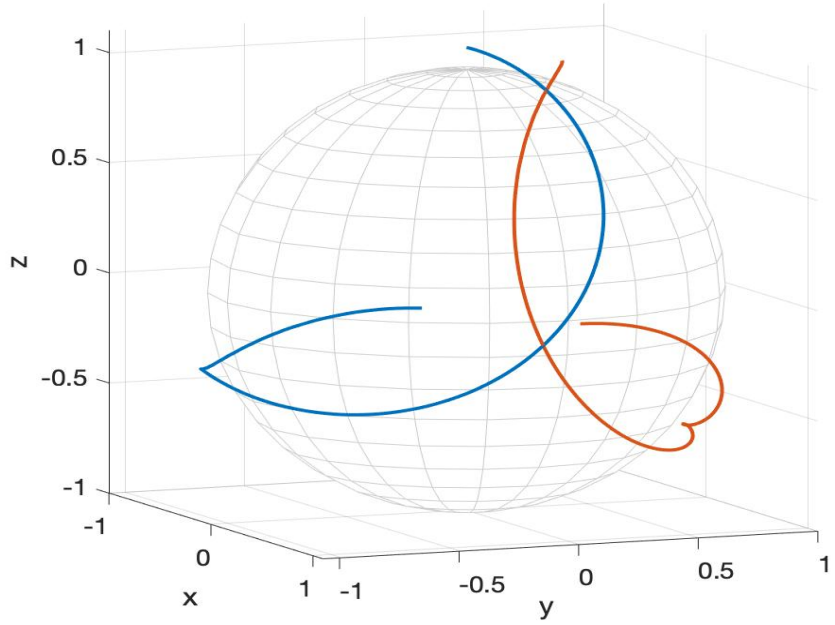

Fig. 6.9 Two traces of a single qubit rotation with a static electric field ($E = 0.008\,75\,\text{eV}$, and E is the potential energy difference across the film) applied perpendicularly to the TI thin film for a whole period T_{res} starting at two different positions (blue: $\theta = 0^\circ$, $\phi = 0^\circ$ and orange: $\theta = 30^\circ$, $\phi = 0^\circ$). T_{res} is the natural period of a combined state $\alpha\,|\Phi_0\rangle + \beta\,|\Phi_1\rangle\,, \alpha \neq 0, \beta \neq 0$ that goes back to its original position on the Bloch sphere when there is no field applied. The traces are viewed in a static frame, with $u_0(t = 0)$ ($u_1(t = 0)$) being the north (south) pole of the Bloch sphere. Note that the Bloch sphere is drawn at 90% size to clarify the diagram.

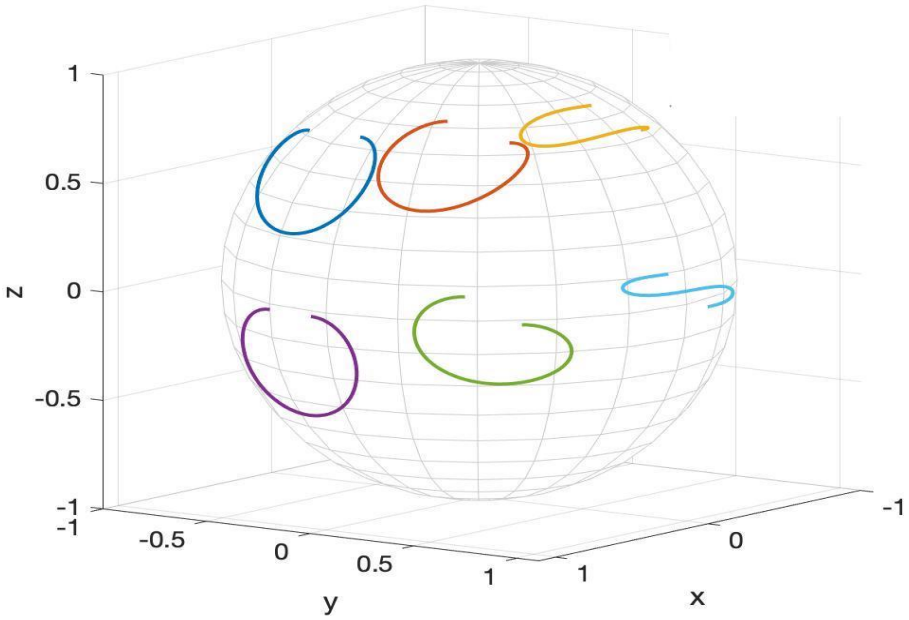

Fig. 6.10 Traces of a single qubit rotation with a static electric field ($E = 0.002\,\text{eV}$, and E is the potential energy difference across the film) applied perpendicularly to the TI thin film for a whole period T_{res} for a qubit starting at different positions. T_{res} is the natural period of a combined state $\alpha\left|\Phi_0\right\rangle + \beta\left|\Phi_1\right\rangle, \alpha \neq 0, \beta \neq 0$ that goes back to its original position on the Bloch sphere when there is no field applied. The traces are viewed in a static frame, with $u_0(t=0)$ ($u_1(t=0)$) being the north (south) pole of the Bloch sphere. Note that the Bloch sphere is drawn at 90% size to clarify the diagram.

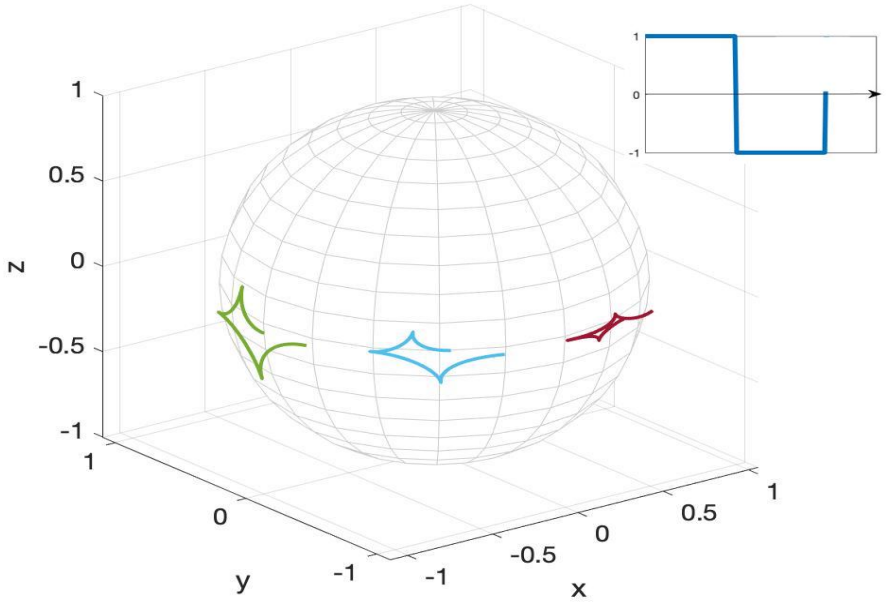

Fig. 6.11 Traces of a single qubit rotation with a square electric field pulse ($E = \pm 0.002\,\text{eV}$, and E is the potential energy difference across the film) applied perpendicularly to the TI thin film for a qubit starting at different positions. The electric field swaps the direction at every interval of time $\frac{T}{4}$ and lasts for $t = T_{res}$. T_{res} is the natural period of a combined state $\alpha|\Phi_0\rangle + \beta|\Phi_1\rangle, \alpha \neq 0, \beta \neq 0$ that goes back to its original position on the Bloch sphere when there is no field applied. The traces are viewed in a static frame, with $u_0(t = 0)$ ($u_1(t = 0)$) being the north (south) pole of the Bloch sphere. The inset shows the shape of the pulse. Note that the Bloch sphere is drawn at 90% size to clarify the diagram.

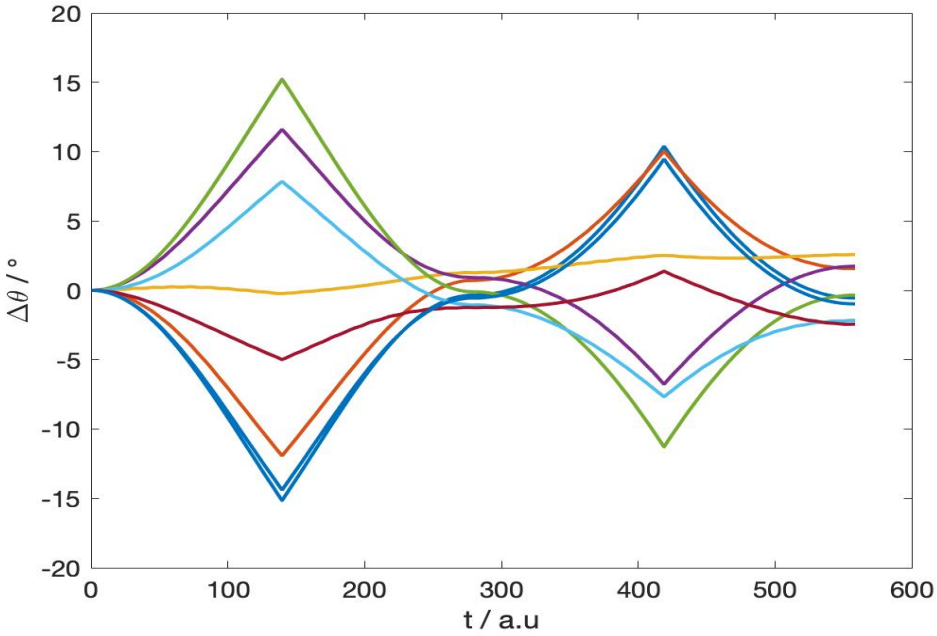

Fig. 6.12 $\Delta\theta$ in a single qubit rotation with a square electric field pulse ($E = \pm 0.002\,\text{eV}$, and E is the potential energy difference across the film) applied perpendicularly to the TI thin film for a qubit starting at different positions. θ is the conventional polar angle used in spherical coordinate systems. The electric field swaps the direction at every interval of time $\frac{T}{4}$ and lasts for $t = T_{res}$. T_{res} is the natural period of a combined state $\alpha\left|\Phi_0\right\rangle + \beta\left|\Phi_1\right\rangle, \alpha \neq 0, \beta \neq 0$ that goes back to its original position on the Bloch sphere when there is no field applied. The traces are viewed in a static frame, with $u_0(t=0)$ ($u_1(t=0)$) being the north (south) pole of the Bloch sphere.

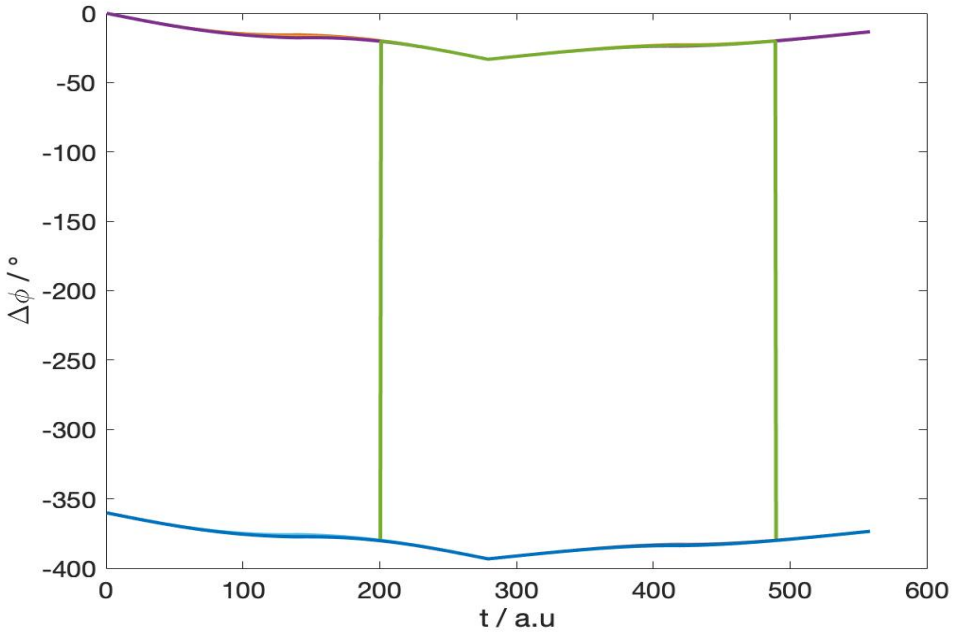

Fig. 6.13 $\Delta\phi$ in a single qubit rotation with a square electric field pulse ($E = \pm 0.002\,\text{eV}$, and E is the potential energy difference across the film) applied perpendicularly to the TI thin film for a qubit starting at different positions. ϕ is the conventional azimuthal angle used in spherical coordinate systems. The electric field swaps the direction at every interval of time $\frac{T}{4}$ and lasts for $t = T_{res}$. T_{res} is the natural period of a combined state $\alpha\left|\Phi_0\right\rangle + \beta\left|\Phi_1\right\rangle, \alpha \neq 0, \beta \neq 0$ that goes back to its original position on the Bloch sphere when there is no field applied. The traces are viewed in a static frame, with $u_0(t=0)$ ($u_1(t=0)$) being the north (south) pole of the Bloch sphere.

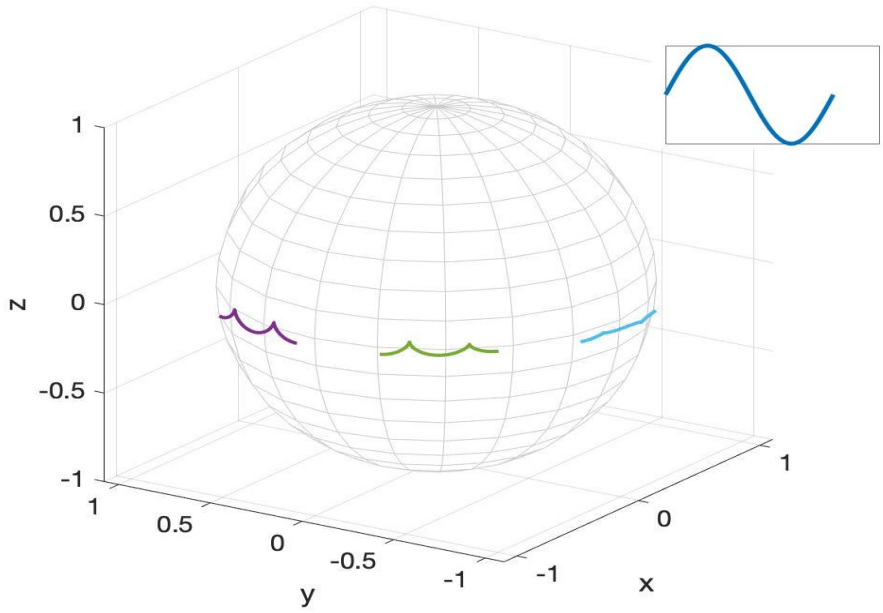

Fig. 6.14 Traces of a single qubit rotation with an oscillating electric field ($|E| = 0.002\,\text{eV}$, where $|E|$ is the amplitude of the potential energy difference across the film, $\omega = \omega_{res}$) applied perpendicularly to the TI thin film during a time T_{res} for a qubit starting at different positions. T_{res} and ω_{res} are, respectively, the natural period and frequency of a combined state $\alpha|\Phi_0\rangle + \beta|\Phi_1\rangle, \alpha \neq 0, \beta \neq 0$ that goes back to its original position on the Bloch sphere when there is no field applied. The traces are viewed in a static frame, with $u_0(t=0)$ ($u_1(t=0)$) being the north (south) pole of the Bloch sphere. The inset shows the shape of the pulse. Note that the Bloch sphere is drawn at 90% size to clarify the diagram.

the frequency. We first apply a pulse at the driven frequency: $\omega_d = \frac{\Delta\varepsilon}{\hbar}$. We see that a cosine pulse at $\omega = \omega_d$ is able to produce a path that is similar to Fig. 6.11, with a smaller $\Delta\theta$ at time $\frac{T}{2}$ and T (See Fig. 6.14). The fidelity of this rotation is very high (Fig. 6.15). We must notice that this cosine pulse produces effective σ_z rotations at $t = \frac{nT}{2}$ with a discrete angle ϕ. In order to obtain other rotational angles we need to change the field amplitude $|E|$ or wait for more periods. We choose to study two points at $\theta = 90^\circ$, $\phi = 0^\circ, 90^\circ$ since, from 6.15, we can see that lowest fidelity of σ_z rotations appear when the qubit is near the equator. From Fig. 6.16 and Fig. 6.19 we see that $\Delta\phi$ obeys a linear relation with $|E|$ (the potential energy difference across the film of the field). By reversing the direction of the oscillating field (equivalent to adding a phase π to the cosine term) we are able to obtain σ_z rotations of other angles. The fidelity of a σ_z rotation decreases when the field amplitude $|E|$ increases given that $\Delta\theta$ becomes larger as $|E|$ increases (see Fig.6.17 and Fig. 6.20). However, this fidelity is still high enough (99.75%) for a pulse at $|E| = 0.005\,\text{eV}$ and it produces a rotation of $\phi = 90^\circ$ ($\phi = 117^\circ$ when the electric field is out of phase respect to with the driving field). Therefore, we are able to produce position-independent high-fidelity rotations for most angles by simply changing the amplitude of the field or by adding a π phase to the driving field. Larger angles can be obtained by keeping the pulse for two full periods. At lower frequencies ($\omega < \frac{\Delta}{\hbar}$), we are not able to find effective σ_z rotations.

Then next question is to study how the qubit rotates if we apply pulses with different frequency. Recalling from subsection 6.2.2, when $\omega \gg \frac{\Delta\varepsilon}{\hbar}$ the field varies too fast and the state enters the Landau-Zener regime. We found that the qubit follows the path of a σ_z rotation at higher frequencies at time $t = \frac{nT}{2}$ (Fig. 6.22 and Fig. 6.23). The higher the frequency, the better the fidelity of the rotation is. However, it is difficult to achieve experimentally since the frequencies are too high and beyond the capacity of experimental apparatus. Also we should notice that at moderate frequencies, $\Delta\theta$ shows an oscillating behaviour with a local minimum at integer numbers of ω_0, the driving frequency.

Measuring this Floquet qubit is similar to measuring a static TI charge qubit discussed in Ch. 4. We can measure the tunnelling current through the top/bottom surfaces and relate it to the coefficients α and β in Eq. 6.16. We notice that because the qubit states $\Phi_0(t)$ and $\Phi_1(t)$ are varying in time, the currents I related to the state $\Phi_0(t)$ and $\Phi_1(t)$ are also time-dependent and should be recorded as $I(t)$. We need to define an initial time t_0 and measure the dynamic currents $I_0(t)$ and $I_1(t)$ for a whole period. Then, we can use the corresponding electron densities $I_0(t')$ and $I_1(t')$ at time t' to perform a measurement at t'. Also, $I_0(t)$ and $I_1(t)$ are important for the σ_x rotation since this one is achieved by relabelling the initial time t.

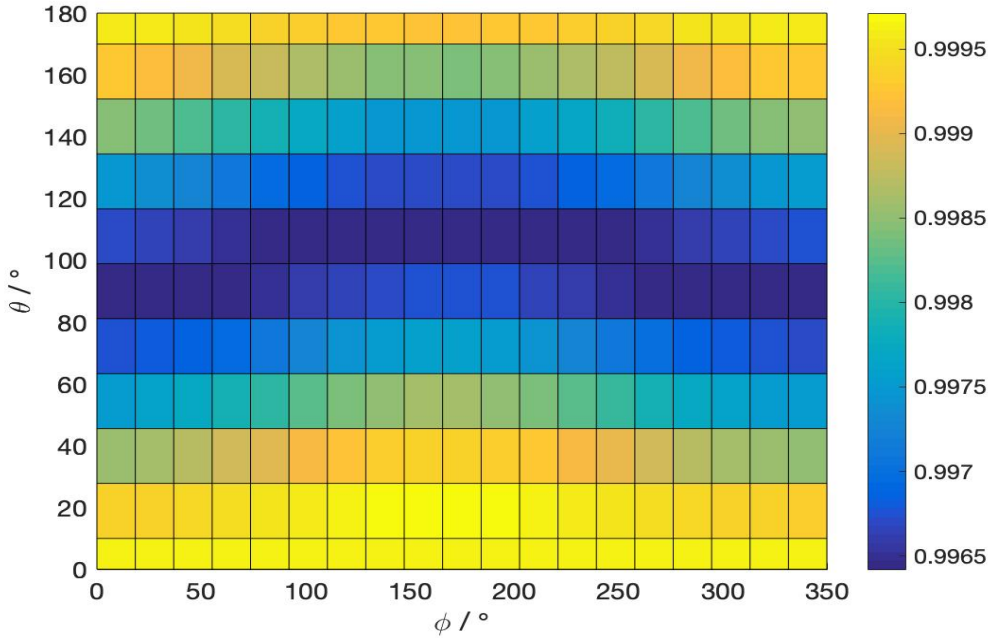

Fig. 6.15 Fidelity of an effective σ_z rotation for $\Delta\phi = 22^\circ$ vs various qubit states (in the range $\theta \in [0^\circ, 180^\circ]$, $\phi \in [0^\circ, 350^\circ]$) on the Bloch sphere with an oscillating electric field ($|E| = 0.002\,\text{eV}$, where $|E|$ is the amplitude of the potential energy difference across the film, $\omega = \omega_{res}$) applied perpendicularly to the TI thin film for T_{res}. θ and ϕ are the conventional polar and azimuthal angles used in spherical coordinate systems. T_{res} and ω_{res} are, resepectively, the natural period and frequency of a combined state $\alpha|\Phi_0\rangle + \beta|\Phi_1\rangle, \alpha \neq 0, \beta \neq 0$ that goes back to its original position on the Bloch sphere when there is no field applied. This figure shows that the effective σ_z is indeed universal and position-independent. The fidelity is extremely high, which is over 99.7%.

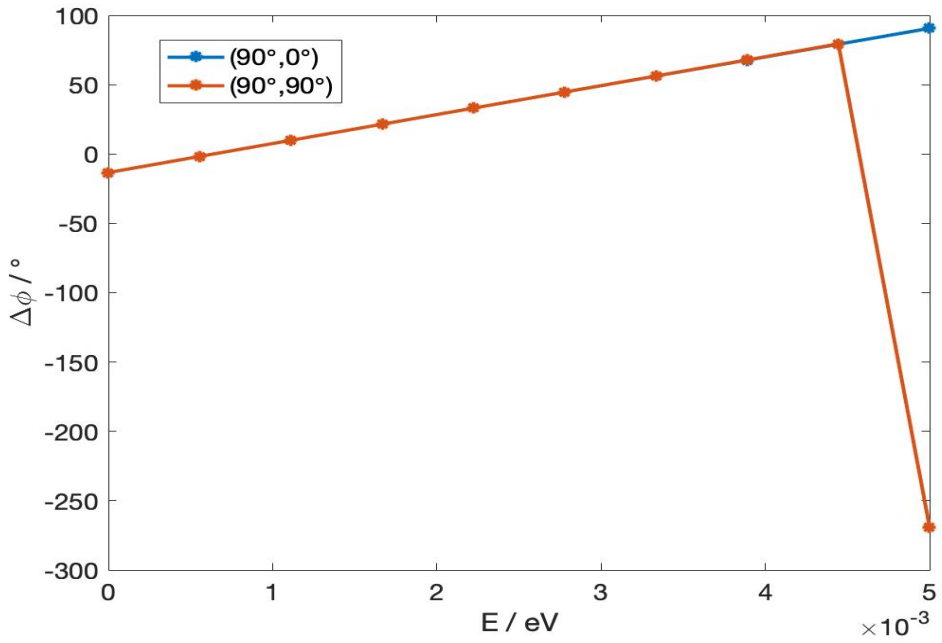

Fig. 6.16 $\Delta\phi$ in an effective σ_z rotation with an oscillating electric field at various amplitudes ($|E| = 0 - 0.005\,\text{eV}$, where $|E|$ is the amplitude of the potential energy difference across the film, $\omega = \omega_{res}$) applied perpendicularly to the TI thin film for T_{res} for a qubit starting at $\theta = 90^\circ$, $\phi = 0^\circ$ (blue) and $\theta = 90^\circ$, $\phi = 90^\circ$ (orange). θ and ϕ are the conventional polar and azimuthal angles used in spherical coordinate systems. T_{res} and ω_{res} are, respectively, the natural period and frequency of a combined state $\alpha\,|\Phi_0\rangle + \beta\,|\Phi_1\rangle\,, \alpha \neq 0, \beta \neq 0$ that goes back to its original position on the Bloch sphere when there is no field applied. The figure shows that $\Delta\phi$ in the effective σ_z rotation increases with the electric field amplitude and it has the same effect for the qubit at different positions. The blue point ($\phi = 90^\circ$) and orange point ($\phi = -270^\circ$) at $|E| = 0.005\,\text{eV}$ refers to the same position on the Bloch sphere.

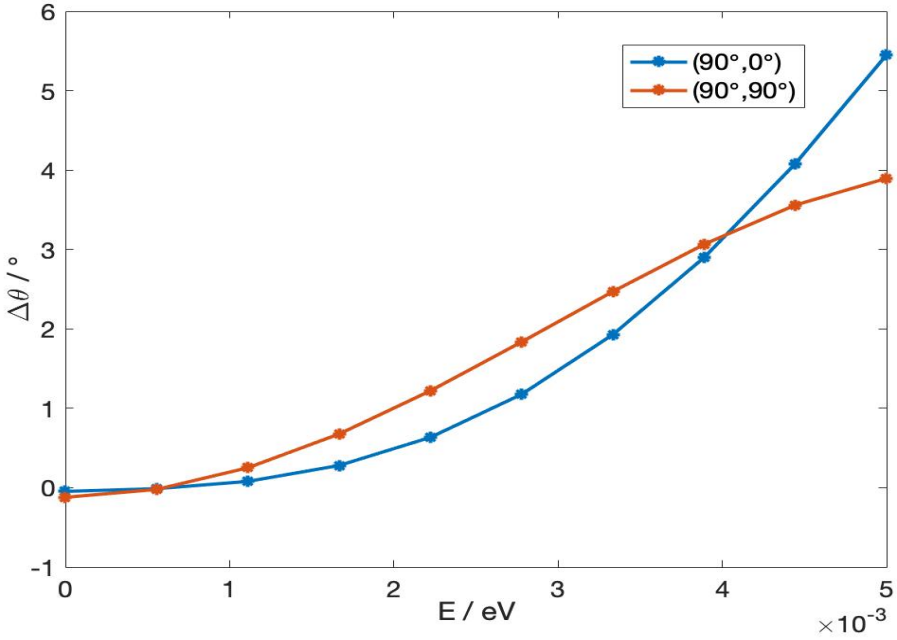

Fig. 6.17 $\Delta\theta$ in an effective σ_z rotation with an oscillating electric field at various amplitudes ($|E| = 0 - 0.005\,\text{eV}$, where $|E|$ is the amplitude of the potential energy difference across the film, $\omega = \omega_{res}$) applied perpendicularly to the TI thin film for T_{res} for a qubit starting at $\theta = 90°$, $\phi = 0°$ (blue) and $\theta = 90°$, $\phi = 90°$ (orange). θ and ϕ are the conventional polar and azimuthal angles used in spherical coordinate systems. T_{res} and ω_{res} are, respectively, the natural period and frequency of a combined state $\alpha\left|\Phi_0\right\rangle + \beta\left|\Phi_1\right\rangle, \alpha \neq 0, \beta \neq 0$ that goes back to its original position on the Bloch sphere when there is no field applied. The figure shows that $\Delta\theta$ in the effective σ_z rotation increases with the electric field amplitude; this reduces the fidelity of the effective σ_z rotation.

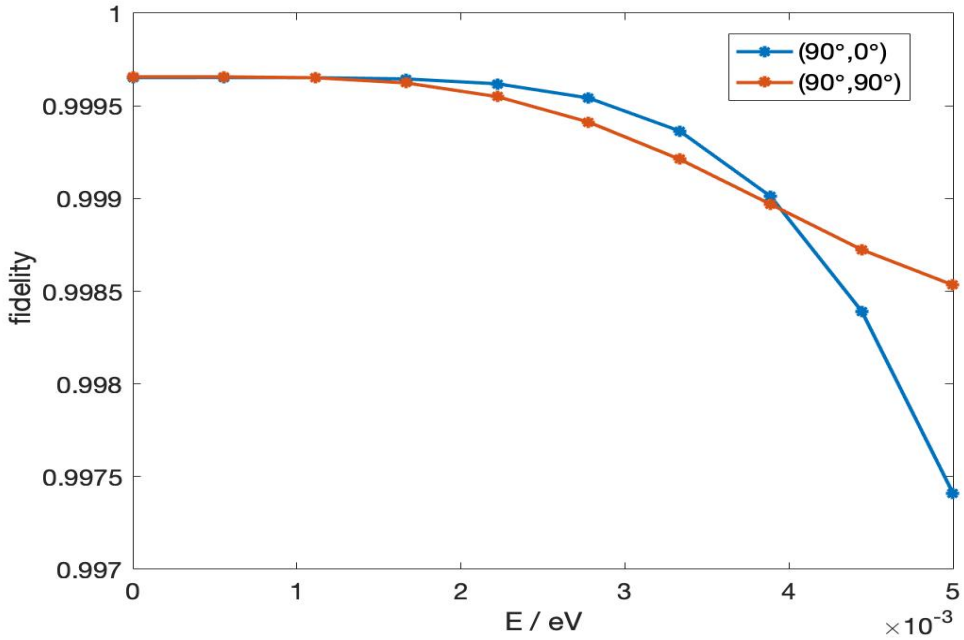

Fig. 6.18 Fidelity of an effective σ_z rotation with an oscillating electric field at various amplitudes ($|E| = 0 - 0.005\,\text{eV}$, where $|E|$ is the amplitude of the potential energy difference across the film, $\omega = \omega_{res}$) applied perpendicularly to the TI thin film for T_{res} for a qubit starting at $\theta = 90°$, $\phi = 0°$ (blue) and $\theta = 90°$, $\phi = 90°$ (orange). θ and ϕ are the conventional polar and azimuthal angles used in spherical coordinate systems. T_{res} and ω_{res} are, respectively, the natural period and frequency of a combined state $\alpha\,|\Phi_0\rangle + \beta\,|\Phi_1\rangle\,, \alpha \neq 0, \beta \neq 0$ that goes back to its original position on the Bloch sphere when there is no field applied. The figure shows that fidelity of the effective σ_z rotation decreases with the electric field amplitude.

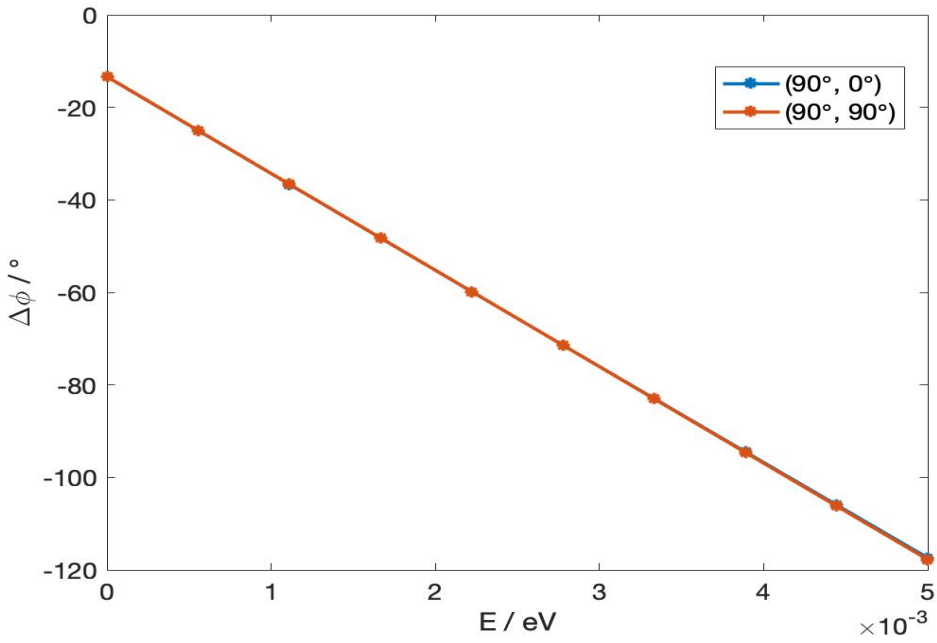

Fig. 6.19 $\Delta\phi$ in an effective σ_z rotation with an oscillating electric field at various amplitudes ($|E| = 0 - 0.005\,\text{eV}$, where $|E|$ is the amplitude of the potential energy difference across the film, $\omega = \omega_{res}$) applied perpendicularly to the TI thin film for T_{res} for a qubit starting at $\theta = 90^\circ$, $\phi = 0^\circ$ (blue) and $\theta = 90^\circ$, $\phi = 90^\circ$ (orange). The pulse is π radians out of phase with respect to the pulse used to obtain the figure Fig.6.16. θ and ϕ are the conventional polar and azimuthal angles used in spherical coordinate systems. T_{res} and ω_{res} are, respectively, the natural period and frequency of a combined state $\alpha\left|\Phi_0\right\rangle + \beta\left|\Phi_1\right\rangle, \alpha \neq 0, \beta \neq 0$ that goes back to its original position on the Bloch sphere when there is no field applied. The figure shows that $\Delta\phi$ in the effective σ_z rotation increases with the electric field amplitude and has the same effect for the qubit at different positions.

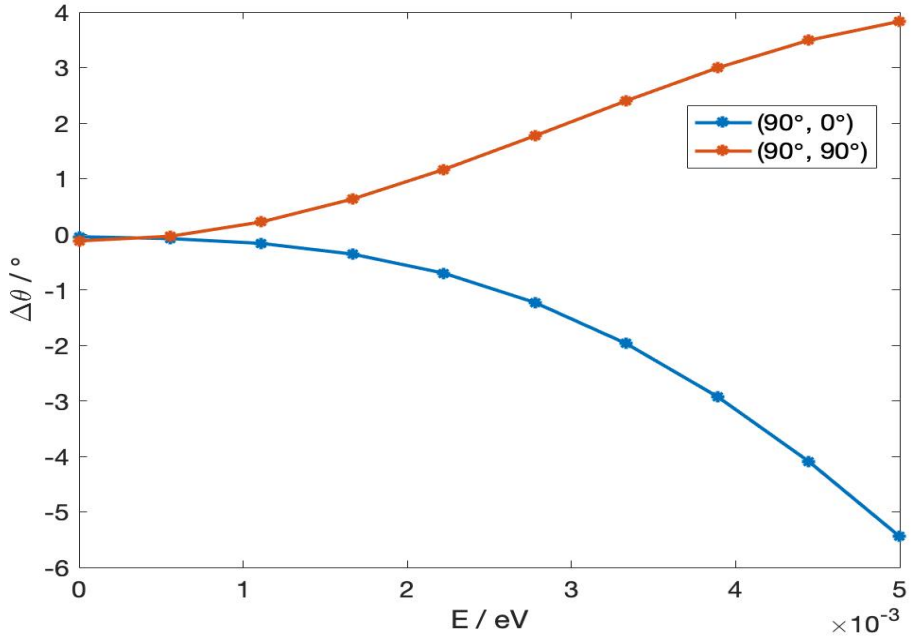

Fig. 6.20 $\Delta\theta$ in an effective σ_z rotation with an oscillating electric field at various amplitudes ($|E| = 0 - 0.005\,\text{eV}$, where $|E|$ is the amplitude of the potential energy difference across the film, $\omega = \omega_{res}$) applied perpendicularly to the TI thin film for T_{res} for qubit starting at $\theta = 90^\circ$, $\phi = 0^\circ$ (blue) and $\theta = 90^\circ$, $\phi = 90^\circ$ (orange). The pulse is π radians out of phase with respect to the pulse used to obtain the figure Fig.6.17. θ and ϕ are the conventional polar and azimuthal angles used in spherical coordinate systems. T_{res} and ω_{res} are, respectively, the natural period and frequency of a combined state $\alpha|\Phi_0\rangle + \beta|\Phi_1\rangle, \alpha \neq 0, \beta \neq 0$ that goes back to its original position on the Bloch sphere when there is no field applied. The figure shows that $\Delta\theta$ in the effective σ_z rotation increases with the electric field amplitude; this reduces the fidelity of the effective σ_z rotation.

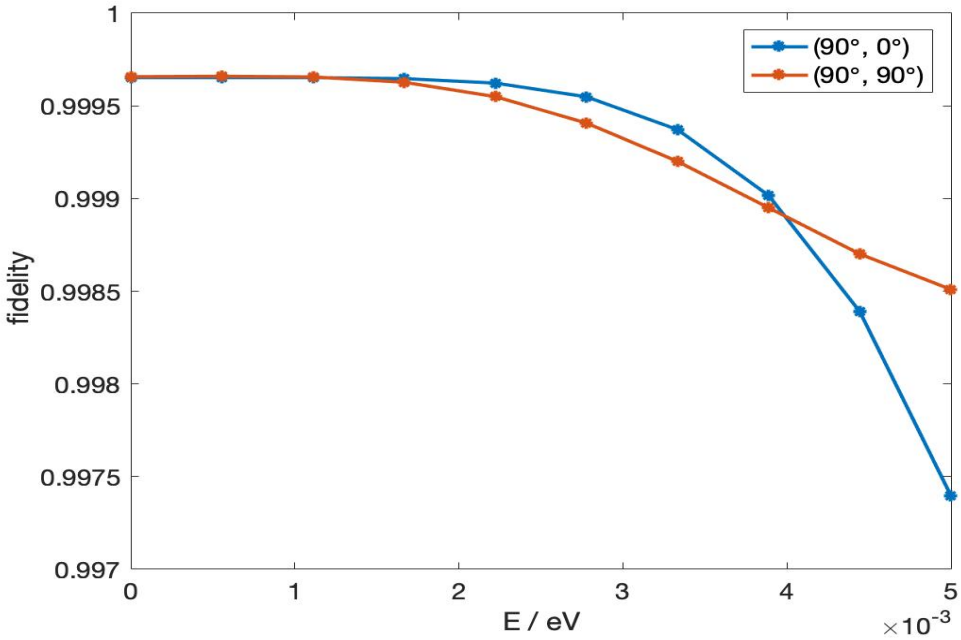

Fig. 6.21 Fidelity of an effective σ_z rotation with an oscillating electric field at various amplitudes ($|E| = 0 - 0.005\,\text{eV}$, where $|E|$ is the amplitude of the potential energy difference across the film, $\omega = \omega_{res}$) applied perpendicular to the TI thin film for T_{res} for a qubit starting at $\theta = 90^\circ$, $\phi = 0^\circ$ (blue) and $\theta = 90^\circ$, $\phi = 90^\circ$ (orange). θ and ϕ are the conventional polar and azimuthal angles used in spherical coordinate systems. The pulse is π radians out of phase with respect to the pulse used to obtain the figure Fig.6.18. T_{res} and ω_{res} are, respectively, the natural period and frequency of a combined state $\alpha |\Phi_0\rangle + \beta |\Phi_1\rangle, \alpha \neq 0, \beta \neq 0$ that goes back to its original position on the Bloch sphere when there is no field applied. The figure shows that the fidelity of the effective σ_z rotation decreases with the electric field amplitude.

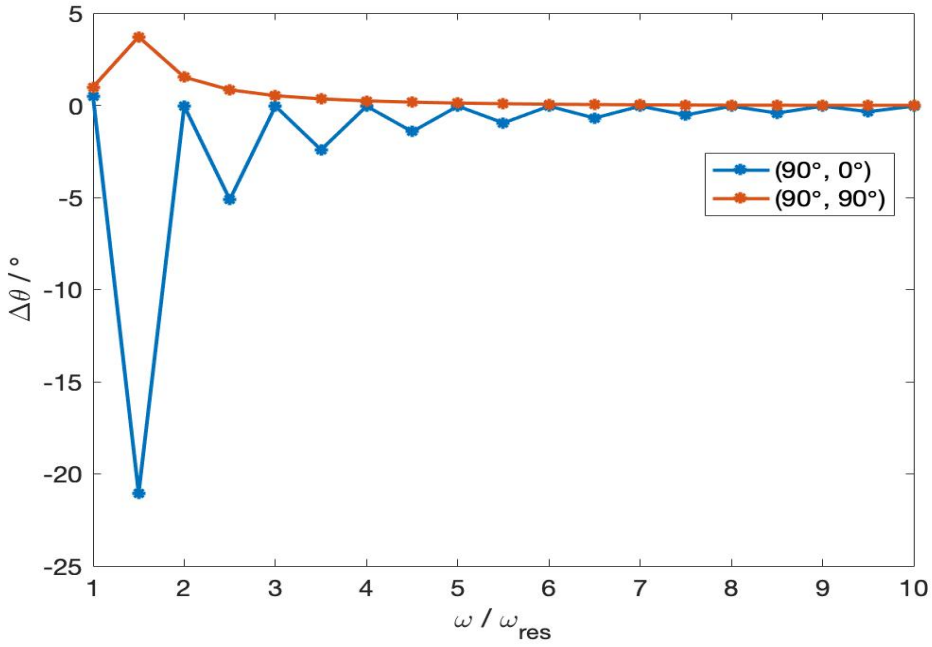

Fig. 6.22 $\Delta\theta$ in a single qubit rotation with an oscillating electric field at various frequencies (ω_{res} to $10\omega_{res}$, $|E| = 0.002\,\text{eV}$, where $|E|$ is the amplitude of the potential energy difference across the film) applied perpendicularly to the TI thin film for T_{res} for qubit starting at $\theta = 90°$, $\phi = 0°$ (blue) and $\theta = 90°$, $\phi = 90°$ (orange). θ and ϕ are the conventional polar and azimuthal angles used in spherical coordinate systems. T_{res} and ω_{res} are, respectively, the natural period and frequency of a combined state $\alpha\,|\Phi_0\rangle + \beta\,|\Phi_1\rangle, \alpha \neq 0, \beta \neq 0$ that goes back to its original position on the Bloch sphere when there is no field applied. The figure shows that $\Delta\theta$ in the single qubit rotation decreases in an oscillating style with the electric field frequency.

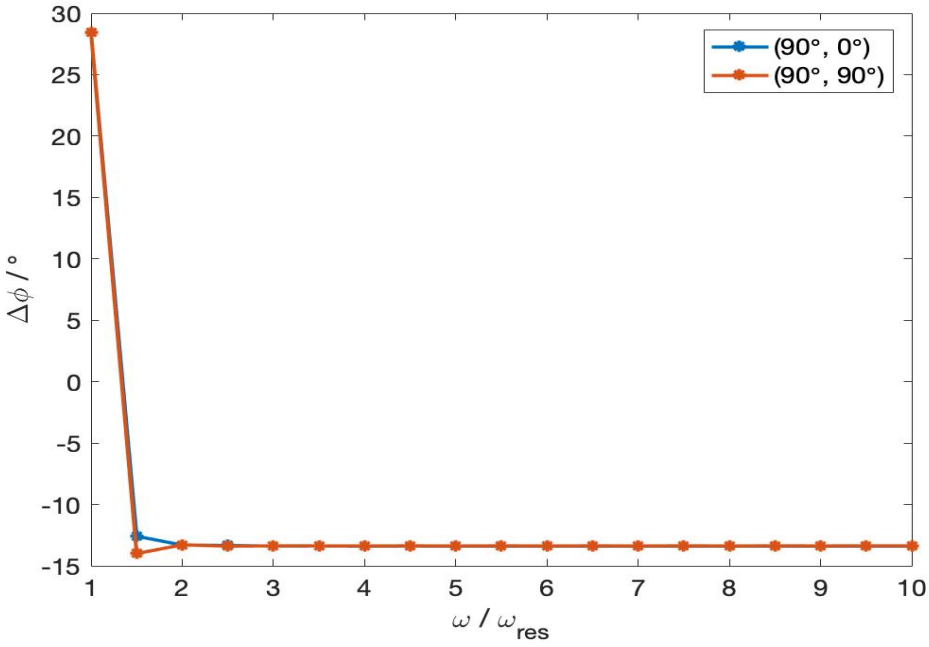

Fig. 6.23 $\Delta\phi$ in a single qubit rotation with an oscillating electric field at various frequencies (ω_{res} to $10\omega_{res}$,$|E| = 0.002\,\text{eV}$, where $|E|$ is the amplitude of the potential energy difference across the film) applied perpendicularly to the TI thin film for T_{res} for a qubit starting at $\theta = 90^\circ$, $\phi = 0^\circ$ (blue) and $\theta = 90^\circ$, $\phi = 90^\circ$ (orange). θ and ϕ are the conventional polar and azimuthal angles used in spherical coordinate systems. T_{res} and ω_{res} are, respectively, the natural period and frequency of a combined state $\alpha\left|\Phi_0\right\rangle + \beta\left|\Phi_1\right\rangle, \alpha \neq 0, \beta \neq 0$ that goes back to its original position on the Bloch sphere when there is no field applied. The figure shows that $\Delta\phi$ in the single qubit rotation decreases dramatically when the field frequency is larger than ω_{res}.

6.2.5 Discussion

In this section we have studied a dynamic charge qubit that can be defined in an ultra-thin TI film under a periodic electric field.The experimental setup, the two-qubit gate and decoherence mechanisms are similar to those of the charge qubit discussed in Ch. 4. This qubit is different from a traditional charge qubit since the Bloch sphere is rotating all the time. This rotation matches the free rotation of the system and gives an advantage to the Floquet qubit. When performing an experiment, we can pause the experiment at any time and resume it at a later time. We can do this by recording the time as t_1, turn on the driving field and resume the operation at a later time $t_1 + nT$, where T is the period of a free rotation and $n \in Z$. Because the Bloch sphere is rotating, pausing the operation and turning on the driving field makes the qubit state rotate with the Bloch sphere. In the rotating frame, the qubit is stationary. At a later time $t_1 + nT$, the qubit is back to the place where it was on the static Bloch sphere at $t = 0$; this is convenient for experimental situations. The next question is the accompanying magnetic field. We know that when a current is passing through an area, a magnetic field is generated in the surrounding area according to Ampère's circuital law. Because the TI film is bulk insulating and we are only interested in the surface states, we can view the model as a magnetic field around a wire with AC current. The resultant magnetic field is:

$$\bigtriangledown \times \mathbf{B} = \mu_0 \varepsilon_0 \frac{\partial \mathbf{E}}{\partial t}, \tag{6.17}$$

where μ_0 and ε_0 are the vacuum permeability and vacuum permittivity respectively, and $\mu_0 \varepsilon_0 = \frac{1}{c^2}$. For an electric field $\mathbf{E}\cos(\omega t)$ in the z direction, the resultant magnetic field is proportional to the strength of the electric field: $\mathbf{B} \propto \frac{1}{c^2} E\omega$. Therefore, we need to use a small field and a frequency to avoid the magnetic field becoming too high. Since the magnetic is located on the xy plane, it does not break the overall TR symmetry so a small magnetic field would not affect the resultant qubit states.

6.3 Floquet spin qubit

6.3.1 Model Hamiltonian

The model Hamiltonian of a TI thin film with a periodically time-varying magnetic field is constructed using the Floquet method described in Ch. 2. The time dependent Schrödinger

equation of the system is :

$$i\hbar\frac{d}{dt}\left|\Phi\right\rangle = H'\left|\Phi\right\rangle, \tag{6.18}$$

$$H' = H_0(\mathbf{k}+\frac{e\mathbf{A}(t)}{\hbar}) + H_{ze}(\mathbf{B}(t)). \tag{6.19}$$

$\mathbf{A}(t)$ and $\mathbf{B}(t)$ are the vector potentials in the z direction and magnetic field in the y direction, respectively. H_0 is the original tight-binding model Hamiltonian of a topological insulator in Ch. 2. H' does not commute with k_z and we replace k_z with $-\frac{\partial}{\partial z}$. Since we are dealing with a Hamiltonian periodic in both space and time, we can apply Floquet-Bloch theory to solve it in the composed Hilbert space $H_{temp}\otimes H_0(z)$ like a stationary Hamiltonian. By applying the Floquet-Bloch ansatz: $\left|\Phi_{\alpha,\mathbf{k}}(\mathbf{r},z,t)\right\rangle = e^{i\mathbf{kr}-i\varepsilon_{\alpha,\mathbf{k}}t/\hbar}\left|u_{\alpha,\mathbf{k}}(\mathbf{r},t)\right\rangle\phi(z)$, where α is the band index and $\mathbf{k}$ is the wave vector $\mathbf{r}=(x,y)$, we get:

$$H_F\left|u_{\alpha,\mathbf{k}}\right\rangle = \varepsilon_{\alpha,\mathbf{k}}\left|u_{\alpha,\mathbf{k}}\right\rangle, \tag{6.20}$$

$$H_F = H' - i\hbar\frac{\partial}{\partial t}. \tag{6.21}$$

Then we use the Floquet matrix method (Ch. 3) to solve the Hamiltonian H_F. The numerical matrix is:

$n=-2$	$n=-1$	$n=0$	$n=+1$	$n=2$	
$\mathbf{H_0}-2\hbar\omega$	$\mathbf{H_{+1}}$	0	$\vdots$	$\vdots$	$n=-2$
$\mathbf{H_{-1}}$	$\mathbf{H_0}-\hbar\omega$	$\mathbf{H_{+1}}$	0	$\vdots$	$n=-1$
0	$\mathbf{H_{-1}}$	$\mathbf{H_0}$	$\mathbf{H_{+1}}$	$\vdots$	$n=0$
$\vdots$	0	$\mathbf{H_{-1}}$	$\mathbf{H_0}+\hbar\omega$	$\mathbf{H_{+1}}$	$n=+1$

Here H_0 and $H_{\pm1}$ are sub-matrices representing the interactions between the Fourier components in temporal space H_{temp}, with $\mathbf{H_0} = \left\langle\vec{\phi_{n_{z2},n}}\middle|H\middle|\vec{\phi_{n_{z1},n}}\right\rangle$ and $\mathbf{H_{\pm1}} = \left\langle\vec{\phi_{n_{z2},m}}\middle|H(\frac{eBz1}{\hbar})+H_{ze}\middle|\vec{\phi_{n_{z1},n}}\right\rangle$. H contains all the spatial information and it is the numerical matrix of H_0 (original time-independent tight-binding Hamiltonian) and $\mathbf{H_{\pm1}}$ contains terms that vary in time. The Peierls substitution stands for the orbit effect of the magnetic field and H_{ze} is the Zeeman Hamiltonian. The time-dependent interaction with the field is included in the off-diagonal blocks and the time evolution of the Fourier states are included as $n\hbar\omega$ on the central diagonal blocks of the numerical matrix 6.3.1. The time dependent Floquet solution and its corresponding energy are:

$$\left|\Phi_{\mathbf{k}}(z,t)\right\rangle = e^{-i\varepsilon_{n,\alpha}t/\hbar}u_{n,\alpha,\mathbf{k}}(z,t), \tag{6.22}$$

$$\varepsilon_{n,\alpha} = \varepsilon_{\alpha} + n\hbar\omega. \tag{6.23}$$

6.3.2 Ultra-thin TI under a periodic magnetic field

Similar to the case when a periodic electric field is applied, the Floquet Hamiltonian produces quasienergy bands that are replicas of bands in a stationary Hamiltonian. When $\hbar\omega < \Delta\varepsilon$, where $\Delta\varepsilon$ is the energy difference between bands in a static system, the Floquet modes $\varepsilon_{\alpha,n}$ are grouped together (Fig. 6.24 and Fig. 6.25). If $\hbar\omega \gg \Delta\varepsilon$, the Floquet modes are further apart and we can distinguish the shape of energy bands of the original system. We can recognise the gapped Dirac cone in Fig. 6.27 and Fig. 6.26. In this thesis, we are more interested in the region where $\hbar\omega \approx \Delta\varepsilon$, with $\Delta\varepsilon = |\varepsilon_{S1(S2)} - \varepsilon_{S3(S4)}|$, specifically ($|S1\rangle$ to $|S4\rangle$ are defined in Sec. 4.3). $|\varepsilon_{S1(S2)} - \varepsilon_{S3(S4)}|$ is the energy difference of a pair of surface states from the electron band and hole band with opposite spins (see Ch. 5). From here, we will study how the surface states change under a periodic magnetic field. When we apply a periodic magnetic field to the system we will obtain a group of Floquet solutions instead of the stationary states. Each time-dependent Floquet solution contains a few Floquet states (modes) with a quantised quasienergy difference of $n\hbar\omega$.

The Floquet states will respond to the periodic magnetic field as in the case of a periodic electric field. This response depends on the frequency ω and amplitude $|B|$ (Fig. 6.28). We have chosen a pair of Floquet states $\Phi_{0,S1}$ and $\Phi_{-1,S3}$ as our example states to show how these states change with respect to ω and $|B|$.

At the region where $\omega \ll \omega_{res}$, the states behave rather like two eigenstates of a TI under a magnetic field. As $|B| \to 0$, the Floquet states recover the shape of the individual states found in a static TI without any field.

In the region where $\omega \approx \omega_{res}$, when there is no interaction ($|B| = 0$), the states are exactly like the bare states in a static system with energies ε_{S1} and $\varepsilon_{S3} - \hbar\omega$. When the interaction is switched on, the state $\Phi_{0,S1}$ interacts with $\Phi_{-1,S3}$ at $\hbar\omega \approx \varepsilon_{n,S1} - \varepsilon_{n-1,S3}$. This interaction produces a pair of combined states at the same energy, which is different from the case discussed in the previous section of a Floquet charge qubit. When the quasi energies of two Floquet states equal each other in the case of an electric-field dressing TI, the combined states will split into two different energy levels and form an avoided crossing. In the case of a magnetic-field dressing TI, the combined Floquet states have equal quasi energies because they have different spins. $\Phi_{0,S1}(\Phi_{-1,S3})$ also interacts with $\Phi_{0,S2}(\Phi_{-1,S4})$ because of the coupling induced by the magnetic field. This interaction tends to split the degenerate Floquet states $\Phi_{0,S1}(\Phi_{-1,S3})$ and $\Phi_{0,S2}(\Phi_{-1,S4})$ and form a pair of states with their spins aligned in the y direction. When the interaction $|B|$ is small, the coupling between $\Phi_{0,S1}$ and $\Phi_{0,S2}$ is weak and the interaction between $\Phi_{0,S1}$ and $\Phi_{-1,S3}$ is more significant. The resultant states

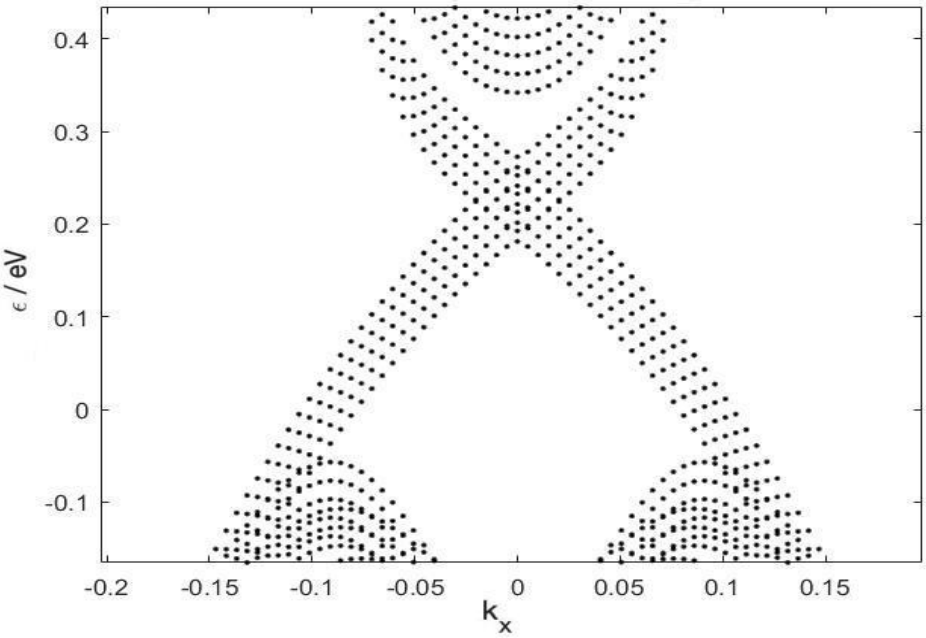

Fig. 6.24 Floquet band structure of a 5 QL TI thin film with an in-plane oscillating magnetic field at $|B| = 1\,\mathrm{T}$ and $\omega < \omega_{res}$ along the k_x axis. The Floquet bands are replicas of the bare TI bands without a field. ω_{res} is the natural frequency of a combined state $\alpha\,|\Phi_0\rangle + \beta\,|\Phi_1\rangle\,, \alpha \neq 0, \beta \neq 0$ that goes back to its original position on the Bloch sphere when there is no field applied.

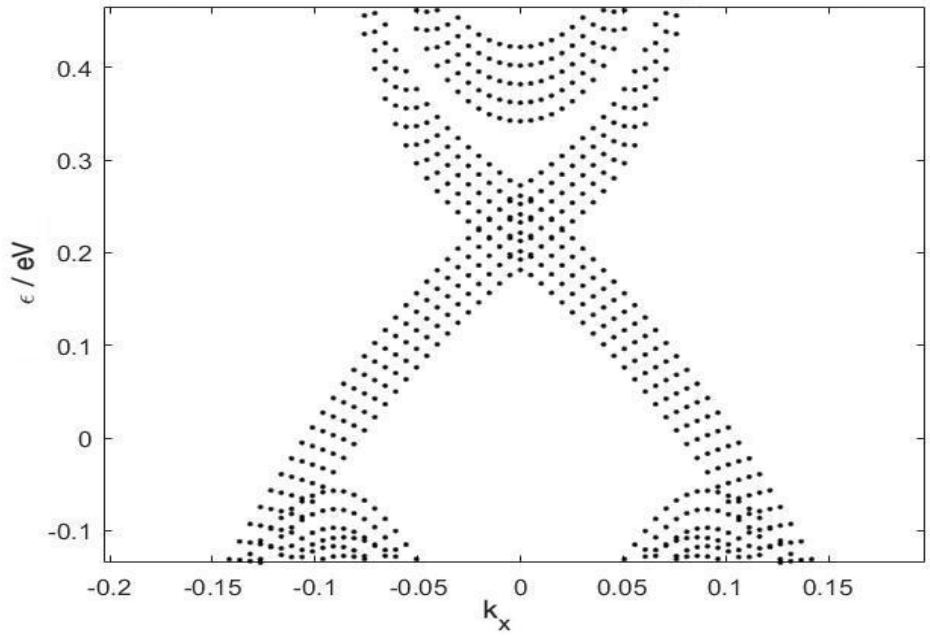

Fig. 6.25 Floquet band structure of a 5 QL TI thin film with an in-plane oscillating magnetic field at $|B| = 1\,\mathrm{T}$ and $\omega < \omega_{res}$ along the k_y axis. The Floquet bands are replicas of the bare TI bands without a field. ω_{res} is the natural frequency of a combined state $\alpha\,|\Phi_0\rangle + \beta\,|\Phi_1\rangle\,, \alpha \neq 0, \beta \neq 0$ that goes back to its original position on the Bloch sphere when there is no field applied.

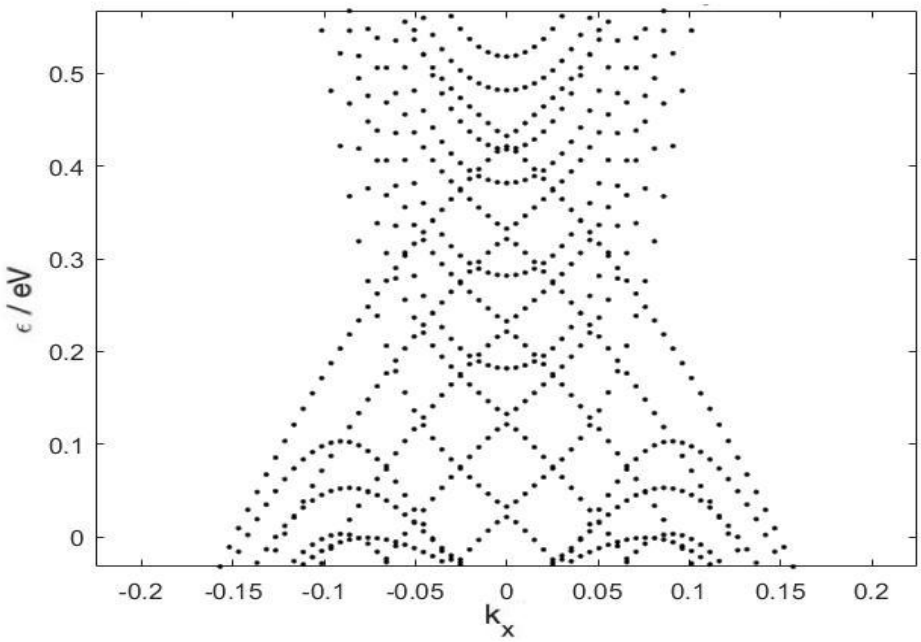

Fig. 6.26 Floquet band structure of a 5 QL TI thin film with an in-plane oscillating magnetic field at $|B| = 1\,\mathrm{T}$ and $\omega \gg \omega_{res}$ along the k_x axis. The Floquet bands are replicas of the bare TI bands without a field. ω_{res} is the natural frequency of a combined state $\alpha\,|\Phi_0\rangle + \beta\,|\Phi_1\rangle\,, \alpha \neq 0, \beta \neq 0$ that goes back to its original position on the Bloch sphere when there is no field applied.

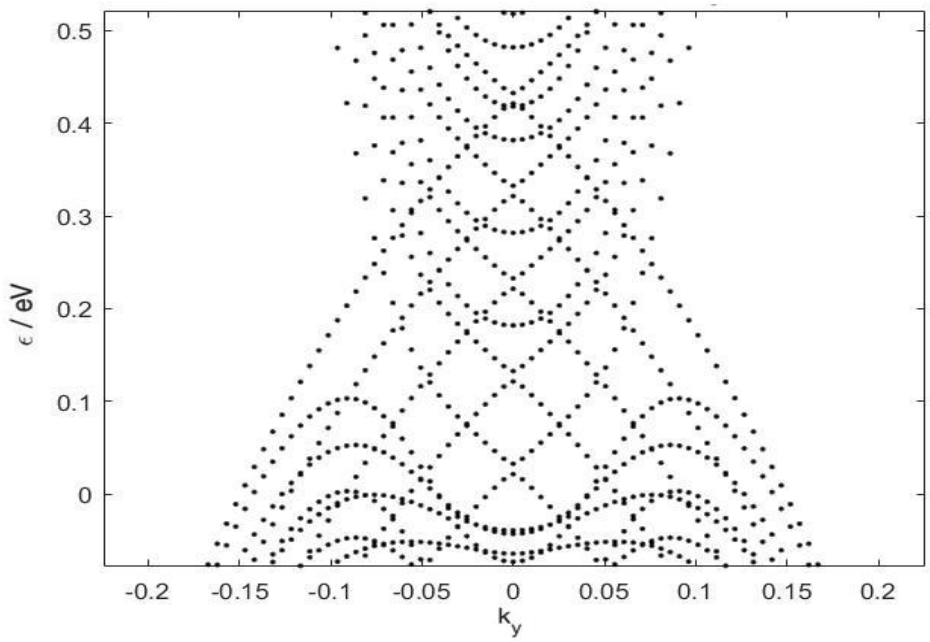

Fig. 6.27 Floquet band structure of a 5 QL TI thin film with an in-plane oscillating magnetic field at $|B| = 1\,\mathrm{T}$ and $\omega \gg \omega_{res}$ along the k_x axis. The Floquet bands are replicas of the bare TI bands without a field. ω_{res} is the natural frequency of a combined state $\alpha\,|\Phi_0\rangle + \beta\,|\Phi_1\rangle\,, \alpha \neq 0, \beta \neq 0$ that goes back to its original position on the Bloch sphere when there is no field applied.

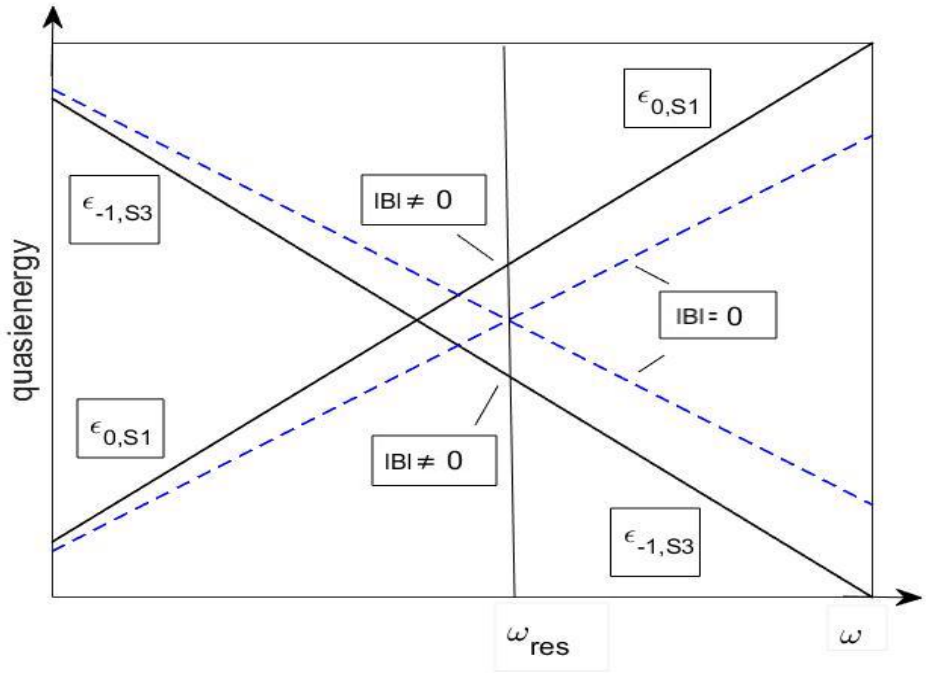

Fig. 6.28 A diagram illustrates the trend of the quasienergies $\varepsilon_{-1,S3}$ and $\varepsilon_{0,S1}$ of Floquet states $\Phi_{-1,S3}$ and $\Phi_{0,S1}$ vs frequency ω for interaction amplitudes $|B| = 0$ and $|B| \neq 0$. When the frequency $\omega \to 0$ and $\omega \gg \omega_{res}$, the Floquet energies $\varepsilon_{-1,S3}$ and $\varepsilon_{0,S1}$ are closer to those energy states obtained without applying a field. When the frequency $\omega \to \omega_{res}$, the Floquet energies of the two states get closer and behave differently in the cases of interaction amplitudes $|B| = 0$ and $|B| \neq 0$. In the case of $|B| = 0$ they will intersect with each other at $\omega = \omega_{res}$. However, if $|E| \neq 0$, they will intersect with each other at $\omega < \omega_{res}$.

are like the combined states $\Phi_{S1} \pm \Phi_{S3}$ found in a static TI system without any field. When $|B|$ is increased, the coupling between the states $\Phi_{0,S1}$ and $\Phi_{0,S2}$ increases and eventually dominates compared to the interaction between $\Phi_{0,S1}$ and $\Phi_{-1,S3}$. The resultant states will be spilt into a pair of states with their spins aligned in the y direction ($s_y = \pm\frac{1}{2}$).

In the region where $\omega \gg \omega_{res}$, the states $\Phi_{0,S1}$ and $\Phi_{-1,S3}$ are far apart; therefore, the states cannot interact with each other and there is no coupling between the two states. The state $\Phi_{0,S1}$ would only couple with the state $\Phi_{0,S2}$ and the coupling increases with $|B|$. At large $|B|$ (e.g. $|B| = 1\,\mathrm{T}$), the states are similar to the eigenstates under a static magnetic field with spin component $s_y = \pm\frac{1}{2}$.

6.3.3 Floquet spin qubit definition

We know from the last subsection that, under a periodic magnetic field, the states $|S1\rangle$ and $|S3\rangle$ will form n Floquet modes with energies $\varepsilon_{S1} + n\hbar\omega$ and $\varepsilon_{S3} + n\hbar\omega$, where n depends on the number of Fourier components used in the calculation. All of these Floquet modes refer to the same physical state. At the resonant frequency ω_{res}, $\Phi_{n,S1}$ and $\phi_{n-1,S3}$ will couple to form $n-1$ pairs of combined Floquet states. With a small magnetic field, these states are like the combined states $|S1\rangle \pm |S3\rangle$ in a bare system without any field. These states can be used for quantum computing since they are on the same Bloch sphere as the spin qubit states studied in Ch. 5. Therefore, we define our Floquet spin qubit states $|\Phi_0\rangle$ and $|\Phi_1\rangle$ as:

$$\Phi_0(t) = e^{i\varepsilon_{0,S1}t/\hbar}\Phi_{0,S1}, \tag{6.24}$$

$$\Phi_1(t) = e^{i\varepsilon_{-1,S3}t/\hbar}\Phi_{-1,S3}. \tag{6.25}$$

These states are dynamic with their phase varying in time. The time evolution of these states is the same as the one for the combined static states $S1 \pm S3$. The electron density is constant over time (Fig. 6.29 and Fig. 6.30). In this chapter, we have chosen a pair of Floquet states in 5 QL TI under a periodic magnetic field along the y direction with $\omega = 0.0113$ (natural units =n.u) and $|B| = 0.0011\,\mathrm{T}$.

6.3.4 Single-qubit study

The initialisation of the qubit state can be performed by controlling the Fermi level within or below the gap, then by applying an in-plane periodic magnetic field. As we tune the frequency to $\omega = \omega_{res}$ and increase the amplitude gradually, the qubit will transit from an eigenstate on the surface band of a TI to a Floquet state in the field dressing TI. The spin current measured on the top and bottom surfaces will be equal and there is a 50% probability

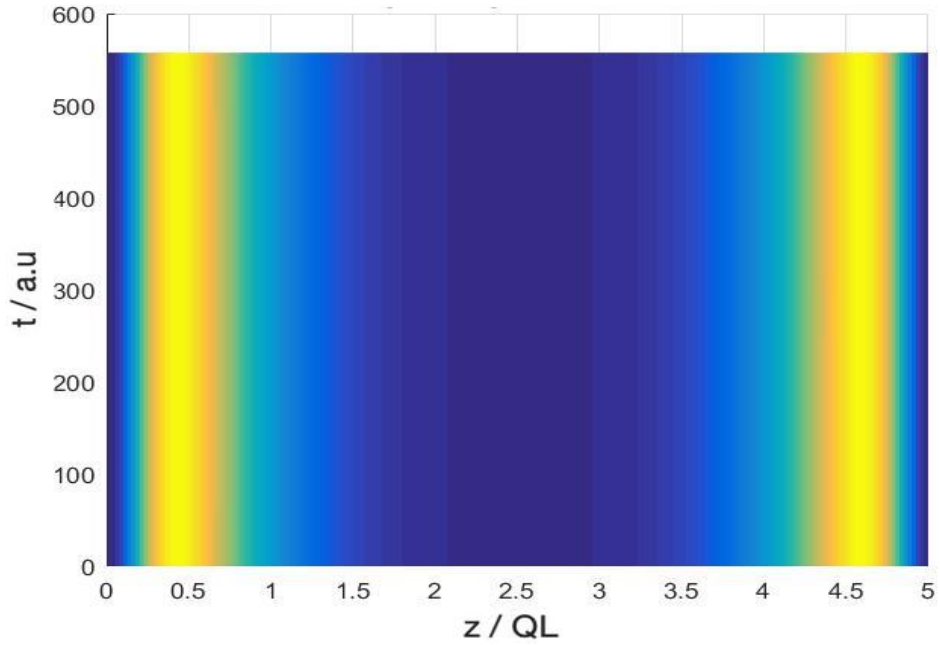

Fig. 6.29 Time evolution of $u_0(t)$ in the TI thin film for T_{res}. T_{res} is the natural period of a combined state $\alpha|\Phi_0\rangle + \beta|\Phi_1\rangle, \alpha \neq 0, \beta \neq 0$ that goes back to its original position on the Bloch sphere when there is no field applied.The vertical axis is time (in picoseconds) and the horizontal axis is depth in the TI thin film. The colour indicates the electron density. The yellow colour indicates that the electron is located on the bottom surface of the thin film at $t = 0$. The figure shows that the electron density of the state is constant in time. The spin of $u_0(t)$ rotates in the plane along with the electron motion's (xy plane) and oppose to $u_1(t)$.

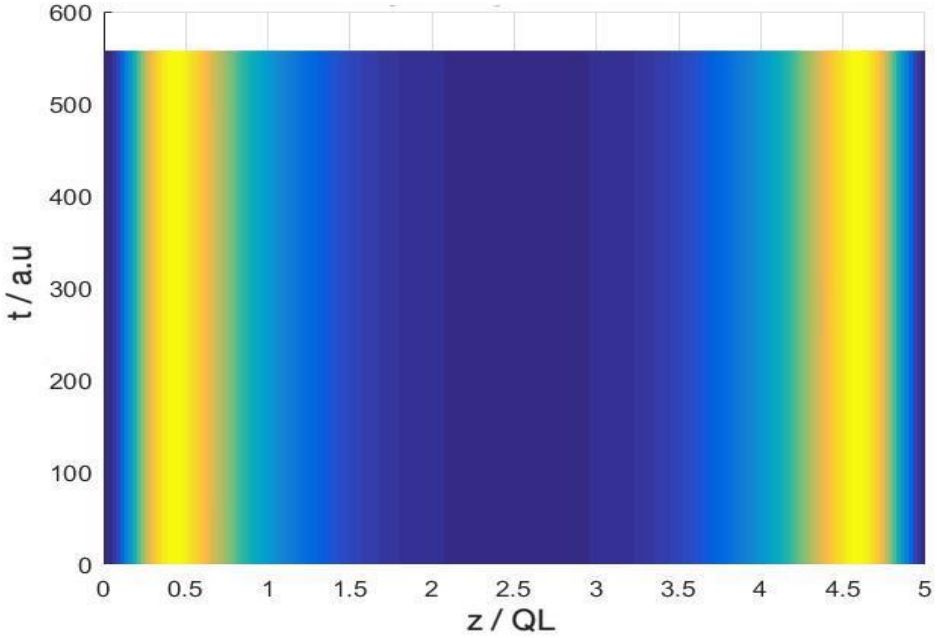

Fig. 6.30 Time evolution of $u_1(t)$ in the TI thin film for T_{res}. T_{res} is the natural period of a combined state $\alpha|\Phi_0\rangle + \beta|\Phi_1\rangle, \alpha \neq 0, \beta \neq 0$ that goes back to its original position on the Bloch sphere when there is no field applied.The vertical axis is time (in picoseconds) and the horizontal axis is depth in the TI thin film. The colour indicates the electron density. The yellow colour indicates that the electron is located on the bottom surface of the thin film at $t = 0$. The figure shows that the electron density of the state is constant in time. The spin of $u_1(t)$ rotates in the plane along with the electron motions (the xy plane) and oppose to $u_0(t)$.

to measure $s_z = \frac{1}{2}$ and $s_z = -\frac{1}{2}$. At this point we prepare the qubit in a state shown in Fig. 6.29 or in Fig. 6.30; this qubit state can be used for the Floquet-spin-qubit study.

Then we shall look at how to manipulate the qubit on the dynamic Bloch sphere. As in the case of a Floquet charge qubit, the Flqouet-spin-qubit states are combined states of the eigenstates on the electron and hole bands in a static TI. They evolve in time (Eq. 6.24 and Eq. 6.25) in the same way as a combined state. This natural time evolution is equivalent to a σ_x rotation in the static frame at $t = 0$. Because the Bloch sphere is rotating along the x axis, we can relabel the states to achieve the σ_x rotation like the case of a Floquet charge qubit and $\Delta\theta \propto \omega_{res}t$.

Now we shall show how a magnetic field pulse affects the qubit and how to perform a σ_z or σ_y rotation with it. We find that if we apply a static field to the Floquet qubit, the path is complicated and position-dependent. In general, a linear pulse cannot produce an effective $\Delta\phi$, but it produces an effective $\Delta\theta$. However, $\Delta\theta$ is small even for strong magnetic fields (Fig. 6.31). We note here that the Bloch spheres in the thesis are plotted at 90% size to clarify the single-qubit rotation diagrams. We know that the Floquet spin qubit is a combined state of the spin qubit states Φ_0 and Φ_1 studied in Ch. 5. Therefore, they are on the same Bloch sphere. The only difference is that the Floquet Bloch sphere is rotating rather than being static. In the case of a spin qubit, we can drive the qubit to do an effective σ_y rotation by applying a cosine pulse at $\omega = \omega_{res}$ and find that this also works for the Floquet spin qubit. We also find that a cosine pulse at the same frequency as the driving field can produce an effective position-independent σ_z rotation at nT_{res}, where T_{res} is the period of the natural rotation of the Bloch sphere. The path is very similar to the σ_z rotation for a Floquet charge qubit studied in the previous section 6.2 (Fig. 6.32). The fidelity of this rotation is extremely high (Fig. 6.35) and is a discrete effective σ_z rotation. Different angles of the rotation can be obtained by tuning the amplitude of the magnetic field $|B|$ (Fig. 6.34). Since $\Delta\phi$ increases linearly with $|B|$, then it is convenient to deduce and find the desired angle by trying a few different amplitudes. We need to notice that the fidelity decreases with $|B|$ (Fig.6.33). However, it is still good enough to cover most angles in the case of our Floquet qubit in a 5 QL TI. By applying the cosine wave with a phase difference of π radians to the driving field, we can achieve rotations of different angles as well (see Fig. 6.34) with $\Delta\phi_\pi = -\Delta\phi_0$. If we decrease (or increase) the frequency of the magnetic field, we are unable to obtain effective σ_z rotations. From Fig. 6.36 and Fig. 6.37 we can see that at high frequencies the magnetic field cannot rotate the qubit effectively. On the other hand, at lower frequencies $\Delta\phi$ can change to some degree. However, the deviation in θ is larger at frequencies lower than ω_{res}. The closer the frequency is to ω_{res}, the better the fidelity of the effective σ_z is.

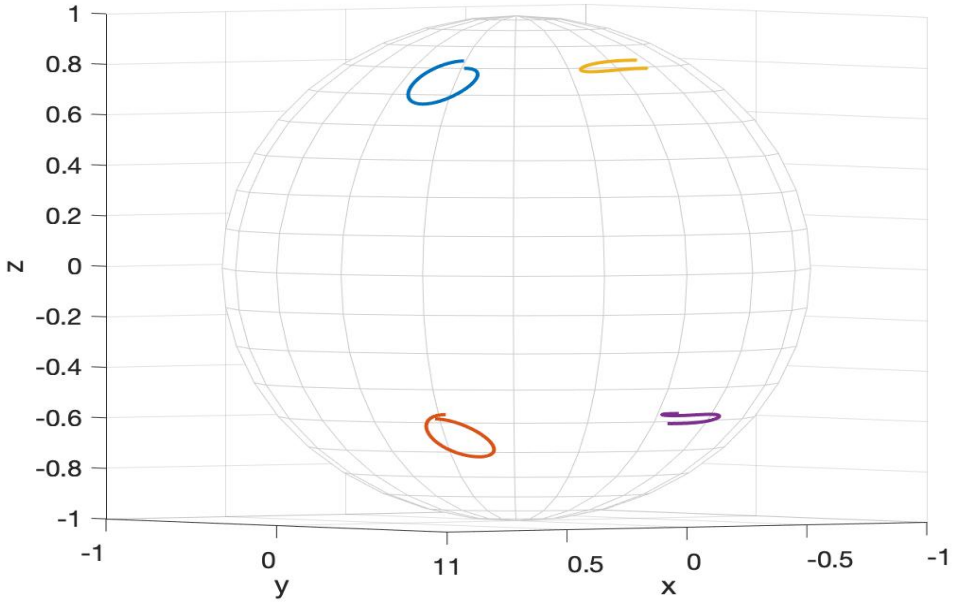

Fig. 6.31 Traces of a single qubit rotation with an in-plane static magnetic field ($B = 1\,\mathrm{T}$) applied to the TI thin film for a whole period T_{res} on the Bloch sphere for a qubit starting at different positions. T_{res} is the natural period of a combined state $\alpha\left|\Phi_0\right\rangle + \beta\left|\Phi_1\right\rangle, \alpha \neq 0, \beta \neq 0$ that goes back to its original position on the Bloch sphere when there is no field applied. The traces are viewed in a static frame, with $u_0(t=0)$ ($u_1(t=0)$) being the north (south) pole of the Bloch sphere. Note that the Bloch sphere is drawn at 90% size to clarify the diagram.

Therefore, we conclude that the frequency of the operation pulse should be the same as the driving field for a high fidelity effective σ_z rotation on the Bloch sphere.

The measurement method of this Floquet spin qubit is similar to the method used for a static spin qubit in Ch. 5. The difference is that the spin current density needs to be measured for a whole period since the Floquet qubit is changing in time. Therefore, by measuring the spin current over a period, we have obtained the information of the qubit states $\left|\Phi_0\right\rangle$ and $\left|\Phi_1\right\rangle$ at every instance. This will allow us to read out the qubit at any time. This continuous measurement is also important for the σ_x rotation since we can define the time $t = t_1$ as the initial time for a state rotated by $\omega_{res} t_1$ along the x axis.

6.3.5 Discussion

In this section we have studied a Floquet spin qubit in an ultra-thin TI under an in-plane periodic magnetic field. The experimental setup, the two-qubit gate and decoherence mech-

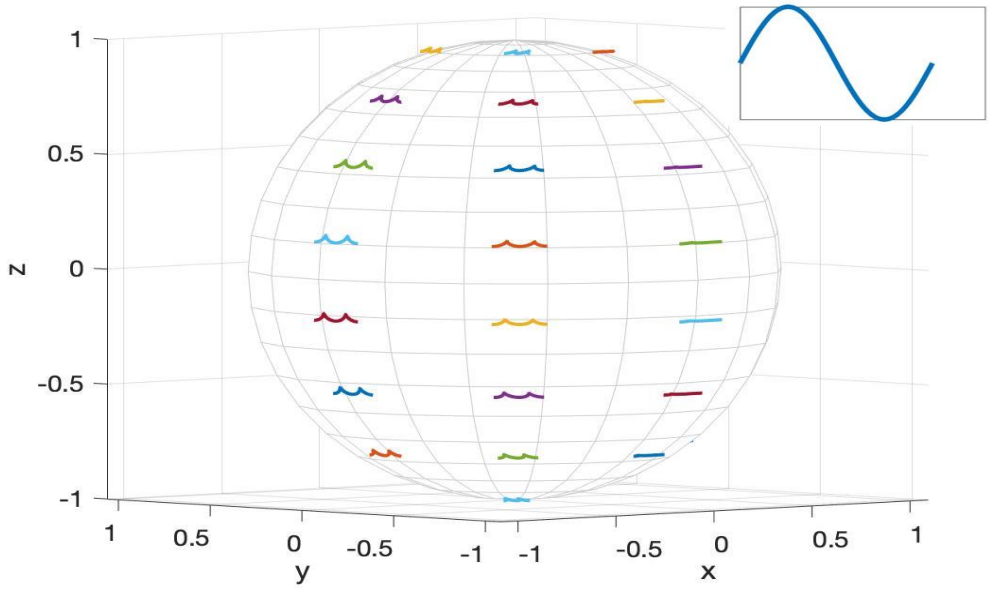

Fig. 6.32 Traces of a single qubit rotation with an in-plane oscillating magnetic field ($|B| = 0.5\,\mathrm{T}$, ω_{res}) applied to the TI thin film for a whole period T_{res} on the Bloch sphere for a qubit starting at different positions. T_{res} and ω_{res} are, respectively, the natural period and frequency of a combined state $\alpha|\Phi_0\rangle + \beta|\Phi_1\rangle, \alpha \neq 0, \beta \neq 0$ that goes back to its original position on the Bloch sphere when there is no field applied. The traces are viewed in a static frame, with $u_0(t=0)$ ($u_1(t=0)$) being the north (south) pole of the Bloch sphere. The inset shows the shape of the pulse. Note that the Bloch sphere is drawn at 90% size to clarify the diagram.

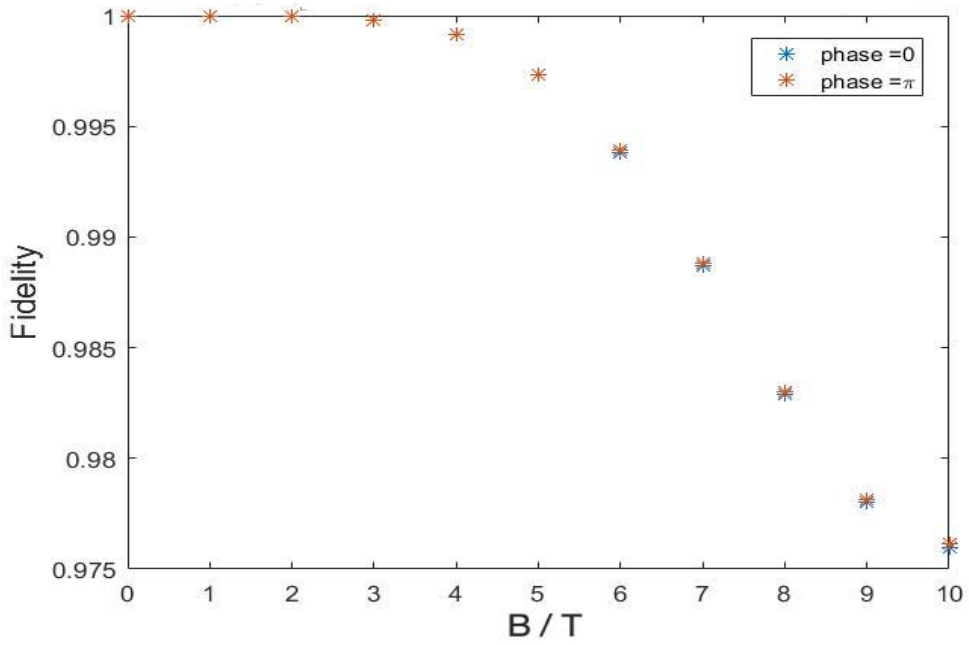

Fig. 6.33 Fidelity of an effective σ_z rotation of a qubit starting at $\theta = 90^\circ$, $\phi = 0^\circ$ on the Bloch sphere with an in-plane oscillating magnetic field of various $|B|$ and frequency $\omega = \omega_{res}$ applied to the TI thin film for T_{res}. θ and ϕ are the conventional polar and azimuthal angles used in spherical coordinate systems. T_{res} and ω_{res} are, respectively, the natural period and frequency of a combined state $\alpha |\Phi_0\rangle + \beta |\Phi_1\rangle$, $\alpha \neq 0, \beta \neq 0$ that goes back to its original position on the Bloch sphere when there is no field applied. Blue points: The cosine pulse is in phase with respect to the driving field. Orange points: The cosine pulse is at π radians out of phase with respect to the driving field. The fidelity of the qubit is high ($> 97.5\%$) and it decreases with the field strength.

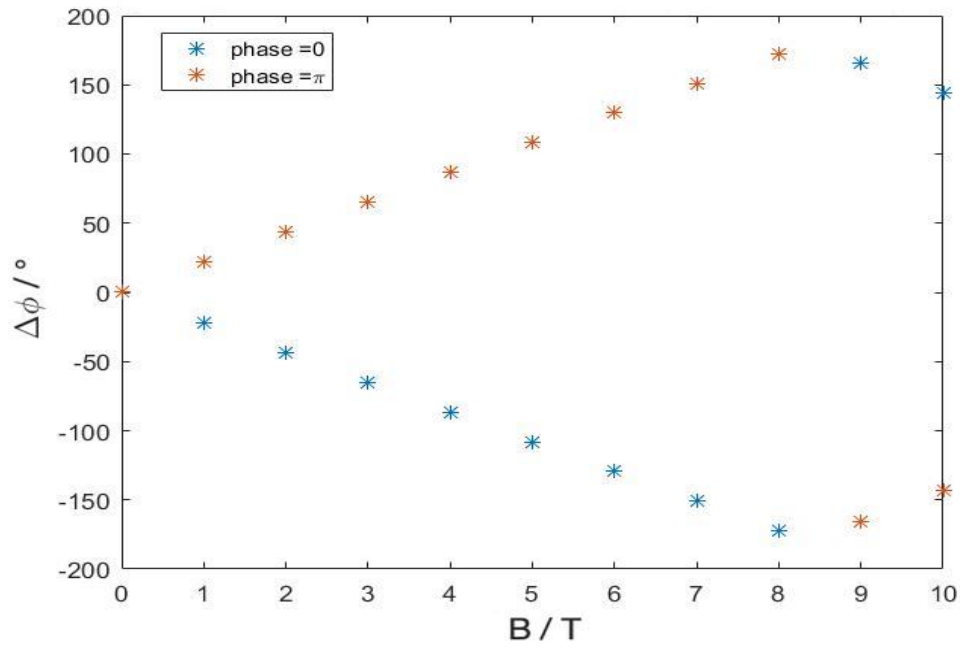

Fig. 6.34 $\Delta\phi$ in an effective σ_z rotation of a qubit starting at $\theta = 90^\circ$, $\phi = 0^\circ$ on the Bloch sphere with an in-plane oscillating magnetic field of various $|B|$ and frequency $\omega = \omega_{res}$ applied to the TI thin film for T_{res}. θ and ϕ are the conventional polar and azimuthal angles used in spherical coordinate systems. T_{res} and ω_{res} are, respectively, the natural period and frequency of a combined state $\alpha|\Phi_0\rangle + \beta|\Phi_1\rangle, \alpha \neq 0, \beta \neq 0$ that goes back to its original position on the Bloch sphere when there is no field applied. Blue points: the cosine pulse is in phase with respect to the driving field. Orange points: the cosine pulse is at π radians out of phase with respect to the driving field. The $\Delta\phi$ in an effective σ_z rotation increases with the field strength.

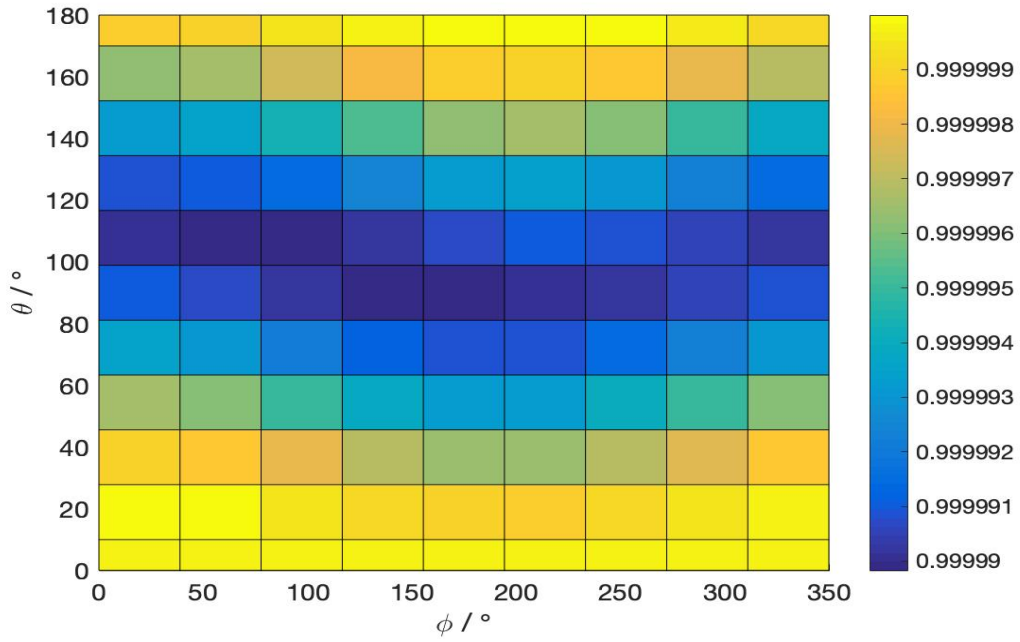

Fig. 6.35 Fidelity of an effective σ_z rotation for $\Delta\phi = 11^\circ$ vs various qubit states (in the range of $\theta \in [0^\circ, 180^\circ]$, $\phi \in [0^\circ, 350^\circ]$) on the Bloch sphere with an in-plane oscillating magnetic field ($|B| = 0.5\,\mathrm{T}$, $\omega = \omega_{res}$) applied to the TI thin film for T_{res}. θ and ϕ are the conventional polar and azimuthal angles used in spherical coordinate systems. T_{res} and ω_{res} are, respectively, the natural period and frequency of a combined state $\alpha|\Phi_0\rangle + \beta|\Phi_1\rangle, \alpha \neq 0, \beta \neq 0$ that goes back to its original position on the Bloch sphere when there is no field applied. This figure shows that the effective σ_z is indeed universal and position-independent. The fidelity is extremely high, which is over 99.999%.

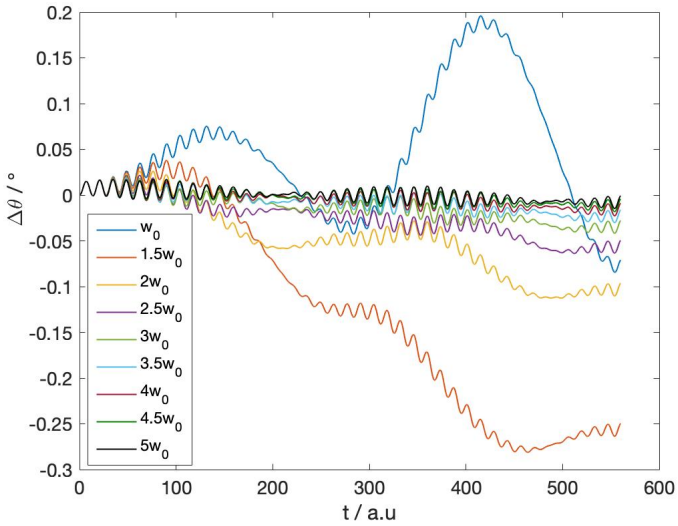

(a)

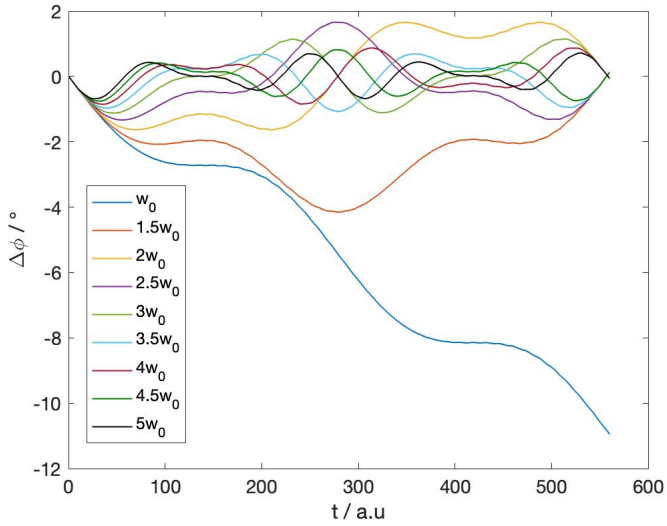

(b)

Fig. 6.36 $\Delta\theta$ (**a**) and $\Delta\phi$ (**b**) in a single qubit rotation with an oscillating magnetic field at various frequencies ($\omega = \omega_{res}$ to $5\omega_{res}$, where $\omega_0 = \omega_{res}$, and $|B| = 0.5\,\mathrm{T}$) of a qubit state at $\theta = 90^\circ, \phi = 90^\circ$ vs time for T_{res}. θ and ϕ are the conventional polar and azimuthal angles used in spherical coordinate systems. T_{res} and ω_{res} are, respectively, the natural period and frequency of a combined state $\alpha\,|\Phi_0\rangle + \beta\,|\Phi_1\rangle\,, \alpha \neq 0, \beta \neq 0$ that goes back to its original position on the Bloch sphere when there is no field applied.

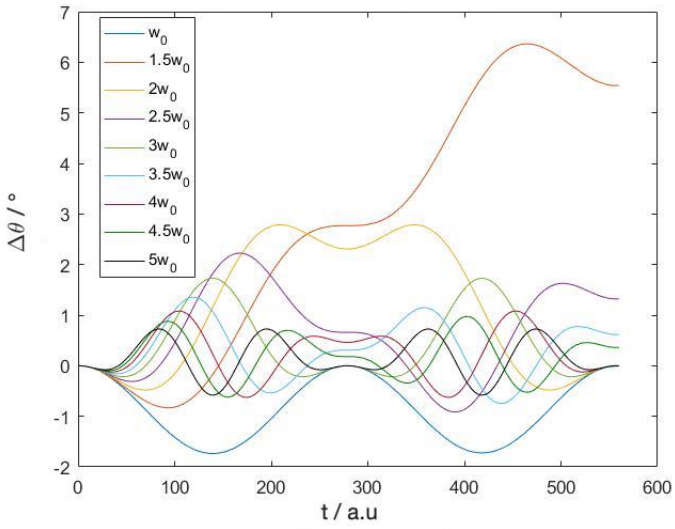

(a)

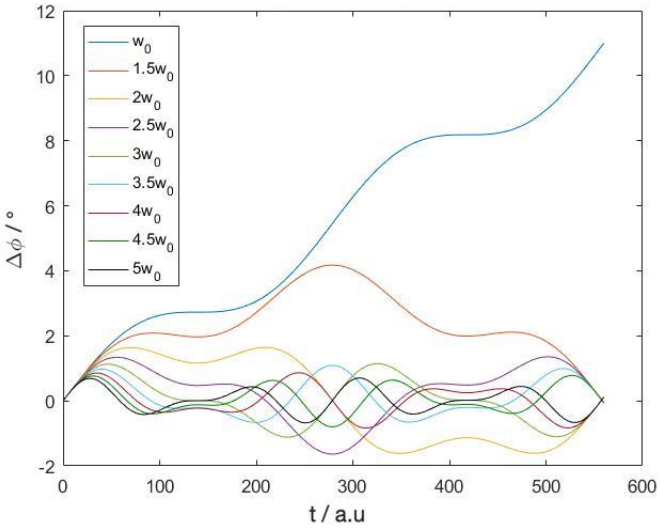

(b)

Fig. 6.37 $\Delta\theta$ (**a**) and $\Delta\phi$ (**b**)in a single qubit rotation with an oscillating magnetic field at various frequencies ($\omega = \omega_{res}$ to $5\omega_{res}$, where $\omega_0 = \omega_{res}$, and $|B| = 0.5\,\mathrm{T}$) of a qubit state at $\theta = 90^\circ, \phi = 0^\circ$ vs time for T_{res}. θ and ϕ are the conventional polar and azimuthal angles used in spherical coordinate systems. T_{res} and ω_{res} are, respectively, the natural period and frequency of a combined state $\alpha\,|\Phi_0\rangle + \beta\,|\Phi_1\rangle\,, \alpha \neq 0, \beta \neq 0$ that goes back to its original position on the Bloch sphere when there is no field applied.

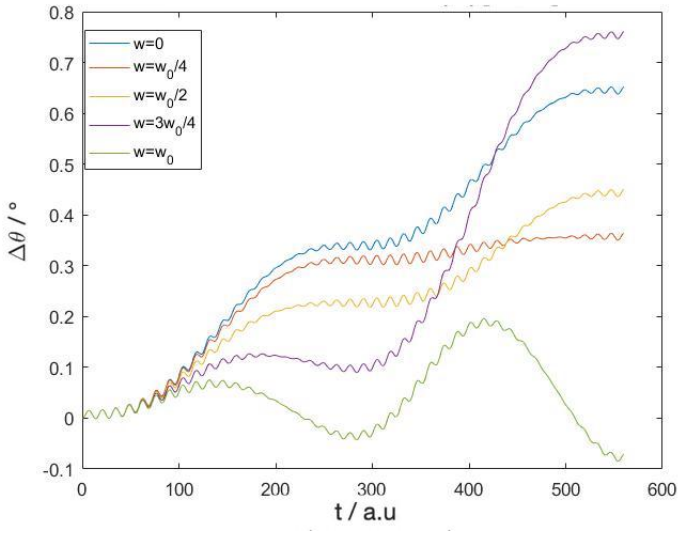

(a)

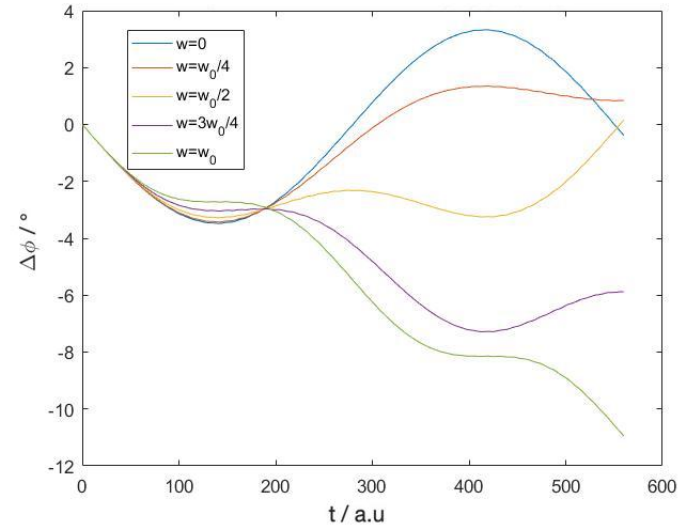

(b)

Fig. 6.38 $\Delta\theta$ (**a**) and $\Delta\phi$ (**b**) in a single qubit rotation with an oscillating magnetic field at various frequencies ($\omega = 0$ to ω_{res}, where $\omega_0 = \omega_{res}$, and $|B| = 0.5\,\mathrm{T}$) of a qubit state at $\theta = 90^\circ, \phi = 90^\circ$ vs time for T_{res}. θ and ϕ are the conventional polar and azimuthal angles used in spherical coordinate systems. T_{res} and ω_{res} are, respectively, the natural period and frequency of a combined state $\alpha\,|\Phi_0\rangle + \beta\,|\Phi_1\rangle\,, \alpha \neq 0, \beta \neq 0$ that goes back to its original position on the Bloch sphere when there is no field applied.

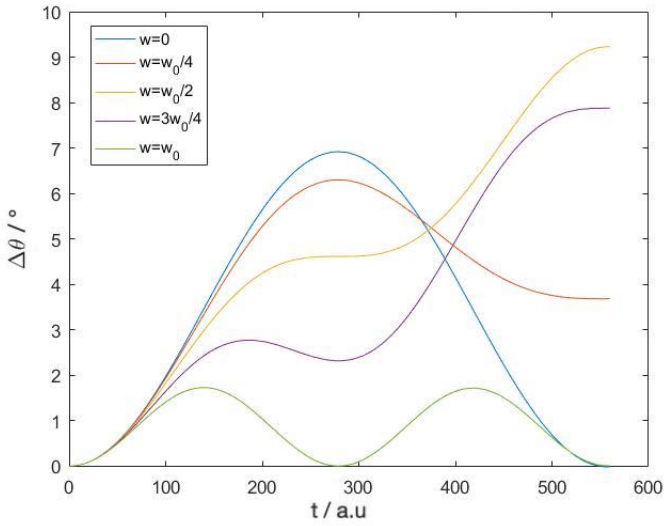

(a)

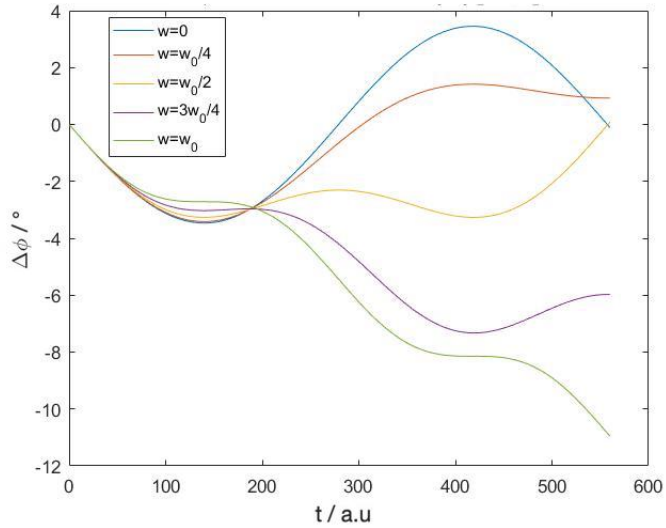

(b)

Fig. 6.39 $\Delta\theta$ (**a**) and $\Delta\phi$ (**b**) in a single qubit rotation with an oscillating magnetic field at various frequencies ($\omega = 0$ to ω_{res}, where $\omega_0 = \omega_{res}$, and $|B| = 0.5\,\mathrm{T}$) of a qubit state at $\theta = 90^\circ$, $\phi = 0^\circ$ vs time for T_{res}. θ and ϕ are the conventional polar and azimuthal angles used in spherical coordinate systems. T_{res} and ω_{res} are, respectively, the natural period and frequency of a combined state $\alpha\left|\Phi_0\right\rangle + \beta\left|\Phi_1\right\rangle, \alpha \neq 0, \beta \neq 0$ that goes back to its original position on the Bloch sphere when there is no field applied.

anisms are similar to those for the charge qubit discussed in Ch. 5. When the field is at the resonant frequency with $\hbar\omega = \Delta\varepsilon$, where $\Delta\varepsilon$ is the band gap energy between the two states on the surface bands, this field will drive the system into a field dressing system and produce Floquet states. The Floquet states are the result of the coherent interaction between the field and TI system. The advantage of this Floquet qubit is that it allows us to pause the operation at any time and resume it later. However, there are still many experimental issues to be explored and solved. As an example, when we apply a periodic magnetic field to the system, a small electric field is generated according to Faraday's law of induction. Since we are interested in surface states and the bulk of a TI is insulating, we can simply view the problem as a wire loop along the xz direction with a magnetic field in the y direction. The voltage V produced is proportional to the rate of change of the magnetic flux encircled by the region:

$$V = -\frac{D\Phi_B}{Dt}, \tag{6.26}$$

with $B = B_0\cos(\omega t)$, which implies that $V \propto AB_0\omega$. Therefore, V can be minimised by constructing a small size system. Also, we should notice that this would be a transverse electric field so it will not cause the state to be transfered from one boundary to another through the bulk and, the spin of the qubit state would not be changed by this electric field. Therefore, as long as we confine our qubit in some region, we can still measure the qubit as before.

6.4 Summary

In this chapter we studied two types of dynamic qubit in an ultra-thin TI film under a periodic electric field and magnetic field. The qubits are defined as dynamic states in the field-interacting TIs. We are able to initialise, rotate the qubit to an arbitrary position on a Bloch sphere and read out the qubit in both cases. Therefore, we have completed our study of various qubit systems found in ultra-thin TI films.

Chapter 7

Conclusion and Future Work

The ultimate aim of this thesis is to study whether an ultra-thin TI film is a suitable platform for quantum computing in terms of initialising, controlling, and measuring a single qubit. This investigation provides an initial theoretical and numerical study of TI qubits under ideal experimental conditions. However, further investigation needs to be carried out, preferably combined with experiments to investigate how to realise the qubit systems in practice. In this chapter, we will summarise our results in the thesis and outline possible further investigation in this area.

7.1 Summary

We have introduced essential concepts to study quantum computing and presented the requirements for building a quantum computer in Ch. 1. We briefly reviewed some active platforms for quantum computation, progress and current challenges in each. We introduced essential concepts in topological field theory which is useful to understand the topological significance of a TI, the low-energy model Hamiltonian of a TI used throughout the thesis, and the Floquet-Bloch theory to study a TI under time-periodic fields in Ch. 2. We introduced the numerical methods used in the thesis in Ch. 3. We presented our results on the investigation of a static charge qubit in an ultra-thin TI film in Ch. 4. We found a static charge qubit that is ultra-fast in terms of operation time and we can generate a position-independent qubit rotation of any desired angles with an electric field control, which is important in single-qubit operations. We can initialise the qubit and measure it at the end of the operation. We investigate a static spin qubit in an ultra-thin TI film in Ch. 5. As the case for the charge qubit, the spin qubit is found to be fast in terms of single-qubit operations. The spin qubit can be initialised and perform position-independent rotations using oscillating magnetic fields. The angle rotated depends on the field strength. We can initialise the qubit and

measure it at the end of the operation. We investigated two types of qubits in field-interacting ultra-thin TI films in Ch. 6. We studied a dynamic charge qubit defined in an ultra-thin TI with a time-periodic electric field. We found that the qubit can be initialised, operated by the standard Amplitude Modulation techniques and measured. We investigated a dynamic spin qubit in an ultra-thin TI under a time-periodic magnetic field. We found that the qubit can be initialised and rotated to arbitrary positions on a Bloch sphere by suitable operation schemes and measured. We have completed our exploration of various qubit systems in an ultra-thin TI film. This is an important first step towards the realisation of using TI systems for quantum computing. This thesis investigates whether we can make a single qubit in an ultra-thin TI film that satisfies the DiVincenzo criteria. There are still many things to explore in this area.

7.2 Future work

In this section, we will discuss possible further investigations in the area. An obvious one is to study in detail how to implement a two-qubit operation in these qubit systems. This is crucial for universal quantum computation. Understanding decoherence mechanisms is also crucial. Experiments investigating decoherence need to be done to push this field forward. Since TI quantum dots are similar to semiconductor quantum dots, the decoherence mechanism could be similar. For a charge qubit, one can study the cotunneling effect in a TI quantum dot; this causes a qubit in the antibonding state to go to the bonding state [49]. The transition rate $\Gamma_{cot} = (8/h)\Delta(\hbar\Gamma)^2/U^2$, with $\hbar$ being the reduced Plank's constant, Δ is the energy difference of the two-level system, Γ is tunnelling rate into the source and drain and U is the electrostatic coupling energy between states $|\phi_0\rangle$ and $|\phi_1\rangle$. Another significant and intrinsic decoherence mechanism in a semiconductor quantum dot is the electron-phonon interaction [49]. The decoherence rate Γ_{sb} predicted by spin-boson model is $\Gamma_{sb} = \frac{4}{\pi} g\Delta \coth(\Delta/2k_B T_{Lat})$, where g is a dimensionless coupling constant, Δ is the energy difference of the two-level system and T_{Lat} is the lattice temperature. By considering those models and carrying out experiments, one can have a better understanding of the decoherence time in a TI quantum dot; this is important for the realization of a TI quantum dot. In a TI, owing to the strong spin-orbit coupling effect, backscattering is forbidden, and this leads to weak anti-localisation in a TI [75], which enhances the conductivity and potentially improves the decoherence time. Moreover, the geometry of a quantum dot is interesting to study. In this thesis, we used localised states at $k = 0$ as our qubits and have ignored the physical shape of the quantum dot. However, the spatial distribution of surface states on the xy plane is interesting to study and may provide useful information in the design of a quantum dot in an experiment. Moreover,

controlling the gap size by external voltages and doping are also of research interest since the pulsing frequency is determined by the gap size. The periodic fields discussed in the thesis might be difficult to obtain owing to experimental limitations, and one may be interested in studying whether a laser field or microwaves could be good substitutes. There are still many possibilities regarding the potential of TI qubits as they are topologically protected qubits with high-fidelity-qubit-operation gates in theory. Therefore, further investigations of this area are worth researching.

References

[1] (2010). *Theory of Confined States in Quantum Dots*, chapter 3, pages 39–66. John Wiley & Sons, Ltd.

[2] Akhlaghi, M. K., Schelew, E., and Young, J. F. (2015). Waveguide integrated superconducting single-photon detectors implemented as near-perfect absorbers of coherent radiation. *Nature Communications*, 6:8233.

[3] Ando, Y. (2013). Topological Insulator Materials. *Journal of the Physical Society of Japan*, 82(10):102001.

[4] Askar, A. and Cakmak, A. S. (1978). Explicit integration method for the time-dependent Schrodinger equation for collision problems. *The Journal of Chemical Physics*, 68(6):2794–2798.

[5] Atatüre, M., Dreiser, J., Badolato, A., Högele, A., Karrai, K., and Imamoglu, A. (2006). Quantum-dot spin-state preparation with near-unity fidelity. *Science*, 312(5773):551–553.

[6] Barenco, A., Bennett, C. H., Cleve, R., DiVincenzo, D. P., Margolus, N., Shor, P., Sleator, T., Smolin, J. A., and Weinfurter, H. (1995). Elementary gates for quantum computation. *Physical Review A*, 52(5):3457–3467.

[7] Barnes, C. H. W., Shilton, J. M., and Robinson, A. M. (2000). Quantum computation using electrons trapped by surface acoustic waves. *Phys. Rev. B*, 62:8410–8419.

[8] Barnes, E. and Das Sarma, S. (2012). Analytically solvable driven time-dependent two-level quantum systems. *Phys. Rev. Lett.*, 109:060401.

[9] Barnes, J. L., Singh, A., Llandro, J., Duffy, L., Stanton, M., Holmes, S., Applegate, M., Phillips, R., Hesjedal, T., and W, C. H. (2019). A low-temperature Kerr effect microscope for the simultaneous magneto-optic and magneto-transport study of magnetic topological insulators. *Measurement Science and Technology*.

[10] Bartels, B. and Mintert, F. (2013). Smooth optimal control with floquet theory. *Phys. Rev. A*, 88:052315.

[11] Benioff, P. (1980). The computer as a physical system: A microscopic quantum mechanical Hamiltonian model of computers as represented by Turing machines. *Journal of Statistical Physics*, 22(5):563–591.

[12] Bennett, C. H., DiVincenzo, D. P., Smolin, J. A., and Wootters, W. K. (1996). Mixed-state entanglement and quantum error correction. *Physical Review A*, 54(5):3824–3851.

[13] BERNEVIG, B. A. and Hughes, T. L. (2013). *Topological Insulators and Topological Superconductors*. Princeton University Press, stu - student edition edition.

[14] Bernevig, B. A., Hughes, T. L., and Zhang, S.-C. (2006). Quantum spin hall effect and topological phase transition in hgte quantum wells. *Science*, 314(5806):1757–1761.

[15] Berry, M. V. (1984). Quantal phase factors accompanying adiabatic changes. *Proceedings of the Royal Society of London. A. Mathematical and Physical Sciences*, 392(1802):45–57.

[16] Bilitewski, T. and Cooper, N. R. (2015). Scattering theory for Floquet-Bloch states. *Physical Review A*, 91(3):33601.

[17] Bluhm, H., Foletti, S., Neder, I., Rudner, M., Mahalu, D., Umansky, V., and Yacoby, A. (2011). Dephasing time of GaAs electron-spin qubits coupled to a nuclear bath exceeding 200. *Nature Physics*, 7(2):109–113.

[18] Boyers, E., Pandey, M., Campbell, D. K., Polkovnikov, A., Sels, D., and Sushkov, A. O. (2019). Floquet-engineered quantum state manipulation in a noisy qubit. *Phys. Rev. A*, 100:012341.

[19] Cerletti, V., Coish, W. A., Gywat, O., and Loss, D. (2005). Recipes for spin-based quantum computing. *Nanotechnology*, 16(4):R27–R49.

[20] Choi, K. and Liu, H. (2016). *Amplitude Modulation*, pages 90–100.

[21] Crane, E., Crane, T., Schuckert, A., Le, N. H., Stockbridge, K., Chick, S., and Fisher, A. J. (2019). Optically controlled entangling gates in randomly doped silicon. *Phys. Rev. B*, 100:064201.

[22] Dawson, C. M. and Nielsen, M. A. (2005). The Solovay-Kitaev algorithm. *arXiv e-prints*, pages quant–ph/0505030.

[23] Dehmelt, H. (1988). A Single Atomic Particle Forever Floating at Rest in Free Space: New Value for Electron Radius. *Physica Scripta*, T22:102–110.

[24] Deutsch, D. and Jozsa, R. (1992). Rapid solution of problems by quantum computation. *Proceedings of the Royal Society of London. Series A: Mathematical and Physical Sciences*, 439(1907):553–558.

[25] Deutsch, D. and Penrose, R. (1985). Quantum theory, the Church–Turing principle and the universal quantum computer. *Proceedings of the Royal Society of London. A. Mathematical and Physical Sciences*, 400(1818):97–117.

[26] DiVincenzo, D. P. (1995). Two-bit gates are universal for quantum computation. *Physical Review A*, 51(2):1015–1022.

[27] DiVincenzo, D. P. (2000). The Physical Implementation of Quantum Computation. *Fortschritte der Physik*, 48(9-11):771–783.

[28] DiVincenzo, D. P., Bacon, D., Kempe, J., Burkard, G., and Whaley, K. B. (2000). Universal quantum computation with the exchange interaction. *Nature*, 408(6810):339–342.

[29] Engel, H.-A., Kouwenhoven, L. P., Loss, D., and Marcus, C. M. (2004). Controlling Spin Qubits in Quantum Dots. *Quantum Information Processing*, 3(1):115–132.

[30] Ferreira, G. J. and Loss, D. (2013). Magnetically defined qubits on 3d topological insulators. *Phys. Rev. Lett.*, 111:106802.

[31] Feynman, R. P. (1982). Simulating physics with computers. *International Journal of Theoretical Physics*, 21(6):467–488.

[32] Fischer, J., Trif, M., Coish, W. A., and Loss, D. (2009). Spin interactions, relaxation and decoherence in quantum dots. *Solid State Communications*, 149(35):1443–1450.

[33] Friis, N., Marty, O., Maier, C., Hempel, C., Holzäpfel, M., Jurcevic, P., Plenio, M. B., Huber, M., Roos, C., Blatt, R., and Lanyon, B. (2018). Observation of Entangled States of a Fully Controlled 20-Qubit System. *Physical Review X*, 8(2):21012.

[34] Fu, L. and Kane, C. L. (2008). Superconducting Proximity Effect and Majorana Fermions at the Surface of a Topological Insulator. *Physical Review Letters*, 100(9):96407.

[35] Fu, L., Kane, C. L., and Mele, E. J. (2007). Topological insulators in three dimensions. *Phys. Rev. Lett.*, 98:106803.

[36] Fujisawa, T., Shinkai, G., Hayashi, T., and Ota, T. (2011). Multiple two-qubit operations for a coupled semiconductor charge qubit. *Physica E: Low-dimensional Systems and Nanostructures*, 43(3):730 – 734. NanoPHYS 09.

[37] Gaebel, T., Domhan, M., Popa, I., Wittmann, C., Neumann, P., Jelezko, F., Rabeau, J. R., Stavrias, N., Greentree, A. D., Prawer, S., Meijer, J., Twamley, J., Hemmer, P. R., and Wrachtrup, J. (2006). Room-temperature coherent coupling of single spins in diamond. *Nature Physics*, 2(6):408–413.

[38] Gerlach, W. and Stern, O. (1922). Der experimentelle Nachweis der Richtungsquantelung im Magnetfeld. *Zeitschrift für Physik*, 9(1):349–352.

[39] Gershenfeld, N. A. and Chuang, I. L. (1997). Bulk Spin-Resonance Quantum Computation. *Science*, 275(5298):350 LP – 356.

[40] Golovach, V. N., Khaetskii, A., and Loss, D. (2004). Phonon-Induced Decay of the Electron Spin in Quantum Dots. *Physical Review Letters*, 93(1):16601.

[41] Gómez-León, A. and Platero, G. (2013). Floquet-Bloch Theory and Topology in Periodically Driven Lattices. *Physical Review Letters*, 110(20):200403.

[42] Gopal, R. K., Singh, S., Chandra, R., and Mitra, C. (2015). Weak-antilocalization and surface dominated transport in topological insulator bi2se2te. *AIP Advances*, 5(4):047111.

[43] Gorman, J., Hasko, D. G., and Williams, D. A. (2005a). Charge-Qubit Operation of an Isolated Double Quantum Dot. *Physical Review Letters*, 95(9):90502.

[44] Gorman, J., Hasko, D. G., and Williams, D. A. (2005b). Charge-qubit operation of an isolated double quantum dot. *Phys. Rev. Lett.*, 95:090502.

[45] Grover, L. K. (1997). Quantum Mechanics Helps in Searching for a Needle in a Haystack. *Physical Review Letters*, 79(2):325–328.

[46] Hasan, M. Z. and Kane, C. L. (2010a). Colloquium: Topological insulators. *Rev. Mod. Phys.*, 82:3045–3067.

[47] Hasan, M. Z. and Kane, C. L. (2010b). Colloquium: Topological insulators. *Reviews of Modern Physics*, 82(4):3045–3067.

[48] Hasan, M. Z. and Moore, J. E. (2011). Three-Dimensional Topological Insulators. *Annual Review of Condensed Matter Physics*, 2(1):55–78.

[49] Hayashi, T., Fujisawa, T., Cheong, H. D., Jeong, Y. H., and Hirayama, Y. (2003a). Coherent manipulation of electronic states in a double quantum dot. *Phys. Rev. Lett.*, 91:226804.

[50] Hayashi, T., Fujisawa, T., Cheong, H. D., Jeong, Y. H., and Hirayama, Y. (2003b). Coherent Manipulation of Electronic States in a Double Quantum Dot. *Physical Review Letters*, 91(22):226804.

[51] He, M., Sun, H., and He, Q. L. (2019). Topological insulator: Spintronics and quantum computations. *Frontiers of Physics*, 14(4):43401.

[52] Huang, G. M., Tarn, T. J., and Clark, J. W. (1983). On the controllability of quantum-mechanical systems. *Journal of Mathematical Physics*, 24(11):2608–2618.

[53] Islam, S., Bhattacharyya, S., Nhalil, H., Banerjee, M., Richardella, A., Kandala, A., Sen, D., Samarth, N., Elizabeth, S., and Ghosh, A. (2019). Low-temperature saturation of phase coherence length in topological insulators. *Phys. Rev. B*, 99:245407.

[54] James, M. (2014). Quantum control theory.

[55] Kane, C. L. and Mele, E. J. (2005). Quantum spin hall effect in graphene. *Phys. Rev. Lett.*, 95:226801.

[56] Keiper, R. (1999). T. Dittrich, P. Hänggi, G.-L. Ingold, B. Kramer, G. Schoen, W. Zwerger: Quantum Transport and Dissipation. *Crystal Research and Technology*, 34(3):411–412.

[57] Khaetskii, A. V. and Nazarov, Y. V. (2001). Spin-flip transitions between Zeeman sublevels in semiconductor quantum dots. *Physical Review B*, 64(12):125316.

[58] Klitzing, K. v., Dorda, G., and Pepper, M. (1980). New Method for High-Accuracy Determination of the Fine-Structure Constant Based on Quantized Hall Resistance. *Physical Review Letters*, 45(6):494–497.

[59] Kloeffel, C. and Loss, D. (2013). Prospects for Spin-Based Quantum Computing in Quantum Dots. *Annual Review of Condensed Matter Physics*, 4(1):51–81.

[60] Knill, E. (2005). Quantum computing with realistically noisy devices. *Nature*, 434(7029):39–44.

[61] Kok, P., Munro, W. J., Nemoto, K., Ralph, T. C., Dowling, J. P., and Milburn, G. J. (2007). Linear optical quantum computing with photonic qubits. *Reviews of Modern Physics*, 79(1):135–174.

[62] Kolodrubetz, M. H., Nathan, F., Gazit, S., Morimoto, T., and Moore, J. E. (2018). Topological Floquet-Thouless Energy Pump. *Physical Review Letters*, 120(15):150601.

[63] König, M., Buhmann, H., Molenkamp, L. W., Hughes, T., Liu, C. X., Qi, X. L., and Zhang, S. C. (2008). The quantum spin Hall effect: Theory and experiment. *Journal of the Physical Society of Japan*, 77(3):1–14.

[64] König, M., Wiedmann, S., Brüne, C., Roth, A., Buhmann, H., Molenkamp, L. W., Qi, X.-L., and Zhang, S.-C. (2007). Quantum spin hall insulator state in hgte quantum wells. *Science*, 318(5851):766–770.

[65] König, M., Wiedmann, S., Brüne, C., Roth, A., Buhmann, H., Molenkamp, L. W., Qi, X.-L., and Zhang, S.-C. (2007). Quantum Spin Hall Insulator State in HgTe Quantum Wells. *Science*, 318(5851):766 LP – 770.

[66] Koppens, F. H. L., Buizert, C., Tielrooij, K. J., Vink, I. T., Nowack, K. C., Meunier, T., Kouwenhoven, L. P., and Vandersypen, L. M. K. (2006). Driven coherent oscillations of a single electron spin in a quantum dot. *Nature*, 442(7104):766–771.

[67] Koppens, F. H. L., Nowack, K. C., and Vandersypen, L. M. K. (2008). Spin echo of a single electron spin in a quantum dot. *Phys. Rev. Lett.*, 100:236802.

[68] Ladd, T. D., Jelezko, F., Laflamme, R., Nakamura, Y., Monroe, C., and O'Brien, J. L. (2010). Quantum computers. *Nature*, 464:45.

[69] Lepage, H. V., Lasek, A. A., Arvidsson-Shukur, D. R. M., and Barnes, C. H. W. (2020). Entanglement generation via power-of-swap operations between dynamic electron-spin qubits. *Phys. Rev. A*, 101:022329.

[70] Liao, J., Ou, Y., Liu, H., He, K., Ma, X., Xue, Q.-K., and Li, Y. (2017). Enhanced electron dephasing in three-dimensional topological insulators. *Nature Communications*, 8(1):16071.

[71] Linder, J., Yokoyama, T., and Sudbø, A. (2009). Anomalous finite size effects on surface states in the topological insulator Bi2Se3. *Physical Review B*, 80(20):205401.

[72] Liu, C.-X., Qi, X.-L., Zhang, H., Dai, X., Fang, Z., and Zhang, S.-C. (2010a). Model Hamiltonian for topological insulators. *Physical Review B*, 82(4):45122.

[73] Liu, C.-X., Zhang, H., Yan, B., Qi, X.-L., Frauenheim, T., Dai, X., Fang, Z., and Zhang, S.-C. (2010b). Oscillatory crossover from two-dimensional to three-dimensional topological insulators. *Physical Review B*, 81(4):41307.

[74] Loss, D. and DiVincenzo, D. P. (1998). Quantum computation with quantum dots. *Physical Review A*, 57(1):120–126.

[75] Lu, H.-Z. and Shen, S.-Q. (2014). Weak localization and weak anti-localization in topological insulators. In *Proc.SPIE*, volume 9167.

[76] Lu, W., Ji, Z., Pfeiffer, L., West, K. W., and Rimberg, A. J. (2003). Real-time detection of electron tunnelling in a quantum dot. *Nature*, 423(6938):422–425.

[77] Luttinger, J. M. and Kohn, W. (1955). Motion of electrons and holes in perturbed periodic fields. *Phys. Rev.*, 97:869–883.

[78] Maestri, J. J. V., Landau, R. H., and Páez, M. J. (2000). Two-particle Schrödinger equation animations of wave packet–wave packet scattering. *American Journal of Physics*, 68(12):1113–1119.

[79] Manin, Y. (1980). Computable and noncomputable (in russian). *Sov. Radio.*, pages 13–15.

[80] Mason, N., Biercuk, M. J., and Marcus, C. M. (2004). Local Gate Control of a Carbon Nanotube Double Quantum Dot. *Science*, 303(5658):655 LP – 658.

[81] Micheli, A., Brennen, G. K., and Zoller, P. (2006). A toolbox for lattice-spin models with polar molecules. *Nature Physics*, 2:341.

[82] Mishra, S. K., Satpathy, S., and Jepsen, O. (1997). Electronic structure and thermoelectric properties of bismuth telluride and bismuth selenide. *Journal of Physics: Condensed Matter*, 9(2):461–470.

[83] Morton, J. J. L., Tyryshkin, A. M., Ardavan, A., Benjamin, S. C., Porfyrakis, K., Lyon, S. A., and Briggs, G. A. D. (2005). Bang–bang control of fullerene qubits using ultrafast phase gates. *Nature Physics*, 2:40.

[84] Müller, K., Rundquist, A., Fischer, K. A., Sarmiento, T., Lagoudakis, K. G., Kelaita, Y. A., Sánchez Muñoz, C., del Valle, E., Laussy, F. P., and Vučković, J. (2015). Coherent Generation of Nonclassical Light on Chip via Detuned Photon Blockade. *Physical Review Letters*, 114(23):233601.

[85] Nielsen, M. A. and Chuang, I. L. (2011). *Quantum Computation and Quantum Information: 10th Anniversary Edition*. Cambridge University Press, New York, NY, USA, 10th edition.

[86] of Sciences Engineering and Medicine (2019). *Quantum Computing: Progress and Prospects*. The National Academies Press, Washington, DC.

[87] Oka, T. and Aoki, H. (2009). Photovoltaic Hall effect in graphene. *Physical Review B*, 79(8):81406.

[88] Oka, T. and Kitamura, S. (2019). Floquet Engineering of Quantum Materials. *Annual Review of Condensed Matter Physics*, 10(1):387–408.

[89] Paul, W. (1990). Electromagnetic traps for charged and neutral particles. *Reviews of Modern Physics*, 62(3):531–540.

[90] Petersson, K. D., Smith, C. G., Anderson, D., Atkinson, P., Jones, G. A. C., and Ritchie, D. A. (2009). Microwave-driven transitions in two coupled semiconductor charge qubits. *Phys. Rev. Lett.*, 103:016805.

[91] Petta, J. R., Johnson, A. C., Taylor, J. M., Laird, E. A., Yacoby, A., Lukin, M. D., Marcus, C. M., Hanson, M. P., and Gossard, A. C. (2005). Coherent manipulation of coupled electron spins in semiconductor quantum dots. *Science*, 309(5744):2180–2184.

[92] Preskill, J. (1998). Reliable quantum computers. *Proceedings of the Royal Society of London. Series A: Mathematical, Physical and Engineering Sciences*, 454(1969):385–410.

[93] Rachel, S. (2018). Interacting topological insulators: a review. *Reports on Progress in Physics*, 81(11):116501.

[94] Rippe, L., Julsgaard, B., Walther, A., Ying, Y., and Kröll, S. (2008). Experimental quantum-state tomography of a solid-state qubit. *Physical Review A*, 77(2):22307.

[95] Roushan, P., Seo, J., Parker, C. V., Hor, Y. S., Hsieh, D., Qian, D., Richardella, A., Hasan, M. Z., Cava, R. J., and Yazdani, A. (2009). Topological surface states protected from backscattering by chiral spin texture. *Nature*, 460(7259):1106–1109.

[96] Sánchez, J. C. R., Vila, L., Desfonds, G., Gambarelli, S., Attané, J. P., De Teresa, J. M., Magén, C., and Fert, A. (2013). Spin-to-charge conversion using Rashba coupling at the interface between non-magnetic materials. *Nature Communications*, 4:2944.

[97] Schleser, R., Ruh, E., Ihn, T., Ensslin, K., Driscoll, D. C., and Gossard, A. C. (2004). Time-resolved detection of individual electrons in a quantum dot. *Applied Physics Letters*, 85(11):2005–2007.

[98] Schlosshauer, M. (2005). Decoherence, the measurement problem, and interpretations of quantum mechanics. *Reviews of Modern Physics*, 76(4):1267–1305.

[99] Schnyder, A. P., Ryu, S., Furusaki, A., and Ludwig, A. W. W. (2008). Classification of topological insulators and superconductors in three spatial dimensions. *Physical Review B*, 78(19):195125.

[100] Sebastiano, F., Homulle, H., Patra, B., Incandela, R., Dijk, J., Song, L., Babaie, M., Vladimirescu, A., and Charbon, E. (2017). *Cryo-CMOS Electronic Control for Scalable Quantum Computing: Invited*.

[101] Shinkai, G., Hayashi, T., Ota, T., and Fujisawa, T. (2009). Correlated coherent oscillations in coupled semiconductor charge qubits. *Phys. Rev. Lett.*, 103:056802.

[102] Shirley, J. H. (1965). Solution of the Schr\"odinger Equation with a Hamiltonian Periodic in Time. *Physical Review*, 138(4B):B979–B987.

[103] Shor, P. (1997). Polynomial-Time Algorithms for Prime Factorization and Discrete Logarithms on a Quantum Computer. *SIAM Journal on Computing*, 26(5):1484–1509.

[104] Silverstone, J. W., Bonneau, D., O'Brien, J. L., and Thompson, M. G. (2016). Silicon Quantum Photonics. *IEEE Journal of Selected Topics in Quantum Electronics*, 22(6):390–402.

[105] Steane, A. M. (1996). Error Correcting Codes in Quantum Theory. *Physical Review Letters*, 77(5):793–797.

[106] Thouless, D. J., Kohmoto, M., Nightingale, M. P., and den Nijs, M. (1982). Quantized Hall Conductance in a Two-Dimensional Periodic Potential. *Physical Review Letters*, 49(6):405–408.

[107] Tokura, Y., Yasuda, K., and Tsukazaki, A. (2019). Magnetic topological insulators. *Nature Reviews Physics*, 1(2):126–143.

[108] Trauzettel, B., Bulaev, D. V., Loss, D., and Burkard, G. (2007). Spin qubits in graphene quantum dots. *Nature Physics*, 3:192.

[109] Trotter, H. F. (1959). On the Product of Semi-Groups of Operators. *Proceedings of the American Mathematical Society*, 10(4):545–551.

[110] Turing, A. M. (1937). On Computable Numbers, with an Application to the Entscheidungsproblem. *Proceedings of the London Mathematical Society*, s2-42(1):230–265.

[111] van der Wiel, W. G., De Franceschi, S., Elzerman, J. M., Fujisawa, T., Tarucha, S., and Kouwenhoven, L. P. (2002). Electron transport through double quantum dots. *Rev. Mod. Phys.*, 75:1–22.

[112] van der Ziel, J. P., Pershan, P. S., and Malmstrom, L. D. (1965). Optically-Induced Magnetization Resulting from the Inverse Faraday Effect. *Physical Review Letters*, 15(5):190–193.

[113] van Weert, M. H. M., Akopian, N., Perinetti, U., van Kouwen, M. P., Algra, R. E., Verheijen, M. A., Bakkers, E. P. A. M., Kouwenhoven, L. P., and Zwiller, V. (2009). Selective Excitation and Detection of Spin States in a Single Nanowire Quantum Dot. *Nano Letters*, 9(5):1989–1993.

[114] Vandersypen, L. M. K., Elzerman, J. M., Schouten, R. N., Willems van Beveren, L. H., Hanson, R., and Kouwenhoven, L. P. (2004). Real-time detection of single-electron tunneling using a quantum point contact. *Applied Physics Letters*, 85(19):4394–4396.

[115] Veldhorst, M., Yang, C. H., Hwang, J. C. C., Huang, W., Dehollain, J. P., Muhonen, J. T., Simmons, S., Laucht, A., Hudson, F. E., Itoh, K. M., Morello, A., and Dzurak, A. S. (2015). A two-qubit logic gate in silicon. *Nature*, 526(7573):410–414.

[116] Verdeny, A., Rudnicki, L., Müller, C. A., and Mintert, F. (2014). Optimal control of effective hamiltonians. *Phys. Rev. Lett.*, 113:010501.

[117] Visscher, P. B. (1991). A fast explicit algorithm for the time-dependent Schrödinger equation. *Computers in Physics*, 5(6):596–598.

[118] von Neumann, J. and Goldstine, H. H. (1947). Numerical inverting of matrices of high order. *Bull. Amer. Math. Soc.*, 53(11):1021–1099.

[119] Wang, H., Li, W., Jiang, X., He, Y.-M., Li, Y.-H., Ding, X., Chen, M.-C., Qin, J., Peng, C.-Z., Schneider, C., Kamp, M., Zhang, W.-J., Li, H., You, L.-X., Wang, Z., Dowling, J., Höfling, S., Lu, C.-Y., and Pan, J.-W. (2018a). Toward Scalable Boson Sampling with Photon Loss. *Physical Review Letters*, 120(23):230502.

[120] Wang, X.-L., Luo, Y.-H., Huang, H.-L., Chen, M.-C., Su, Z.-E., Liu, C., Chen, C., Li, W., Fang, Y.-Q., Jiang, X., Zhang, J., Li, L., Liu, N.-L., Lu, C.-Y., and Pan, J.-W. (2018b). 18-Qubit Entanglement with Six Photons' Three Degrees of Freedom. *Physical Review Letters*, 120(26):260502.

[121] Wang, Y. H., Steinberg, H., Jarillo-Herrero, P., and Gedik, N. (2013). Observation of Floquet-Bloch States on the Surface of a Topological Insulator. *Science*, 342(6157):453 LP – 457.

[122] Xia, Y., Qian, D., Hsieh, D., Wray, L., Pal, A., Lin, H., Bansil, A., Grauer, D., Hor, Y. S., Cava, R. J., and Hasan, M. Z. (2009). Observation of a large-gap topological-insulator class with a single Dirac cone on the surface. *Nature Physics*, 5(6):398–402.

[123] Yin, J., Cao, Y., Li, Y.-H., Liao, S.-K., Zhang, L., Ren, J.-G., Cai, W.-Q., Liu, W.-Y., Li, B., Dai, H., Li, G.-B., Lu, Q.-M., Gong, Y.-H., Xu, Y., Li, S.-L., Li, F.-Z., Yin, Y.-Y., Jiang, Z.-Q., Li, M., Jia, J.-J., Ren, G., He, D., Zhou, Y.-L., Zhang, X.-X., Wang, N., Chang, X., Zhu, Z.-C., Liu, N.-L., Chen, Y.-A., Lu, C.-Y., Shu, R., Peng, C.-Z., Wang, J.-Y., and Pan, J.-W. (2017). Satellite-based entanglement distribution over 1200 kilometers. *Science*, 356(6343):1140 LP – 1144.

[124] Zeh, H. D. (1970). On the interpretation of measurement in quantum theory. *Foundations of Physics*, 1(1):69–76.

[125] Zener, C. and Fowler, R. H. (1934). A theory of the electrical breakdown of solid dielectrics. *Proceedings of the Royal Society of London. Series A, Containing Papers of a Mathematical and Physical Character*, 145(855):523–529.

[126] Zhang, H., Liu, C.-X., Qi, X.-L., Dai, X., Fang, Z., and Zhang, S.-C. (2009). Topological insulators in Bi2Se3, Bi2Te3 and Sb2Te3 with a single Dirac cone on the surface. *Nature Physics*, 5:438.

[127] Zhang, Y., He, K., Chang, C.-Z., Song, C.-L., Wang, L.-L., Chen, X., Jia, J.-F., Fang, Z., Dai, X., Shan, W.-Y., Shen, S.-Q., Niu, Q., Qi, X.-L., Zhang, S.-C., Ma, X.-C., and Xue, Q.-K. (2010). Crossover of the three-dimensional topological insulator Bi2Se3 to the two-dimensional limit. *Nature Physics*, 6:584.